LIFR-Mediated Tumor Dormancy and Mechanisms of Breast Cancer Dissemination to Bone

By

Miranda Elise Clements

Dissertation

Submitted to the Faculty of the

Graduate School of Vanderbilt University

in partial fulfillment of the requirements

for the degree of

DOCTOR OF PHILOSOPHY

in

Cancer Biology

May 10, 2019

Nashville, Tennessee

Approved:

Alissa Weaver, M.D. Ph.D.

Barbara Fingleton, Ph.D.

Julie Sterling, Ph.D.

Thomas Stricker, M.D. Ph.D.

Rachelle Johnson, Ph.D.

To my parents, for your endless love, support, and guidance

and

To my husband, for your unwavering encouragement, understanding, and love.

ACKNOWLEDGEMENTS

The work presented in this dissertation was made possible by the financial support of the Microenvironmental Influences in Cancer Training Program, the R00 “Characterization of breast cancer dormancy in bone” (Rachelle Johnson), and the DoD Breakthrough Award Level 2 “Targeting histone modifications to promote LIFR and tumor dormancy” (Rachelle Johnson). This work would also not have been possible without the support and guidance of many individuals during my graduate career.

First, I am truly thankful for my mentor, Rachelle Johnson, who has been an endless source of encouragement and support. My time in her lab has provided me invaluable opportunities to flourish as a scientist and a person. Her enthusiasm for science and dedication to mentoring the next generation of scientists have truly inspired me and strengthened my love of science. I would also like to thank the members of my dissertation committee, Alissa Weaver, Barbara Fingleton, Julie Sterling, and Tom Stricker, for their continued support throughout my training. I am incredibly appreciative of your constructive criticism and guidance.

I would also like to thank the many “unofficial” mentors who have helped me navigate graduate school and become lifelong friends. To Lejla Pasic, Romek Mrozowski, and Kasia Ludwik, I cannot thank you enough for taking me under your wings and teaching me everything you know. Without you all, I would not be the scientist that I am today. To Erica Shannon, Erin Breland, and Carissa Jones, thank you for being an amazing support system, keeping me sane, and for the many wonderful adventures.

To the members of the Johnson lab, you have all made graduate school more enjoyable. To Vera Todd, Tolu Omokehinde, and Courtney Edwards, it has been a pleasure watching you grow as scientists and I wish you all the best in graduate/medical school. To Lawrence Vecchi III and Jasmine Johnson, thank you for all your help and for keeping the lab afloat. To Dhivyaa Anandan and Alec Jotte, I have truly enjoyed your inquisitiveness in lab and cannot wait to see where life takes you. To Lauren Holtslander, there are no words to describe how proud I am to be “your graduate student” and of the independent, driven, and inspiring young woman you have become. I am incredibly thankful for your enthusiasm and positive energy even after seemingly endless hours in lab.

Finally, none of this would have been possible without the love and support of my family. To my parents, Robert and Denise, thank you for being my biggest supporters and always pushing me to pursue my dreams. To my grandparents, Dick, Shirley, Sandra, and stepmother Jo, your continued support and encouragement means more than you will ever know. To my husband, Greg, I am forever grateful for you. Your love and support have meant the world to me and I cannot thank you enough for helping me through this journey.

Table of Contents

LIST OF TABLES

Table **Page**

LIST OF FIGURES

Figure **Page**

ABBREVIATIONS

ADAMTS1	ADAM Metallopeptidase with Thrombospondin Type 1 Motif 1
AKT	RAC-alpha Serine/Threonine-Protein Kinase
AMOT	Angiomotin
ANOVA	Analysis of Variance
ANXA2	Annexin A2
ANXA2R	Annexin A2 receptor
Axl	Axl Tyrosine Kinase
B2M	Beta-2-Microglobulin
BMP	Bone Morphogenetic Protein
BSA	Bovine Serum Albumin
CCL2	C-C Motif Chemokine Ligand 2
CD146	Melanoma Cell Adhesion Molecule
CD298	Sodium/potassium-transporting ATPase Subunit Beta-3
CD62E	E-selectin
CDH1	E-cadherin
CDH2	N-cadherin
ChIP	Chromatin Immunoprecipitation
CSC	Cancer Stem Cell
CTGF	Connective Tissue Growth Factor.
CTV	CellTrace Violet
CX3CR1	CX3C chemokine receptor 1
CXCL12	C-X-C Motif Chemokine Ligand 12
CXCR4	C-X-C Chemokine Receptor Type 4
CYTIP	Cytohesin 1 Interacting Protein
DAPI	4',6-Diamidino-2-Phenylindole
DKK1	Dickkopf WNT Signaling Pathway Inhibitor 1
DMEM	Dulbecco’s Modified Eagle’s Media
DMSO	Dimethyl Sulfoxide
DNMT	DNA Methyltransferase
DTC	Disseminated Tumor Cell
DUSP4	Dual Specificity Phosphatase 4

E2	17β-estradiol
EDTA	Ethylenediaminetetraacetic Acid
EGF	Epidermal Growth Factors
EpCAM	Epithelial Cell Adhesion Molecule
ER	Estrogen Receptor
ERK	Extracellular Signal–Regulated Kinase
FBS	Fetal Bovine Serum
FGF	Fibroblast Growth Factor
GAS6	Growth Arrest-Specific Protein 6
GFP	Green Fluorescent Protein
GLI2	GLI Family Zinc Finger 2
GP130	Glycoprotein 130
HDAC	Histone Deacetylase
HDACi	Histone Deacetylase inhibitors
HIF	Hypoxia Inducible Factor
HMBS	Hydroxymethylbilane Synthase
HPRT1	Hypoxanthine Phosphoribosyltransferase 1
HSC	Hematopoietic Stem Cell
HSPB1	Heat Shock Protein Family B (Small) Member 1
IGF1R	Insulin Like Growth Factor 1 Receptor
IL-11	Interleukin 11
IL-6	Interleukin 6
IRF	Interferon Regulatory Factor
ITGA5	Integrin Alpha 5
JAG1	Jagged1
KRT18	Keratin-18
LIF	Leukemia Inhibitory Factor
LIFR	Leukemia Inhibitory Factor Receptor
LOX	Lysyl Oxidase
MAPK	Mitogen Activated Protein Kinase
MCP1	Monocyte Chemotactic Protein-1
MERTK	MER Proto-oncogene Tyrosine Kinase
MMP1	Matrix Metallopeptidase 1
MSK1	Mitogen- and Stress-Activated Kinase 1

NR2F1	Nuclear Receptor Subfamily 2 Group F Member 1
OSM	Oncostatin M
p38 MAPK	Mitogen-Activated Protein Kinase
PARP	Poly ADP Ribose Polymerase
PBS	Phosphate Buffered Saline
PCR	Polymerase Chain Reaction
PMN	Pre-Metastatic Niche
PREX1	PIP3 Dependent Rac Exchange Factor 1
PTHR1	Parathyroid Hormone 1 Receptor
PTHrP	Parathyroid Hormone-related Protein
RANKL	Receptor Activator of NFκB Ligand
RARβ	Retinoic Acid Receptor Beta
ROCK	Rho-associated Kinase
RPPA	Reverse Phase Protein Array
RUNX2	Runt-related transcription factor 2
SASP	Senescence-associated Secretory Phenotype
shRNA	Small Hairpin RNA
siRNA	Small Interfering RNA
SOX9	(Sex-Determining Region Y)-Box 9
STAT3	Signal Transducer and Activator of Transcription 3
TGFβ2	Transforming Growth Factor-beta 2
TSP1	Thrombospondin 1
TUNEL	Terminal Deoxynucleotidyl Transferase dUTP Nick End Labeling
Tyro3	Tyrosine-Protein Kinase Receptor
uPAR	Urokinase Plasminogen Activator Receptor
VCAM-1	Vascular Cell Adhesion Molecule-1
VEGF	Vascular Endothelial Growth Factor

CHAPTER I

INTRODUCTION

Text adapted from: Sowder, ME and Johnson RW. Bone as a preferential site for metastasis. *JBMR Plus* (in press). December 2018. doi:10.1002/jbm4.10126.

Overview

The mechanisms that regulate tumor cell dissemination from a primary tumor and the establishment of a metastasis are complex and poorly understood. Metastasis is the leading cause of cancer-related deaths but disseminated tumor cells (DTCs) encounter multiple challenges, making metastatic progression a highly inefficient process. Initially, DTCs must survive in the circulation before homing to and colonizing a foreign microenvironment in a distant organ. Upon arrival at the metastatic site, DTCs enter a dormant state for some period of time, often months to decades, before eventually becoming reactivated and developing into an overt metastasis. An extensive body of clinical and experimental research supports Stephen Paget's "seed and soil" hypothesis (1) that proposed tumor cells preferentially metastasize to particular secondary sites. This non-random tumor cell distribution, referred to as metastatic organotropism, is likely facilitated in part by blood flow dynamics, but most prominently by the fertile "soil" at distant sites (2).

Metastasis to the bone occurs in ~60% of patients with metastatic breast or prostate cancer and to a lesser extent in other cancers, including lung and melanoma (3). The bone microenvironment provides a uniquely fertile soil for the homing of DTCs for several reasons. First, the bone marrow houses numerous cell types implicated in metastatic progression, including hematopoietic and mesenchymal stem cells, endothelial cells, osteoblasts, and osteoclasts, and the bone matrix itself provides a rich source of growth factors and cytokines (4). Second, the bone marrow is the primary site for hematopoietic stem cell (HSC) maintenance and contains two specialized niches: the endosteal "osteoblastic" niche and the perivascular niche (5). These niches are established and maintained by systemic signals and HSC interaction with resident cells, including osteoblasts and endothelial cells. Finally, the vasculature of the bone marrow results in varying oxygen levels ranging from <1% to 6% throughout the bone marrow, making the bone a particularly hypoxic tissue (Figure 1) (6). Thus, the bone marrow provides an ideal microenvironment for metastasis and ample opportunities for DTCs to co-opt these physiological niches to promote their own survival and outgrowth.

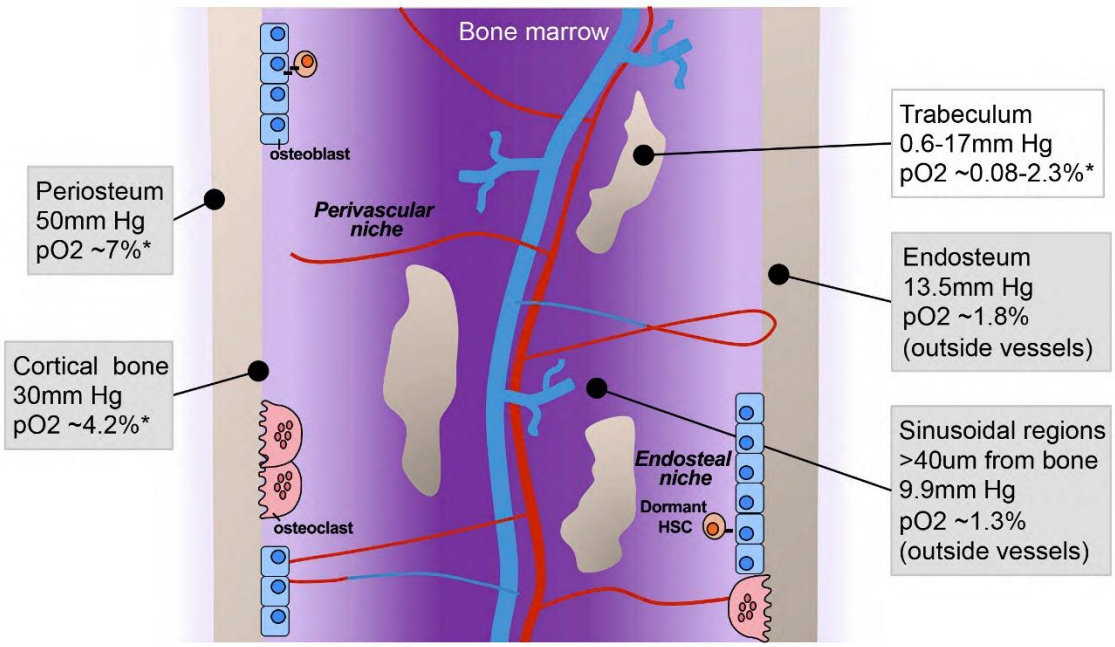

Figure 1. The hypoxic bone marrow microenvironment. The bone marrow is a naturally hypoxic microenvironment, with anatomical fluctuations in oxygen levels. Gray boxes = oxygen levels derived from calvarial measurements. White box = oxygen levels derived from mathematical modeling of long bone measurements. * = estimated conversion to pO2 from mm Hg. Adapted from (6).

Genetic drivers of bone metastasis

Metastatic progression has traditionally been thought of as a late event that occurs following numerous genetic or epigenetic aberrations; however, recent literature suggests that dissemination can occur early in tumor progression (7, 8). Currently, two fundamental models of metastatic progression exist: linear progression and parallel progression. The linear progression model implies that metastatic founder cells evolve with the primary tumor, arising late in tumor progression, followed by delayed dissemination and adaptation to the microenvironment at the distant metastatic site. In contrast, parallel progression suggests early dissemination and acquisition of additional mutations in the metastatic tumor cells that are not detected in the primary tumor.

Advancement of single-cell genomic analyses that can identify rare clonal populations and evaluate genetic alterations in DTCs has allowed for investigation into the biological significance of these progression models. The competing views and the evidence for each model in various tumor types have recently been reviewed (9). In the context of bone metastasis, early evidence of parallel progression came from analysis of DTCs in the bone marrow of breast cancer patients with and without clinically detectable metastasis (10, 11). Patients without metastasis harbored DTCs with less genetic heterogeneity compared to the primary tumor or DTCs isolated from M1 patients (10, 11). These findings suggest that metastatic cells in the bone follow the parallel progression model, acquiring additional genetic abnormalities after dissemination to a distant site. Similar results have been reported for patients with prostate cancer (12, 13). In support of these clinical data, studies using murine models of breast cancer demonstrated that invasive sub-populations disseminate from very early lesions to distant organs and eventually initiate overt metastasis (14, 15). Despite these corroborative findings, it is possible these genomic analyses failed to capture every unique subclone within the primary tumor and DTC populations. Thus, the presence of a rare subclone within the primary tumor that is able to give rise to DTCs and metastasis cannot be excluded.

While these comparative genomic studies have illuminated the timing of tumor cell dissemination to distant metastatic sites, they have not provided considerable insight into the specific mechanisms controlling the ability of tumor cells to disseminate and home to a distant site. Thus, gene expression studies comparing primary human tumors and respective bone metastases have been performed to identify metastasis-promoting genes that are associated with bone metastasis and poor outcome. Pioneering work by the Massague lab reported a bone metastasis 102 gene signature (16), which included genes involved in bone marrow homing (CXCR4), extracellular matrix alteration (MMP1, ADAMTS1, proteoglycan-1), angiogenesis

(FGF5, CTGF), and osteoclastogenesis (IL11). Several of these genes were shown to cooperate to promote bone colonization and tumor-induced osteolysis *in vivo*, and likely cooperate with other unidentified genes to promote this phenotype. Subsequently, several other bone metastasis gene signatures, including signatures driven by Src-dependent (17) or Irf7-regulated genes (18), have been described. Of important note, very little overlap occurs between the reported gene signatures, which may be due to tumor heterogeneity or differences in tumor source (e.g. analysis of primary tumors versus metastatic tumors to predict bone metastasis). Thus, the clinical significance and applicability of these gene signatures remains unclear.

To date, no metastasis-specific mutations have been identified, implying that numerous genes become altered and act cooperatively to drive metastatic progression (19). These global gene expression changes are proposed to be a result of alterations to the epigenetic landscape, including DNA methylation and histone acetylation modifications (20, 21). Among the most frequently mutated genes in human cancers are epigenetic modifying enzymes (21), which are likely responsible for the increased DNA and histone methylation observed in tumors that efficiently metastasize to bone, brain, lung, and liver (22, 23). Presumably, these global epigenetic changes would result in abnormal gene expression and generation of additional mutations to promote a pro-metastatic phenotype. For example, DNA and histone methylation changes allow for the accessibility of VHL-HIF target genes, namely CYTIP and CXCR4, to promote bone and lung metastasis in clear cell renal carcinoma (24).

Pre-metastatic niches

Accumulating evidence suggests that several types of pre-metastatic niches (PMNs) exist to support the homing, survival, and colonization of metastatic tumor cells (4). The PMN is established by systemic signals secreted from the primary tumor that alter the extracellular matrix and recruit supportive stromal cells to create a conducive environment in the secondary site. The importance of tumor-derived factors in establishing the PMN through recruitment of bone marrow derived cells to the secondary site has been extensively investigated (4). However, since these cells normally reside in the bone marrow, the mechanisms controlling PMN formation in the bone remain less clear. Nonetheless, disruption of normal bone homeostasis appears to be a driving mechanism in PMN establishment in the bone (Figure 2). For example, hypoxic breast cancer cells in the primary tumor secrete the collagen-crosslinking enzyme lysyl oxidase (LOX), which acts directly on osteoblasts and osteoclasts in the bone marrow to favor bone resorption and promote colonization of DTCs (25). Additional secreted

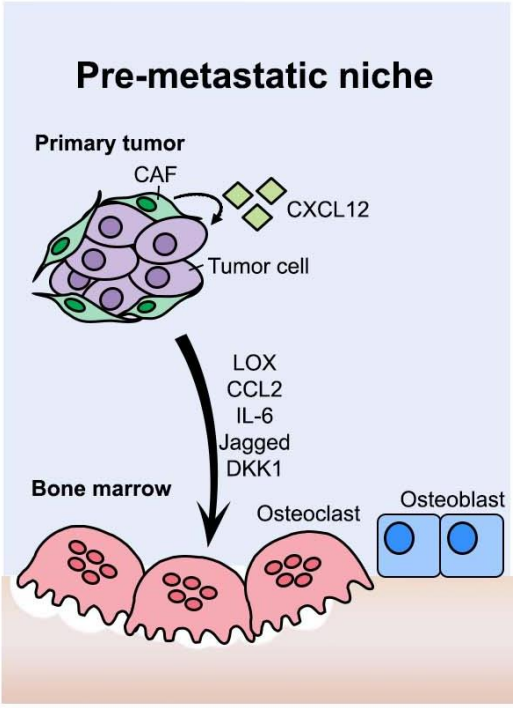

Figure 2. Development of the pre-metastatic niche in the bone. (A) Tumor-derived factors promote the formation of a pre-metastatic niche in the bone prior to tumor cell dissemination. Factors such as lysyl oxidase (LOX) and C-C Motif Chemokine Ligand 2 (CCL2) disrupt normal bone homeostasis thereby favoring tumor cell colonization**.**

factors, including tumor-derived CCL2 (25, 26), interleukin-6 (IL-6) (27-29), the Notch ligand, Jagged1 (JAG1) (30), and the Wnt inhibitor, DKK1 (31), can enhance osteoclast differentiation and activity to promote skeletal metastasis. Interestingly, while CCL2 also promotes lung metastasis by recruiting macrophages to the metastatic site (25), tumor-secreted DKK1 prevents lung metastasis by inhibiting stromal cell recruitment (31). These data suggest that there may be site-specific effects of these tumor-derived factors that require further investigation.

Metastatic homing

The CXCL12:CXCR4 axis is one of the most well described and prominent mechanisms favoring tumor cell homing and colonization of the bone (Figure 3). Bone marrow stromal cells and osteoblasts normally express high levels of CXCL12 (also known as SDF-1) to regulate the homing of HSCs to the bone marrow (32). Overexpression of its cognate receptor, CXCR4, by many cancer types (33) including breast and prostate facilitates the priming of tumor cells by CXCL12-secreting cancer associated fibroblasts to colonize and survive in the CXCL12-rich bone microenvironment (34). This signaling cascade is further propagated by recruitment of endothelial cells are the initial cell type encountered by tumor cells after homing to the bone microenvironment (Figure 3). Therefore, understanding the mechanisms controlling tumor cell adhesion to the endothelium is critical. Following intravasation, CXCL12:CXCR4 also serves as a chemoattractant to the bone (35) and facilitates tumor cell binding to marrow endothelial cells (36, 37). Cell adhesion molecules and integrins have been heavily implicated in regulating tumor cell colonization of the bone (38, 39). Loss of E-selectin ligand, β1 integrin, and Rac1 disrupts the ability of prostate tumor cells to adhere to and breach E-selectin (also known as CD62E or ELAM-1) positive bone marrow endothelial cells, resulting in decreased metastasis incidence (40). Similarly, CX3CL1:CX3CR1 (41, 42) and ANXA2: ANXA2R (43) promote the adhesion of breast and prostate tumor cells to bone marrow endothelial cells.

Pre-existing niches and bone colonization

Pre-existing niches within the secondary site, especially those involved in maintaining adult stem cell populations, are often exploited by metastatic tumor cells as receptive microenvironments. The endosteal and perivascular niches are the two specialized compartments critical for HSC maintenance and self-renewal in the bone marrow (5). Bone lining osteoblasts are the key component of the endosteal niche necessary for HSC maintenance, while endothelial and mesenchymal cells regulate this process in the perivascular

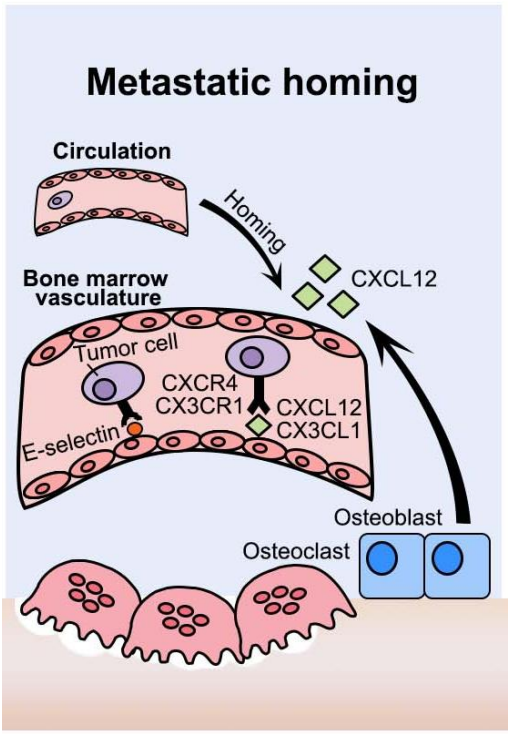

Figure 3. Metastatic homing of tumor cells to the bone. Disseminated tumor cells (DTCs) enter the circulation and can eventually home to the bone via microenvironmental signals including CXCL12:CXCR4 and E-selectin.

niche (5). Direct competition of HSCs with tumor cells for occupancy of the endosteal niche has been demonstrated in murine models of prostate cancer (44). This competition is facilitated by the direct interaction of tumor cells with osteoblasts and induction of HSC maturation by tumor cells, resulting in HSC egression from the niche (44). Notably, manipulation of the niche size resulted in a concomitant change in the number of DTCs. Specifically, osteoblast ablation led to decreased colonization by prostate cancer cells (44). Substantial evidence indicates that interaction of metastatic tumor cells with bone resident cells facilitates their successful colonization of the bone marrow. For example, bone colonization is mediated by the formation of heterotopic adherens junctions between E-cadherin (CDH1) positive breast cancer cells and N-cadherin (CDH2) positive osteoblasts (45). Additionally, tumor cell αvβ3 integrin expression is a critical mediator of tumor cell adhesion to bone matrix proteins and bone resident cells such as osteoblasts and osteoclasts through vitronectin and osteopontin (46). These interactions have been shown to be necessary for successful colonization of breast and prostate cancer cells and enhance tumor-induced osteolysis (47-49). Recent clinical and experimental evidence in breast cancer implicates RUNX2 as a transcriptional driver of αv (ITGA5) expression to promote circulating tumor cell colonization of the bone (50).

Using murine models and organotypic cultures, Ghajar et al. demonstrated that breast cancer cells preferentially localize to the perivascular niche, where they are maintained in a non-proliferative state through interactions with endothelial-derived thrombospondin-1 (TSP1) (51). This preferential homing of breast cancer cells was recently observed using real-time *in vivo* microscopy in which DTCs home to E-selectin- and CXCL12-rich perivascular regions (52). Similarly, disseminated melanoma cancer cells interact with mesenchymal stem cells through CD146 (also known as melanoma cell adhesion molecule (MCAM)) and CXCR4 to facilitate their colonization (53). Although the perivascular niche also contains resident stem cells, direct competition of tumor cells for niche occupancy has not been reported.

Tumor dormancy

The physiological role of the stem cell niche is to provide survival, quiescence, and self-renewal signals from the microenvironment. Thus, tumor cells preferentially localize to these niches within the bone marrow to promote their own survival and dormancy (Figure 4). Increasing clinical evidence suggests that even patients without detectable metastasis harbor reservoirs of dormant tumor cells in the bone marrow. Breast cancer patients without nodal involvement have an approximate 20% risk of developing bone metastases 5-20 years after primary diagnosis (54). Accordingly, non-proliferating DTCs have been detected in the

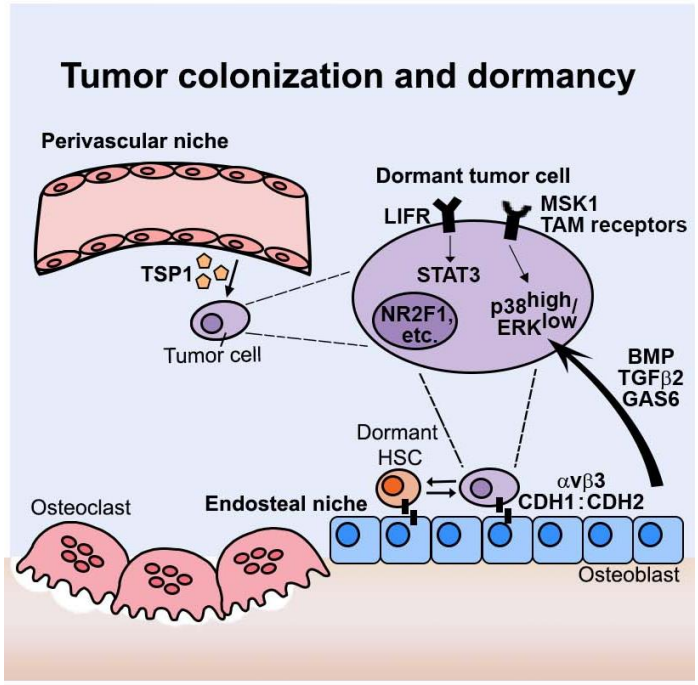

Figure 4. Tumor colonization and dormancy in the bone. Following extravasation, interaction with resident bone cells and signaling molecules such as leukemia inhibitory factor receptor (LIFR), p38, and thrombospondin-1 (TSP1) maintain tumor cells in a dormant state.

circulation (55, 56) as well as in the bone upon autopsy (57, 58) in approximately 70% of breast or prostate cancer patients (57). Intriguingly, the presence of DTCs in the bone marrow of patients is not only predictive of metastasis to the bone, but also to the lungs, liver, and brain (59). This predictive capability also applies to cancer types that rarely metastasize to the bone. For example, despite the low incidence of bone metastasis, DTCs are detected in patients with colorectal and gastric cancer, suggesting that these cells very rarely escape dormancy (55). Combined, these studies suggest that dormant DTCs may lie in the bone marrow for an extended period of time, putting cancer survivors at significant risk of developing bone metastases should these DTCs become reactivated. Despite the recent advances in our understanding of tumor dormancy, many of the complex molecular mechanisms remain unclear.

Microenvironmental factors known to regulate HSC quiescence include bone morphogenetic proteins (BMPs) (60), TGFβ2 (61, 62), and growth arrest-specific protein 6 (GAS6) (63, 64), which were among the first factors identified to induce dormancy of prostate cancer cells and head and neck squamous cell carcinoma. These secreted factors as well as other molecular signals, including retinoic acid (65) and urokinase plasminogen activator receptor (uPAR) (66, 67), have been shown to alter the ratio of ERK and p38 MAPK signaling, which has become one of the most well established mechanisms for inducing tumor cell dormancy (62). Specifically, preferential activation of p38 MAPK over ERK signaling ($p38^{high}$/ ERK^{low}) results in the induction of DTC dormancy. Clinical data also implicate p38 MAPK/ERK in bone metastasis since a p38-regulated dormancy gene signature was associated with increased time to metastasis in breast cancer patients (68, 69). TGFβ2, which is proposed to activate the p38 MAPK pathway in bone-disseminated tumor cells, has been shown to be more abundant in the bone marrow compared to other organs (liver, spleen, lung), suggesting potential organ-specific mechanisms of tumor dormancy (70). Additionally, a downstream mediator of p38 MAPK signaling, mitogen- and stress-activated kinase 1 (MSK1) was recently identified as an important regulator of metastatic dormancy using an unbiased *in vivo* shRNA screen. Studies using the human estrogen receptor positive (ER+) T47D cells revealed that knockdown of MSK1 increased bone homing and metastatic outgrowth. These findings were further supported with clinical patient data showing a correlation between low MSK1 expression and early relapse in ER+ breast cancer (71).

The Tyro3, Axl, and MERTK (TAM) receptor tyrosine kinases compete for the GAS6 ligand secreted by osteoblasts (63, 64). Xenograft models of prostate cancer revealed that GAS6-mediated Axl signaling induces dormancy while GAS6-activated Tyro3 promotes escape into a proliferative state. Recent evidence indicates that GAS6:Axl signaling is critical for

TGFβ2-mediated dormancy (72). MERTK was recently shown to promote dormancy escape in prostate cancer cells through multiple transcriptional and epigenetic mechanisms (73). Combined, these data suggest that the ratio of the TAM receptors on DTCs may be one mechanism controlling the fate of DTCs in the bone marrow.

The tumor suppressor leukemia inhibitory factor (LIF) receptor (LIFR) was also recently identified as a mediator of tumor dormancy in breast cancer cells (74-76). Loss of LIFR and downstream STAT3 signaling in DTCs resulted in dormancy escape and enhanced osteolytic bone destruction *in vivo* (74). Activation of LIFR:STAT3 is mediated by several IL-6 family cytokines including oncostatin M (OSM) and LIF, which have been previously implicated in regulating metastasis to the bone, lung, and liver (77-79). Thus far, due to the complexity of LIFR signaling and abundance of ligands in the bone marrow, the specific factor(s) responsible for the pro-dormancy effects of LIFR signaling has not yet been identified. Of particular interest are the findings that LIFR expression is downregulated by hypoxia (74, 80) suggesting that oxygen gradients in the bone marrow may regulate the emergence of tumor cells from a dormant state.

As discussed in more detail later, reversible epigenetic modifications are known to regulate stem cell plasticity, suggesting that these mechanisms are also likely to be involved in tumor dormancy. Indeed, several genes belonging to the aforementioned p38-regulated gene signature (68, 69), including NR2F1, TGFβ2, and DNMT1, are known epigenetic modulators of stem cell quiescence and have been identified as key regulators of tumor dormancy. Further investigation using experimental head and neck squamous cell carcinoma models revealed that NR2F1 drives global chromatin changes to primarily promote the survival of DTCs and, to a lesser extent, their dormancy in the bone marrow (65). In contrast to the bone, NR2F1 predominantly drives DTC dormancy in the lung and spleen through SOX9 and RARβ (65). Examination of stemness in prostate cancer DTCs revealed that traditional stem cell markers (e.g. CD44 and CD133) were not enriched in quiescent DTCs in the bone marrow, but these cells were far more tumorigenic than their proliferative counterparts. Interestingly, these cells also expressed higher levels of CXCR4, suggesting that the quiescent cells may be more adept at bone marrow homing (81).

Metastatic outgrowth

DTCs can persist in a dormant state for years to decades before becoming reactivated and developing into overt metastases. While our understanding of metastatic outgrowth remains incomplete, many mechanisms regulating the switch of dormant tumor cells into proliferative

metastases have been identified (Figure 5). Disruption of bone homeostasis is one of the primary switches that causes tumor cells to exit a dormant state. The “vicious cycle” of osteolytic bone metastasis is the most well defined mechanism that disrupts bone homeostasis and is observed in numerous cancer types including breast, lung, and multiple myeloma (Figure 6) (82). The vicious cycle is initiated by the secretion of molecules by tumor cells, including parathyroid hormone-related protein (PTHrP) and IL-11, which stimulate RANKL-mediated differentiation and activation of osteoclasts (82). Osteoclasts resorb the surrounding bone matrix, releasing stored mitogenic factors, namely TGFβ, that subsequently fuel cancer cell proliferation and the feed-forward cycle by stimulating PTHrP (83) and its upstream regulator GLI2 (84, 85).The role for TGFβ signaling through the TGFβ type I receptor in propagating the vicious cycle is well established (83, 86-88) and is in contrast with the proposed role for TGFβ2 induction of tumor cell dormancy in the bone marrow. This suggests an important temporal role for TGFβ signaling that extends beyond its dual role at the primary and metastatic sites. In contrast to breast cancer, prostate cancer cells predominantly form osteoblastic lesions as a result of excessive induction of osteoblast differentiation and proliferation (89). The positive-feedback loop for osteoblastic metastases is initiated by the secretion of osteoblast-activating factors such as BMPs) and epidermal growth factors (EGFs) from tumor cells, which in turn results in the production of osteoblast-derived factors including IL-6 and monocyte chemotactic protein-1 (MCP1) that promote tumor cell proliferation (89). It is worth noting that anti-resorptive therapies have been effective in reducing bone pain in prostate cancer patients (90, 91), suggesting that a resorptive phase precedes the formation of osteoblastic lesions.

While it remains largely unclear whether PTHrP is expressed in breast cancer cells prior to dissemination or turned on following extravasation into the bone marrow, there have been several studies investigating how the rigidity of the bone microenvironment impacts breast cancer cell expression of PTHrP. Highly bone metastatic breast and lung cancer cells grown on increasingly rigid substrates exhibited similar increases in PTHrP and GLI2, which was mediated by Rho-associated kinase (ROCK) activation of TGFβ signaling (92), as well as integrinβ3 (93). Interestingly, MCF7 cells, which home to bone but do not induce much bone destruction (74, 94), do not increase PTHrP levels in response to increasing rigidity (92). This suggests that cells primed for the bone are more responsive to bone matrix rigidity.

Due to the initiating role of PTHrP in osteolytic bone destruction, numerous studies have investigated its role in bone colonization. Inhibition of PTHrP shortly after tumor inoculation (95) or two weeks after inoculation(88) effectively reduces tumor-induced osteolysis. Overexpression

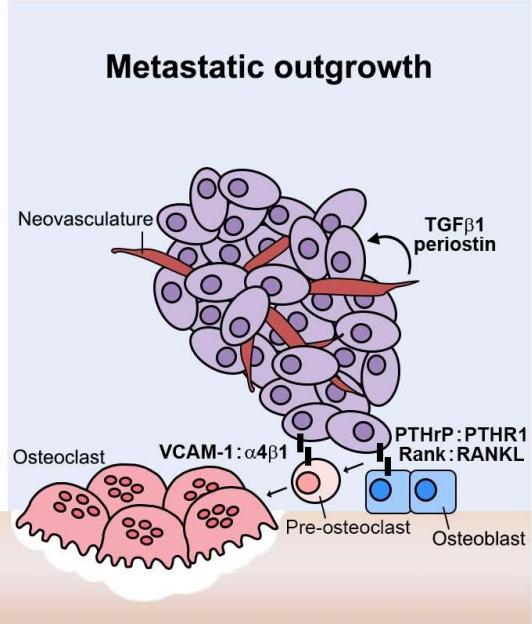

Figure 5. Metastatic outgrowth of tumor cells in the bone. Emergence of DTCs from dormancy results in the outgrowth into overt metastases. Tumor cell proliferation and osteolytic bone destruction is mediated by parathyroid hormone-related protein (PTHrP), receptor activator of NFκB ligand (RANKL), and vascular cell adhesion molecule-1 (VCAM-1). The growth of neovasculature within the metastasis produces transforming growth factor beta 1 (TGFβ1) and periostin to further promote the proliferation of metastatic tumor cells.

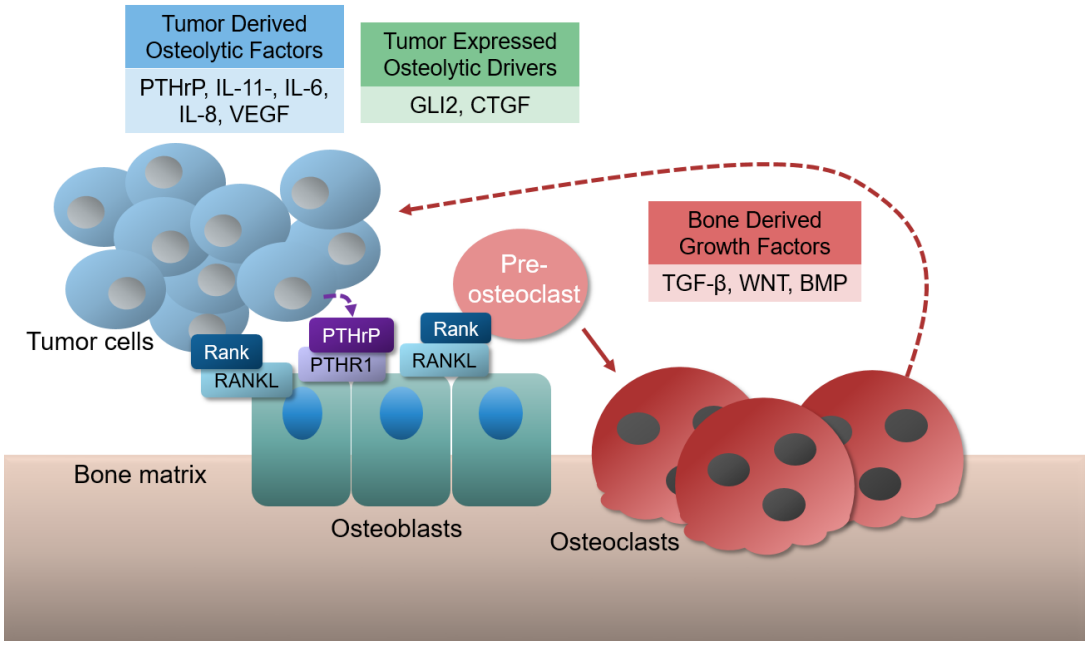

Figure 6. Tumor-induced bone destruction. Breast tumor cells secrete factors (e.g. PTHrP, etc.) that stimulate osteoclastogenesis via osteoblast^{RANKL} expression. Growth factors are then released from the bone matrix and further promote tumor growth and secretion of osteolytic factors

of PTHrP in otherwise dormant human MCF7 breast cancer cells results in aggressive colonization and osteolysis of the bone through enhanced osteoclastogenesis (96). PTHrP overexpression in breast cancer cells also reduces pro-dormancy gene expression, suggesting that PTHrP may play a role in tumor cell exit from dormancy (74, 97). Further, the enabling of dormant tumor cells to aggressively colonize the bone following PTHrP overexpression appears to be independent of PTHR1 and cAMP-mediated signaling and may rely on the calcium signaling pathway (97).

Aberrant expression of vascular cell adhesion molecule 1 (VCAM-1) on breast cancer cells has been shown to recruit osteoclast progenitors expressing the cognate receptor integrin α4β1, thus enhancing local osteoclast activity (98). Pharmacological targeting of VCAM-1 or integrin α4 effectively reduced progression from dormancy into overt metastasis (98). Clinical data suggests Src activation is associated with bone metastasis (17). While Src has no effect on the homing of breast cancer cells to the bone, its activation results in enhanced metastatic outgrowth in the bone (17). Similar to the primary tumor, the vasculature is known to play an important role in metastasis (4). In contrast to the suppressive cues of mature vessels, the sprouting neovasculature promotes progression of metastatic outgrowth by secreting TGFβ1 and periostin (51). These findings identified an unexpected source of these tumor-promoting factors, suggesting that vascular homeostasis is critical for initiating emergence from dormancy. Recent work by Lawson et al. provides a novel look at the vicious cycle and multiple myeloma dormancy using longitudinal intravital imaging through an optical window in the mouse tibia (99). Using this model, myeloma cells colonized the endosteal niche and their dormancy status was determined by the balance between pro-dormancy signals from osteoblasts and pro-proliferative signals from osteoclasts in the endosteal niche (99). Intriguingly, when proliferative tumor cells were isolated and subsequently reintroduced into mice, a small portion localized to the endosteal niche and did not divide (99). Thus, regardless of their prior proliferative capacity, re-engagement of tumor cells with the endosteal niche was able to induce dormancy.

A critical question arises from the findings presented above: What initiates the eventual switch from a dormant to proliferative state? Given the evidence supporting early dissemination of tumor cells, it is possible that primary tumor-derived factors are responsible for altering DTCs or the bone metastatic niche prior to detection of the primary tumor. Age-related changes have also been postulated to trigger the emergence of tumor cells from dormancy. With increasing age, more cells enter an irreversible senescent state which is associated with a senescence-associated secretory phenotype (SASP) (100). This SASP results in the elevated secretion of cytokines, chemokines, and growth factors that may establish a tumor-promoting

microenvironment that can act on surrounding dormant tumor cells. Indeed, senescent osteoblasts enhanced breast cancer bone colonization through IL-6 mediated osteoclastogenesis (27). Additionally, systemic sex steroid levels may also play a role in this process. These molecules can regulate bone homeostasis by inducing osteoclast apoptosis and promoting osteoblast proliferation (101-103). Reduced hormone levels can also result in enhanced bone resorption, which leads to accelerated metastasis formation in hormone-responsive tumors, including breast and prostate (104, 105).

Therapeutically targeting the bone microenvironment

Over the past decade, significant progress has been made in elucidating the molecular mechanisms that control metastatic niches, tumor dormancy, and the emergence of clinically detectable bone metastases. Preferential metastasis to the bone marrow occurs for many tumor types, with breast and prostate being the most notable (57). However, there are currently no therapeutic options to cure bone metastasis. Bone-modifying agents that target resorption, including bisphosphonates and denosumab, are commonly used to effectively manage bone metastasis-related morbidities including pain and hypercalcemia (105-107). Since these therapies target osteolysis and not tumor cells themselves, mortality rates in patients with bone metastasis has not significantly improved. Conventional therapies have limited success in preventing or treating bone metastasis in part due to the complex nature of the bone microenvironment, tumor heterogeneity, and therapeutic resistance of DTCs. Until recently, the persistence of dormant tumor cells in secondary sites and their resistance to therapeutics that preferentially target proliferating cells was not appreciated. Thus, there is significant need to identify novel therapeutic strategies to prevent the colonization and outgrowth of DTCs in the bone.

Preventing tumor cell dissemination and colonization by disrupting the factors shown in Table 1 may prove to be a promising strategy to prevent metastasis. In support of this notion, disruption of the CX3CR1 or CXCR4 pathway in murine models of breast and prostate cancer, respectively, reduces metastatic incidence and tumor burden in the bone (34, 41, 108, 109). Similarly, substantial pre-clinical evidence suggests that pharmacological targeting of αvβ3 integrin effectively prevents metastatic colonization of the bone (110-112). Clinical trials using neutralizing antibodies and small molecule inhibitors against αvβ3 have shown promise, however these have not specifically focused on bone metastasis (113, 114). Microenvironmental factors such as TGFβ and VEGF have also been identified as potential therapeutic targets to prevent bone metastasis (115, 116). Therapeutic approaches targeting

tumor cell intrinsic mechanisms have also been proposed for bone metastases. A combination of Src and ERK inhibition has been shown to effectively reduce breast cancer metastasis to the lungs (117). Given the known roles of Src (17) and ERK (61, 62, 67) signaling in promoting dormancy escape of tumor cells in the bone, this combination treatment may be an effective treatment to maintain tumor cells in a dormant state and prevent recurrence.

Epigenetic therapy for breast cancer metastasis

A complicating factor of bone metastasis is that the kinetics of tumor cell dissemination and metastatic outgrowth remain unclear, and the emergence of DTCs from a dormant state may not be a synchronized event (99). Temporally or spatially regulated factors may promote dormancy escape in a subset of DTC clones and maintain dormancy of others. These possibilities complicate the development of therapies targeting dissemination, colonization, and metastatic outgrowth. Therapeutic strategies designed to induce DTC dormancy and/or prevent reactivation or those that promote proliferation and mobilization of bone DTCs into the circulation have been proposed (118). Both strategies have advantages and disadvantages, highlighting the need for more investigation into their effectiveness in preclinical animal models. Given the newly identified role of epigenetic modifiers (i.e. NR2F1, MERTK) in regulating tumor dormancy, epigenetic-modulating therapies may also represent promising options to induce dormancy in DTCs.

The epigenetic landscape is regulated by the activity of histone- and DNA-modifying enzymes that read, erase, or write post-translational modifications to the chromatin and DNA. These modifications alter chromatin conformation thus regulating the transcriptional activation and silencing status of genes. DNA methylation patterns are regulated by the activities of DNA methyltransferases and DNA demethylases (119). In general, methylation of DNA decreases gene expression by hindering the binding of transcriptional activators and promote other chromatin remodeling enzymes such as those involved in histone modification to further silence gene transcription (119). Histone tail modifications including methylation and acetylation marks are manipulated by several enzymes families including histone deacetylases (HDACs), histone acetyltransferases, histone methyltransferases, and histone demethylases (120). These enzymes can greatly alter gene transcription based on the specific histone/residue targeted and the type of modification. Typically, acetylation of lysine residues, such as H3K9 and H3K27, results in transcriptional activation whereas lysine methylation including H3K27me3, causes transcriptional repression (120).

Table 1. Factors controlling metastatic progression in the bone.

	Function	Protein/Interaction	Reference(s)
Pre-metastatic Niches	Disrupt bone homeostasis to promote colonization	LOX	25
		CCL2	25, 26
		IL-6	27-29
		JAG1	30
		DKK1	31
	Promote colonization	Extracellular vesicles (MET proteins)	32-38
Metastatic Homing	Tumor-derived chemoattractants for bone marrow derived cells	CXCL16 : CXCR6	46
	Bone-derived chemoattractants for tumor cells	CXCL12 : CXCR4	43-45
	Promote endothelial cell adhesion	CXCL12 : CXCR4	47-49
		CD62E	52
		CX3CL1 : CX3CR1	53, 54
		ANXA2 : ANXA2R	55
Pre-exisiting Niches	Interaction with bone marrow cells	Competition of tumor cells with HSCs for niche occupancy	56
		CDH1 (tumor cells) and CDH2 (osteoblasts)	57
		Integrin $\alpha v\beta 3$	58-62
		CD62E	64
		CXCL12 : CXCR4	64
		CD146, CXCR4	65
Tumor dormancy	Regulate tumor dormancy	TSP1	63
		BMP7	72
		TGFβ2	73, 74
		GAS6	75, 76
		ATRA	77
		uPAR	78, 79
		$p38^{high}$/ ERK^{low} signaling	74, 80, 82, 83
		MSK1	81
		Gas6 : Tyro3, Axl, MERTK	75, 76
		LIFR	86-88
		Epigenetic modifiers (NR2F1, TGFβ2, DNMT1)	77, 82, 83
Metastatic outgrowth	Regulate tumor cell proliferation	"Vicious cycle" (PTHrP, RANKL, TGFβ)	94, 95-100
		VCAM-1	110
		SRC	17
		TGF-β1, periostin (endothelial-derived)	63

LOX, lysyl oxidase; CCL2, C-C Motif Chemokine Ligand 2; IL6, Interleukin-6; JAG1, Jagged1; DKK1, Dickkopf WNT Signaling Pathway Inhibitor 1; CXCL, CXC Chemokine Ligand; CXCR, CXC Motif Chemokine Receptor; CD62E, E-selectin; CX3CL, CX3C motif Chemokine Ligand; CX3CR, CX3C Motif Chemokine Recptor; ANXA2, Annexin II; ANXA2R, Annexin A2 Receptor; CDH1, E-cadherin; CDH2, N-cadherin; CD146, Melanoma Cell Adhesion Molecule; TSP1, Thrombospondin-1; BMP7, Bone Morphogenetic Protein 7; TGFβ, Transforming Growth Factor Beta; GAS6, Growth Arrest Specific 6; ATRA, All-trans Retinoic Acid; uPAR, urokinase plasminogen activator receptor; p38, Mitogen Activated Protien Kinase 14; ERK, Extracellular-signal Regulated Kinase; MSK1, Ribosomal Protein S6 Kinase A5; Tyro3, TYRO3 Protein Tyrosine Kinase; Axl, AXL Receptor Tyrosine Kinase; MERTK, MER Proto-Oncognee Tyrosine Kinase; LIFR, Leukemia Inhibitory Factor Receptor; NR2F1, Nuclear Receptor Subfamily 2 Group F Member 1, DNMT1, DNA Methyltransferase 1; PTHrP, Parathyroid Hormone related Protein; RANKL, TNF Superfamily Member 11, VCAM1, Vascular Cell Adhesion Molecule 1; SRC, SRC Proto-Oncogene

As previously mentioned, many of these chromatin-modifying enzymes are deregulated in cancer to drive tumorigenesis and thus are a main therapeutic focus to reprogram tumor cells (121). Many epigenetic therapies currently being tested target the DNMTs or HDACs as a means to reactivate tumor suppressors and induce cell-cycle arrest, apoptosis, and differentiation. Treatment with DNMT inhibitors such as decitabine and azacytidine effectively reduce tumor cell proliferation in various cancer types (122-125). Additionally, decitabine treatment in combination with all-trans retinoic acid has been shown to induce dormancy in a p38-dependent manner in a murine model of head and neck squamous cell carcinoma (65). Based on promising preclinical studies, DNMT inhibitors are currently being tested in clinical trials for several cancer types including metastatic breast cancer (clinicaltrials.gov) (126).

HDAC inhibitors (HDACi) can be divided into four classes based on their structural properties: hydroxyamate, cyclic peptide, benzamide, and short-chain fatty acid (127). In addition to these structural differences, HDACi also exhibit selectivity for the various HDAC classes and isoforms when tested at pharmacologically relevant concentrations as shown in Table 2. While the development of selective HDACi is challenging due to high isoform homology, significant effort is being put forth to develop class- and HDAC-selective inhibitors. Nonetheless, several HDAC inhibitors are currently FDA approved for various diseases such as valproic acid for chronic treatment of epilepsy and migraines. Several HDACi are now FDA approved as anti-cancer drugs including vorinostat and romidepsin for the treatment of cutaneous T-cell lymphoma and panobinostat for multiple myeloma. In addition to the aforementioned HDACi, several others such as mocetinostat and belinostat are currently in clinical trials for the treatment of various solid tumors including recurrent and metastatic breast cancer.

In the context of tumor dormancy, previous work demonstrated upregulation of LIFR and other pro-dormancy genes in breast cancer cells following HDAC inhibitor treatment (74) *in vitro*, indicating these epigenetic therapies may be a mechanism to induce a chronic state of dormancy. However, several reports have suggested that HDAC inhibitors, specifically valproic acid and vorinostat, may negatively affect normal bone remodeling resulting in a significant reduction in bone volume (128-130). One concern with these findings is that the disruption of bone homeostasis by HDAC inhibitor treatment may result in the release of tumor-promoting cytokines stored within the bone matrix and fuel tumor growth rather than tumor dormancy. Thus, further investigation into the long-term effects of HDAC inhibitor treatment on DTCs within the bone is necessary.

Table 2. HDAC inhibitors and their pharmacological properties. Yellow box = HDAC isoform suspected to be inhibited at indicated concentrations based on literature. Gray box = HDAC isoform not suspected to be affected at indicated concentrations based on literature

			Class I				Class IIA				Class IIB		Class IV
Inhibitor name	Structural class	Concentrations	HDAC1	HDAC2	HDAC3	HDAC8	HDAC4	HDAC5	HDAC7	HDAC9	HDAC6	HDAC10	HDAC11
Valproic acid	Aliphatic acid	1mM; 10mM											
Romidepsin	Cyclic peptide	5nM; 50nM											
Panobinostat	Hydroxymate	5nM; 50nM											
Vorinostat	Hydroxymate	1μM; 5μM											
Entinostat	Benzamide	0.5μM; 5μM											

Experimental models of bone metastasis

A major limitation to our understanding of tumor dormancy and bone colonization is the limited number of preclinical animal models. Historically, several types of models have been used to study bone metastasis and colonization with each having their own advantages and limitations. Spontaneous models such as the MMTV-PyMT and 4T1 models best recapitulate the natural metastatic cascade in patients (131). However, these models do not efficiently metastasize to the bone, making it difficult to reproducibly investigate bone colonization and outgrowth. Thus, intracardiac (132, 133)and occasionally tail vein injection (134) of murine-derived mammary carcinoma cell lines into syngeneic mice or human breast cancer cell lines into immunocompromised mice are the most commonly used experimental models of bone metastasis. Since the tumor cells are injected directly into the bloodstream, these are not true bone metastasis models, but rather models of bone colonization. Further, these models are more conducive to genetic manipulation of tumor cells and have a relatively shorter latency period. By far, the murine 4T1 and human MDA-MB-231 are the most commonly used cell lines for breast tumor-bone studies since they rapidly induce osteolytic bone destruction (132). Importantly, these models do not recapitulate the latency behavior of DTCs that are thought to occur in breast cancer patients.

The human estrogen receptor positive (ER+) MCF7 cells have been used by several groups (69, 74, 135, 136) as a model of tumor dormancy in the bone since these cells remain in a non-proliferative state for prolonged periods of time and induce little osteolytic bone destruction. Recently, the dormant bone metastatic (DBM) T47D breast cancer cell derivative was described as a latent tumor model that, similar to the MCF7 model, will eventually develop overt bone metastases with exogenous estradiol supplementation (71). However, a major drawback to these models is the requirement of exogenous 17β-estradiol by tumor cells to form orthotopic tumors and overt bone metastases. Estradiol supplementation in both tumor-inoculated and naïve mice causes adverse urinary tract effects and perturbs normal bone homeostasis resulting in dramatically increased bone volume (135-139). Thus, while these tumor models are useful tools to better understand regulators of DTC dormancy in the bone, the negative effects of exogenous estradiol make these models less physiologically relevant and may be a confounding factor in these models. Importantly, in contrast to the human ER+ models, there are currently no established ER- cell lines that mimic this latency period in mice.

Given the suspected role of the immune system in tumor dormancy and outgrowth of disseminated tumor cells, the inoculation of tumor cells into mice with fully functioning immune systems is highly advantageous. Besides the aggressive 4T1 model mentioned previously, very

few mouse cell lines are currently used to investigate bone colonization. The SSM2 and SSM3 cell lines derived by the Faccio lab from spontaneous mammary carcinomas in STAT1$^{-/-}$ mice (140) represent the first mouse ER+ models that consistently form osteolytic lesions in the bone. Although it has not yet been investigated, bone destruction in these models was observed 4 - 7 weeks after inoculation suggesting that these cells may lie dormant or proliferate slowly in the bone for some period of time before developing into an overt metastasis. Thus, further development of mouse models in which to investigate bone colonization, particularly in the absence of estrogen supplementation, are needed.

Summary and study aims

Although bone metastases remain one of the leading causes of morbidity and mortality in breast cancer patients, our mechanistic understanding of bone colonization and metastatic outgrowth by DTCs remains poorly understood. These deficits are partially due to the lack of preclinical animal models that faithfully recapitulate the latency period observed in breast cancer patients, particularly those with ER+ disease, and methodologies to detect low tumor burden in the bone. Additionally, while numerous studies have focused on identifying dormancy associated factors, few have investigated possible therapies to induce these factors and maintain DTCs in a dormant state and/or revert proliferative DTCs into a dormant state. Continued exploration within these areas using clinically relevant mouse models is of critical importance to identify additional mechanisms controlling bone metastasis and potential therapeutic interventions.

We sought to address several gaps within the field by establishing novel models of prolonged tumor latency and investigating the therapeutic potential of HDAC inhibitors to induce dormancy in breast cancer cells. Specifically, Chapter II describes two novel models of prolonged tumor latency in the bone using the human ER- cell line (SUM159) and syngeneic mouse ER+ cell line (D2.OR) and explores the effects of exogenous estradiol on tumor cell colonization and outgrowth. Further, robust methodologies to detect rare DTCs in each of these models are presented. In Chapter III, we establish an ER+ bone-selective MCF7 model (MCF7b) that exhibits enhanced metastatic potential and identify the PIP3-dependent guanine exchange factor, PREX1, as a mediator of this phenotype *in vitro*. While previous studies have reported the induction of LIFR by HDAC inhibitors, none have investigated their potential use to therapeutically induce tumor dormancy. Thus, Chapter IV explores the use of HDAC inhibitors to induce and maintain breast cancer cells in a persistent state of dormancy by stimulating LIFR and other dormancy genes. Tumor-induced bone disease results in increased patient morality

and co-morbidities; therefore, it is of the utmost importance to better understand the mechanisms controlling bone metastasis and tumor dormancy in clinically relevant animal models. Such efforts may ultimately lead to the identification of novel therapeutic options and/or prevent breast tumor recurrence in the bone.

CHAPTER II

MATERIALS AND METHODS

Cells. Human MCF7 breast cancer cells were obtained from ATCC. The MCF7 bone-selective (MCF7b) line was generated from parental MCF7 cells that were transduced with a lentiviral vector containing GFP and a non-silencing control (NSC) shRNA (discussed further below). For simplicity, these MCF7 NSC cells are referred to as "MCF7" cells in all MCF7b-related studies. Murine D2.0R and D2.A1 mammary carcinoma cells (141) were a gift from J. Green at the National Cancer Institute. Human bone-metastatic MDA-MB-231 cells (MDA-MD-231b) (132, 142) were established from the bone clone generated by the Mundy laboratory. Murine 4T1BM2 bone metastatic cells (143) were gifted by Dr. Normand Pouliot at the Peter MacCallum Cancer Centre. All cells were cultured in DMEM supplemented with 10% fetal bovine serum (FBS) and penicillin/streptomycin (P/S). Human SUM159 breast cancer cells were a gift from the Rutgers Cancer Institute of New Jersey and cultured in Ham's F12 medium supplemented with 5% FBS, 5 $\mu g\ ml^{-1}$ insulin and 1 $\mu g\ ml^{-1}$ hydrocortisone as previously described (74). All human cell lines were recently re-authenticated by ATCC. At this time there is no authentication service available for mouse cell lines. Cell lines are regularly tested for mycoplasma contamination.

shRNA and siRNA. Parental MCF7 cells transduced with a non-silencing control (NSC) shRNA, LIFR shRNA#3 and STAT3 shRNA were previously generated (74). Additional LIFR knockdown lines were generated by transfection of GIPZ lentiviral vectors (Dharmacon, shLIFR#6: V3LHS_347496 and shLIFR#8: V3LHS_347498) into 293T cells to produce lentivirus followed by transduction of MCF7 cells with virus and 5μg/ml polybrene. PREX1 knockdown lines were generated as described above using GIPZ lentiviral vectors (Dharmacon, NSC: RHS4346, shPREX1#4: V3LHS_333004, and shPREX1#6: V3LHS_333006) transduced into MCF7b cells. All lentiviral transduced cells were selected with 1 μg/ml puromycin for 3 days. For siRNA experiments, ON-TARGETplus SMARTpool siRNAs for PREX1 (Dharmacon, Catalog No. L-010063-01-0005) or non-targeting siRNAs (Dharmacon, Catalog No. D-001810-10-20) were transfected into cells using Lipofectamine 2000 (Thermo Fisher) according to the manufacturer's instructions.

RNA extraction and real-time qPCR. Cells were harvested for real-time qPCR as previously described (74). Briefly, cells grown in monolayer were harvested in TRIzol (Thermo Fisher), extracted, purified and DNase treated (TURBO DNA-free kit, Thermo Fisher), and cDNA synthesized (1000ng RNA, iScript cDNA Synthesis Kit, Bio-Rad) per the manufacturer's instructions. Whole femur homogenates and real-time qPCR analysis was performed as previously described (135). Briefly, intact snap-frozen femurs were homogenized in TRIzol, RNA extracted, and cDNA synthesized as above per the manufacturer's instructions. The same process was applied to spine, lung, and primary tumor homogenates. Real-time PCR was performed using iTaqTM Universal SYBR Green Supermix (Bio-Rad) on a QuantStudio 5 (Thermo Fisher) with the following conditions: 2 min at 50°C, 10 min at 95°C, (15 s at 95°C, 1 min 60°C) x40 cycles followed by dissociation curve (15 s 95°C, 1 min 60°C, 15 s 95°C). Human primers for *B2M, LIFR, THBS1, TPM1, AMOT, TGFB2, P4HA1, HIST1H2BK, IGFBP5, MIR190, PDCD4, SELENBP1, CDKN1B, QSOX1*, and *STAT3* were previously published (74). Primers for *HSPB1*, *PREX1*, *DUSP4*, and *MSK1* were designed using PrimerBlast (NCBI) and validated by dissociation. Primer sequences are shown in Table 3.

Western blotting. Cells grown in monolayer were rinsed with 1X PBS and harvested for protein in RIPA buffer (Sigma) supplemented with protease and phosphatase inhibitors (Roche). Protein was extracted from whole bone homogenates using the TRIzol method (Thermo Fisher) according to the manufacturer's instructions. Protein concentration was determined by BCA assay (Thermo Fisher) and 20-50 μg protein was loaded onto an SDS-PAGE gel in reducing conditions and transferred to nitrocellulose membranes using standard techniques. Membranes were probed with antibodies against pSTAT3 Y705 (Cell Signaling, Catalog No. 9131, 1:1000), STAT3 (Cell Signaling, clone 124H6, Catalog No. 9139, 1:1000), pAKT Ser473 (Cell Signaling, Catalog No. 9271, 1:1000), AKT (Cell Signaling, Catalog No. 9272S, 1:1000), pERK1/2 Thr202/Tyr204 (Cell Signaling, Catalog No. 9101, 1:1000), ERK1/2 (Cell Signaling, Catalog No. 9102, 1:1000), PREX1 (Cell Signaling Technology, Catalog No. 13168S, 1:1000), alpha-tubulin (Antibody & Protein Resource at Vanderbilt University, Catalog No. VAPRTUB, 1:5000), vinculin (Millipore, Catalog No. AB6039, 1:10,000), LIFR (Santa Cruz, Catalog No. sc-659 (discontinued), 1:1000), and acetylated Histone H3 (Millipore, Catalog No. 06-599, 1:1000).

Table 3. Primer sequences for real-time qPCR.

Gene		Primer
HSPB1	Forward	CTTCACGCGGAAATACACGC
	Reverse	CGAAGGTGACTGGGATGGTG
PREX1	Forward	AGGCTACCTGTTGTCTCCGA
	Reverse	GAGCAAACGGTCTTCATGGC
DUSP4	Forward	GGCATCACGGCTCTGTTGAAT
	Reverse	GTCGGCCTTGTGGTTATCTTC
MSK1	Forward	TTCCTTTGTTGCTCCTTCCATC
	Reverse	CAACATTTGTCACTCCAGGACG

Flow cytometry.

In vitro experiments. MCF7 and MDA-MB-231b cells were treated with vehicle (DMSO), entinostat (0.5 μM) or panobinostat (5 nM) for a total of 8 days. Cells were fixed on day 0, 2, 4, 6, and 8 in 10% formalin for 20 minutes at room temperature, washed with PBS, and stored in PBS at 4°C prior to staining. Cells were stained in 100ul of 1% BSA+PBS with CD24 (BV711-conjugated, BD Biosciences, Catalog No. 563371, 1:300) and CD44 (PE-conjugated, BD Biosciences, Catalog No. 550989, 1:150) for 30 minutes on ice, washed with 1% BSA+PBS, and resuspended in 300ul of 1% BSA+PBS for analysis. Cells were analyzed in the VMC Flow Cytometry Shared Resource using the BD Fortessa cytometer. Datasets were analyzed using FlowJo software (FlowJo, LLC).

In vivo experiments. One hindlimb was flushed using centrifugation (mice without 17β-estradiol supplementation) or crushed using a mortar and pestle (mice with 17β-estradiol supplementation) to obtain the bone marrow. The bone marrow was filtered through a 40 μm cell strainer to separate the cells from bone debris. Cells were suspended in red blood cell lysis buffer (150 mM NH4Cl, 10 mM KHCO3, 0.1 mM Na2EDTA, pH 7.2) for 5 minutes on ice, spun down, and washed twice with PBS. Bone marrow ($1x10^6$ cells) was stained in 100ul of 1% BSA in PBS with 175ng PE-conjugated CD298 antibody (BioLegend, Catalog No. 341704) for 30 minutes on ice in the dark. Cells were washed with PBS and resuspended with 1% BSA+PBS and 25ng Propidium Iodide (BD Pharmingen, Catalog No. 556463). Flow cytometry experiments were analyzed in the VMC Flow Cytometry Shared Resource using the 5-laser BD LSRII. Datasets were analyzed using FlowJo software (FlowJo, LLC). Cells were gated based on forward scatter and side scatter and then live cells (PI-) were gated using PE-CD298 stained bone marrow as a fluorescence minus one negative control. The dead cells (PI+) were gated out and are not included in the representative plots shown in the figures.

Proliferation assays. For trypan blue exclusion assays, cells were trypsinized and mixed with 0.4% trypan blue solution. Viable cells were determined based on dye exclusion and counted using a TC20 Automated Cell Counter (Bio-Rad). Proliferation of HDAC inhibitor treated cells was monitored in 48-hour increments for a total of eight days by repeatedly trypsinizing cells, counting viable cells by trypan blue exclusion, and reseeding of equal cell numbers onto new plates. These data are presented in the figure as fold proliferation (viable cells / initial seeding number) within each 48-hour period. CellTrace Violet proliferation assays were performed by staining 10 million cells with CellTrace Violet dye (Thermo Fisher) according to the

manufacturer's instructions. A subset of stained cells was fixed immediately (D0 sample) and the remaining cells were plated onto multiple 10cm plates at 1.5 million cells each in medium containing entinostat (0.5μM), panobinostat (5nM), or vehicle. Medium containing fresh drug was replaced every 24 hours. Each day, cells were trypsinized and fixed with 10% formalin for 20 minutes, washed with PBS, and stored in PBS at 4°C until analysis. On days 2, 4, and 6, portion of trypsinized cells (~1.5 million cells) were reseeded onto 10cm plates for analysis at later time points. CellTrace Violet fluorescence intensity was analyzed in the VMC Flow Cytometry Shared Resource using the 5-laser BD LSRII and analyzed using FlowJo software (FlowJo, LLC).

Migration and invasion assays. Cells were seeded at $1x10^5$ cells per well into 24-well transwell inserts with 8 μm pores (Corning). For invasion assays, transwell inserts were coated with 0.5 mg/ml matrigel for 30 minutes at 37°C prior to cell seeding. Serum-free medium was added to the upper chamber and medium containing 1% FBS was added to the bottom chamber to create a chemoattractant gradient. Cells were incubated for 72 hours and fixed/permeabilized with methanol for 10 minutes. Transwell inserts were stained with 0.5% crystal violet for 10 minutes, washed with water, and dried overnight. Bright-field images were acquired using an inverted microscope. Transwell membranes were removed and mounted onto coverslips using VECTASHIELD HardSet Antifade Mounting Medium with DAPI (Vector Laboratories). Images were collected on an Olympus BX41 Microscope equipped with an Olympus DP71 camera using 10X and 40X plan objectives and quantified using ImageJ software.

Adhesion assays. Fibronectin (Thermo Fisher) was diluted to 5μg/ml or 10μg/ml and incubated on a 96-well plate for 1 hour at room temperature. Wells were washed twice with PBS and allowed to dry. Cells were seeded at $0.5x10^5$ in 100μl of serum-free medium per well and incubated for 30 minutes or 1 hour. Following incubation, the medium was removed and wells were gently washed with PBS. Cells were fixed/permeabilized in methanol for 10 minutes followed by staining with 0.5% crystal violet for 10 minutes. The 96-well plate was immersed in water to remove excess crystal violet and allowed to dry. Bright-field images were collected on an inverted microscope using the 10X plan objective and analyzed using ImageJ software. For absorbance measurements, 100 μl of 30% acetic acid in PBS was added to each well and incubated on an orbital shaker for 10 minutes. The absorbance was read at 600nm using a GloMax Discover microplate reader (Promega Corp).

HDAC inhibitor treatment. Cells were seeded in a 6-well plate at 2x105 cells/well or 10cm plate at 1.5 million cells/plate for RNA and protein analysis, respectively. The following day, cells were treated with vehicle (DMSO), entinostat (0.5 μM, 5 μM; SelleckChem, Catalog No. S1053), panobinostat (5 nM, 50 nM; SelleckChem, Catalog No. S1030), romidepsin (5 nM, 50 nM; SelleckChem, Catalog No. S3020), or vorinostat (1 μM, 5 μM; SelleckChem, Catalog No. S1047) for 1-24 hours in full serum medium. Cells were harvested for RNA in TRIzol (Thermo Fisher) or protein in RIPA buffer (Sigma) as discussed above. For HDAC inhibitor washout experiments, cells were treated with HDAC inhibitors for 24 hours, washed twice with PBS to remove the drug, and then incubated for an additional 24 or 48 hours in medium without drug.

Cytokine treatment. Cells were treated with vehicle (DMSO), entinostat (5 μM) or panobinostat (50 nM) for a total of 6 hours (MCF7) or 24 hours (MDA-MB-231b). Recombinant LIF (R&D Systems, 50 ng/ml^{-1}) or vehicle (0.1% BSA+PBS) was added to the medium for the final 15 minutes of HDAC inhibitor treatment and harvested for protein in RIPA buffer (Sigma) as discussed above. All treatments were performed in full serum medium.

Chromatin Immunoprecipitation and qPCR. Cells were plated onto 500cm2 plates (~20-25 million cells per plate) and allowed to grow overnight before treatment with vehicle (DMSO), entinostat (5 μM) or panobinostat (50 nM) for 6 hours (MCF7) or 24 hours (MDA-MB-231b). Chromatin was prepared as previously described (144). Briefly, cells were fixed with 7% formaldehyde, quenched with 2.5M glycine, and lysed with Farnham lysis buffer (5 mM HEPES pH 8.0, 85 mM KCL, 0.5% NP-40, PIC) followed by nuclei lysis buffer (50 mM Tris-HCL pH 8.0, 10 mM EDTA pH 8.0, 1% SDS). Chromatin was sonicated using a Covaris LE220 with the following conditions: 35 minutes at peak power 350, duty factor 15, 200 cycles/burst, and average power 52.5. Sonicated chromatin was diluted with the following: 0.9ml ChIP Dilution Buffer (50 mM Tris-HCl pH 8.0, 0.167 M NaCl, 1.1% Triton X-100, 0.11% sodium deoxycholate), 0.5ml RIPA-150, 28ul 50X protease inhibitors, and 14ul 1M sodium butyrate per 0.1ml sonicated chromatin. Acetylated Histone H3 (Lys9) antibody (Millipore, Catalog No. 07-352) was linked to magnetic anti-rabbit Dynabeads (Thermo Scientific) and incubated with 1.5ml chromatin overnight at 4°C. Immunoprecipitates were washed with the following buffers for 5 minutes each: RIPA-150, RIPA-500, RIPA-LiCl, and TE. Chromatin immunoprecipitates were eluted from the beads and treated with RNase A (Qiagen) followed by proteinase-K (Sigma). DNA was purified using phenol-chloroform extraction/ethanol precipitation, quantified using Qubit, and analyzed by real-time qPCR using iTaqTM Universal SYBR Green Supermix (Bio-Rad) on a

QuantStudio 5 (Thermo Fisher) at cycle conditions indicated above. The fold enrichment of ChIP samples was calculated using 2ΔCt (threshold cycle) and normalized to input DNA Ct values and then to the negative control (IgG-coated beads) Ct values. The primers used for *LIFR*, *AMOT*, *TGFB2*, and *STAT3* promoters are listed in Table 4. Primers for *LIFR*prom4 and *LIFR*prom5 were previously published (145).

Reverse Phase Protein Array (RPPA). Cells were seeded at 2 x 10^6 cells per well in a 6-well plate and cultured overnight. Cells were washed twice with PBS and 100µl of RIPA buffer was added to each well and incubated for 20 minutes at 4°C. Protein concentration was determined by BCA, adjusted to 1.5µg/µl, and mixed with sample buffer (4X SDS and beta-mercaptoethanol). Samples were boiled for 5 minutes and stored at -80°C until sent to MD Anderson Cancer Center. RPPA was performed, processed, and analyzed by the RPPA Core facility at MD Anderson Cancer Center.

RNA-sequencing and bioinformatics. RNA samples for MCF7 and MCF7b cells (n= 3 independent replicates/group) were submitted to and sequenced by the Stanford Functional Genomics Facility on an Illumina NextSeq 500 with a 1 x 75 run length and approximately 40 million reads per sample (single-end) and bioinformatics analysis was performed by the Vanderbilt Technologies for Advanced Genomics Analysis and Research Design (VANGARD) core at Vanderbilt University Medical Center as previously described (97). Log2 fold change values were computed using Empirical Analysis of Digital Gene Expression Data in R (edgeR) package. All RNAseq data has been deposited with GEO (accession number GSE12167).

In silico analyses. *TCGA patient data analysis.* The cBioPortal for Cancer Genomics was accessed on 10 September 2018 to determine PREX1 genetic alterations in breast cancer using the TCGA provisional dataset and the METABRIC, Nature 2012, & Nat Commun 2016 dataset (144, 145). PREX1 mRNA levels from the second dataset were downloaded and entered into Prism to determine statistical differences between breast cancer subtypes. *Kimbung et al, Mol Oncol dataset (GSE46141).* The microarray data were queried for PREX1 expression (100308105_TGI_at and 100152751_TGI_at) and patients were separated into local-regional relapse (skin, breast), lymph node metastasis, or distant metastasis (liver, bone, lung).

Table 4. Primer sequences for ChIP-qPCR.

Promoter		Primer
LIFRprom1	Forward	TGATTCTGCGCCATCAAACG
	Reverse	GTGGGCTTATTTGTGCGGAG
LIFRprom2	Forward	GGGGTAACAGGAGGCGTTTT
	Reverse	TCACAGCTAGATACGGTCGC
LIFRprom3	Forward	TTACAGAGGCGGCGAAAACA
	Reverse	ATCCTCGAGAAAGGCCGAGT
AMOTprom1	Forward	GGAAACCCATTCAAGCCAGC
	Reverse	CTCCCACAAGGCAACAGACA
AMOTprom2	Forward	GGGAAAGGAGCAGAGTGCTT
	Reverse	TGCCTGATGCAGACCCAAAT
AMOTprom3	Forward	AAGCAGCCACCTCCTTTCAA
	Reverse	CACAACCAGCTCTGCTCTGA
TGFB2prom1	Forward	TGCCTACCTACCCTAAGCGA
	Reverse	TTATTCCTGAGGGGGTTGCG
TGFB2prom2	Forward	GTTGGCGTTTGGAGCAAGAG
	Reverse	CTGACCCGCTTGGTTACTCC
TGFB2prom3	Forward	GACCGAACCGCTCCTTCTTT
	Reverse	CCGGCCAAAAGGGAAGAGAT
TGFB2prom4	Forward	CCCCATCTCATTGCTCCAAGA
	Reverse	TTAATACGGGACGGGCAGAG
STAT3prom1	Forward	GACCGGAATGTCCTGCTGAA
	Reverse	AGGAGGGAGCTGTATCAGGG
STAT3prom2	Forward	CCCGTACTCCGTTCCATCAC
	Reverse	CTTCTGCATTCGCCTGTACG
STAT3prom3	Forward	ATTCAGACCGCTCGTACCAC
	Reverse	TTCTCACCACCAGTGACCCT

Animal studies and imaging.

Animals. All experiments were performed following the relevant guidelines and regulations of the Animal Welfare Act and the Guide for the Care and Use of Laboratory Animals and were approved by the Institutional Animal Care and use Committee (IACUC) at Vanderbilt University. For intracardiac inoculation studies, female mice were inoculated with 1x105 tumor cells as previously described (74,96) (n=10 mice injected per group). Specifically, 4-6 week old female athymic nude mice (Jackson, Catalog No. 7850) were used for the human MCF7, MCF7b, and MDA-MB-231b models. For the D2.0R and 4T1BM2 models, 4-6 week old female BALB/c mice (Envigo Corp, Catalog No. 4702) were used. For MCF7 and D2.0R cohorts with 17β-estradiol supplementation (+E2), mice were subcutaneously implanted with a slow-release 17β-estradiol pellet (0.36mg/pellet; Innovative Research of America, Catalog No. SE-121) 24 hours prior to tumor inoculation as previously described (74,94). For studies using HDAC inhibitors and zoledronic acid, mice were given zoledronic acid (0.2 mg/kg; Selleckchem, Catalog No. S1314) via tail vein injection 24 hours prior to tumor cell inoculation. Treatment with vehicle (7.5% DMSO+10% HPBCD in sterile water), entinostat (10 mg/kg; Selleckchem, Catalog No. S1053), or panobinostat (5 mg/kg; SelleckChem, Catalog No. S1030) was initiated 24-hours post tumor cell inoculation and given 5 days per week until sacrifice. Mice were euthanized at 4 weeks (MDA-MB-231b +/- HDAC inhibitor and ZA), 7 weeks (D2.0R +/- E2), 8 weeks (MCF7 +/-E2), 13 weeks (SUM159), or 22 weeks (MCF7 vs MCF7b) post-tumor cell inoculation.

The number of mice indicated in the figure legends (n=6-10 mice per group) represents the number of mice included in the final analysis. For each cohort, a total of n=10 mice were originally injected. Mice that 1) died during intracardiac inoculation, 2) became moribund and had to be sacrificed early but had no evidence of tumor burden, or 3) were found deceased, were not included in the analysis. Specifically, for the MCF7 +E2 model, one mouse died during intracardiac inoculation and one mouse was found deceased (final analysis = 8 mice). For the D2.0R +E2 model, one mouse died during intracardiac inoculation and 3 mice were found deceased (final analysis = 6 mice). For the D2.0R -E2 model, two mice were found deceased (final analysis = 8 mice). For the SUM159 model, one mouse died during intracardiac inoculation and one mouse had to be sacrificed early (week 10 of the experiment), but had no evidence of metastatic tumor burden upon gross dissection and examination of radiographs (final analysis = 8 mice). Two +E2 mice in each of the non-tumor-inoculated (naïve) cohorts (athymic nude and Balb/c mice) became moribund and were sacrificed early, presumably due to non-tumor related side effects of estradiol implantation (i.e. bladder stones; final analysis = 8 mice per group).

For the mammary fat pad study, 17β-estradiol pellets (0.36mg/pellet; Innovative Research of America, Catalog No. SE-121) were implanted subcutaneously into female athymic nude mice 24 hours prior to tumor inoculation. The following day, $5x10^5$ tumor cells in 20µl PBS+50% matrigel (Fisher Scientific) were injected into the fourth mammary fat pad (n=10 mice injected per group). Tumor volume was assessed by caliper measurement. Several mice had to be sacrificed early due to estrogen toxicities resulting in eight mice per group in the final analysis.

Radiography. Radiographic (x-ray) images were obtained as previously described (85). Briefly, a Faxitron LX-60 (34kV for 8 seconds) was used to acquire x-ray images and images were quantified for osteolytic lesion number and area using ImageJ software.

Maestro imaging. Following injection of MDA-MB-231b cells expressing GFP, metastatic tumor growth was monitored using the CRI Maestro optical imaging system. Mice were anesthetized using isoflurane and placed on the Maestro imaging equipment. Images were acquired using the GFP filters (ex 485nm, em 515nm) and 500 msec exposure time. GFP fluorescence area was quantified using thresholding in the ImageJ software.

Microcomputed tomography (microCT). *Ex vivo* microCT was performed on the proximal tibia using the Scanco µCT 50. Scans were initiated from the proximal end of the metaphyseal growth plate and progressed 200 slices distal. Tibiae were scanned at 7µM voxel resolution, 55-kV voltage, and 200µA current. Scans were reconstructed and analyzed using the Scanco Medical Imaging Software to determine the bone volume/total volume (BV/TV), trabecular number, thickness, and separation. The most distal slice of the growth plate was used as a reference slice and analysis was set to begin 20 slices distal from this point. A 100 slice region of interest was selected for analysis. For mice supplemented with 17β-estradiol, contours were drawn manually due to the difficulty in distinguishing the cortical bone. For mice without 17β-estradiol, an automated contouring procedure was applied to separate the trabecular bone from the cortical bone and visually verified for each sample.

Histology. Hind limbs were dissected and fixed in 10% formalin for 48hr and decalcified in EDTA (20% pH 7.4) solution for 72 hours. Decalcified bones were embedded in paraffin and 5-µM thick sections were prepared for staining. Hematoxylin and eosin (H&E) staining was performed as previously described (74). H&E stained sections were analyzed by

histomorphometry in the proximal secondary spongiosa using the OsteoMeasure software (Osteometrics, Decatur, GA). Histological analysis of H&E stained tibiae was performed blinded by me and in some studies by an ACVP board-certified veterinary anatomic pathologist who has specific expertise in mouse models of breast cancer. Specifically, tumor cells in the bone were identified based on abnormal features such as prominent nucleoli, increased mitotic rate, large nuclei, high nuclear:cytoplasmic area, epithelial morphology, spindly cells that do not resemble normal bone cells (e.g. osteoblasts), and cells that disrupt the normal architecture of the bone (growth plate, cortical bone).

Immunostaining. Sections were deparaffinized by heating the slides to 50°C and placed in xylene for 5 minutes and then 3 minutes. Next, slides were soaked in 100%, 95%, and then 75% ethanol for 3 minutes each. Slides were slowly changed to deionized water and then rinsed twice in water. The slides were immersed in 10 mM TRIS (pH 9.0) and 1 mM EDTA heated to 150°C for 20 minutes. After cooling, slides were rinsed twice with water and then three times with PBS. The deparaffinized sections were blocked in 10% BSA in PBS for 4 hours and incubated with FITC-conjugated pan-cytokeratin (1:50; Sigma; Catalog No F0397), GFP (1:100; Genetex; Catalog No GTX20290) or Ki67 (1:500; Thermo Fisher; Catalog No RM9106S0) in 3% BSA in PBS overnight at 4°C. For unconjugated primary antibodies, sections were incubated in the dark with secondary antibody (1:1000; Thermo Fisher, Catalog No A-11034, goat anti-rabbit IgG (H+L) Alexa Fluor 488) for 1 hour at room temperature. The sections were washed three times with 3% BSA in PBS and coverslips mounted using VECTASHIELD HardSet Antifade Mounting Medium with DAPI (Vector Laboratories). All images were collected on an Olympus BX41 Microscope equipped with an Olympus DP71 camera using the 4X, 20X, 40X, or 100X plan objectives.

Pan-cytokeratin (AE1/AE3) staining was performed by the Vanderbilt University Medical Center Translational Pathology Shared Resource (TPSR, Nashville, TN) as follows: Slides were placed on the Leica Bond Max IHC stainer. All steps besides dehydration, clearing and coverslipping were performed on the Bond Max. Slides were deparaffinized and enzyme retrieval was performed using Proteinase K (Dako, Carpentinera, CA) for 5 minutes. Slides were placed in a Protein Block (Ref# x0909, DAKO) for 10 minutes. The sections were incubated with Cytokeratin (Catalog No. Z0622, Dako) diluted 1:4,000 for one hour. The Bond Refine Polymer detection system was used for visualization and slides were then dehydrated, cleared and coverslipped.

Statistical methods. For all studies, *n* per group is as indicated in the figure legend and the scatter dot plots indicate the mean of each group and error bars indicate the standard error of the mean. All graphs and statistical analyses were generated using Prism software (Graphpad). All *in vitro* and *in vivo* assays were analyzed for statistical significance using an unpaired t-test, Mann-Whitney U-test or ANOVA with Sidak's multiple comparisons test. For all analyses $P < 0.05$ was statistically significant, and * $P < 0.05$, ** $P < 0.01$, *** $P < 0.001$, **** $P < 0.0001$.

CHAPTER III

ENRICHMENT AND DETECTION OF BONE DISSEMINATED TUMOR CELLS IN MODELS OF LOW TUMOR BURDEN

The work presented in this chapter is published with the same title in Scientific Reports, September 2018 [Volume 8, Issue 1].

Summary

Breast cancer cells frequently home to the bone, but the mechanisms controlling tumor colonization of the bone marrow remain unclear. We report significant enrichment of bone-disseminated estrogen receptor positive human MCF7 cells by 17β-estradiol (E2) following intracardiac inoculation. Using flow cytometric and quantitative PCR approaches, tumor cells were detected in >80% of MCF7 tumor-inoculated mice, regardless of E2, suggesting that E2 is not required for MCF7 dissemination to the bone marrow. Furthermore, we propose two additional models in which to study prolonged latency periods by bone-disseminated tumor cells: murine D2.0R and human SUM159 breast carcinoma cells. Tumor cells were detected in bone marrow of up to 100% of D2.0R and SUM159-inoculated mice depending on the detection method. These findings establish novel models of bone colonization in which to study mechanisms underlying tumor cell seeding to the marrow and prolonged latency and provide highly sensitive methods to detect these rare events.

Introduction

Increased morbidity and mortality of breast cancer patients is strongly associated with the development of metastatic lesions by disseminated tumor cells (DTCs). Breast cancer cells frequently metastasize to skeletal sites, where they can cause adverse effects including bone pain, fractures, spinal cord compression, and hypercalcemia (146, 147). Recent evidence, including the detection of DTCs in the bone marrow of patients with early stage breast cancer (7) and comparative genomic analysis of DTCs and primary tumors (14), suggests that dissemination of breast cancer cells is an early event. Although systemic adjuvant therapies have improved the relapse-free and overall survival of patients, there is evidence to suggest that DTCs can evade therapy-induced or microenvironment-induced stresses and ultimately evolve into a clinically detectable metastasis (70, 148). A recent meta-analysis of ~63,000 women with

estrogen receptor-positive (ER+) breast cancer reported that primary tumor diameter and nodal status, which are indicators of tumor aggressiveness, were most strongly correlated with the risk of distant recurrence (54). Of particular interest, even patients with no nodal involvement at diagnosis had an appreciable 10-17% risk of developing distant metastasis during years 5-20 after primary diagnosis, suggesting prolonged periods of tumor dormancy. Additionally, approximately 70% of breast cancer patients who succumb to disease have evidence of bone metastasis at autopsy (57, 58). Together, these studies suggest that DTCs may remain in a dormant state for an extended period of time (149) and that breast cancer survivors are at a significant risk of developing overt bone lesions from DTCs.

Despite the high prevalence of skeletal metastases in breast cancer patients, there are currently no therapeutic options to cure metastatic disease. This deficit is in part due to our limited understanding of the mechanisms that regulate bone colonization and tumor dormancy (150, 151). The identification of factors regulating bone colonization is complicated by the multitude of microenvironmental factors in distant metastatic sites, which differentially affect the homing of DTCs and metastatic progression. Interestingly, several studies have proposed that dormancy-associated factors may act in a tissue-specific manner (152). In breast cancer, these mechanisms are further complicated by the clinical association of estrogen receptor (ER) status and time to recurrence. At first relapse, skeletal metastases commonly present in ER- breast cancer patients within 5 years of diagnosis; while skeletal recurrence in ER+ breast cancer patients can also present within these first 5 years, the majority of patients recur 8-10 years after diagnosis (153, 154). While differential recurrence patterns between subtypes may not apply to all patients, these clinical observations suggest that there may also be subtype-specific mechanisms underlying tumor cell dormancy and/or reactivation of DTCs in the bone.

A major limitation to studying mechanisms that regulate tumor dormancy and metastatic outgrowth in the bone is the lack of *in vivo* models that recapitulate prolonged tumor latency, as well as our limited ability to detect low levels of tumor burden in bone. Many studies have used the human MDA-MB-231 (ER-) and murine 4T1 (ER-) cells, or sub-clones of these cell lines, but these cell lines are highly aggressive and rapidly induce osteolytic lesions in the bone (132). We (74) and others (69, 136) have reported that the human MCF7 (ER+) cell line is non-proliferative in the lung and bone and induces little osteolytic bone destruction, and have proposed this cell line as a clinically relevant model of tumor dormancy. Previous literature reports that MCF7 cells require exogenous 17β-estradiol (E2) to form orthotopic tumors and bone metastases (137, 155); however, E2 results in a dramatic increase in bone volume (136, 138) and perturbation of normal bone microarchitecture in tumor-inoculated as well as naïve mice. Further, estrogen

supplementation causes adverse urinary tract effects resulting in mice being sacrificed before the experimental end-point (137, 139). Importantly, the presence of micrometastatic bone lesions in the absence of E2 has not been rigorously investigated using methods that can detect low tumor burden in the bone.

We report that MCF7 cells are able to colonize the bone marrow following intracardiac inoculation in the presence and absence of E2. Furthermore, we report for the first time that murine D2.0R (ER+) mammary carcinoma and human SUM159 (ER-) breast cancer cells, which have been shown to lie dormant in the lungs following tail vein injection (75, 136), disseminate to the bone marrow with extended latency periods. For the MCF7 and SUM159 models, a highly sensitive and human-specific flow cytometry protocol using CD298 (also known as ATP1B3) expression was implemented, which has been used to identify human breast cancer cells in PDX mice (156). Further, we capitalized on the human origin of these cells to analyze human versus mouse housekeeping genes by qPCR from whole bone homogenates to quantify tumor burden in bone. In order to detect murine D2.0R cells in the bone marrow, cytokeratin expression was analyzed using immunostaining and qPCR analysis. These highly sensitive methods to detect low metastatic burden are ultimately summarized for their applicability to each tumor model. The proposed techniques to detect small, but significant, changes in metastatic burden, in combination with these novel tumor models, will be instrumental in investigating breast tumor cell homing and extended latency periods in the bone.

Results

Establishment of the MCF7, SUM159, and D2.0R timelines

Human MCF7 (ER+) and SUM159 (ER-) tumor cells, and syngeneic murine D2.0R (ER+) cells were inoculated by intracardiac injection. In order to test the estrogen dependence of MCF7 and D2.0R cells in the bone, we implanted a cohort of mice with 17β-estradiol pellets (+E2 mice, dark red and dark blue lines) 24 hours prior to tumor cell intracardiac inoculation while another cohort of mice received no 17β-estradiol pellet (-E2 mice, light red and light blue lines) (Figure 7A). Osteolytic bone destruction was monitored *in vivo* by radiography every other week until sacrifice. A gradual increase in lesion number and lesion area was observed by radiography for the -E2 and +E2 MCF7 (B, E), +E2 D2.0R (C, F), and SUM159 (D, G) tumor models throughout the time course. A slight reduction in lesion number and lesion area was observed over time in the -E2 D2.0R tumor model (C). The MCF7

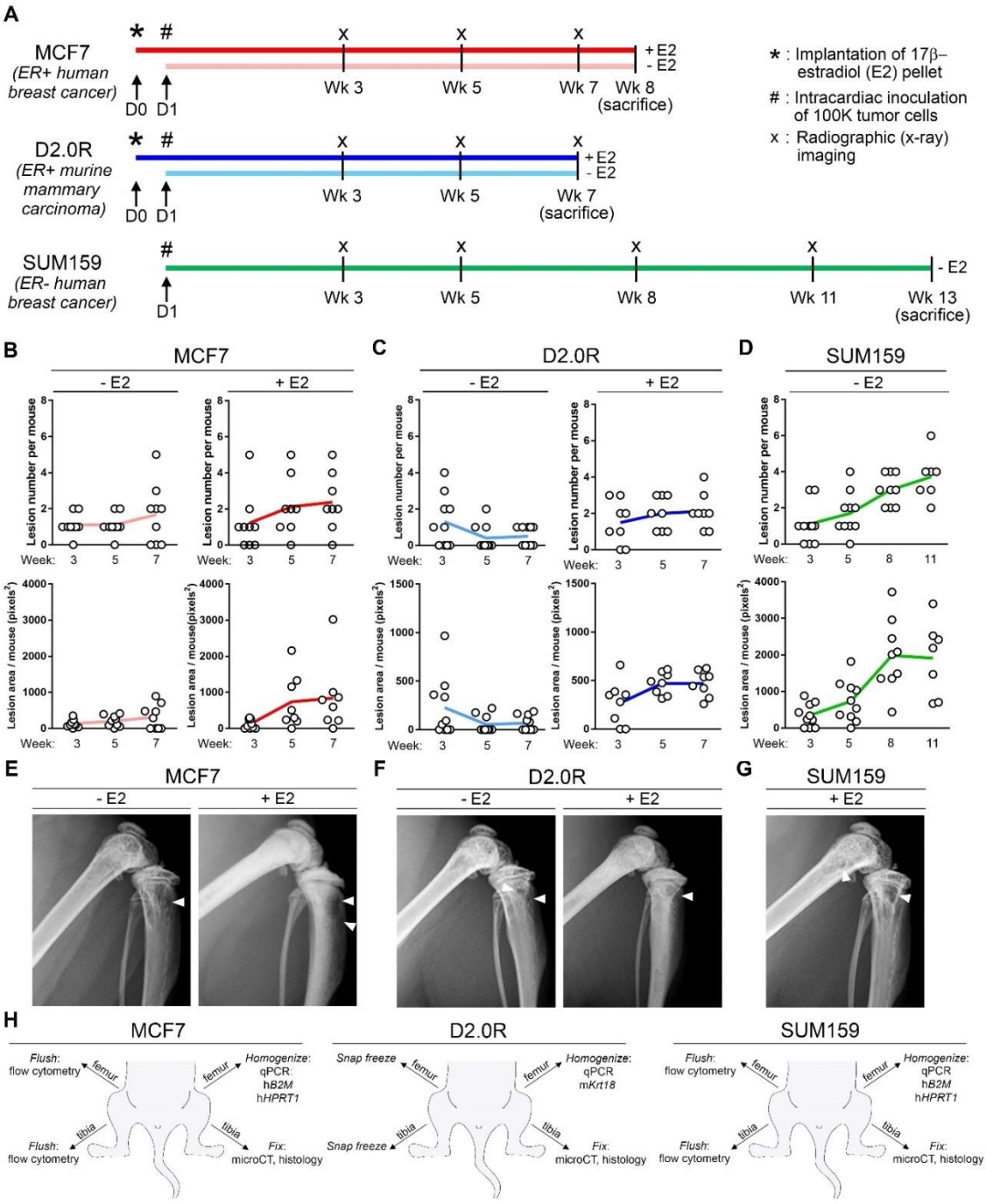

Figure 7. Experimental timeline for MCF7, D2.0R, and SUM159 models and osteolysis. (A) Schematic of model timelines from implantation of 17β-estradiol pellets (indicated by asterisk) and inoculation of tumor cells (indicated by pound symbol) to sacrifice. Light colored lines = -E2 mice and dark colored lines = +E2 mice. n=10 mice inoculated per group. (B-D) Radiographic assessment of total lesion number per mouse and total lesion area per mouse over time and in the (B) MCF7 (n=10 E2 mice, n=8 +E2 mice), (C) D2.0R (n=10 -E2 mice, n=8 +E2 mice) and (D) SUM159 models (n=8 mice). (E-G) Radiographic images at week 7 for the (E) MCF7 and (F) D2.0R models and at week 11 for the (G) SUM159 models. White arrowheads indicate osteolytic lesions. (H) Schematic indicating the methods performed on the hind limbs for each tumor model.

and D2.0R tumor models were sacrificed 7-8 weeks post-inoculation and the SUM159 model 13 weeks after tumor inoculation (A). These timelines were established in order to maintain statistical power for each cohort following several mice becoming moribund or found deceased. Notably, mice in the +E2 cohorts were lost due to the negative urinary tract effects of estradiol supplementation. Mice lost in the D2.0R- and SUM159-inoculated -E2 mice were moribund or found deceased with no evidence of macrometastatic disease or other illness (e.g. infection). Importantly, -E2 and +E2 mice for the MCF7 and D2.0R models were sacrificed at the same time point in order to directly compare tumor burden between the groups. To assess tumor burden in the bone, the hind limbs were dissected at sacrifice and processed for flow cytometry, qPCR, microcomputed tomography (microCT), or histology depending on the tumor model (H).

E2 enrichment for human tumor cells in the bone marrow by CD298 flow cytometric analysis

For flow cytometry analysis of tumor burden in bone, the human specificity of the CD298 antibody was confirmed by staining non-tumor-inoculated (naïve) mouse bone marrow, which produced no background staining (Figure 8A). Murine D2.0R cells, which do not express human CD298 and therefore serve as an additional negative control, showed no enrichment for human CD298 after staining (Figure 8B). In contrast, >99% of human MCF7 (Figure 8C) and SUM159 (Figure 8D) cell lines were positive for CD298. Human-specific EpCAM and pan-cytokeratin, which are commonly used to detect tumor cells (157, 158), were also tested but resulted in background staining of mouse bone marrow (data not shown). For flow cytometry analysis, gates were established based on staining of non-tumor-inoculated (naïve) mouse bone marrow controls for each experiment and tumor model.

Staining of non-tumor-inoculated (naïve) mouse bone marrow showed 0% staining for CD298 and was used as a negative control to establish the gates for each experiment and tumor model (Figure 9A). Bone marrow isolated from mice inoculated with MCF7 cells showed significant enrichment for CD298 staining in mice supplemented with E2 (+E2) by flow cytometry (Figure 9B) compared to mice that did not receive E2 (-E2). MCF7-inoculated mice showed an average of 2.8 (0.0032%) and 42.5 (0.149%) CD298+ cells in -E2 and +E2 mice, respectively (Figure 9C, D). By this method, we detected significant enrichment in the number and percent of MCF7 tumor cells in the bones of +E2 mice compared to -E2 mice. Importantly, although the yield of CD298+ tumor cells per mouse was low, MCF7 cells were detected in 8/10 (80%) - E2 and 7/8 (88%) +E2 mice (Figure 9D). Similarly, compared to non-tumor-inoculated

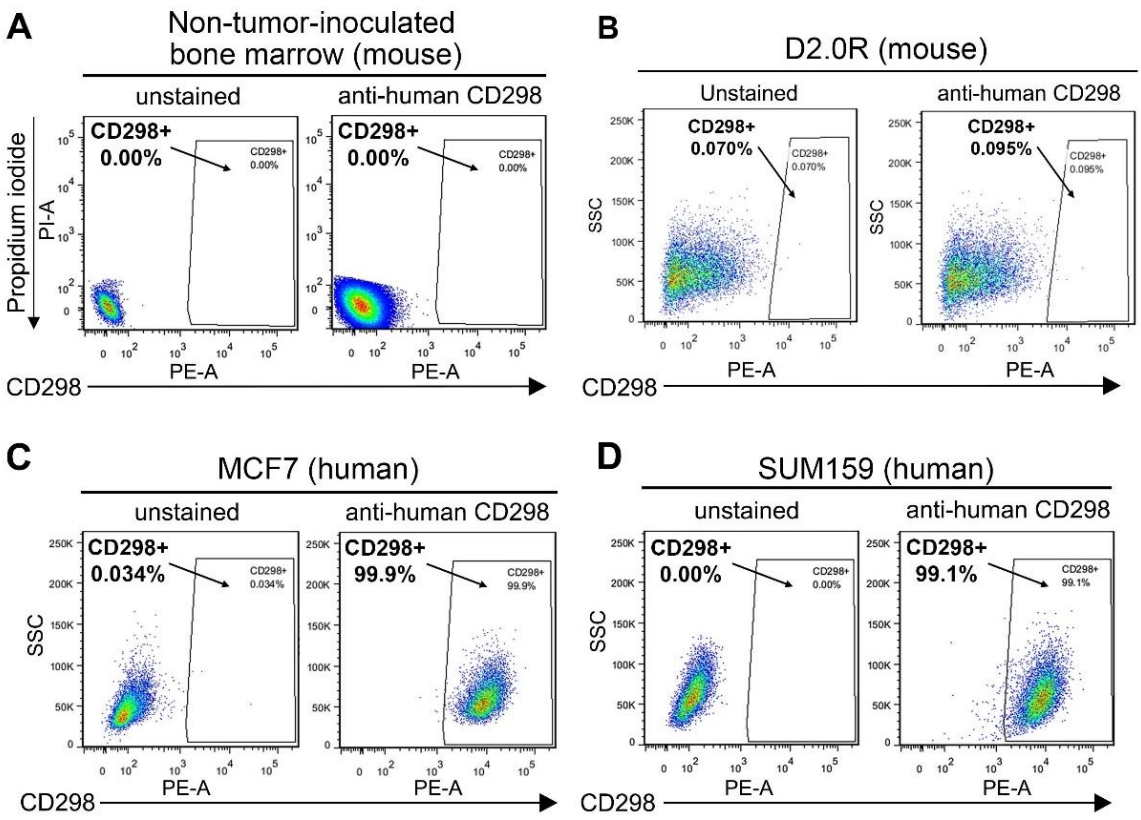

Figure 8. CD298 expression in non-tumor-bearing bone marrow and cells grown in vitro. (A) Representative flow cytometry plot of CD298 staining in non-tumor-inoculated (naïve) mouse bone marrow (representative of n=3 mice). (B-D) Flow cytometry plot of CD298 staining in (B) mouse D2.0R, (C) human MCF7, and (D) human SUM159 cells grown in vitro (n=1 experiment).

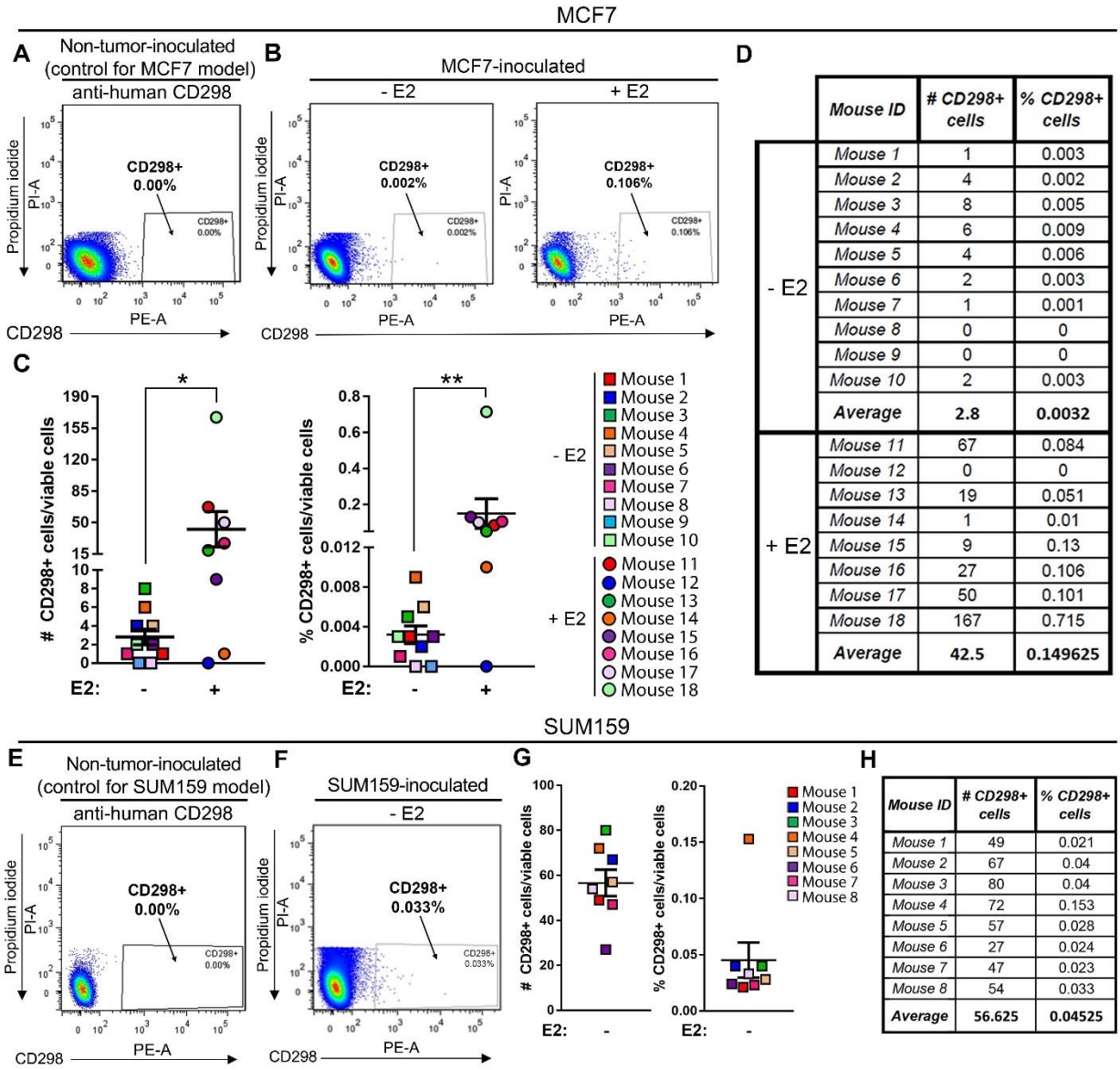

	Mouse ID	# CD298+ cells	% CD298+ cells
- E2	Mouse 1	1	0.003
	Mouse 2	4	0.002
	Mouse 3	8	0.005
	Mouse 4	6	0.009
	Mouse 5	4	0.006
	Mouse 6	2	0.003
	Mouse 7	1	0.001
	Mouse 8	0	0
	Mouse 9	0	0
	Mouse 10	2	0.003
	Average	**2.8**	**0.0032**
+ E2	Mouse 11	67	0.084
	Mouse 12	0	0
	Mouse 13	19	0.051
	Mouse 14	1	0.01
	Mouse 15	9	0.13
	Mouse 16	27	0.106
	Mouse 17	50	0.101
	Mouse 18	167	0.715
	Average	**42.5**	**0.149625**

Mouse ID	# CD298+ cells	% CD298+ cells
Mouse 1	49	0.021
Mouse 2	67	0.04
Mouse 3	80	0.04
Mouse 4	72	0.153
Mouse 5	57	0.028
Mouse 6	27	0.024
Mouse 7	47	0.023
Mouse 8	54	0.033
Average	**56.625**	**0.04525**

Figure 9. Detection of CD298+ tumor cells in the bone using flow cytometry. (A) Representative flow cytometry plot of CD298 staining in non-tumor-inoculated (naïve) mouse bone marrow used as a negative control for the MCF7 model (representative of n=3 mice). Dead cells (PI+) have been excluded. (B) Representative flow cytometry plots of bone marrow from MCF7-inoculated -E2 (n=10 mice) and +E2 (n=8 mice) mice. Dead cells (PI+) have been excluded. (C, D) Quantitation of total number and percent of CD298+ tumor cells from (b). (E) Representative flow cytometry plot of CD298 staining in non-tumor-inoculated (naïve) mouse bone marrow used as a negative control for the SUM159 model (representative of n=3 mice). Dead cells (PI+) have been excluded. (F) Representative flow cytometry plot of bone marrow from SUM159-inoculated mice (n=8 mice). Dead cells (PI+) have been excluded. (G, H) Quantitation of total number and percent of CD298+ tumor cells from (F). c: Mann-Whitney U-Test, * $P < 0.05$ and ** $P < 0.01$.

(naïve) control bone marrow (Figure 9E), which showed 0% staining for CD298, the SUM159 model had detectable tumor cells in 8/8 (100%) mice with an average of 56.6 (0.045%) CD298+ cells (Figure 9F-H).

Assessment of E2 effects on MCF7 tumor burden in bone

Hematoxylin and eosin (H&E) stained tibiae from MCF7-inoculated mice were assessed for the presence of tumor cells based on features including prominent nucleoli, large pale nuclei, increased mitoses, and epithelial morphology. Tumor cells were detected in 2/8 (25%) +E2 mice by our own morphological assessment, but were not detected in any (0/10) -E2 mice compared to non-tumor-inoculated mice (Figure 10A and Figure 11A). Evaluation of these tibiae by an ACVP board-certified veterinary anatomic pathologist identified tumor cells in two additional +E2 mice resulting in a total of 4/8 (50%) +E2 mice harboring tumor cells in the bone marrow. As previously reported (159), histomorphometric analysis revealed a significant increase in the average bone volume from ~1% in -E2 mice to ~60% in +E2 mice (Figure 10A, B) in both non-tumor-inoculated and MCF7-inoculated mice. Further, there was a significant reduction in bone volume in +E2 MCF7-incoulated mice compared to non-tumor-inoculated mice (Figure 10B). These changes in bone volume were supported by microcomputed tomography (microCT) analysis of a separate cohort of -E2 and +E2 MCF7-inoculated mice (Figure 10C, D). Further, a significant increase in trabecular number and thickness and a concomitant decrease in trabecular spacing was observed in +E2 compared to -E2 mice, independent of tumor inoculation.

We were unable to find a CD298 antibody that was suitable for immunostaining, and therefore performed pan-cytokeratin staining, which has been previously used to detect neoplastic epithelial cells in the bone marrow of xenograft mouse models and breast cancer patients (7, 14, 160). We confirmed cytokeratin expression on MCF7 cells using two independent pan-cytokeratin antibodies (PCK-26 and AE1/AE3) (Figure 11B). The staining pattern was consistent between antibodies and detected tumor cells in 0/10 (0%) -E2 mice and in the same 3/8 (38%) +E2 mice (Figure 10E, F and Figure 11C). We confirmed that tibiae stained with DAPI alone were not auto-fluorescent in the green channel (Figure 11D). The specificity of the pan-cytokeratin (AE1/AE3) staining was confirmed using adult skin as a positive control and brain and non-tumor-inoculated (naïve) tibiae as negative controls (Figure 11D).

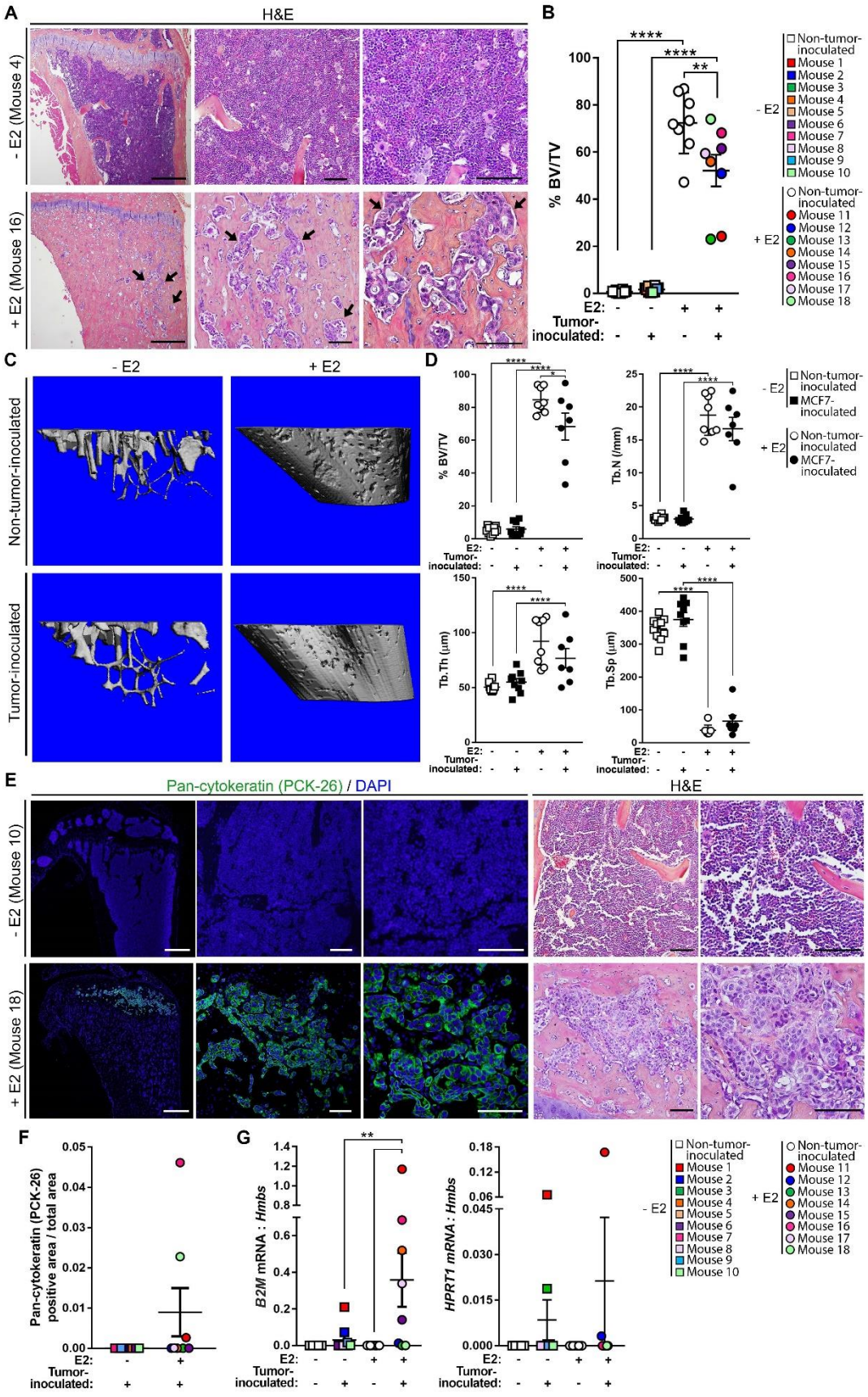
A
H&E
- E2 (Mouse 4)
+ E2 (Mouse 16)
B
% BV/TV
E2:
Tumor-inoculated:
- E2
+ E2
Non-tumor-inoculated
Mouse 1
Mouse 2
Mouse 3
Mouse 4
Mouse 5
Mouse 6
Mouse 7
Mouse 8
Mouse 9
Mouse 10
Mouse 11
Mouse 12
Mouse 13
Mouse 14
Mouse 15
Mouse 16
Mouse 17
Mouse 18
C
- E2
+ E2
Non-tumor-inoculated
Tumor-inoculated
D
% BV/TV
Tb.N (/mm)
Tb.Th (μm)
Tb.Sp (μm)
MCF7-inoculated
E
Pan-cytokeratin (PCK-26) / DAPI
H&E
- E2 (Mouse 10)
+ E2 (Mouse 18)
F
Pan-cytokeratin (PCK-26) positive area / total area
G
B2M mRNA : Hmbs
HPRT1 mRNA : Hmbs

Figure 10. Assessment of MCF7 tumor burden in the bone by histology, immunofluorescence, and qPCR. (A) Representative hematoxylin and eosin (H&E) images of tibiae from MCF7-inoculated mice from -E2 (n=10 mice) and +E2 (n=8 mice) mice. Arrows indicate tumor cells. Panels left to right = 4X, 20X, 40X of same tibia. Scale bars = 500μM (left) and 100μM (right two panels). (B) Histomorphometric analysis of bone volume/total volume (%BV/TV) from mice described in (A) and non-tumor-inoculated (naïve) mice (n=10 -E2 mice, n=8 +E2 mice). (C) Representative microCT images of mice described in (A) and (B). (D) micro-CT analysis of mice described in (C). (E) Representative images of immunostaining for pan-cytokeratin (PCK-26) and DAPI or H&E from mice described in (A). Immunofluorescence panels left to right = 4X, 20X, 40X of same tibia. H&E panels, left = 20X, right = 40X. Scale bars = 500μM (far left panel) and 100μM (right four panels). (F) Quantitation of pan-cytokeratin (PCK-26) area over total bone area from (E). (G) qPCR of whole bone homogenate from non-tumor-inoculated (naïve) mice (n=10 -E2 mice, n=8 +E2 mice) and MCF7-inoculated mice (n=10 -E2 mice, n=8 +E2 mice) for human *B2M* or human *HPRT1* normalized to mouse *Hmbs* (housekeeping gene). B, D, G: One-way ANOVA with Sidak's multiple comparisons test, ** $P < 0.01$ and **** $P < 0.0001$.

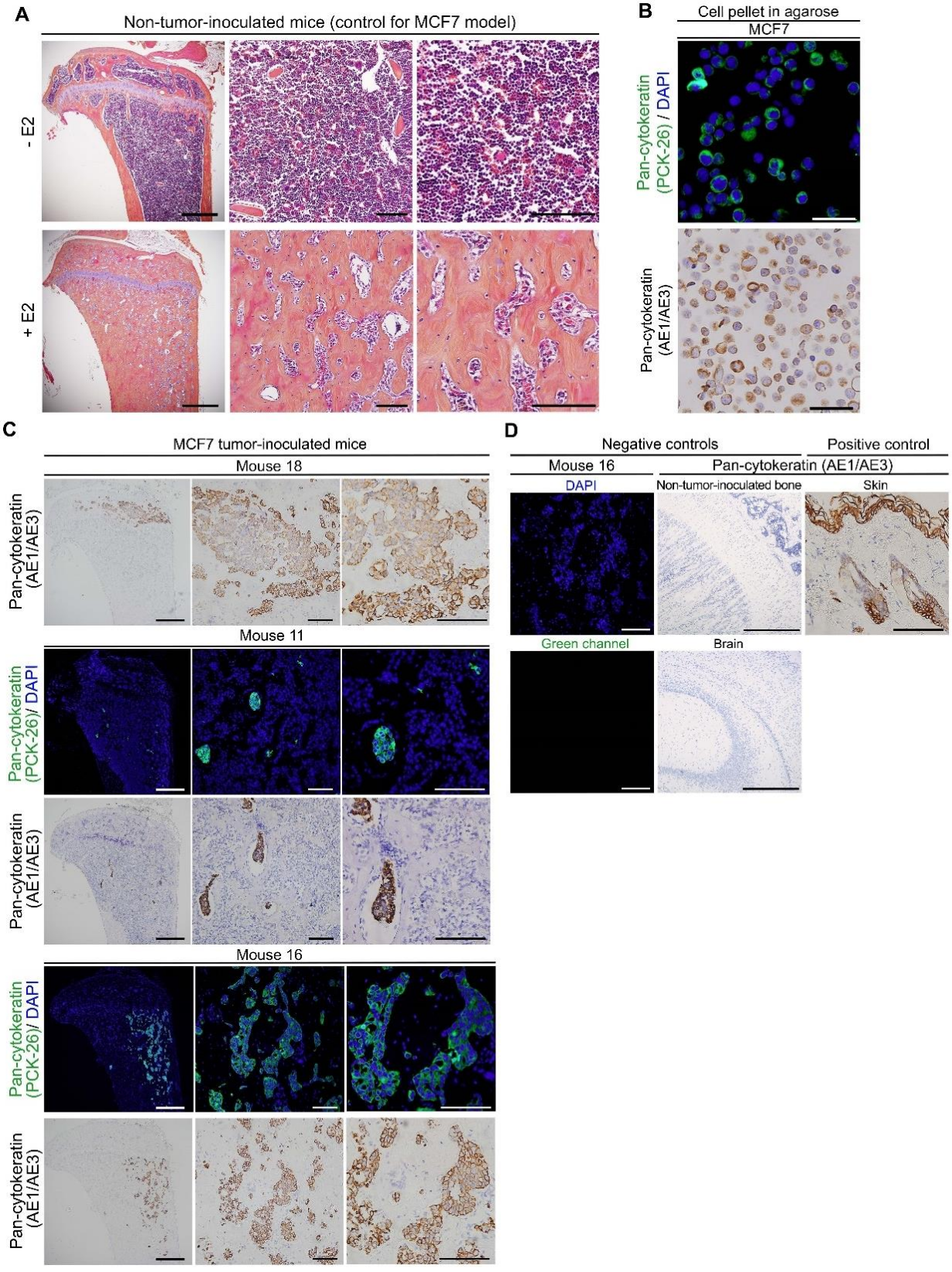
A
Non-tumor-inoculated mice (control for MCF7 model)
- E2
+ E2
B
Cell pellet in agarose
MCF7
Pan-cytokeratin (PCK-26) / DAPI
Pan-cytokeratin (AE1/AE3)
C
MCF7 tumor-inoculated mice
Mouse 18
Pan-cytokeratin (AE1/AE3)
Mouse 11
Pan-cytokeratin (PCK-26)/ DAPI
Pan-cytokeratin (AE1/AE3)
Mouse 16
Pan-cytokeratin (PCK-26)/ DAPI
Pan-cytokeratin (AE1/AE3)
D
Negative controls
Positive control
Mouse 16
Pan-cytokeratin (AE1/AE3)
DAPI
Non-tumor-inoculated bone
Skin
Green channel
Brain

Figure 11. Immunostaining for pan-cytokeratin in tumor cells and bones of tumor-inoculated mice. (A) Representative hematoxylin and eosin (H&E) images of tibiae from non-tumor-inoculated -E2 (n=10) and +E2 (n=8) mice. Panels left to right = 4X, 20X, 40X of same tibia. Scale bars = 500μM (left) and 100μM (right two panels). (B) Representative images of pan-cytokeratin staining (PCK-26 and AE1/AE3) in MCF7 cells grown *in vitro* and prepared as a cell pellet in agarose for sectioning and staining (n=1 experiment). Scale bars = 100μM. (C) Positive immunostaining for pan-cytokeratin (PCK-26 and AE1/AE3) in the tibiae of three different MCF7-inoculated mice. Panels left to right = 4X, 20X, 40X of same tibia. Scale bars = 500μM (left panel) and 100μM (right two panels). (D) Representative images of tibiae stained with DAPI alone showing no autofluorescence in the green channel and non-tumor-bearing (naïve) tibiae or brain stained with pan-cytokeratin (AE1/AE3) as negative controls. Skin stained with pan-cytokeratin (AE1/AE3) was used as a positive control. Scale bars = 100μM (left panels, top and bottom) and 500 μM (right two panels, top and bottom).

Expression of human beta-2-microglobulin (*B2M*), a human housekeeping gene (74, 161), was detected in bone homogenates from MCF7-inoculated mice in 5/10 (50%) -E2 mice and 5/8 (63%) +E2 mice (Figure 10G and Table 5) by qPCR, making this the second most sensitive method of MCF7 tumor cell detection in bone after flow cytometry. qPCR for the human housekeeping gene *HPRT1* (74, 161) was less sensitive but detected tumor cells in 4/10 (40%) -E2 mice and 2/8 (25%) +E2 mice (Figure 10G and Table 5).

Dissemination to bone by murine D2.0R and human SUM159 cells

H&E staining of tibiae from D2.0R-inoculated mice did not reveal any dramatic tumor lesions, irrespective of E2 supplementation compared to non-tumor-inoculated mice (Figure 12A and Figure 13A). However, assessment of these sections by a veterinary pathologist revealed the presence of tumor cells in 1/9 (11%) -E2 and 2/6 (33%) +E2 mice. Histomorphometric analysis of tibiae from non-tumor-inoculated and D2.0R-inoculated mice revealed a significant increase in bone volume from ~4.5% to ~75% with E2 supplementation (+E2) (Figure 12B), similar to that observed in the MCF7 model. A significant reduction in bone volume was observed in +E2 D2.0R-inoculated mice compared to non-tumor-inoculated mice (Figure 12B). To further assess whether bone microarchitecture was altered with D2.0R inoculation and/or E2 supplementation, microCT analysis was performed on -E2 and +E2 non-tumor-inoculated and D2.0R-inoculated mice (Figure 12C, D). Consistent with histomorphometric analysis of these bones (Figure 12B), microCT analysis revealed a significant increase in trabecular bone volume and trabecular number and a decrease in trabecular separation in +E2 mice compared to -E2 mice regardless of tumor inoculation.(Figure 12D). Trabecular thickness was significantly greater in +E2 versus -E2 non-tumor-inoculated (naïve) mice (Figure 12D), but was not statistically different in tumor-inoculated mice. Within the +E2 mice, a significant decrease in bone volume and increase in trabecular separation, with a trend toward a reduction in trabecular thickness, was observed in D2.0R-inoculated mice (Figure 12D). Surprisingly, there was also a significant increase in trabecular number in these mice (Figure 12D).

Since the syngeneic D2.0R cell line is of mouse, rather than human origin, cytokeratin 18 (*Krt18*) expression, which is commonly used to identify mammary epithelial cells (162, 163), was used in place of human *B2M* expression following validation of *Krt18* expression in D2.0R cells (Figure 13B). A significant increase in *Krt18* expression was observed in -E2 D2.0R-inoculated mice compared to -E2 non-tumor-inoculated (naïve) mice (Figure 12E and Table 6). Interestingly, there was significantly less *Krt18* expression in +E2 D2.0R-inoculated mice compared to -E2 D2.0R-inoculated mice (Figure 12E). Immunostaining for

Table 5. Raw data for qPCR analysis of MCF7 model. Raw Ct values and deltaCt analysis of technical and biological replicates for hydroxymethylbilane synthase (*Hmbs*), hypoxanthine phosphoribosyltransferase 1 (*HPRT1*), and beta-2-microglobulin (*B2M*).

Sample name	Gene	Technial replicate #	Ct value	$\Delta Ct = Ct_{hGene} - Ct_{mHbms(avg)}$	$2^{-\Delta Ct}$	Avg
MCF7-inoculated -E2 mouse #9	m*Hbms*	1	22.819			
	m*Hbms*	2	22.649			
	m*Hbms*	3	22.375			
	h*B2M*	1	28.466	5.852	0.0173	
	h*B2M*	2	29.123	6.509	0.0110	0.016237
	h*B2M*	3	28.229	5.615	0.0204	
	h*HPRT1*	1	Undetermined	0.000	0.0000	
	h*HPRT1*	2	Undetermined	0.000	0.0000	0.000000
	h*HPRT1*	3	33.864	11.250	0.0004	
MCF7-inoculated -E2 mouse #10	m*Hbms*	1	23.184			
	m*Hbms*	2	23.912			
	m*Hbms*	3	24.729			
	h*B2M*	1	Undetermined	0.000	0.0000	
	h*B2M*	2	Undetermined	0.000	0.0000	0.000000
	h*B2M*	3	Undetermined	0.000	0.0000	
	h*HPRT1*	1	33.017	9.075	0.0019	
	h*HPRT1*	2	32.602	8.660	0.0025	0.001828
	h*HPRT1*	3	33.695	9.753	0.0012	
MCF7-inoculated +E2 mouse #11	m*Hbms*	1	27.841			
	m*Hbms*	2	27.802			
	m*Hbms*	3	27.740			
	h*B2M*	1	30.011	2.217	0.2151	
	h*B2M*	2	31.477	3.683	0.0779	0.167987
	h*B2M*	3	30.039	2.245	0.2110	
	h*HPRT1*	1	27.818	0.024	0.9836	
	h*HPRT1*	2	27.064	-0.730	1.6588	1.174072
	h*HPRT1*	3	27.979	0.185	0.8798	
MCF7-inoculated +E2 mouse #12	m*Hbms*	1	23.834			
	m*Hbms*	2	24.521			
	m*Hbms*	3	23.837			
	h*B2M*	1	30.078	6.014	0.0155	
	h*B2M*	2	30.435	6.371	0.0121	0.012338
	h*B2M*	3	30.788	6.724	0.0095	
	h*HPRT1*	1	31.922	7.858	0.0043	
	h*HPRT1*	2	32.433	8.369	0.0030	0.003135
	h*HPRT1*	3	32.979	8.915	0.0021	
MCF7-inoculated +E2 mouse #13	m*Hbms*	1	27.489			
	m*Hbms*	2	27.156			
	m*Hbms*	3	28.068			
	h*B2M*	1	35.665	8.094	0.0000	
	h*B2M*	2	Undetermined	0.000	0.0000	0.000000
	h*B2M*	3	Undetermined	0.000	0.0000	
	h*HPRT1*	1	Undetermined	0.000	0.0000	
	h*HPRT1*	2	Undetermined	0.000	0.0000	0.000000
	h*HPRT1*	3	Undetermined	0.000	0.0000	
MCF7-inoculated +E2 mouse #14	m*Hbms*	1	27.599			
	m*Hbms*	2	27.254			
	m*Hbms*	3	27.579			
	h*B2M*	1	27.679	0.202	0.8695	
	h*B2M*	2	29.009	1.532	0.3459	0.517360
	h*B2M*	3	29.048	1.571	0.3367	
	h*HPRT1*	1	Undetermined	0.000	0.0000	
	h*HPRT1*	2	Undetermined	0.000	0.0000	0.000000
	h*HPRT1*	3	Undetermined	0.000	0.0000	
MCF7-inoculated +E2 mouse #15	m*Hbms*	1	24.689			
	m*Hbms*	2	24.566			
	m*Hbms*	3	24.454			
	h*B2M*	1	27.721	3.151	0.1126	
	h*B2M*	2	27.569	2.999	0.1251	0.142189
	h*B2M*	3	26.974	2.404	0.1889	
	h*HPRT1*	1	Undetermined	0.000	0.0000	
	h*HPRT1*	2	Undetermined	0.000	0.0000	0.000000
	h*HPRT1*	3	Undetermined	0.000	0.0000	
MCF7-inoculated +E2 mouse #16	m*Hbms*	1	26.124			
	m*Hbms*	2	26.195			
	m*Hbms*	3	28.749			
	h*B2M*	1	28.229	1.206	0.4334	
	h*B2M*	2	27.016	-0.007	1.0046	0.687457
	h*B2M*	3	27.702	0.679	0.6244	
	h*HPRT1*	1	Undetermined	0.000	0.0000	
	h*HPRT1*	2	Undetermined	0.000	0.0000	0.000000
	h*HPRT1*	3	Undetermined	0.000	0.0000	
MCF7-inoculated +E2 mouse #17	m*Hbms*	1	25.132			
	m*Hbms*	2	27.425			
	m*Hbms*	3	26.894			
	h*B2M*	1	28.684	2.200	0.2176	
	h*B2M*	2	27.650	1.166	0.4456	0.338554
	h*B2M*	3	27.988	1.504	0.3525	
	h*HPRT1*	1	Undetermined	0.000	0.0000	
	h*HPRT1*	2	Undetermined	0.000	0.0000	0.000000
	h*HPRT1*	3	Undetermined	0.000	0.0000	
MCF7-inoculated +E2 mouse #18	m*Hbms*	1	27.794			
	m*Hbms*	2	28.489			
	m*Hbms*	3	27.067			
	h*B2M*	1	Undetermined	0.000	0.0000	
	h*B2M*	2	Undetermined	0.000	0.0000	0.000000
	h*B2M*	3	Undetermined	0.000	0.0000	
	h*HPRT1*	1	Undetermined	0.000	0.0000	
	h*HPRT1*	2	Undetermined	0.000	0.0000	0.000000
	h*HPRT1*	3	Undetermined	0.000	0.0000	
No template control	m*Hbms*	1	Undetermined	0.000	0.0000	
	m*Hbms*	2	Undetermined	0.000	0.0000	0.000000
	m*Hbms*	3	Undetermined	0.000	0.0000	
	h*B2M*	1	Undetermined	0.000	0.0000	
	h*B2M*	2	Undetermined	0.000	0.0000	0.000000
	h*B2M*	3	Undetermined	0.000	0.0000	
	h*HPRT1*	1	Undetermined	0.000	0.0000	
	h*HPRT1*	2	Undetermined	0.000	0.0000	0.000000
	h*HPRT1*	3	Undetermined	0.000	0.0000	

Sample name	Gene	Technial replicate #	Ct value	$\Delta Ct = Ct_{hGene} - Ct_{mHbms(avg)}$	$2^{-\Delta Ct}$	Avg
Non-tumor-inoculated -E2 nude mouse #9	m*Hbms*	1	25.750			
	m*Hbms*	2	25.627			
	m*Hbms*	3	26.230			
	h*HPRT1*	1	Undetermined	0.000	0.0000	
	h*HPRT1*	2	Undetermined	0.000	0.0000	0.000000
	h*HPRT1*	3	Undetermined	0.000	0.0000	
	h*B2M*	1	Undetermined	0.000	0.0000	
	h*B2M*	2	Undetermined	0.000	0.0000	0.000000
	h*B2M*	3	Undetermined	0.000	0.0000	
Non-tumor-inoculated -E2 nude mouse #10	m*Hbms*	1	25.304			
	m*Hbms*	2	25.373			
	m*Hbms*	3	25.412			
	h*HPRT1*	1	Undetermined	0.000	0.0000	
	h*HPRT1*	2	Undetermined	0.000	0.0000	0.000000
	h*HPRT1*	3	Undetermined	0.000	0.0000	
	h*B2M*	1	Undetermined	0.000	0.0000	
	h*B2M*	2	Undetermined	0.000	0.0000	0.000000
	h*B2M*	3	Undetermined	0.000	0.0000	
Non-tumor-inoculated +E2 nude mouse #1	m*Hbms*	1	26.931			
	m*Hbms*	2	27.755			
	m*Hbms*	3	26.828			
	h*HPRT1*	1	Undetermined	0.000	0.0000	
	h*HPRT1*	2	Undetermined	0.000	0.0000	0.000000
	h*HPRT1*	3	Undetermined	0.000	0.0000	
	h*B2M*	1	Undetermined	0.000	0.0000	
	h*B2M*	2	Undetermined	0.000	0.0000	0.000000
	h*B2M*	3	Undetermined	0.000	0.0000	
Non-tumor-inoculated +E2 nude mouse #2	m*Hbms*	1	26.979			
	m*Hbms*	2	27.103			
	m*Hbms*	3	29.008			
	h*HPRT1*	1	Undetermined	0.000	0.0000	
	h*HPRT1*	2	Undetermined	0.000	0.0000	0.000000
	h*HPRT1*	3	Undetermined	0.000	0.0000	
	h*B2M*	1	Undetermined	0.000	0.0000	
	h*B2M*	2	Undetermined	0.000	0.0000	0.000000
	h*B2M*	3	Undetermined	0.000	0.0000	
Non-tumor-inoculated +E2 nude mouse #3	m*Hbms*	1	26.016			
	m*Hbms*	2	28.279			
	m*Hbms*	3	27.512			
	h*HPRT1*	1	Undetermined	0.000	0.0000	
	h*HPRT1*	2	Undetermined	0.000	0.0000	0.000000
	h*HPRT1*	3	Undetermined	0.000	0.0000	
	h*B2M*	1	Undetermined	0.000	0.0000	
	h*B2M*	2	Undetermined	0.000	0.0000	0.000000
	h*B2M*	3	Undetermined	0.000	0.0000	
Non-tumor-inoculated +E2 nude mouse #4	m*Hbms*	1	24.567			
	m*Hbms*	2	25.906			
	m*Hbms*	3	24.108			
	h*HPRT1*	1	Undetermined	0.000	0.0000	
	h*HPRT1*	2	Undetermined	0.000	0.0000	0.000000
	h*HPRT1*	3	Undetermined	0.000	0.0000	
	h*B2M*	1	Undetermined	0.000	0.0000	
	h*B2M*	2	Undetermined	0.000	0.0000	0.000000
	h*B2M*	3	Undetermined	0.000	0.0000	
Non-tumor-inoculated +E2 nude mouse #5	m*Hbms*	1	24.406			
	m*Hbms*	2	25.129			
	m*Hbms*	3	24.210			
	h*HPRT1*	1	Undetermined	0.000	0.0000	
	h*HPRT1*	2	Undetermined	0.000	0.0000	0.000000
	h*HPRT1*	3	Undetermined	0.000	0.0000	
	h*B2M*	1	Undetermined	0.000	0.0000	
	h*B2M*	2	Undetermined	0.000	0.0000	0.000000
	h*B2M*	3	Undetermined	0.000	0.0000	
Non-tumor-inoculated +E2 nude mouse #6	m*Hbms*	1	28.780			
	m*Hbms*	2	27.486			
	m*Hbms*	3	27.156			
	h*HPRT1*	1	Undetermined	0.000	0.0000	
	h*HPRT1*	2	Undetermined	0.000	0.0000	0.000000
	h*HPRT1*	3	Undetermined	0.000	0.0000	
	h*B2M*	1	Undetermined	0.000	0.0000	
	h*B2M*	2	Undetermined	0.000	0.0000	0.000000
	h*B2M*	3	Undetermined	0.000	0.0000	
Non-tumor-inoculated +E2 nude mouse #7	m*Hbms*	1	27.858			
	m*Hbms*	2	27.277			
	m*Hbms*	3	27.311			
	h*HPRT1*	1	Undetermined	0.000	0.0000	
	h*HPRT1*	2	Undetermined	0.000	0.0000	0.000000
	h*HPRT1*	3	Undetermined	0.000	0.0000	
	h*B2M*	1	Undetermined	0.000	0.0000	
	h*B2M*	2	Undetermined	0.000	0.0000	0.000000
	h*B2M*	3	Undetermined	0.000	0.0000	
Non-tumor-inoculated +E2 nude mouse #8	m*Hbms*	1	25.943			
	m*Hbms*	2	26.915			
	m*Hbms*	3	26.855			
	h*HPRT1*	1	Undetermined	0.000	0.0000	
	h*HPRT1*	2	Undetermined	0.000	0.0000	0.000000
	h*HPRT1*	3	Undetermined	0.000	0.0000	
	h*B2M*	1	Undetermined	0.000	0.0000	
	h*B2M*	2	Undetermined	0.000	0.0000	0.000000
	h*B2M*	3	Undetermined	0.000	0.0000	
No template control	m*Hbms*	1	Undetermined	0.000	0.0000	
	m*Hbms*	2	Undetermined	0.000	0.0000	0.000000
	m*Hbms*	3	Undetermined	0.000	0.0000	
	h*HPRT1*	1	Undetermined	0.000	0.0000	
	h*HPRT1*	2	Undetermined	0.000	0.0000	0.000000
	h*HPRT1*	3	Undetermined	0.000	0.0000	
	h*B2M*	1	Undetermined	0.000	0.0000	
	h*B2M*	2	Undetermined	0.000	0.0000	0.000000
	h*B2M*	3	Undetermined	0.000	0.0000	

Sample name	Gene	Technial replicate #	Ct value	$\Delta Ct = Ct_{hGene} - Ct_{mHbms(avg)}$	$2^{-\Delta Ct}$	Avg
MCF7-inoculated -E2 mouse #1	m*Hbms*	1	25.841			
	m*Hbms*	2	25.802			
	m*Hbms*	3	25.740			
	h*B2M*	1	28.011	2.217	0.2151	0.204401
	h*B2M*	2	28.477	2.683	0.1557	
	h*B2M*	3	27.839	2.045	0.2424	
	h*HPRT1*	1	30.489	4.389	0.0477	0.063100
	h*HPRT1*	2	30.122	4.022	0.0616	
	h*HPRT1*	3	29.744	3.644	0.0800	
MCF7-inoculated -E2 mouse #2	m*Hbms*	1	23.979			
	m*Hbms*	2	24.190			
	m*Hbms*	3	23.845			
	h*B2M*	1	27.419	3.414	0.0938	0.072821
	h*B2M*	2	28.128	4.123	0.0574	
	h*B2M*	3	27.898	3.893	0.0673	
	h*HPRT1*	1	Undetermined	0.000	0.0000	0.000000
	h*HPRT1*	2	Undetermined	0.000	0.0000	
	h*HPRT1*	3	Undetermined	0.000	0.0000	
MCF7-inoculated -E2 mouse #3	m*Hbms*	1	23.161			
	m*Hbms*	2	23.270			
	m*Hbms*	3	23.029			
	h*B2M*	1	30.391	7.237	0.0066	0.005786
	h*B2M*	2	30.966	7.812	0.0044	
	h*B2M*	3	30.468	7.314	0.0063	
	h*HPRT1*	1	29.349	6.195	0.0136	0.018752
	h*HPRT1*	2	28.221	5.067	0.0298	
	h*HPRT1*	3	29.443	6.289	0.0128	
MCF7-inoculated -E2 mouse #4	m*Hbms*	1	25.832			
	m*Hbms*	2	25.587			
	m*Hbms*	3	24.020			
	h*B2M*	1	35.587	10.441	0.0000	0.000000
	h*B2M*	2	Undetermined	0.000	0.0000	
	h*B2M*	3	Undetermined	0.000	0.0000	
	h*HPRT1*	1	Undetermined	0.000	0.0000	0.000000
	h*HPRT1*	2	Undetermined	0.000	0.0000	
	h*HPRT1*	3	Undetermined	0.000	0.0000	
MCF7-inoculated -E2 mouse #5	m*Hbms*	1	26.019			
	m*Hbms*	2	25.555			
	m*Hbms*	3	26.168			
	h*B2M*	1	Undetermined	0.000	0.0000	0.000000
	h*B2M*	2	Undetermined	0.000	0.0000	
	h*B2M*	3	Undetermined	0.000	0.0000	
	h*HPRT1*	1	Undetermined	0.000	0.0000	0.000000
	h*HPRT1*	2	Undetermined	0.000	0.0000	
	h*HPRT1*	3	Undetermined	0.000	0.0000	
MCF7-inoculated -E2 mouse #6	m*Hbms*	1	24.422			
	m*Hbms*	2	23.934			
	m*Hbms*	3	24.293			
	h*B2M*	1	34.149	9.933	0.0010	0.000742
	h*B2M*	2	33.914	9.698	0.0012	
	h*B2M*	3	Undetermined	0.000	0.0000	
	h*HPRT1*	1	Undetermined	0.000	0.0000	0.000000
	h*HPRT1*	2	Undetermined	0.000	0.0000	
	h*HPRT1*	3	Undetermined	0.000	0.0000	
MCF7-inoculated -E2 mouse #7	m*Hbms*	1	24.564			
	m*Hbms*	2	24.604			
	m*Hbms*	3	24.482			
	h*B2M*	1	Undetermined	0.000	0.0000	0.000000
	h*B2M*	2	Undetermined	0.000	0.0000	
	h*B2M*	3	Undetermined	0.000	0.0000	
	h*HPRT1*	1	34.698	10.148	0.0009	0.000688
	h*HPRT1*	2	34.273	9.723	0.0012	
	h*HPRT1*	3	Undetermined	0.000	0.0000	
MCF7-inoculated -E2 mouse #8	m*Hbms*	1	24.423			
	m*Hbms*	2	24.271			
	m*Hbms*	3	24.226			
	h*B2M*	1	Undetermined	0.000	0.0000	0.000797
	h*B2M*	2	34.063	9.756	0.0012	
	h*B2M*	3	33.968	9.661	0.0012	
	h*HPRT1*	1	Undetermined	0.000	0.0000	0.000886
	h*HPRT1*	2	33.626	9.319	0.0016	
	h*HPRT1*	3	34.146	9.839	0.0011	

Sample name	Gene	Technial replicate #	Ct value	$\Delta Ct = Ct_{hGene} - Ct_{mHbms(avg)}$	$2^{-\Delta Ct}$	Avg
Non-tumor-inoculated -E2 nude mouse #1	m*Hbms*	1	24.503			
	m*Hbms*	2	25.647			
	m*Hbms*	3	25.015			
	h*HPRT1*	1	Undetermined	0.000	0.0000	0.000000
	h*HPRT1*	2	Undetermined	0.000	0.0000	
	h*HPRT1*	3	Undetermined	0.000	0.0000	
	h*B2M*	1	Undetermined	0.000	0.0000	0.000000
	h*B2M*	2	Undetermined	0.000	0.0000	
	h*B2M*	3	Undetermined	0.000	0.0000	
Non-tumor-inoculated -E2 nude mouse #2	m*Hbms*	1	23.867			
	m*Hbms*	2	24.596			
	m*Hbms*	3	24.115			
	h*HPRT1*	1	Undetermined	0.000	0.0000	0.000000
	h*HPRT1*	2	Undetermined	0.000	0.0000	
	h*HPRT1*	3	Undetermined	0.000	0.0000	
	h*B2M*	1	Undetermined	0.000	0.0000	0.000000
	h*B2M*	2	Undetermined	0.000	0.0000	
	h*B2M*	3	Undetermined	0.000	0.0000	
Non-tumor-inoculated -E2 nude mouse #3	m*Hbms*	1	24.326			
	m*Hbms*	2	24.399			
	m*Hbms*	3	24.320			
	h*HPRT1*	1	Undetermined	0.000	0.0000	0.000000
	h*HPRT1*	2	Undetermined	0.000	0.0000	
	h*HPRT1*	3	Undetermined	0.000	0.0000	
	h*B2M*	1	Undetermined	0.000	0.0000	0.000000
	h*B2M*	2	Undetermined	0.000	0.0000	
	h*B2M*	3	Undetermined	0.000	0.0000	
Non-tumor-inoculated -E2 nude mouse #4	m*Hbms*	1	24.846			
	m*Hbms*	2	24.688			
	m*Hbms*	3	24.620			
	h*HPRT1*	1	Undetermined	0.000	0.0000	0.000000
	h*HPRT1*	2	Undetermined	0.000	0.0000	
	h*HPRT1*	3	Undetermined	0.000	0.0000	
	h*B2M*	1	Undetermined	0.000	0.0000	0.000000
	h*B2M*	2	Undetermined	0.000	0.0000	
	h*B2M*	3	Undetermined	0.000	0.0000	
Non-tumor-inoculated -E2 nude mouse #5	m*Hbms*	1	22.760			
	m*Hbms*	2	22.531			
	m*Hbms*	3	22.615			
	h*HPRT1*	1	Undetermined	0.000	0.0000	0.000000
	h*HPRT1*	2	Undetermined	0.000	0.0000	
	h*HPRT1*	3	Undetermined	0.000	0.0000	
	h*B2M*	1	Undetermined	0.000	0.0000	0.000000
	h*B2M*	2	Undetermined	0.000	0.0000	
	h*B2M*	3	Undetermined	0.000	0.0000	
Non-tumor-inoculated -E2 nude mouse #6	m*Hbms*	1	24.159			
	m*Hbms*	2	24.104			
	m*Hbms*	3	24.531			
	h*HPRT1*	1	Undetermined	0.000	0.0000	0.000000
	h*HPRT1*	2	Undetermined	0.000	0.0000	
	h*HPRT1*	3	Undetermined	0.000	0.0000	
	h*B2M*	1	Undetermined	0.000	0.0000	0.000000
	h*B2M*	2	Undetermined	0.000	0.0000	
	h*B2M*	3	Undetermined	0.000	0.0000	
Non-tumor-inoculated -E2 nude mouse #7	m*Hbms*	1	25.530			
	m*Hbms*	2	25.403			
	m*Hbms*	3	25.424			
	h*HPRT1*	1	Undetermined	0.000	0.0000	0.000000
	h*HPRT1*	2	Undetermined	0.000	0.0000	
	h*HPRT1*	3	Undetermined	0.000	0.0000	
	h*B2M*	1	Undetermined	0.000	0.0000	0.000000
	h*B2M*	2	Undetermined	0.000	0.0000	
	h*B2M*	3	Undetermined	0.000	0.0000	
Non-tumor-inoculated -E2 nude mouse #8	m*Hbms*	1	24.284			
	m*Hbms*	2	24.404			
	m*Hbms*	3	24.360			
	h*HPRT1*	1	Undetermined	0.000	0.0000	0.000000
	h*HPRT1*	2	Undetermined	0.000	0.0000	
	h*HPRT1*	3	Undetermined	0.000	0.0000	
	h*B2M*	1	Undetermined	0.000	0.0000	0.000000
	h*B2M*	2	Undetermined	0.000	0.0000	
	h*B2M*	3	Undetermined	0.000	0.0000	

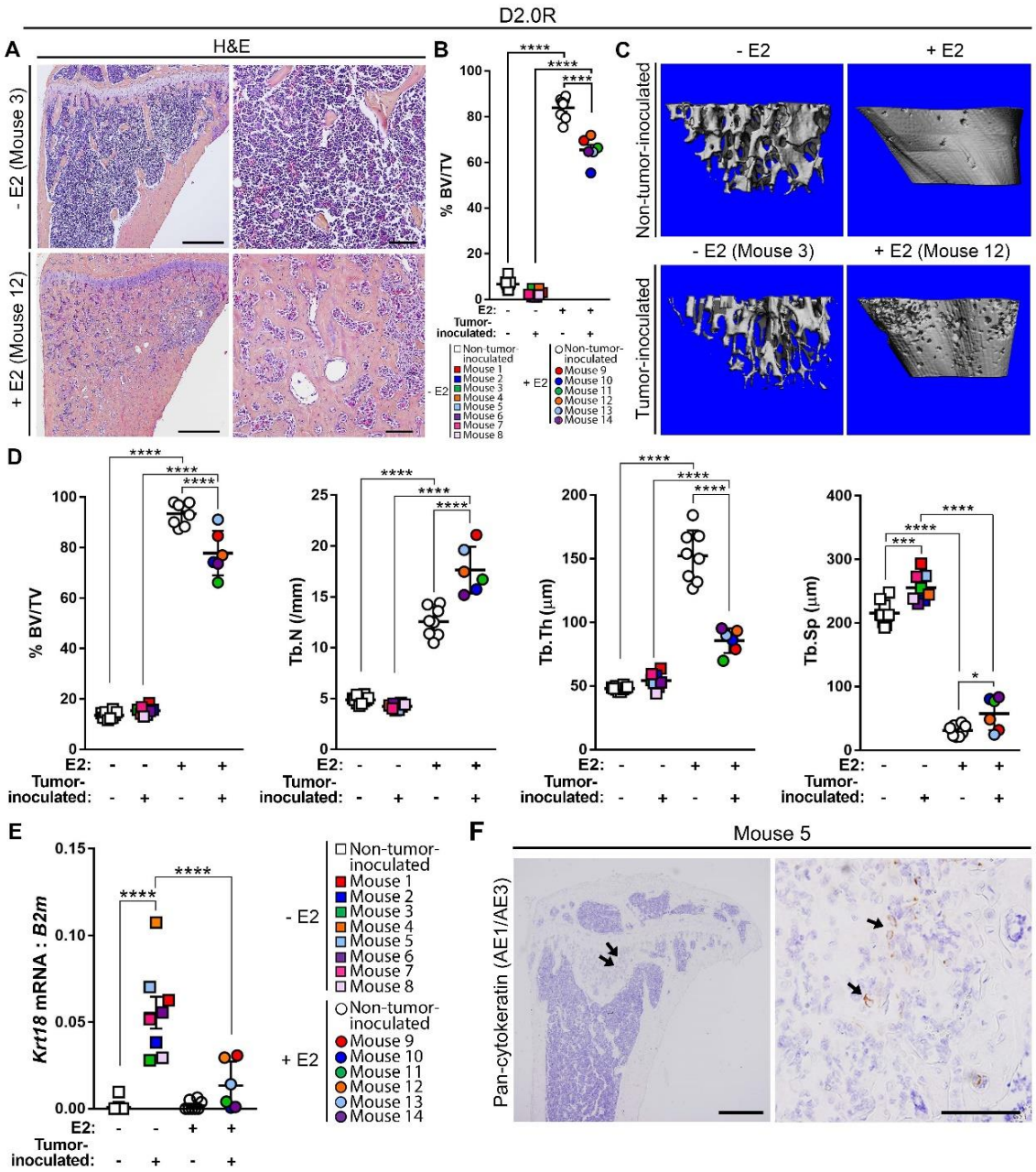

Figure 12. Characterization of D2.0R dissemination to bone. (A) Representative hematoxylin and eosin (H&E) images of D2.0R-inoculated tibiae from -E2 (n=8 mice) and +E2 (n=6 mice) mice. Left panels = 4X, right panels = 20X of same tibiae. Scale bars = 500μM (left panel) and 100μM (right panel). (B) Histomorphometric analysis of bone volume/total volume (%BV/TV) from mice described in (A) and non-tumor-inoculated (naïve) mice (n=10 -E2 mice, n=8 +E2 mice). (C) Representative microCT images of mice described in (A) and (B). (D) micro-CT analysis of mice described in (C). (E) qPCR analysis of whole bone homogenates from non-tumor-inoculated mice and D2.0R-inoculated mice described in (A) and (B) for *Krt18,* normalized to mouse *B2m.* (F) Positive pan-cytokeratin (AE1/AE3) staining in the tibia from a D2.0R-inoculated mouse (mouse number 5). Arrows indicate cytokeratin-positive tumor cells. Left panel = 4X, right panel = 40X of the same tibia. Scale bars = 500μM (left panel) and 100μM (right panel). B, D, E: One-way ANOVA with Sidak's multiple comparisons test, * $P < 0.05$, ***$P < 0.001$ and **** $P < 0.0001$.

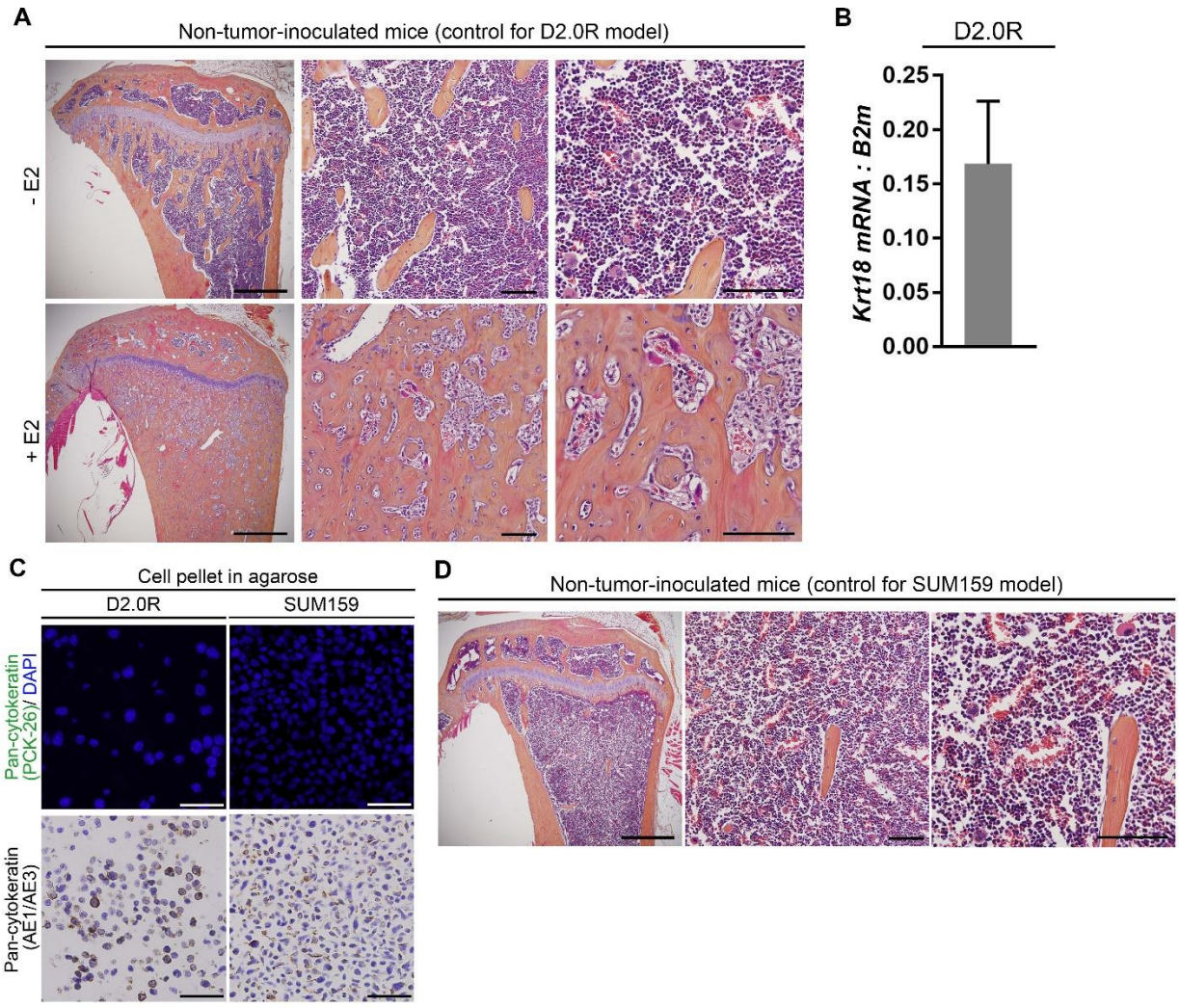

Figure 13. H&E images of non-tumor-inoculated mice for D2.0R and SUM159 models and immunostaining for pan-cytokeratin in D2.0R and SUM159 cells grown *in vitro.* (A) Representative hematoxylin and eosin (H&E) images of tibiae from non-tumor-inoculated -E2 (n=10) and +E2 (n=8) mice as controls for the D2.0R model. Panels left to right = 4X, 20X, 40X of same tibia. Scale bars = 500μM (left) and 100μM (right two panels). (B) Expression of *Krt18* in D2.0R cells grown *in vitro* (n=3 replicates from 3 experiments). (C) Pan-cytokeratin (PCK-26 and AE1/AE3) staining of D2.0R and SUM159 cells grown *in vitro* and prepared as cell pellets in agarose for sectioning and staining. (D) Representative hematoxylin and eosin (H&E) images of tibiae from non-tumor-inoculated (n=10) mice as controls for the SUM159 model. Panels left to right = 4X, 20X, 40X of same tibia. Scale bars = 500μM (left) and 100μM (right two panels).

Table 6. Raw data for qPCR analysis of D2.0R model. Raw Ct values and deltaCt analysis of technical and biological replicates for hydroxymethylbilane synthase (*Hmbs*) and keratin 18 (*Krt18*).

Sample name	Gene	Technial replicate #	Ct value	$\Delta Ct = Ct_{hGene} - Ct_{mHbms(avg)}$	$2^{-\Delta Ct}$	Avg
D2.0R-inoculated -E2 mouse #1	m*Hbms*	1	27.597			
	m*Hbms*	2	27.700			
	m*Hbms*	3	27.622			
	m*k18*	1	31.411	3.771	0.0732	
	m*k18*	2	32.229	4.589	0.0415	0.0626
	m*k18*	3	31.418	3.778	0.0729	
D2.0R-inoculated -E2 mouse #2	m*Hbms*	1	22.811			
	m*Hbms*	2	22.793			
	m*Hbms*	3	22.958			
	m*k18*	1	27.568	4.714	0.0381	
	m*k18*	2	27.504	4.649	0.0398	0.0383
	m*k18*	3	27.613	4.759	0.0369	
D2.0R-inoculated -E2 mouse #3	m*Hbms*	1	21.554			
	m*Hbms*	2	21.447			
	m*Hbms*	3	21.571			
	m*k18*	1	26.876	5.352	0.0245	
	m*k18*	2	26.620	5.096	0.0292	0.0280
	m*k18*	3	26.574	5.050	0.0302	
D2.0R-inoculated -E2 mouse #4	m*Hbms*	1	21.712			
	m*Hbms*	2	21.855			
	m*Hbms*	3	22.345			
	m*k18*	1	25.256	3.285	0.1026	
	m*k18*	2	24.921	2.950	0.1294	0.1074
	m*k18*	3	25.442	3.471	0.0902	
D2.0R-inoculated -E2 mouse #5	m*Hbms*	1	24.966			
	m*Hbms*	2	25.316			
	m*Hbms*	3	25.277			
	m*k18*	1	28.569	3.383	0.0959	
	m*k18*	2	29.388	4.201	0.0544	0.0702
	m*k18*	3	29.238	4.052	0.0603	
D2.0R-inoculated -E2 mouse #6	m*Hbms*	1	24.610			
	m*Hbms*	2	24.524			
	m*Hbms*	3	24.716			
	m*k18*	1	28.541	3.924	0.0659	
	m*k18*	2	28.886	4.269	0.0519	0.0555
	m*k18*	3	28.972	4.356	0.0488	
D2.0R-inoculated -E2 mouse #7	m*Hbms*	1	22.234			
	m*Hbms*	2	21.718			
	m*Hbms*	3	21.982			
	m*k18*	1	26.114	4.136	0.0569	
	m*k18*	2	26.363	4.385	0.0479	0.0512
	m*k18*	3	26.335	4.357	0.0488	
D2.0R-inoculated -E2 mouse #8	m*Hbms*	1	22.264			
	m*Hbms*	2	22.406			
	m*Hbms*	3	22.934			
	m*k18*	1	27.568	5.033	0.0305	
	m*k18*	2	27.504	4.969	0.0319	0.0307
	m*k18*	3	27.613	5.079	0.0296	
D2.0R-inoculated +E2 mouse #9	m*Hbms*	1	24.974			
	m*Hbms*	2	25.010			
	m*Hbms*	3	25.063			
	m*k18*	1	29.524	4.508	0.0440	
	m*k18*	2	30.316	5.300	0.0254	0.0307
	m*k18*	3	30.465	5.449	0.0229	
D2.0R-inoculated +E2 mouse #10	m*Hbms*	1	19.565			
	m*Hbms*	2	22.870			
	m*Hbms*	3	22.473			
	m*k18*	1	34.533	11.897	0.0003	
	m*k18*	2	31.881	9.245	0.0016	0.0007
	m*k18*	3	35.102	12.466	0.0002	
D2.0R-inoculated +E2 mouse #11	m*Hbms*	1	23.858			
	m*Hbms*	2	23.477			
	m*Hbms*	3	23.815			
	m*k18*	1	32.496	8.779	0.0023	
	m*k18*	2	31.549	7.833	0.0044	0.0041
	m*k18*	3	31.198	7.482	0.0056	

Sample name	Gene	Technial replicate #	Ct value	$\Delta Ct = Ct_{hGene} - Ct_{mHbms(avg)}$	$2^{-\Delta Ct}$	Avg
Non-tumor-inoculated Balb/c - E2 mouse #1	m*Hbms*	1	24.745			
	m*Hbms*	2	24.830			
	m*Hbms*	3	24.741			
	m*k18*	1	Undetermined	0.000	0.0000	
	m*k18*	2	Undetermined	0.000	0.0000	0.0000
	m*k18*	3	Undetermined	0.000	0.0000	
Non-tumor-inoculated Balb/c - E2 mouse #2	m*Hbms*	1	24.137			
	m*Hbms*	2	24.382			
	m*Hbms*	3	24.224			
	m*k18*	1	Undetermined	0.000	0.0000	
	m*k18*	2	Undetermined	0.000	0.0000	0.0000
	m*k18*	3	Undetermined	0.000	0.0000	
Non-tumor-inoculated Balb/c - E2 mouse #3	m*Hbms*	1	24.464			
	m*Hbms*	2	24.317			
	m*Hbms*	3	25.591			
	m*k18*	1	Undetermined	0.000	0.0000	
	m*k18*	2	Undetermined	0.000	0.0000	0.0000
	m*k18*	3	Undetermined	0.000	0.0000	
Non-tumor-inoculated Balb/c - E2 mouse #4	m*Hbms*	1	26.505			
	m*Hbms*	2	26.358			
	m*Hbms*	3	25.202			
	m*k18*	1	Undetermined	0.000	0.0000	
	m*k18*	2	Undetermined	0.000	0.0000	0.0000
	m*k18*	3	Undetermined	0.000	0.0000	
Non-tumor-inoculated Balb/c - E2 mouse #5	m*Hbms*	1	24.377			
	m*Hbms*	2	23.881			
	m*Hbms*	3	25.624			
	m*k18*	1	Undetermined	0.000	0.0000	
	m*k18*	2	Undetermined	0.000	0.0000	0.0000
	m*k18*	3	Undetermined	0.000	0.0000	
Non-tumor-inoculated Balb/c - E2 mouse #6	m*Hbms*	1	24.966			
	m*Hbms*	2	25.225			
	m*Hbms*	3	24.906			
	m*k18*	1	Undetermined	0.000	0.0000	
	m*k18*	2	Undetermined	0.000	0.0000	0.0000
	m*k18*	3	Undetermined	0.000	0.0000	
Non-tumor-inoculated Balb/c - E2 mouse #7	m*Hbms*	1	25.607			
	m*Hbms*	2	25.670			
	m*Hbms*	3	25.394			
	m*k18*	1	Undetermined	0.000	0.0000	
	m*k18*	2	Undetermined	0.000	0.0000	0.0000
	m*k18*	3	Undetermined	0.000	0.0000	
Non-tumor-inoculated Balb/c - E2 mouse #8	m*Hbms*	1	23.307			
	m*Hbms*	2	23.284			
	m*Hbms*	3	23.807			
	m*k18*	1	Undetermined	0.000	0.0000	
	m*k18*	2	Undetermined	0.000	0.0000	0.0000
	m*k18*	3	Undetermined	0.000	0.0000	
Non-tumor-inoculated Balb/c - E2 mouse #9	m*Hbms*	1	23.399			
	m*Hbms*	2	23.865			
	m*Hbms*	3	23.647			
	m*k18*	1	30.047	6.410	0.0118	
	m*k18*	2	30.489	6.852	0.0087	0.0092
	m*k18*	3	30.757	7.120	0.0072	
Non-tumor-inoculated Balb/c - E2 mouse #10	m*Hbms*	1	25.562			
	m*Hbms*	2	25.459			
	m*Hbms*	3	25.668			
	m*k18*	1	Undetermined	0.000	0.0000	
	m*k18*	2	Undetermined	0.000	0.0000	0.0000
	m*k18*	3	Undetermined	0.000	0.0000	
Non-tumor-inoculated Balb/c +E2 mouse #1	m*Hbms*	1	24.741			
	m*Hbms*	2	24.832			
	m*Hbms*	3	24.808			
	m*k18*	1	33.274	8.481	0.0028	
	m*k18*	2	31.592	6.798	0.0090	0.0051
	m*k18*	3	32.996	8.202	0.0034	

Sample name	Gene	Technial replicate #	Ct value	$\Delta Ct = Ct_{hGene} - Ct_{mHbms(avg)}$	$2^{-\Delta Ct}$	Avg
D2.0R-inoculated +E2 mouse #12	m*Hbms*	1	23.832			
	m*Hbms*	2	24.153			
	m*Hbms*	3	24.022			
	m*k18*	1	29.338	5.336	0.0248	
	m*k18*	2	29.034	5.032	0.0306	0.0295
	m*k18*	3	28.916	4.914	0.0332	
D2.0R-inoculated +E2 mouse #13	m*Hbms*	1	21.509			
	m*Hbms*	2	21.505			
	m*Hbms*	3	21.624			
	m*k18*	1	27.482	5.936	0.0163	
	m*k18*	2	27.664	6.118	0.0144	0.0142
	m*k18*	3	27.945	6.399	0.0118	
D2.0R-inoculated +E2 mouse #14	m*Hbms*	1	22.003			
	m*Hbms*	2	22.128			
	m*Hbms*	3	23.439			
	m*k18*	1	31.929	9.406	0.0015	
	m*k18*	2	32.514	9.991	0.0010	0.0011
	m*k18*	3	32.829	10.305	0.0008	
No template control	m*Hbms*	1	Undetermined	0.000	0.0000	
	m*Hbms*	2	Undetermined	0.000	0.0000	0.0000
	m*Hbms*	3	Undetermined	0.000	0.0000	
	m*k18*	1	Undetermined	0.000	0.0000	
	m*k18*	2	Undetermined	0.000	0.0000	0.0000
	m*k18*	3	Undetermined	0.000	0.0000	

Sample name	Gene	Technial replicate #	Ct value	$\Delta Ct = Ct_{hGene} - Ct_{mHbms(avg)}$	$2^{-\Delta Ct}$	Avg
Non-tumor-inoculated Balb/c +E2 mouse #2	m*Hbms*	1	20.871			
	m*Hbms*	2	20.927			
	m*Hbms*	3	20.924			
	m*k18*	1	29.035	8.128	0.0036	
	m*k18*	2	28.923	8.016	0.0039	0.0038
	m*k18*	3	28.939	8.032	0.0038	
Non-tumor-inoculated Balb/c +E2 mouse #3	m*Hbms*	1	21.920			
	m*Hbms*	2	22.082			
	m*Hbms*	3	22.799			
	m*k18*	1	Undetermined	0.000	0.0000	
	m*k18*	2	Undetermined	0.000	0.0000	0.0000
	m*k18*	3	Undetermined	0.000	0.0000	
Non-tumor-inoculated Balb/c +E2 mouse #4	m*Hbms*	1	24.453			
	m*Hbms*	2	24.356			
	m*Hbms*	3	23.105			
	m*k18*	1	Undetermined	0.000	0.0000	
	m*k18*	2	Undetermined	0.000	0.0000	0.0000
	m*k18*	3	Undetermined	0.000	0.0000	
Non-tumor-inoculated Balb/c +E2 mouse #5	m*Hbms*	1	24.890			
	m*Hbms*	2	25.693			
	m*Hbms*	3	24.986			
	m*k18*	1	Undetermined	0.000	0.0000	
	m*k18*	2	Undetermined	0.000	0.0000	0.0000
	m*k18*	3	Undetermined	0.000	0.0000	
Non-tumor-inoculated Balb/c +E2 mouse #6	m*Hbms*	1	24.868			
	m*Hbms*	2	24.653			
	m*Hbms*	3	23.557			
	m*k18*	1	32.538	7.348	0.0061	
	m*k18*	2	32.296	7.107	0.0073	0.0063
	m*k18*	3	32.676	7.487	0.0056	
Non-tumor-inoculated Balb/c +E2 mouse #7	m*Hbms*	1	24.214			
	m*Hbms*	2	24.270			
	m*Hbms*	3	24.176			
	m*k18*	1	Undetermined	0.000	0.0000	
	m*k18*	2	Undetermined	0.000	0.0000	0.0000
	m*k18*	3	Undetermined	0.000	0.0000	
Non-tumor-inoculated Balb/c +E2 mouse #8	m*Hbms*	1	23.615			
	m*Hbms*	2	23.663			
	m*Hbms*	3	23.683			
	m*k18*	1	Undetermined	0.000	0.0000	
	m*k18*	2	Undetermined	0.000	0.0000	0.0000
	m*k18*	3	Undetermined	0.000	0.0000	
No template control	m*Hbms*	1	Undetermined	0.000	0.0000	
	m*Hbms*	2	Undetermined	0.000	0.0000	0.0000
	m*Hbms*	3	Undetermined	0.000	0.0000	
	m*k18*	1	Undetermined	0.000	0.0000	
	m*k18*	2	Undetermined	0.000	0.0000	0.0000
	m*k18*	3	Undetermined	0.000	0.0000	

pan-cytokeratin (AE1/AE3) was detected in a subset of D2.0R cells grown *in vitro* (Figure 13C) and pan-cytokeratin positive tumor cells were detected in the bone marrow of 1/9 (11%) -E2 mice (Figure 12F).

H&E staining and morphological assessment of tibiae from SUM159-inoculated mice failed to detect tumor cells in any (0/10) mice compared to non-tumor-inoculated mice (Figure 13D and Figure 14A), which was confirmed by a veterinary pathologist. Bone microarchitecture was evaluated by histomorphometric analysis (Figure 14B) and microCT (Figure 14C, D), which revealed no significant alterations in bone volume or trabecular structure between age-matched non-tumor-inoculated (naïve) and SUM159-inoculated mice. However, consistent with flow cytometric analysis of marrow isolated from SUM159-inoculated mice (Figure 9F-H), we detected tumor cells by qPCR analysis for human *B2M* expression in 2/8 (25%) mice and human *HPRT1* in 3/8 (38%) mice (Figure 14E and Table 7). Similar to D2.0R cells, immunostaining for pan-cytokeratin (AE1/AE3) was detected in a subset of SUM159 cells grown *in vitro* (Figure 13C); however, pan-cytokeratin did not detect tumor cells in the bone marrow of any (0/8) SUM159-inoculated mice (data not shown).

Discussion

Little is known about the mechanisms that regulate tumor cell homing to the bone marrow and subsequent entry into and exit from dormancy. This is, in part, due to the lack of available *in vivo* models that recapitulate long latency periods observed in humans. Here, we investigated the ability of three different breast carcinoma cell lines (ER+ human MCF7, ER+ murine D2.0R, and ER- human SUM159), to disseminate to the bone following intracardiac inoculation in the presence (+E2) or absence (-E2) of estrogen supplementation. Our data indicate that exogenous estrogen is not required for tumor cell dissemination to the bone marrow in the MCF7 or D2.0R model. However, estrogen is necessary for tumor cells to grow in and colonize the bone marrow in the MCF7 model, since micrometastases detectable by immunostaining were only evident in the +E2 MCF7 model. While MCF7s have been used by multiple groups in bone colonization studies (45, 74, 155), this is the first report describing the ability of D2.0R and SUM159 cells to home to the bone marrow. The D2.0R cells exhibit a time-course of approximately 7 weeks (similar to the MCF7 model), while the SUM159 cells exhibit an extended latency period (13 weeks), which may be particularly useful for the study of prolonged tumor latency. These groups were sacrificed at the indicated times due to several mice becoming moribund or found deceased due to estrogen toxicities or unknown causes. Thus, the maximum amount of time for the SUM159 model appears to be 13 weeks, since these

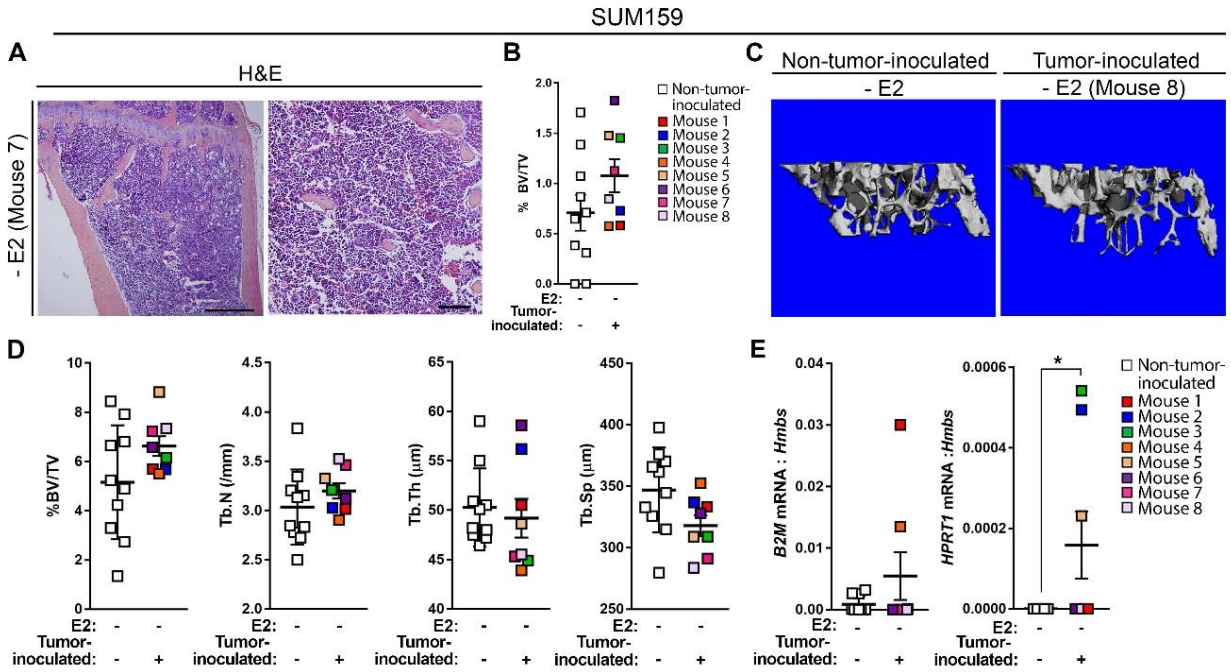

Figure 14. Characterization of SUM159 dissemination to bone. (A) Representative H&E images of the tibia from a SUM159-inoculated mouse (n=8 mice). Left panel = 4X, right panel = 20X of the same tibia. Scale bars = 500μM (left panel) and 100μM (right panel). (B) Histomorphometric analysis of bone volume/total volume (%BV/TV) from mice described in (A). (C) Representative microCT images of non-tumor-inoculated (naïve) mice (n=10 mice) and SUM159-inoculated mice (n=8 mice). (D) micro-CT analysis of mice described in (C). (E) qPCR of whole bone homogenate from mice described in (C) for human *B2M* or human *HPRT1* normalized to mouse *Hmbs* (housekeeping gene). E: Mann-Whitney U-test, * $P < 0.05$.

Table 7.Raw data for qPCR analysis of SUM159 model. Raw Ct values and deltaCt analysis of technical and biological replicates for hydroxymethylbilane synthase (*Hmbs*), hypoxanthine phosphoribosyltransferase 1 (*HPRT1*), and beta-2-microglobulin (*B2M*).

Sample name	Gene	Technial replicate #	Ct value	$\Delta Ct = Ct_{hGene} - Ct_{mHbms(avg)}$	$2^{-\Delta Ct}$	Avg
SUM159-inoculated-E2 mouse #1	m*Hbms*	1	25.803			
	m*Hbms*	2	25.981			
	m*Hbms*	3	25.682			
	h*B2M*	1	31.231	5.409	0.0235	0.0303
	h*B2M*	2	30.480	4.658	0.0396	
	h*B2M*	3	30.994	5.172	0.0277	
	h*HPRT1*	1	Undetermined	0.000	0.0000	0.0000
	h*HPRT1*	2	Undetermined	0.000	0.0000	
	h*HPRT1*	3	Undetermined	0.000	0.0000	
SUM159-inoculated-E2 mouse #2	m*Hbms*	1	23.259			
	m*Hbms*	2	23.832			
	m*Hbms*	3	23.214			
	h*B2M*	1	Undetermined	0.000	0.0000	0.0000
	h*B2M*	2	Undetermined	0.000	0.0000	
	h*B2M*	3	Undetermined	0.000	0.0000	
	h*HPRT1*	1	34.762	11.327	0.0004	0.0005
	h*HPRT1*	2	33.993	10.557	0.0007	
	h*HPRT1*	3	34.548	11.113	0.0005	
SUM159-inoculated-E2 mouse #3	m*Hbms*	1	23.226			
	m*Hbms*	2	23.045			
	m*Hbms*	3	23.321			
	h*B2M*	1	Undetermined	0.000	0.0000	0.0000
	h*B2M*	2	Undetermined	0.000	0.0000	
	h*B2M*	3	Undetermined	0.000	0.0000	
	h*HPRT1*	1	33.897	10.700	0.0006	0.0006
	h*HPRT1*	2	34.084	10.887	0.0005	
	h*HPRT1*	3	33.925	10.727	0.0006	
SUM159-inoculated-E2 mouse #4	m*Hbms*	1	23.246			
	m*Hbms*	2	23.353			
	m*Hbms*	3	23.657			
	h*B2M*	1	29.804	6.385	0.0120	0.0135
	h*B2M*	2	29.432	6.013	0.0155	
	h*B2M*	3	29.687	6.268	0.0130	
	h*HPRT1*	1	Undetermined	0.000	0.0000	0.0000
	h*HPRT1*	2	Undetermined	0.000	0.0000	
	h*HPRT1*	3	Undetermined	0.000	0.0000	
SUM159-inoculated-E2 mouse #5	m*Hbms*	1	22.607			
	m*Hbms*	2	22.867			
	m*Hbms*	3	21.986			
	h*B2M*	1	Undetermined	0.000	0.0000	0.0000
	h*B2M*	2	Undetermined	0.000	0.0000	
	h*B2M*	3	Undetermined	0.000	0.0000	
	h*HPRT1*	1	34.423	11.937	0.0003	0.0003
	h*HPRT1*	2	34.568	12.082	0.0002	
	h*HPRT1*	3	34.123	11.637	0.0003	
SUM159-inoculated-E2 mouse #6	m*Hbms*	1	23.544			
	m*Hbms*	2	23.752			
	m*Hbms*	3	23.641			
	h*B2M*	1	Undetermined	0.000	0.0000	0.0000
	h*B2M*	2	Undetermined	0.000	0.0000	
	h*B2M*	3	Undetermined	0.000	0.0000	
	h*HPRT1*	1	Undetermined	0.000	0.0000	0.0000
	h*HPRT1*	2	Undetermined	0.000	0.0000	
	h*HPRT1*	3	Undetermined	0.000	0.0000	
SUM159-inoculated-E2 mouse #7	m*Hbms*	1	24.155			
	m*Hbms*	2	24.260			
	m*Hbms*	3	24.263			
	h*B2M*	1	Undetermined	0.000	0.0000	0.0000
	h*B2M*	2	Undetermined	0.000	0.0000	
	h*B2M*	3	Undetermined	0.000	0.0000	
	h*HPRT1*	1	Undetermined	0.000	0.0000	0.0000
	h*HPRT1*	2	Undetermined	0.000	0.0000	
	h*HPRT1*	3	Undetermined	0.000	0.0000	
SUM159-inoculated-E2 mouse #8	m*Hbms*	1	25.459			
	m*Hbms*	2	25.629			
	m*Hbms*	3	25.666			
	h*B2M*	1	Undetermined	0.000	0.0000	0.0000
	h*B2M*	2	Undetermined	0.000	0.0000	
	h*B2M*	3	Undetermined	0.000	0.0000	
	h*HPRT1*	1	Undetermined	0.000	0.0000	0.0000
	h*HPRT1*	2	Undetermined	0.000	0.0000	
	h*HPRT1*	3	Undetermined	0.000	0.0000	

Sample name	Gene	Technial replicate #	Ct value	$\Delta Ct = Ct_{hGene} - Ct_{mHbms(avg)}$	$2^{-\Delta Ct}$	Avg
Non-tumor-inoculated - E2 nude mouse #1	m*Hbms*	1	23.673			
	m*Hbms*	2	23.655			
	m*Hbms*	3	23.472			
	h*B2M*	1	Undetermined	0.0000	0.0000	0.0000
	h*B2M*	2	Undetermined	0.0000	0.0000	
	h*B2M*	3	Undetermined	0.0000	0.0000	
	h*HPRT1*	1	Undetermined	0.0000	0.0000	0.0000
	h*HPRT1*	2	Undetermined	0.0000	0.0000	
	h*HPRT1*	3	Undetermined	0.0000	0.0000	
Non-tumor-inoculated - E2 nude mouse #2	m*Hbms*	1	24.546			
	m*Hbms*	2	24.501			
	m*Hbms*	3	24.467			
	h*B2M*	1	33.182	8.6768	0.0024	0.0022
	h*B2M*	2	33.046	8.5410	0.0027	
	h*B2M*	3	34.013	9.5080	0.0014	
	h*HPRT1*	1	Undetermined	0.0000	0.0000	0.0000
	h*HPRT1*	2	Undetermined	0.0000	0.0000	
	h*HPRT1*	3	Undetermined	0.0000	0.0000	
Non-tumor-inoculated - E2 nude mouse #3	m*Hbms*	1	25.315			
	m*Hbms*	2	25.180			
	m*Hbms*	3	25.243			
	h*B2M*	1	33.337	8.0910	0.0037	0.0028
	h*B2M*	2	33.784	8.5380	0.0027	
	h*B2M*	3	34.146	8.9000	0.0021	
	h*HPRT1*	1	Undetermined	0.0000	0.0000	0.0000
	h*HPRT1*	2	Undetermined	0.0000	0.0000	
	h*HPRT1*	3	Undetermined	0.0000	0.0000	
Non-tumor-inoculated - E2 nude mouse #4	m*Hbms*	1	24.918			
	m*Hbms*	2	25.066			
	m*Hbms*	3	24.918			
	h*B2M*	1	Undetermined	0.0000	0.0000	0.0000
	h*B2M*	2	Undetermined	0.0000	0.0000	
	h*B2M*	3	Undetermined	0.0000	0.0000	
	h*HPRT1*	1	Undetermined	0.0000	0.0000	0.0000
	h*HPRT1*	2	Undetermined	0.0000	0.0000	
	h*HPRT1*	3	Undetermined	0.0000	0.0000	
Non-tumor-inoculated - E2 nude mouse #5	m*Hbms*	1	24.475			
	m*Hbms*	2	24.658			
	m*Hbms*	3	24.588			
	h*B2M*	1	Undetermined	0.0000	0.0000	0.0000
	h*B2M*	2	Undetermined	0.0000	0.0000	
	h*B2M*	3	Undetermined	0.0000	0.0000	
	h*HPRT1*	1	Undetermined	0.0000	0.0000	0.0000
	h*HPRT1*	2	Undetermined	0.0000	0.0000	
	h*HPRT1*	3	Undetermined	0.0000	0.0000	
Non-tumor-inoculated - E2 nude mouse #6	m*Hbms*	1	23.005			
	m*Hbms*	2	23.195			
	m*Hbms*	3	23.105			
	h*B2M*	1	Undetermined	0.0000	0.0000	0.0000
	h*B2M*	2	Undetermined	0.0000	0.0000	
	h*B2M*	3	Undetermined	0.0000	0.0000	
	h*HPRT1*	1	Undetermined	0.0000	0.0000	0.0000
	h*HPRT1*	2	Undetermined	0.0000	0.0000	
	h*HPRT1*	3	Undetermined	0.0000	0.0000	
Non-tumor-inoculated - E2 nude mouse #7	m*Hbms*	1	24.112			
	m*Hbms*	2	24.305			
	m*Hbms*	3	23.966			
	h*B2M*	1	Undetermined	0.0000	0.0000	0.0000
	h*B2M*	2	Undetermined	0.0000	0.0000	
	h*B2M*	3	Undetermined	0.0000	0.0000	
	h*HPRT1*	1	Undetermined	0.0000	0.0000	0.0000
	h*HPRT1*	2	Undetermined	0.0000	0.0000	
	h*HPRT1*	3	Undetermined	0.0000	0.0000	
Non-tumor-inoculated - E2 nude mouse #8	m*Hbms*	1	24.070			
	m*Hbms*	2	23.875			
	m*Hbms*	3	24.046			
	h*B2M*	1	Undetermined	0.0000	0.0000	0.0000
	h*B2M*	2	Undetermined	0.0000	0.0000	
	h*B2M*	3	Undetermined	0.0000	0.0000	
	h*HPRT1*	1	Undetermined	0.0000	0.0000	0.0000
	h*HPRT1*	2	Undetermined	0.0000	0.0000	
	h*HPRT1*	3	Undetermined	0.0000	0.0000	

Sample name	Gene	Technial replicate #	Ct value	$\Delta Ct = Ct_{hGene} - Ct_{mHbms(avg)}$	$2^{-\Delta Ct}$	Avg
No template control	m*Hbms*	1	Undetermined	0.000	0.0000	0.0000
	m*Hbms*	2	Undetermined	0.000	0.0000	
	m*Hbms*	3	Undetermined	0.000	0.0000	
	h*B2M*	1	Undetermined	0.000	0.0000	0.0000
	h*B2M*	2	Undetermined	0.000	0.0000	
	h*B2M*	3	Undetermined	0.000	0.0000	
	h*HPRT1*	1	Undetermined	0.000	0.0000	0.0000
	h*HPRT1*	2	Undetermined	0.000	0.0000	
	h*HPRT1*	3	Undetermined	0.000	0.0000	

Sample name	Gene	Technial replicate #	Ct value	$\Delta Ct = Ct_{hGene} - Ct_{mHbms(avg)}$	$2^{-\Delta Ct}$	Avg
Non-tumor-inoculated - E2 nude mouse #9	m*Hbms*	1	24.732			
	m*Hbms*	2	24.458			
	m*Hbms*	3	24.585			
	h*B2M*	1	Undetermined	0.0000	0.0000	0.0000
	h*B2M*	2	Undetermined	0.0000	0.0000	
	h*B2M*	3	Undetermined	0.0000	0.0000	
	h*HPRT1*	1	Undetermined	0.0000	0.0000	0.0000
	h*HPRT1*	2	Undetermined	0.0000	0.0000	
	h*HPRT1*	3	Undetermined	0.0000	0.0000	
Non-tumor-inoculated - E2 nude mouse #10	m*Hbms*	1	23.446			
	m*Hbms*	2	23.286			
	m*Hbms*	3	23.156			
	h*B2M*	1	31.251	7.9552	0.0040	0.0029
	h*B2M*	2	32.513	9.2167	0.0017	
	h*B2M*	3	31.668	8.3723	0.0030	
	h*HPRT1*	1	Undetermined	0.0000	0.0000	0.0000
	h*HPRT1*	2	Undetermined	0.0000	0.0000	
	h*HPRT1*	3	Undetermined	0.0000	0.0000	
No template control	m*Hbms*	1	Undetermined	0.0000	0.0000	0.0000
	m*Hbms*	2	Undetermined	0.0000	0.0000	
	m*Hbms*	3	Undetermined	0.0000	0.0000	
	h*B2M*	1	Undetermined	0.0000	0.0000	0.0000
	h*B2M*	2	Undetermined	0.0000	0.0000	
	h*B2M*	3	Undetermined	0.0000	0.0000	
	h*HPRT1*	1	Undetermined	0.0000	0.0000	0.0000
	h*HPRT1*	2	Undetermined	0.0000	0.0000	
	h*HPRT1*	3	Undetermined	0.0000	0.0000	

mice were all –E2 and did not have estradiol toxicity. It also remains unclear whether the D2.0R model, particularly without E2, will spontaneously grow into overt metastases. The data suggest that each of these cell lines home to the bone in >80% of mice (with the exception of the +E2 D2.0R model, which is detected in 50% of mice) as assessed by either flow cytometry, qPCR, or histological assessment, and that different methods of detection are better suited to individual models (Table 8). Interestingly, across all models, qPCR is most reliable for detecting tumor burden in bone, but is not as sensitive as flow cytometry, since we have yet to identify an appropriate flow marker for the D2.0R model.

The majority of bone colonization studies use intracardiac inoculation of tumor cells due to inconsistent metastasis and that is requires months to detect disseminated tumor cells in transgenic mouse models of bone metastasis. While most studies use highly metastatic cell lines including the human MDA-MB-231 and murine 4T1, these models do not recapitulate the latency period observed in breast cancer patients. Several human ER+ models, including the MCF7 and T47D DBM lines, have successfully contributed to our understanding of tumor dormancy. However, the requirements of exogenous E2 and resulting negative effects on the bone and urinary tract, limit their physiologic relevance.

In the present study, we observed a significant increase in tumor burden in MCF7 +E2 mice versus -E2 mice by flow cytometry, qPCR, and pan-cytokeratin staining. These results suggest that E2 promotes the growth of MCF7 tumors in the bone but is not necessary for initial colonization and survival since we detected tumor cells in the bone marrow in 80% of -E2 mice by flow cytometry. These data further suggest that MCF7 cells residing in the bone may lie in a dormant state in the absence of E2, which are confirmatory of reports demonstrating the estrogen dependence of MCF7 parental (155) and bone-tropic variants (164) in bone colonization. Importantly, these previous studies relied exclusively on *ex vivo* fluorescence imaging or *in vivo* bioluminescence imaging for the detection of DTCs in the bones of -E2 mice. Similarly, radiographic analysis is classically used to assess bone destruction in tumor models; however, there is no direct correlation with tumor burden given that normal and tumor-induced bone remodeling are indistinguishable by radiography (96). Therefore, it is critical that other methodologies, especially those that comprehensively analyze the bone marrow, are used to confirm the presence of tumor cells following *in vivo* imaging. This point is evidenced by the presence of osteolytic lesions in the -E2 MCF7 model by radiography at 7 weeks and the detection of rare tumor cells by flow cytometry and qPCR but not histology. Thus, the findings presented herein improve upon the current methods to confirm tumor burden following *in vivo*

Table 8.Summary of method efficiency in detecting tumor cells in the bone by model.
Check mark indicates positive detection of tumor cells in the bone by the indicated method. N.D. indicates no detectable tumor cells by the given method despite the use of appropriate positive and negative controls. Question mark indicates the lack of a specific tumor cell marker to detect tumor cells in the bone by the indicated method.

	MCF7		D2.0R		SUM159
	- E2	+ E2	- E2	+ E2	- E2
Flow cytometry	✓ *(8/10 mice; 80%)*	✓ *(7/8 mice; 88%)*	?	?	✓ *(8/8 mice; 100%)*
qPCR	✓ *(5/10 mice; 50%)*	✓ *(5/8 mice; 63%)*	✓ *(6/6 mice; 100%)*	✓ *(3/6 mice; 50%)*	✓ *(4/8 mice; 50%)*
Immunostaining	N.D.	✓ *(3/8 mice; 38%)*	✓ *(1/9 mice; 11%)*	N.D.	N.D.
Histology	N.D.	✓ *(2/8 mice; 25%)*	N.D.	N.D.	N.D.
Veterinary Pathologist assessment	N.D.	✓ *(4/8 mice; 50%)*	✓ *(1/9 mice; 11%)*	✓ *(2/6 mice; 33%)*	N.D.

imaging given our ability to detect and quantify ultra-low tumor burden in the bone using multiple modalities.

Compared to the +E2 MCF7 model, we propose that the -E2 MCF7 model provides a more physiologically relevant system in which to study the timeline of bone colonization, and that flow cytometry, which detected tumor cells in 8/10 (80%) mice, is the best method to detect bone-disseminated tumor cells in this model (Table 8). Importantly, because the -E2 and +E2 MCF7-inoculated mice were sacrificed at the same time point, the question remains whether MCF7 cells in -E2 mice would eventually proliferate into an overt metastasis if the time course was extended. Likewise, it is unknown whether the -E2 D2.0R model would also develop into overt metastases if allowed to continue indefinitely.

Histological assessment by a veterinary pathologist identified a subset of +E2 mice, independent of tumor inoculation, with appreciable endosteal osteosclerosis, myelopthisis, and atypical expansion of mesenchymal cells appearing to be osteoblasts and osteoclasts. Presumably, these manifestations are due to estrogen toxicity as they also appear in non-tumor-inoculated mice (data not shown); however, they can be erroneously identified as tumor cells that have acquired a mesenchymal phenotype. The most extreme cases of this cellular expansion also present as a slight decrease in bone volume as observed for mouse 11 and mouse 13 in Figure 10B. These observations further demonstrate the importance of confirming the presence of tumor cells by additional methods presented herein besides H&E. MicroCT analysis of estrogen supplemented bones can also prove to be difficult due to the dramatic changes in bone microarchitecture that are observed in +E2 long bones. We observed inconsistencies in bone microarchitecture in the D2.0R model in particular, where there was a significant reduction in bone volume and increase in trabecular spacing, but a paradoxical increase in trabecular number in D2.0R-inoculated versus non-tumor-inoculated (naïve) mice. These results are likely due to the difficulty in contouring the microCT scans as a result of the dramatic increase in bone volume, which can be better appreciated by viewing cross-sections of the tibiae (Figure 15A). It is also possible that the presence of D2.0R cells, even at low numbers, may directly impact bone-resident cells, such that centers of ossification are increased but overall bone volume is significantly reduced.

Importantly, the D2.0R model is advantageous over other tumor models given that the cells are ER+ and are inoculated into immunocompetent mice. Data from several groups suggests that depletion of T cells results in the awakening of dormant tumor cells (165, 166), but the specific role for the immune system in the outgrowth of metastatic tumor cells remains unclear (167). Thus, the D2.0R model allows for the investigation of the potential impact of the

immune system in mediating tumor cell dissemination and colonization of the bone. Because D2.0R cells are of mouse origin, we were unable to use CD298 to detect tumor cells and although we attempted PNA, EpCAM, and mouse cytokeratin staining of these cells *in vitro* (data not shown), we were unable to find a cell marker suitable for flow cytometry that was uniquely expressed on tumor cells and not on mouse bone marrow cells. Surprisingly, a slight reduction in osteolysis was observed over time in the -E2 D2.0R-inoculated mice. These results suggest that D2.0R cells may initially disrupt osteoclast-mediated resorption in the absence of E2 but that this effect diminishes over time. These results are further supported by histomorphometry and microCT analysis of -E2 non-tumor-inoculated (naïve) and D2.0R-inoculated mice at the end point, which revealed no significant difference in bone volume. However, a significant reduction in bone volume was observed in +E2 D2.0R-inoculated mice compared to +E2 non-tumor-inoculated (naïve) mice suggesting that D2.0R cells induce bone loss in the presence of E2. Although tumor burden was enriched for in these mice by *Krt18* expression (Figure 12E), 4/6 mice did not show evidence of tumor infiltration by pathologic inspection, suggesting that any effects of the tumor cells on the bone microarchitecture are due to changes in bone homeostasis rather than an increase in tumor-induced osteolysis. A significant reduction in *Krt18* expression was observed in +E2 versus -E2 D2.0R-inoculated mice suggesting that, in contrast to the MCF7 model, E2 may not promote tumor growth in the D2.0R model. Additionally, based on the variable pan-cytokeratin staining of D2.0R cells *in vitro* (Figure 13C), we cannot rule out the possibility that E2 alters the cytokeratin expression of inoculated D2.0R cells *in vivo.*

It has been previously reported that SUM159 cells persist as dormant tumor cells in the lung following tail vein injection (75). Until now, the behavior of these cells in the bone has not been investigated. Using qPCR and flow cytometry, we found that SUM159 cells are detectable in the bone marrow in 50-100% of mice following intracardiac inoculation, and therefore propose the SUM159 cells as a novel human model of ER- breast cancer dissemination to bone. SUM159 cells resemble the claudin-low tumor subtype of breast cancer and thus have reduced expression of epithelial cell adhesion markers and increased stem cell markers including $CD44^{hi}/CD24^{lo}$ (168). In addition to pan-cytokeratin, we also attempted to detect SUM159 tumor cells in the bone marrow using CD44, which stained tumor cells *in vitro*, but did not detect any tumor cells *in vivo* (data not shown). Although pan-cytokeratin and CD44 did not reveal any SUM159 cells in the bone, these results do not rule out the possibility that the tumor burden was below the level of detection by immunostaining, particularly since we detected tumor cells by flow cytometry in 100% of SUM159-inoculated mice. Importantly, gene expression profiling of

breast cancers suggest that each subtype is a unique disease and that the drivers and effective therapeutics for each subtype may differ (169, 170). Furthermore, patients with ER- breast cancer develop bone metastases at similar rates as those patients with ER+ disease (171). Thus, the SUM159 model provides a model in which to study factors that regulate homing of tumor cells to the bone or tumor dormancy in a subtype-specific manner.

One limitation of analyzing low tumor burden by immunostaining or H&E is that each histological section represents only a small fraction of the three-dimensional structure of the tibia. In support of this notion, the +E2 MCF7-inoculated mice in which we observed tumor cells by H&E or pan-cytokeratin staining were three of the four mice with the highest number or percentage of CD298+ cells by flow cytometry. Further, small clusters of MCF7 cells were clearly discernible with pan-cytokeratin staining in the bone marrow of +E2 mice suggesting that the level of tumor burden in the -E2 mice was below the level of immunohistochemical detection. In the D2.0R model, tumor cells heterogeneously expressed pan-cytokeratin (Figure 13C), suggesting that we are likely missing a portion of the tumor cells in the bone marrow using this marker. These conclusions are further supported by the identification of tumor cells in the bone marrow of two +E2 D2.0R-inoculated mice by the veterinary pathologist that were negative for pan-cytokeratin staining. Another source of confusion in the immunohistochemical detection of tumor cell in the bone marrow can be the brown staining of blood pigment, particularly within the synovium and periosteum of the bone (Figure 15B) that is observed in both non-tumor-inoculated (naïve) and tumor-inoculated mice. However, cell morphology and the pigment granularity allow for distinction from pan-cytokeratin positive tumor cells.

These data suggest the superiority of analyzing CD298 expression by flow cytometry, when available, to detect low levels of tumor in the bone over other methods. Additionally, MDA-MB-231 (ER-), T47D (ER+), and human PDX samples have also been shown to express CD298 (156). Analysis of CD298 expression by flow cytometry is a broadly applicable method to investigate tumor burden in the bone following inoculation of various breast cancer cell lines or patient samples. In the context of tumor dormancy, this method can be combined with Hoechst-Pyronin Y staining to distinguish cells that are in a quiescent G_0 state (172, 173). Furthermore, several groups have reported the use of cell division dyes, such as DiD (99) or CellTrace Violet (69), to monitor cell proliferation *in vivo*. Identification of dormant tumor cells at the cellular level *in vivo* remains challenging, in part due to our lack of understanding of whether dormant disseminated tumor cells are truly quiescent or simply growth-restricted (174); however, in the future these cell division protocols may be optimized in conjunction with CD298 staining to

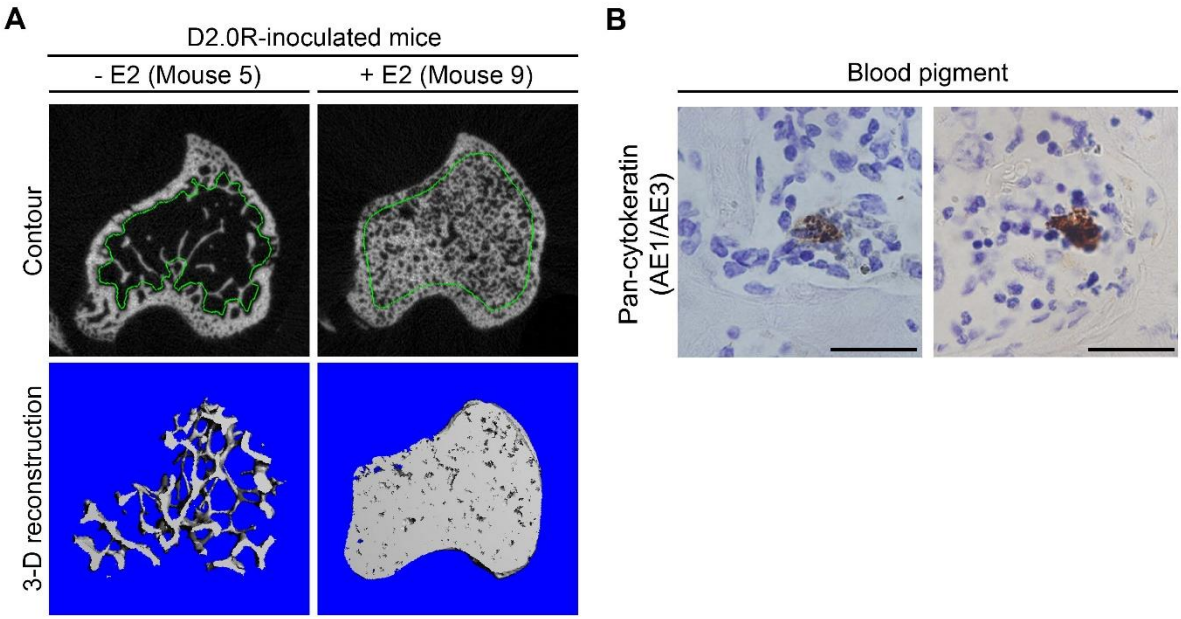

Figure 15. microCT reconstruction and non-specific staining for cytokeratin in the bone marrow. (A) Representative images of drawn microCT contours (green line) and corresponding 3-D reconstruction for -E2 (n=8 mice) and +E2 (n=6 mice) D2.0R-inoculated mice. (B) Blood pigment present in pan-cytokeratin (AE1/AE3) stained tibiae. Scale bars = 25μM.

assess cell quiescence. As such, these mouse models may not serve as strict models of tumor dormancy but do accurately re-capitulate prolonged tumor latency in the bone marrow. In the absence of suitable flow cytometry markers, such as in the D2.0R mammary carcinoma model, qPCR is the second most sensitive method of detection and is recommended for the quantification of tumor burden in the bone marrow. Application of these methods to transgenic mouse tumor models may provide significant advancement to the detection of ultra-low tumor burden in models that do not extensively metastasize to the bone.

In conclusion, our data characterize three distinct models of bone colonization and summarize the most effective methods of detection for each model (Table 8). Although the ability to develop into overt metastases has yet to be investigated, these clinically relevant tumor models mimic early tumor dissemination observed in patients during which DTCs survive in the bone marrow for extended periods of time. Further, the ability of flow cytometry or qPCR analysis to detect significant enrichment of low levels of bone-disseminated tumor cells across these cell lines provides a significant advancement to study tumor burden in the bone and illustrates their applicability to future mechanistic studies. These tumor models will allow for the investigation of mechanisms that regulate prolonged latency periods of bone-disseminated tumor cells and for the identification of factors and/or therapeutics that induce a proliferative switch in tumor cells residing in the bone.

CHAPTER IV

PREX1 MEDIATES AN INVASIVE PHENOTYPE IN BREAST CANCER CELLS THAT SPONTANEOUSLY DISSEMINATE TO THE SKELETON

Summary

Although a significant proportion of breast cancer patients develop bone metastases, the mechanisms regulating tumor cell dissemination to bone are largely unknown. Here, we report the establishment of a bone-selective MCF7 cell line (MCF7b) that exhibits increased metastatic potential *in vitro* and *in vivo*. Molecular profiling identified PREX1 as a mediator of the MCF7b phenotype *in vitro*, and knockdown of PREX1 ablated the enhanced migration, invasion, and adhesion phenotypes. Intracardiac inoculation of tumor cells revealed enhanced osteolytic bone destruction and tumor burden in MCF7b-inoculated mice. Furthermore, when inoculated orthotopically, MCF7b cells grew poorly as primary tumors but preferentially disseminated to skeletal sites with a higher frequency than the MCF7 parental line. PREX1 expression was elevated in MCF7b primary tumors, consistent with the finding that breast cancer patients who developed bone metastases had significantly higher PREX1 expression in the primary tumor. These findings establish a clinically relevant estrogen receptor positive (ER+) model in which to study bone colonization and implicate PREX1 in regulating ER+ tumor cell dissemination to bone.

Introduction

Despite advances in early diagnosis and treatment, relapse occurs in approximately 20-30% of breast cancer patients (175), and nearly 80% of breast cancer patients who succumb to disease harbor bone metastases upon autopsy, suggesting these patients are at significant risk of developing distant metastasis (57, 58). Metastasis is initiated by the invasion of tumor cells through the local basement membrane and survival in the circulation, followed by homing to a distant site and eventual outgrowth into a clinically detectable metastasis. The most frequent, and often first, site of metastasis in breast cancer patients is the bone, which results in significant morbidities including bone pain, hypercalcemia, and fractures (146, 147). Estrogen receptor (ER) positive tumors comprise approximately 70% of all breast cancers and exhibit a greater propensity to metastasize to bone than the visceral organs (176). Interestingly, ER+ patients exhibit prolonged latency periods; bone metastasis most frequently occurs 8-10 years after diagnosis compared to ER- patients, who typically relapse within five years of diagnosis

(153, 171). While these clinical data suggest subtype-specific progression patterns, the molecular mechanisms driving these differences remain unclear. Thus, further investigation into the mechanisms controlling breast cancer cell dissemination and bone colonization, particularly in ER+ disease, is necessary to advance the prevention and effective treatment of bone metastases.

The limited number of available preclinical animal models severely limits our ability to study the mechanisms controlling spontaneous ER+ breast cancer cell dissemination to the bone. Transgenic models of spontaneous tumor development and metastasis such as the MMTV-PyMT model most closely recapitulate the metastatic process observed in humans (7); however, these models are infrequently used because they do not readily metastasize to the bone and require months to detect disseminated tumor cells in the bone.

Due to these limitations, the majority of bone metastasis studies use intracardiac inoculation of tumor cells as an experimental model of metastasis. We (74, 135) and others (69, 136) have used intracardiac inoculation of human ER+ MCF7 cells to model prolonged tumor latency, since these cells remain in a non-proliferative state and induce little osteolytic bone destruction. Recently, comparison of parental MCF7 or human ER+ T47D cell lines to their bone metastatic derivatives have been performed to identify pathways regulating metastatic colonization of the bone (71, 164). However, the physiologic relevance of these models is limited due to these tumor cells requiring exogenous 17β-estradiol in order to form overt metastases. Numerous studies have detailed the perturbations caused by 17β-estradiol in non-tumor bearing mice, including dramatically increased bone volume and adverse urinary tract effects (135-139). Thus, further development and investigation of bone-selective ER+ lines that do not require estrogen supplementation are needed.

In this study, we characterize a novel MCF7 subclone that spontaneously metastasized to the bone from the mammary fat pad in the absence of exogenous estradiol and identify PREX1 as an important regulator of this aggressive phenotype *in vitro*.

Results

Establishment of the MCF7b cell line

Parental MCF7 cells (MCF7p) were transduced with a lentiviral vector containing GFP and a non-silencing shRNA (hereinafter referred to as MCF7 cells) and were implanted into the mammary fat pad without exogenous estradiol (Figure 16A). As expected based on previous literature (177-179), the inoculated tumor cells developed into small, palpable nodules, but did

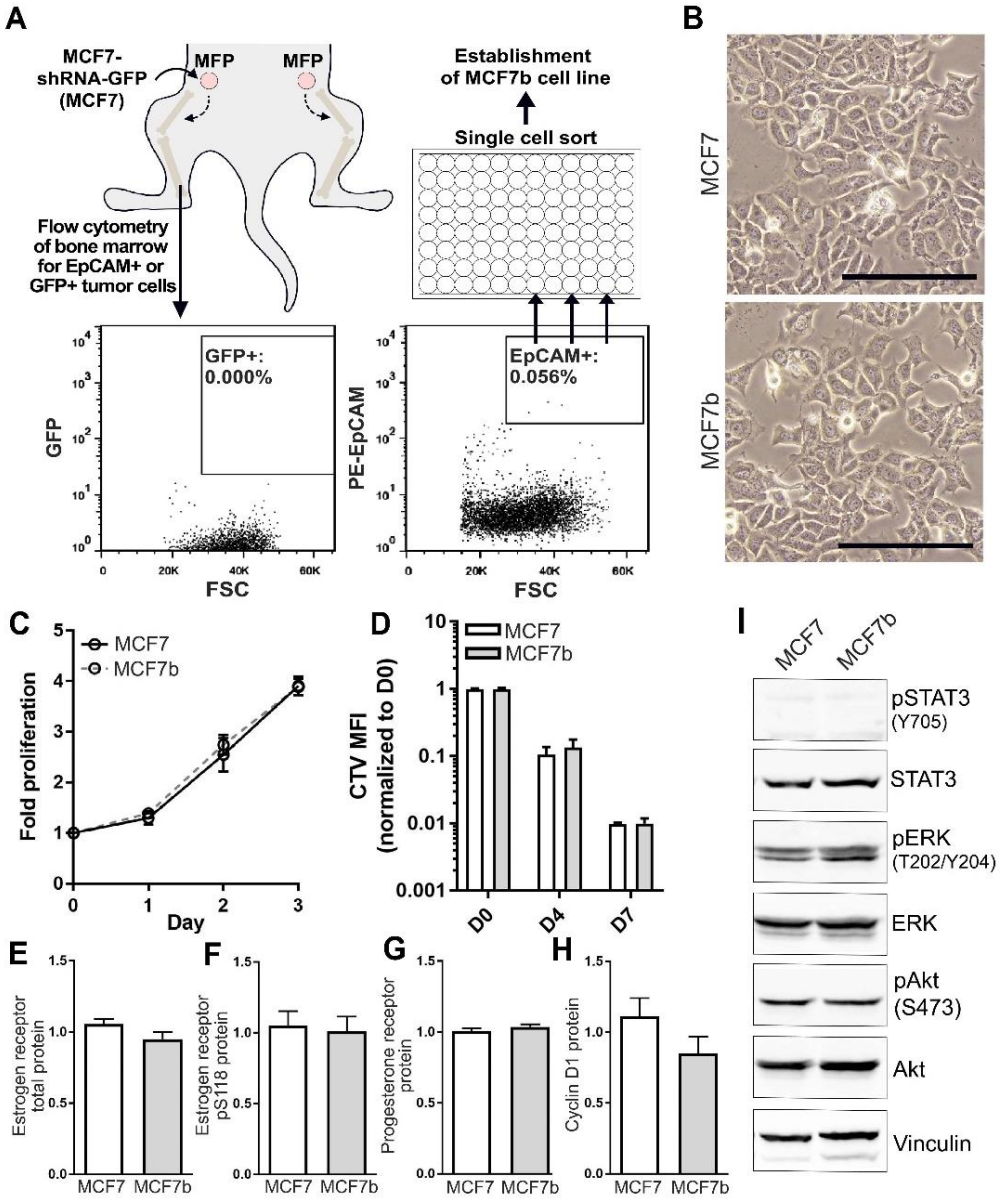

Figure 16. MCF7 bone-metastatic (MCF7b) cells do not have altered cell morphology, proliferation, or basal signaling. (A) MCF7-shRNA-GFP (MCF7) were injected into the mammary fat pad of nude mice (n=4) in the absence of exogenous estradiol and bone marrow was analyzed for EpCAM and GFP by flow cytometry approximately 6 months after tumor injection. EpCAM+ cells were sorted as single cells into a 96-well plate and the MCF7b line was established from one of the recovered clones. (B) Representative DIC images of MCF7 and MCF7b cell morphology following in vitro culture. All panels = 10X, scale bars = 200μm. (C) Trypan blue exclusion assay to assess fold proliferation in MCF7 and MCF7b cells over 3 days. (D) MCF7 and MCF7b cells were dyed with CellTrace Violet proliferation dye and mean fluorescence intensity (MFI) was tracked over seven days to assess proliferation. (E-H) Normalized linear protein expression from RPPA analysis of (E) total ERα, (F) ERα-p118, (G) progesterone receptor, and (H) cyclin D1 in MCF7 and MCF7b cells. (I) Representative western blot for pSTAT3-Y705, total STAT3, ERK-pT202/Y204, total ERK, pAKT-pS473, total AKT, and vinculin in MCF7 and MCF7b cells. C-I: n= three independent biological replicates. Bar graphs and points indicate mean + standard error of the mean.

not progress, and in most cases dissipated, due to the absence of exogenous estrogen; however, one mouse presented with a limp approximately 6 months after tumor inoculation, suggesting the development of bone metastases. Flow cytometric analysis of the bone marrow (n=4 mice) using the epithelial cell marker, EpCAM, positively detected tumor cells in one mouse, which were sorted into single cell clones (Figure 16A). Notably, these tumor cells no longer expressed GFP (Figure 16A). Two of the single cell clones (RJ4#5a and RJ4#5b) survived and grew *in vitro*, and we renamed one of these clones (RJ4#5b) the MCF7 bone metastatic line (MCF7b). We recently validated its MCF7 origin using STR profiling by the ATCC, where MCF7b cells were confirmed to have a 100% match to MCF7 cells banked at ATCC.

Compared to the parental cell line, MCF7b cells appeared similar morphologically (Figure 16B) and did not display an altered proliferation rate by trypan blue exclusion or CellTrace Violet dilution assays (Figure 16C, D). MCF7 cells are ER+ and respond to estrogen (180); however, ERα expression and transcriptional activity, as assessed by pS118, were unchanged between MCF7 and MCF7b cells by RPPA analysis (Figure 16E, F). Evaluation of ERα target genes progesterone receptor and cyclin D1 revealed no significant changes in downstream ERα signaling (Figure 16G, H). Total levels and basal activity of AKT, ERK, and STAT3 were also unchanged in MCF7b cells by western blot and RPPA analysis (Figure 16I and Figure 17A-C).

MCF7b cells exhibit enhanced metastatic potential

In comparison to the parental line, MCF7b cells displayed a significant 2-3-fold increase in cell migration (Figure 18A, B) and invasion (Figure 18C, D). Crystal violet staining revealed a significant increase in adherent MCF7b cells compared to the parental line by both absorbance and area (Figure 18E-G). Importantly, the number of cells per field was significantly increased (Figure 18H) while the area per cell remained unchanged (Figure 18I), suggesting that adhesive ability rather than cell spreading is significantly increased in MCF7b cells.

Genomic and proteomic profiling identifies PREX1 as potential driver of the invasive phenotype

In order to identify potential mechanisms mediating the metastatic phenotype of MCF7b cells, we performed molecular profiling by reverse phase protein array (RPPA) and RNA sequencing (RNAseq). Of the 296 total and phospho-specific antibodies that were tested by

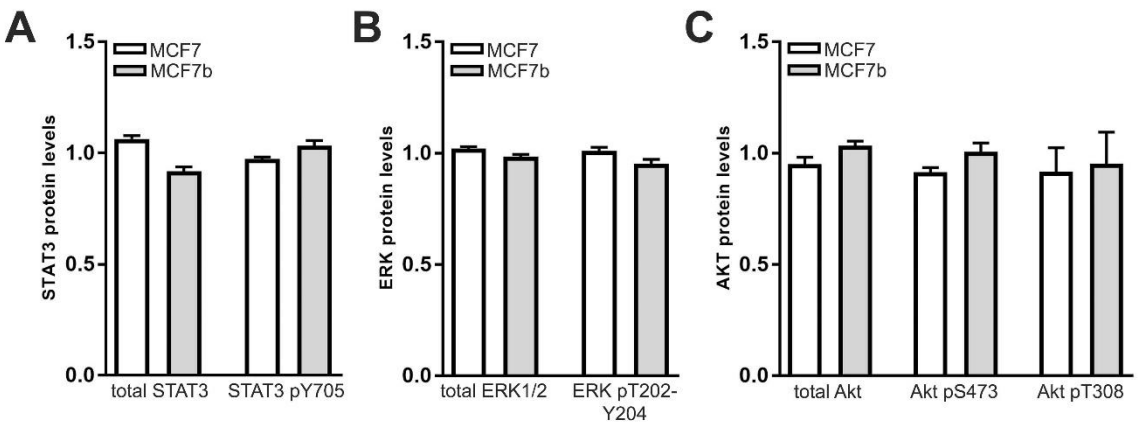

Figure 17. STAT3, ERK, and AKT are unchanged in MCF7b cells. (A-C) Normalized linear protein expression from RPPA of (A) total STAT3 and STAT3-pY705, (B) total ERK and ERK-pT202/Y204, and (C) total AKT, AKT-pS473, and AKT-pT308. n= three independent biological replicates. Bar graphs indicate mean + standard error of the mean.

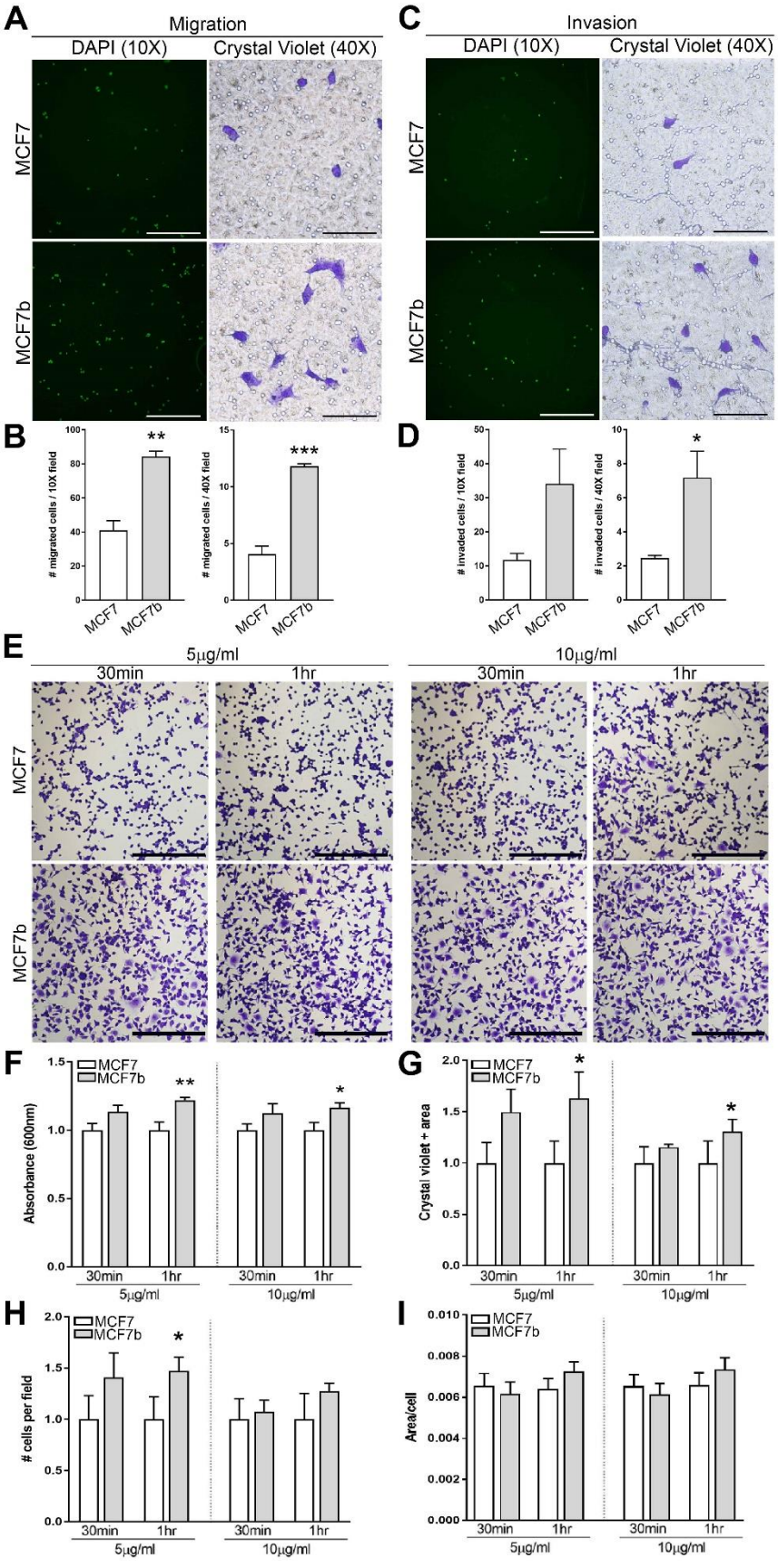
A
Migration
DAPI (10X)
Crystal Violet (40X)
MCF7
MCF7b
C
Invasion
DAPI (10X)
Crystal Violet (40X)
MCF7
MCF7b
B
migrated cells / 10X field
**
MCF7
MCF7b
migrated cells / 40X field
***
MCF7
MCF7b
D
invaded cells / 10X field
MCF7
MCF7b
invaded cells / 40X field
*
MCF7
MCF7b
E
5μg/ml
30min
1hr
10μg/ml
30min
1hr
MCF7
MCF7b
F
MCF7
MCF7b
Absorbance (600nm)
**
*
30min
1hr
30min
1hr
5μg/ml
10μg/ml
G
MCF7
MCF7b
Crystal violet + area
*
*
30min
1hr
30min
1hr
5μg/ml
10μg/ml
H
MCF7
MCF7b
cells per field
*
30min
1hr
30min
1hr
5μg/ml
10μg/ml
I
MCF7
MCF7b
Area/cell
30min
1hr
30min
1hr
5μg/ml
10μg/ml

Figure 18. MCF7b cells exhibit enhanced cell migration, invasion, and adhesive ability. (A) Representative images of MCF7 and MCF7b cell migration assessed by DAPI (green pseudocolor) or crystal violet staining. Left panel = 10X, scale bar = 500μm; right panel = 40X, scale bar = 100μm. (B) Quantitation of the number of migrated cells per 10X or 40X field from (A). (C) Representative images of cell invasion assessed in (A). (D) Quantitation of the number of migrated cells per 10X or 40X field from (C). (E) Representative images of MCF7 and MCF7b cells on 5μg/ml or 10μg/ml fibronectin for 30 minutes or 1 hour. All panels = 10X, scale bar = 500μm. (F) Crystal Violet absorbance at 600nm to assess adherent cells from (A). (G-I) Quantitation of (G) total crystal violet area per field, (H) number of cells per field, and (I) area per cell from (E). B, D, F-I: Mann-Whitney test. n=three independent biological replicates. *p<0.05, **p<0.01, ***p<0.001. Bar graphs = mean + standard error of the mean.

RPPA, twelve proteins were significantly altered in MCF7b cells (Figure 19A, B and Table 9). Further examination of these genes in the RNA-seq dataset revealed three genes (*PREX1*, *HSPB1*, *DUSP4*) that were significantly altered in MCF7b cells by more than 2-fold (1 log2 fold change by edgeR analysis with a significance of $p<0.05$) (Figure 19C). Elevated *PREX1* and *HSPB1* expression in MCF7b cells compared to MCF7 or parental MCF7 (MCF7p) cells was validated by qPCR analysis Figure 19D, E). *DUSP4* was modestly decreased in MCF7b cells, but this change was not significant (Figure 19F). Consistent with the expression pattern of these genes in MCF7b cells, PREX1 and HSPB1 were amplified/upregulated in 5-10% of breast cancer patients, whereas DUSP4 was deleted/downregulated in ~9% of patients from The Cancer Genome Atlas (TCGA) provisional dataset (Figure 19G). Analysis of the TCGA METABRIC dataset revealed similar genetic alterations for PREX1 and HSPB1 (Figure 20). In contrast to the provisional cohort, DUSP4 was predominantly amplified/upregulated in this dataset, prompting us to pursue PREX1.

As previously reported (181, 182), we confirmed that ER+ primary tumors express significantly higher PREX1 mRNA levels compared to other subtypes in TCGA (Figure 21A). Expression of PREX1, a PI(3,4,5)P3-dependent guanine exchange factor, predicts sensitivity to PI3K inhibition (183, 184), and it is a mediator of Rac1 activation by ErbB receptors to promote breast cancer progression (181, 185). Thus, we postulated that PREX1 overexpression may contribute to the metastatic potential of MCF7b cells. Western blot analysis confirmed nearly 2-fold higher PREX1 protein levels in MCF7b cells compared to the parental line (Figure 21B). Knockdown of PREX1 in MCF7b cells was maintained for approximately five days and resulted in PREX1 expression levels similar to those of MCF7 cells (Figure 21C). MCF7b cells transfected with NT-siRNA exhibited increased migration and invasion (Figure 22A-D), confirming our previous results, and PREX1 knockdown blunted the increased migration (Figure 22B) and almost completely reversed the invasive phenotype (Figure 22D). Similarly, knockdown of PREX1 partially ablated the increased adhesive ability of MCF7b cells (Figure 23A-D) and had no effect on the area per cell (Figure 23E).

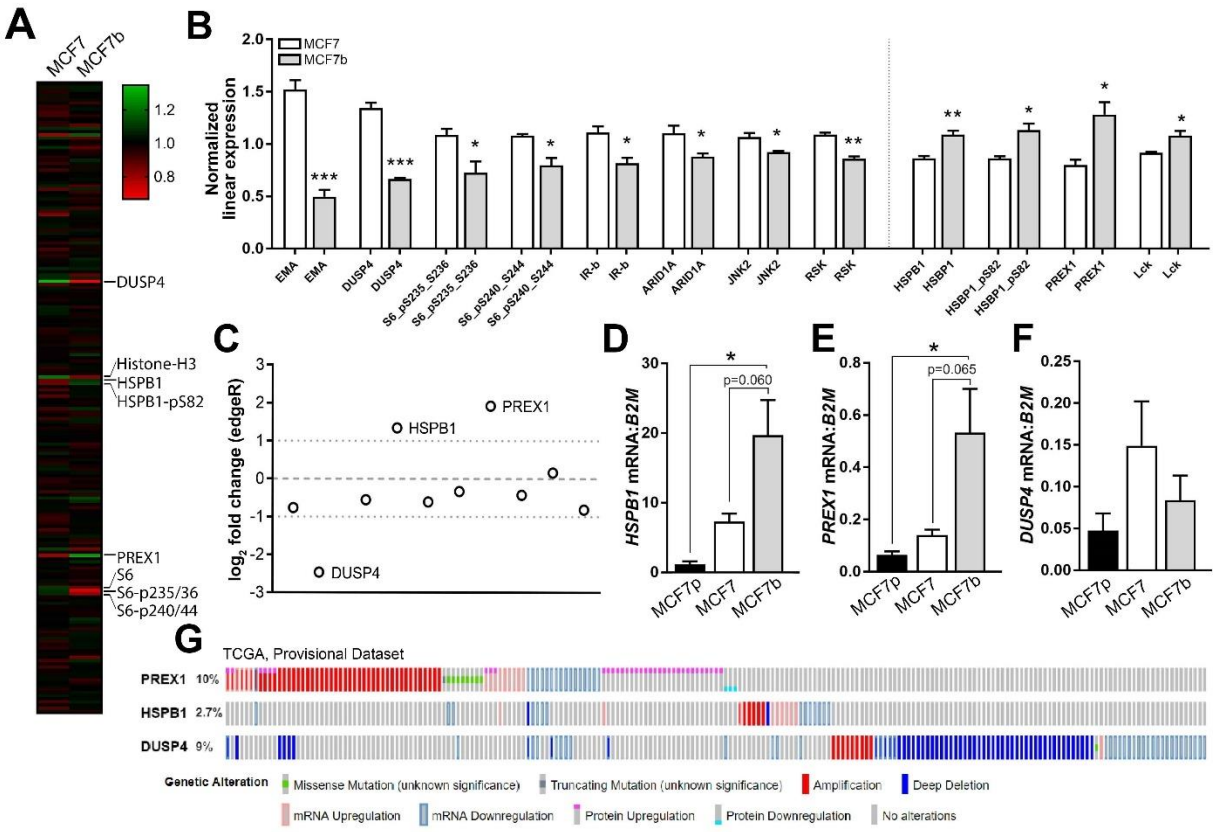

Figure 19. Molecular profiling identifies PREX1 overexpression in MCF7b cells. (A) Heatmap representing the normalized linear protein expression of the 296 total and phospho-specific proteins evaluated by RPPA in MCF7 and MCF7b cells. (B) Normalized linear protein expression of the significantly altered total and phospho-proteins in MCF7b cells. (C) Log2 fold change in mRNA of the significantly altered proteins from (B) as assessed by RNA-sequencing of MCF7 and MCF7b cells. (D-F) qPCR of parental (MCF7p), MCF7, and MCF7b cells for (D) *HSPB1*, (E) *PREX1*, and (F) *DUSP4* mRNA normalized to *B2M* (housekeeping gene). (G) Genetic alterations of PREX1, HSPB1, and DUSP4 in breast cancer patients from the TCGA Provisional dataset. B: Mann-Whitney test. D, E: One-way ANOVA with Sidak's multiple comparisons test. *p<0.05, **p<0.01, ***p<0.001. A-F: n= three independent biological replicates. Bar graphs indicate mean + standard error of the mean.

Table 9. Normalized linear RPPA data from MCF7 and MCF7b cells.

Antibody Name	Antibody Origin	Gene Name	Validation Status	Probabilities (QC Score)	MCF7 NSC BR1	MCF7 NSC BR2	MCF7 NSC BR3	MCF7b BR1	MCF7b BR2	MCF7b BR3
14-3-3-zeta	R	YWHAZ	V	0.968772531	1.004493211	0.912787038	1.024957131	0.984047616	1.021529436	1.020825337
14-3-3-beta	R	YWHAB	V	0.946698276	0.960701589	0.983815915	1.178590931	1.019134282	1.019134177	1.120959692
4E-BP1	R	EIF4EBP1	V	0.959204903	0.946571884	0.884797494	1.066689806	0.981162229	1.055168171	1.108116651
4E-BP1_pS65	R	EIF4EBP1	V	0.968123694	0.994263229	0.929485184	0.945218056	1.014409	1.043147973	0.937695382
53BP1	R	TP53BP1	V	0.970929325	1.091130634	0.949876916	1.068077405	0.912601468	0.938322162	1.140366471
A-Raf	R	ARAF	V	0.95602738	0.969188852	0.921478873	0.978272395	1.024295587	1.0142363	1.045375599
ACC1	R	ACACA/ ACACB	C	0.964754789	0.992324531	0.922067212	0.967166695	0.968122074	1.033216334	0.9956075
ACC_pS79	R	ACACA/A CACB	V	0.962379471	1.094100018	1.030699853	0.938106084	0.936145813	0.977128471	0.865609747
ADAR1	M	ADAR	V	0.956602154	0.910239225	0.946056735	0.960544047	0.995525955	1.041537556	1.033891206
Akt	R	AKT1/2/3	V	0.950847515	0.918218735	0.918649456	1.013219296	0.995659185	1.041411125	1.065405796
Akt_pS473	R	AKT1/2/3	V	0.948134731	0.916902879	0.876968306	0.948548024	1.084579927	0.957028819	0.97802729
Akt_pT308	R	AKT1/2/3	V	0.952234577	1.037770254	1.011313324	0.703149585	1.173329697	0.996109184	0.687780179
AMPK-a2_pS345	R	PRKAA2	V	0.813856662	1.004843337	1.020638234	1.02278324	0.995710227	0.986979471	1.024971584
AMPKa	R	PRKAA1/2	C	0.968017078	0.951492137	0.954382329	0.948509769	1.022115958	1.016304683	0.972996117
AMPKa_pT172	R	PRKAA1/2	C	0.970022055	1.338143935	1.020762587	0.460558114	1.160489771	0.986857722	0.474889547
Annexin-I	M	ANXA1	V	0.94579664	0.974748675	0.966531971	1.291816806	0.992274041	1.039953132	1.277816958
Annexin-VII	M	ANXA7	V	0.907008667	1.017969237	1.017419702	1.030453973	0.998732251	0.99013063	1.02732395
AR	R	AR	V	0.911237562	0.517278563	1.008250908	0.856018907	1.344858022	1.250620832	0.915242037
ARID1A	R	ARID1A	C	0.967797914	1.125254122	1.215320284	0.971940374	0.917279008	0.90554969	0.818986451
Atg3	R	ATG3	V	0.898049053	1.027294045	0.986036875	0.992885489	0.980195914	0.999631333	0.990523037
Atg7	R	ATG7	V	0.964326654	0.909607636	1.078927033	1.054717109	0.990077403	0.945237149	0.953632372
ATM	R	ATM	V	0.940870632	0.982427838	1.065015079	1.200729859	0.822241566	0.814548609	1.012749862
ATM_pS1981	R	ATM	V	0.813413911	1.024372053	1.023870237	0.968496357	0.949766274	0.963018469	0.968924406
ATR_pS428	R	ATR	C	0.949816347	0.990423201	1.026155326	0.95870087	0.995665771	0.981577869	0.937040079
Aurora-B	R	AURKB	V	0.944426284	0.974335944	1.000440917	0.898064659	1.040123247	1.029250344	0.921761625
Axl	R	AXL	V	0.963768443	0.778096554	0.935353952	1.217646254	1.013383219	1.024591711	1.167632505
b-Actin	R	ACTB	C	0.851858666	1.116694263	1.031704421	0.897959781	1.040246214	0.925093314	0.746232184
b-Catenin	R	CTNNB1	V	0.949272002	0.977456029	0.955574487	0.865326051	1.078508453	1.063754109	0.939564921
b-Catenin_pT41_S45	R	CTNNB1	V	0.943188911	1.030526071	1.027590325	0.932411033	1.016637364	0.973075136	0.912878397
B-Raf	R	BRAF	C	0.950431991	0.767169252	0.993305044	0.827642152	1.069645443	1.013740498	0.957912199
B-Raf_pS445	R	BRAF	V	0.963535157	0.94299059	0.861254936	0.948473783	1.004007135	1.033489248	1.042440759
B7-H4	R	VTCN1	C	0.868121621	0.975899414	1.011648776	1.059102996	1.007272611	0.995780754	1.071555548
Bad_pS112	R	BAD	V	0.943000673	1.020109114	0.994591334	0.974854424	0.983733825	1.006531799	0.994051957
Bak	R	BAK1	C	0.937225544	1.027839192	1.004288744	1.008568063	0.99626153	0.99910777	0.978053942
BAP1	M	BAP1	V	0.865125583	1.014383366	0.999395377	1.00598977	1.004868933	1.007777653	1.031939781
Bax	R	BAX	V	0.910008962	0.997862929	0.961603555	1.042762635	1.012455405	1.02547217	1.058081732
Bcl-xL	R	BCL2L1	V	0.968713605	1.02479972	0.988582215	1.082873859	0.980186409	1.002026902	0.996220203
Bcl2	M	BCL2	V	0.899984021	1.008501445	1.039438384	1.126116828	0.863482139	0.905869113	0.943281596
Beclin	G	BECN1	C	0.850013485	0.956724941	0.973633061	1.038608855	0.997661863	1.033000689	1.047337141
Bid	R	BID	C	0.942305951	1.030179013	0.979483337	1.092616444	0.978183262	0.996860586	0.968372135
Bim	R	BCL2L11	V	0.834236002	0.939426488	0.839813877	0.878907592	1.062584433	1.093147673	1.038920914
BiP-GRP78	M	HSPA5	C	0.869190431	0.976735795	0.992945034	1.049659517	1.017088194	1.014092972	1.050237727
BRD4	R	BRD4	V	0.966216355	1.016795881	1.055208645	0.940743805	0.947287026	0.918097081	0.924958094
c-Abl	R	ABL1	V	0.958025659	1.008940843	1.039007359	1.015551038	1.000834403	0.952307004	1.016597294

Antibody Name	Antibody Origin	Gene Name	Validation Status	Probabilities (QC Score)	MCF7 NSC BR1	MCF7 NSC BR2	MCF7 NSC BR3	MCF7b BR1	MCF7b BR2	MCF7b BR3
c-IAP2	R	BIRC3	C	0.935815567	1.024390778	1.005006846	1.061153848	1.032632302	1.002283649	1.023476009
c-Jun_pS73	R	JUN	V	0.922138262	1.133093951	1.015386822	0.976548384	0.964524493	0.992120956	0.901340698
c-Kit	R	KIT	V	0.921297138	1.043417237	0.968023523	0.965741443	0.959850189	0.98414649	0.978068072
c-Met_pY1234_Y1235	R	MET	V	0.94911097	1.024384106	1.009048965	1.011252654	0.983770785	0.998326143	1.005571195
c-Myc	R	MYC	C	0.9501397	0.938976959	0.898253158	0.903763986	1.033440928	1.108751637	0.994360549
C-Raf	R	RAF1	C	0.974411623	0.999345031	1.02433952	0.976735695	0.965972212	0.983355665	0.966297714
C-Raf_pS338	R	RAF1	V	0.94751423	1.107045048	1.053455576	1.003853443	0.93891968	0.942385122	0.874698702
Caspase-3	R	CASP3	C	0.950992377	1.007491992	1.005442306	1.002322032	0.962152384	1.001857305	0.984175337
Caspase-7-cleaved-	R	CASP7	C	0.95152612	1.010109162	0.900983536	0.931633989	0.914105674	1.016135832	0.980418615
Caspase-8	M	CASP8	Q	0.851418719	0.887901036	0.86136623	0.982796427	0.988104504	1.048580223	1.073532282
Caveolin-1	R	CAV1	V	0.952655477	0.849975488	0.783448234	0.865075479	1.078938193	1.023741146	0.971921652
CD134	R	TNFRSF4	V	0.702758133	1.073203408	0.95286529	1.055485485	0.932192293	0.955539613	1.082388639
CD20	R	MS4A1	C	0.841922043	1.019136622	0.990117554	1.048882559	1.031248627	1.007465787	0.969629435
CD29	M	ITGB1	V	0.788901695	1.007346784	1.004956583	1.034479687	1.009266937	1.00233286	1.048389712
CD31	M	PECAM1	V	0.8472708	1.052520781	0.996257968	1.069719334	0.975431396	0.96312435	1.050457087
CD4	R	CD4	V	0.705427276	1.022159576	1.026040549	1.060490136	0.961773142	0.971515972	1.004987972
CD45	M	CD45	V	0.777487333	0.901323746	0.956458793	1.000076118	1.029601085	1.00920159	1.096685089
CD49b	M	ITGA2	V	0.900388065	1.037733439	1.010763493	1.099958823	1.000751102	0.981804118	1.064776721
cdc25C	R	CDC25C	V	0.894157072	1.022254269	0.966091076	0.983268143	1.049293025	0.990514709	0.982196367
cdc2_pY15	R	CDK1	C	0.866803716	0.988427633	1.002494488	1.010609493	0.933220213	1.004743416	0.979426541
CDK1_pT14	R	CDK1/2/3	C	0.964244788	1.069085898	0.980008549	0.475059869	1.315520907	1.042430224	0.542924428
Chk1	M	CHEK1	C	0.945585047	1.006122337	1.016027732	0.905730247	1.031446109	0.991493462	0.913504986
Chk1_pS296	R	CHEK1	V	0.919052847	1.032181091	1.066493761	0.926390058	0.966623882	0.994937775	0.882348258
Chk2_pT68	R	CHEK2	C	0.92726389	1.006354368	0.927794122	0.936851742	0.933364562	1.019741966	0.991307214
Claudin-7	R	CLDN7	V	0.84573944	0.962876395	0.884002071	0.971077379	0.991485361	1.045371922	1.170542378
COG3	R	COG3	V	0.958355528	0.995109264	1.03317779	0.953929226	1.010409075	0.974702405	0.941133254
Collagen-VI	R	COL6A1	V	0.95116786	1.038038617	1.060285543	0.621902278	1.042521521	1.017660302	0.871862445
Connexin-43	R	GJA1	C	0.937843476	0.959066473	0.918635324	1.129741064	0.878930673	1.065157639	1.097082779
Cox-IV	R	COX4I1	V	0.946181169	0.967444158	0.885775062	1.073665869	1.004190969	1.033314796	1.052768088
Cox2	R	PTGS2	C	0.932987791	0.994117453	0.935075058	1.091916058	1.018749748	1.019499084	1.068077139
Creb	R	CREB1	C	0.794547124	0.957181176	1.065015563	0.979987526	0.994278153	0.932273148	1.073388063
Cyclin-B1	R	CCNB1	V	0.973543841	1.046136241	1.002520831	0.787514231	1.110234822	1.079918292	0.771427927
Cyclin-D3	M	CCND3	V	0.940618013	0.987421108	0.975164485	1.095378822	1.027774394	1.010935049	1.133969523
Cyclin-E1	M	CCNE1	V	0.954303089	0.949598771	0.970336784	1.042147438	1.014419531	1.023608291	1.073883844
Cyclin-D1	R	CCND1	V	0.923744194	0.991231473	0.982684943	1.04678212	1.030597341	1.008256182	1.070143896
Cyclophilin-F	M	PPIF	V	0.922405404	0.996116327	0.982539173	1.233300841	0.972616167	1.024281008	1.180473846
D-a-Tubulin	R	TUBA4A/TUBA3C	V	0.949506703	1.03510912	0.974525571	1.041999755	0.948027298	0.992125673	1.030286978
DJ1	R	PARK7	V	0.972606489	1.050534628	0.998206268	1.176905736	0.829385172	0.872994178	0.947172745
DM-Histone-H3	R	HIST1H3A	V	0.753043944	1.181193933	0.870037069	1.148885008	0.715421221	0.723789116	1.774580607
DM-K9-Histone-H3	R	HIST3H3	C	0.798831574	1.099792391	0.949887261	1.005233601	0.765587461	0.788788785	1.159230476
DUSP4	R	DUSP4	V	0.962415059	1.321555667	1.27717045	1.441068493	0.681420083	0.641928918	0.674052452
E-Cadherin	R	CDH1	V	0.934862312	0.897352928	0.780584758	0.987109575	0.998244026	1.038958213	1.019999298
E2F1	M	E2F1	V	0.836990192	1.04018908	1.008354651	1.08129152	1.014274114	1.036792218	0.778098871

Antibody Name	Antibody Origin	Gene Name	Validation Status	Probabilities (QC Score)	MCF7 NSC BR1	MCF7 NSC BR2	MCF7 NSC BR3	MCF7b BR1	MCF7b BR2	MCF7b BR3
eEF2	R	EEF2	C	0.965474112	0.92724339	0.939406104	0.892632045	1.052076341	0.993080798	0.945780494
eEF2K	R	EEF2K	V	0.972405613	1.023492126	0.994915021	1.054697082	1.035899719	1.003224432	1.008635533
EGFR	R	EGFR	V	0.964138071	1.015478448	1.006962771	0.971479582	1.004537191	1.000368667	0.964484922
EGFR_pY1173	R	EGFR	V	0.966934694	1.017063249	0.96480497	0.985458423	0.963646784	1.009457071	1.009195786
eIF4E	R	EIF4E	V	0.980786127	0.992480643	0.918491041	0.994724705	1.002399294	1.033066403	1.018899218
eIF4E_pS209	R	EIF4E	V	0.8826756	0.99934233	1.016942934	1.019366607	1.01417034	0.990597418	1.006538302
eIF4G	R	EIF4G1	C	0.970789284	1.004440392	1.020465509	0.894187965	1.061461912	0.99134963	0.898855724
Elk1_pS383	R	ELK1	C	0.927589369	1.055436448	0.993397867	1.00272378	0.934086087	0.966871006	0.961740088
EMA	M	MUC1	C	0.914753486	1.360132604	1.54130409	1.666497282	0.460953877	0.406434424	0.622893535
ENY2	M	ENY2	C	0.84494658	1.052301048	0.991322522	1.196389607	0.94774554	0.975614407	1.120886147
ER	R	ESR1	V	0.969100632	1.002213221	1.045606767	1.119987578	0.882544708	0.919703177	1.04756037
ER-a_pS118	R	ESR1	V	0.941814026	0.88478631	1.025903359	1.238890462	0.842547059	0.98182456	1.204181081
ERCC1	M	ERCC1	V	0.834286696	0.993531182	1.054123343	1.095704992	0.958446442	0.936231375	1.058868094
Ets-1	R	ETS1	V	0.937205874	1.03459726	0.999190111	1.031826563	1.00945894	1.000953568	0.909296601
FAK	R	PTK2	C	0.839529429	1.028344327	1.013343724	0.993993841	0.971675453	0.994121286	1.037111326
FAK_pY397	R	PTK2	V	0.890898841	0.993115078	1.033851705	0.968292438	1.023263328	0.974042597	1.05133371
FASN	R	FASN	V	0.953680518	0.968511528	1.026057275	1.052717076	1.016799451	0.981673867	0.978252415
Fibronectin	R	FN1	V	0.941501383	1.218646483	0.967210007	0.830261903	1.108944514	1.039289289	0.799453275
FOXM1	R	FOXM1	V	0.953687552	0.990124894	1.050736414	0.813264151	1.106994417	1.109427459	0.877137474
FoxO3a_pS318_S321	R	FOXO3	C	0.947421877	1.051311901	0.997443809	0.935170405	0.984365153	0.952397063	0.933694884
G6PD	R	G6PD	V	0.834775323	0.9689901	0.9735952	0.937784435	1.059922193	0.980428044	1.004925394
Gab2	R	GAB2	V	0.953158815	0.99769399	1.01555178	0.952556814	1.003146976	0.991959451	0.927468802
GAPDH	M	GAPDH	C	0.855650037	0.975080674	1.618292901	0.915556293	1.01961474	0.675198285	0.943036163
GATA-6	R	GATA6	C	0.864557431	0.975266945	0.999864784	1.002024177	1.054104064	0.98594922	0.944502117
GATA3	M	GATA3	V	0.962537058	1.038290013	0.904531088	0.98838043	0.991994532	0.991716317	0.911054682
GCLM	R	GCLM	C	0.88751951	1.025004207	1.023250131	0.969388106	0.946219285	0.919516469	0.984723647
GCN5L2	R	KAT2A	V	0.971841992	0.994757573	1.036442081	1.005022919	0.941977731	0.971506445	0.931911969
Glutamate-D1-2	R	GLUD1	C	0.79926457	0.908788959	0.891723355	0.914847912	1.020445299	1.033981282	0.963403968
Glutaminase	R	GLS	C	0.937105164	0.925439152	1.042319143	1.05126166	0.927201689	0.965752408	1.04242753
Granzyme-B	R	GZMB	V	0.815348764	0.98264912	0.986307046	0.958339394	1.040381182	0.998971699	1.103503353
GSK-3a-b	M	GSK3A/GSK3B	V	0.966374478	1.024103791	1.024133387	0.983253858	1.017949912	0.964697154	0.995491693
GSK-3a-b_pS21_S9	R	GSK3A/GSK3B	V	0.974963226	1.070253936	1.006147171	0.913372119	1.009182886	1.001167194	0.882305286
Gys	R	GYS1	V	0.940121492	0.911601099	0.93928834	1.112500339	0.963601461	1.066626474	1.23349443
Gys_pS641	R	GYS1	V	0.868674971	0.938949793	1.027537902	1.063360165	0.924422023	0.980224233	1.095544454
H2AX_pS140	M	H2AFX	C	0.962095146	0.885094896	1.05937684	0.777007906	1.000095767	1.047909886	1.149145883
HER2	M	ERBB2	V	0.919424019	0.970733568	1.012228292	1.035114462	1.056619444	0.995213368	0.845109233
HER2_pY1248	R	ERBB2	C	0.852679008	1.02626135	1.022016946	1.002143956	0.990197619	0.970674997	0.981774446
HER3	R	ERBB3	V	0.949438212	1.051929225	0.99683825	1.060108538	1.014168302	0.975691844	1.042414873
HER3_pY1289	R	ERBB3	C	0.955152337	1.022451974	0.984844705	0.975201934	1.044468228	0.995093253	0.963083101
Heregulin	R	NRG1	V	0.969398842	0.922649668	0.902125464	1.018799892	1.034189263	1.004847589	1.032615463
HES1	R	HES1	V	0.969206486	1.001684832	0.970827275	0.935876617	1.005489717	1.024226627	1.025818561
Hexokinase-II	R	HK2	V	0.705903642	1.022844149	0.984229523	0.92844351	1.015406815	1.003905049	0.925628867
Hif-1-alpha	M	HIF1A	C	0.899741104	0.956797862	0.98307765	1.008551807	1.07863854	0.962666962	1.056511107
Histone-H3	R	HIST3H3	V	0.910427862	1.743846156	0.843638269	1.042818432	0.528493084	0.570817277	1.411839925

Antibody Name	Antibody Origin	Gene Name	Validation Status	Probabilities (QC Score)	MCF7 NSC BR1	MCF7 NSC BR2	MCF7 NSC BR3	MCF7b BR1	MCF7b BR2	MCF7b BR3
HSP27	M	HSBP1	C	0.937772046	0.85868369	0.826297254	0.903926756	1.033250084	1.069643186	1.162493136
HSP27_pS82	R	HSBP1	V	0.899345664	0.895094008	0.824980697	0.869138679	1.074038241	1.069660574	1.258750161
HSP70	R	HSPA1A	C	0.950155445	0.967083271	0.946772782	0.963403441	0.989633468	1.047129296	1.005350988
IGF1R_pY1135_Y1136	R	IGF1R/INSR	V	0.921496299	0.990975977	1.003947278	1.009574135	1.027695176	1.003321037	1.028193811
IGFBP2	R	IGFBP2	V	0.930722754	0.965041562	0.885866239	0.87388294	1.081587932	1.053942105	0.928831028
IGFRb	R	IGF1R	C	0.958692825	0.965859358	0.907680389	1.010873986	1.019963071	1.018347688	1.059687787
INPP4b	R	INPP4B	V	0.945348185	1.002198936	0.970408365	0.9844798	1.026743754	1.011913086	1.036123049
IR-b	R	INSR	C	0.974236981	1.128474175	1.002375434	1.201557833	0.760192912	0.773410139	0.920511654
IRF-1	R	IRF1	C	0.946302249	0.990377568	0.964842016	1.040871871	1.023103229	1.015367801	1.024874889
IRS1	R	IRS1	V	0.91587254	0.820261279	0.954556642	0.879595752	1.061777582	1.050245147	0.973177153
Jagged1	R	JAG1	V	0.922651865	0.988160829	1.014940809	1.00773336	0.967208999	0.992557633	1.010404428
Jak2	R	JAK2	V	0.959872382	0.977000377	1.042033193	0.993116147	0.977990792	0.966032371	0.996135206
JNK2	R	MAPK9	C	0.937650913	1.023835425	1.145197485	1.033173472	0.913728225	0.94192439	0.918764767
JNK_pT183_Y185	R	MAPK8	V	0.96625681	1.044129765	1.004489068	1.008002495	0.998637403	0.97896855	1.004514874
LC3A-B	R	MAP1LC3A/B	C	0.896057756	1.069399366	1.031044404	0.847193096	0.981364178	1.068976021	0.89479892
Lck	R	LCK	V	0.953302058	0.896291695	0.925106698	0.926115107	1.007234792	1.07344588	1.161306577
LDHA	R	LDHA	C	0.878896596	0.944597665	1.046521952	1.08883051	0.980935424	0.961637576	1.078990609
LRP6_pS1490	R	LRP6	V	0.903239328	0.938438089	1.03027333	0.949180268	0.923215486	0.977546066	0.957873634
MAPK_pT202-Y204	R	MAPK1/MAPK3	V	0.918581504	0.982994617	1.038690576	1.011547759	0.957892617	0.984948975	0.917253971
Mcl-1	R	MCL1	V	0.954725129	0.961912115	0.884831707	0.901930999	1.035590059	1.083398744	1.038715186
MCT4	R	SLC16A3	V	0.951612905	0.972052686	1.000255871	1.125133203	0.991168686	1.006935172	1.160033077
MDM2_pS166	R	MDM2	V	0.95431293	1.031417119	1.015131848	0.95970079	1.000994808	1.003558406	0.909070634
MEK1	R	MAP2K1	V	0.938988348	0.979926195	0.99641336	0.936065671	0.997315014	1.010697248	0.938514307
MEK1_p_S217-S221	R	MAP2K1/MAP2K1	V	0.96483854	1.002810009	1.01006697	1.040977487	0.967192733	0.997329448	1.037592121
MERIT40_pS29	R	BABAM1	V	0.855409131	1.02578462	1.016658875	1.010478349	0.997092885	0.990875531	0.994184603
Merlin	R	NF2	C	0.975817177	0.975085416	0.974741654	0.881959891	1.059005688	1.020134803	0.943822822
MIF	R	MIF	C	0.9481427	0.999213332	0.92382031	1.083713611	0.956234392	1.026600275	1.081308786
MIG6	M	ERRFI1	V	0.912870258	1.011144968	1.011921478	0.969703326	1.04905667	0.986828349	1.003797062
MMP2	R	MMP2	V	0.965735169	1.000926455	1.004470543	1.016282702	0.997719847	1.002808726	0.990425111
Mnk1	R	MKNK1	V	0.953518156	1.0865407	1.046064949	1.048991282	0.969675065	0.955929252	0.881327235
MSH6	R	MSH6	C	0.965680629	1.018597133	1.029535099	1.031766033	0.951429193	0.942738188	0.997157147
MSI2	R	MSI2	C	0.931634443	1.001538542	1.046268587	1.253596425	0.967774122	0.937069294	1.150509447
mTOR	R	MTOR	V	0.962507112	1.055758442	0.99308201	0.986162436	0.957552433	0.97045467	0.939956777
mTOR_pS2448	R	MTOR	C	0.972142498	1.064838833	1.016334977	0.955267928	0.955348118	0.935523072	0.907991567
Myosin-11	R	MYH11	V	0.720652657	0.976247002	0.978259108	0.948107284	1.01853583	1.019702084	0.94505946
Myosin-IIa_pS1943	R	MYH9	V	0.91157762	1.110217327	1.264665186	0.818739815	1.171662535	0.909503018	0.842766747
Myt1	R	PKMYT1	C	0.931586218	1.038293166	1.005094599	0.878943394	1.061085424	0.989067689	0.937905344
N-Cadherin	R	CDH2	V	0.827245375	1.016940707	0.974550867	1.002494124	0.996910014	1.009574762	0.981310426
N-Ras	M	NRAS	V	0.807310962	0.956468458	0.950502141	1.020898239	1.003006182	1.034439113	1.058658229
NAPSIN-A	R	NAPSA	C	0.824500532	1.008095055	1.027272729	1.147350844	1.021289096	0.980483856	1.188002534
NDRG1_pT346	R	NDRG1	V	0.959397371	0.865047693	0.981995725	1.014219292	0.987025009	1.02481308	0.989999606
NDUFB4	M	NDUFB4	V	0.78848167	1.008867014	1.013268913	1.091565741	0.965932149	0.994194531	1.008399134
NF-kB-p65_pS536	R	RELA	C	0.827684541	1.014844612	1.023374219	1.051690006	0.957387377	0.984300759	0.974067993

Antibody Name	Antibody Origin	Gene Name	Validation Status	Probabilities (QC Score)	MCF7 NSC BR1	MCF7 NSC BR2	MCF7 NSC BR3	MCF7b BR1	MCF7b BR2	MCF7b BR3
Notch1	R	NOTCH1	V	0.969859466	1.038482255	1.145947046	0.970388675	1.018230143	0.951151335	0.905878618
Notch3	R	NOTCH3	C	0.955795406	0.895695337	0.857008494	0.994593527	0.995785699	1.041291069	1.093922525
Oct-4	R	POU5F1	C	0.900429604	1.03613607	0.987172275	1.093563489	0.950385908	0.991139381	1.075153084
P-Cadherin	R	CDH3	C	0.901739397	1.022968286	0.784662592	0.954856094	1.033063289	1.003785826	1.010298943
p21	R	CDKN1A	V	0.843795191	0.97766372	0.983192012	1.093086506	0.993129144	1.023641835	1.076578681
p27-Kip-1	R	CDKN1B	V	0.96428525	1.021615302	0.988203142	1.009065152	1.00216123	1.005085243	1.016743031
p27_pT198	R	CDKN1B	V	0.955697703	1.003955653	0.94179647	0.924922942	0.937959351	1.022045712	0.944288559
p38-MAPK	R	MAPK14/11/12	V	0.975428997	0.991258711	0.940352238	0.913288847	1.022273265	1.023720418	0.988662778
p38_pT180_Y182	R	MAPK11/12/13/14	V	0.939528092	0.992138515	1.002462107	0.925740567	0.965355578	1.004775119	0.930012654
p44-42-MAPK	R	MAPK1/MAPK3	V	0.954860635	1.038996295	1.009524704	1.015284241	1.001477931	0.965170269	0.98551467
p53	R	TP53	C	0.954828158	1.018925712	0.957857044	0.980182964	1.029541326	1.007668347	0.999790208
p70-S6K1	R	RPS6KB1	V	0.97022586	0.995044979	0.943901088	0.826124699	1.086033782	1.131478595	0.96538335
p70-S6K_pT389	R	RPS6KB1	V	0.967964518	1.209421473	1.050921092	0.761499899	1.095928576	0.957330522	0.788184124
p90RSK_pT573	R	RPS6K	C	0.95728635	1.012367743	1.091233043	1.03174163	0.999083058	0.948230795	0.92885393
PAI-1	M	SERPINE1	V	0.921125873	0.982646216	0.995784626	1.233882244	1.06570547	0.964713003	1.362587072
PAICS	R	PAICS	C	0.95322103	0.979444626	1.046691895	0.98855909	0.996108877	0.96147119	0.992994934
PAK1	R	PAK1	V	0.958151437	0.845767571	0.92289484	1.179507854	0.968397243	1.067281643	1.216266625
PAK4	R	PAK4	V	0.952139622	1.137011157	0.91337781	0.996719154	0.880753929	0.884215551	1.194413048
PAR	R	PAR	C	0.945023441	1.090448027	0.868409057	1.258589544	0.878828791	0.938977743	1.126804874
PARP	R	PARP1	V	0.917402188	1.026761258	1.06513626	0.967316637	1.0084099	0.916715706	0.916190646
Paxillin	R	PXN	C	0.944795577	1.013070557	0.952899008	0.910715025	1.021102389	1.024273749	1.01409146
PCNA	M	PCNA	C	0.870676848	1.033374399	0.910004354	1.108211472	0.981542453	0.993791712	1.119977244
PD-1	M	PDCD1	V	0.755624116	1.024749354	1.009885064	1.022470435	0.953159269	0.997507546	1.045003486
PD-L1	R	CD274	C	0.811828305	1.029702725	1.00261517	1.042422766	1.044460194	0.995100876	1.040967513
Pdcd4	R	PDCD4	C	0.960521608	0.834266812	0.962383335	1.546357848	0.882129953	1.044014925	1.653513213
PDHK1	R	PDHK1	C	0.736649195	0.989698991	0.879468234	0.978807565	0.870992661	1.13379464	0.948797694
PDK1	R	PDPK1	V	0.921928257	0.997990613	0.946530815	0.927201252	1.014700457	1.023341703	0.942203388
PDK1_pS241	R	PDPK1	V	0.975382966	0.99475044	0.920430489	0.897717637	1.040530122	1.062944082	0.935230438
PEA-15	R	PEA15	V	0.96592673	0.962867727	0.872116901	0.966080477	0.992996961	1.043937472	1.016948632
PEA-15_pS116	R	PEA15	V	0.773399692	0.963378256	0.937905051	0.966562716	1.009857246	1.124223697	0.941652243
PI3K-p110-a	R	PIK3CA	C	0.966210884	0.900180885	0.932560248	1.013012469	0.996651902	1.040469077	1.047385372
PI3K-p110-b	M	PIK3BC	C	0.83340117	0.843371495	0.992933658	0.975855854	0.944720994	1.01410411	1.096999356
PI3K-p85	R	PIK3R1	V	0.971969279	1.02041655	0.962478302	1.07416927	0.941442947	1.006236534	1.027279132
PKA-a	R	PRKAR1A	V	0.964379873	0.929590278	0.856296648	0.920009345	1.014393647	1.048547067	0.992049246
PKC-b-II_pS660	R	PRKCA/B/D/E/H/Q	V	0.967122859	1.039225862	1.035969713	0.798103154	1.179084803	0.982826799	0.905224399
PKC-delta_pS664	R	PRKCD	V	0.936228955	1.031148283	1.004222282	1.084097433	1.006412418	0.995929692	1.142745849
PKCa	R	PRKCA	V	0.953627436	0.849349502	1.092482115	1.076440812	0.957362579	0.925400371	0.971804043
PKM2	R	PKM	C	0.758574546	0.995282126	1.043419273	1.019147039	1.016559594	0.912950399	1.032638929
PLC-gamma2_pY759	R	PLCG2	C	0.863808735	1.011656533	1.013814616	1.035049213	1.010146243	0.993660251	1.058596064
PLK1	R	PLK1	C	0.972037077	1.040018992	1.008521498	0.796976648	1.081111965	1.07387613	0.804621559
PMS2	R	PMS2	V	0.96285705	0.983683197	1.077062133	1.03752914	0.908970031	0.918542765	0.954090336
Porin	M	VDAC1	V	0.921729468	0.983904899	0.956595529	0.991463642	1.012658365	1.025279569	1.040572591

Antibody Name	Antibody Origin	Gene Name	Validation Status	Probabilities (QC Score)	MCF7 NSC BR1	MCF7 NSC BR2	MCF7 NSC BR3	MCF7b BR1	MCF7b BR2	MCF7b BR3
PR	R	PGR	V	0.962199058	0.854352588	1.19064947	1.285985534	0.730319743	0.729520677	1.087491986
PRAS40	M	AKT1S1	C	0.880730875	0.944035628	0.960400492	1.059394176	1.024821946	1.013736806	1.081259131
PRAS40_pT246	R	AKT1S1	V	0.958393495	1.014935731	0.960116494	0.929234943	0.989321272	1.011500357	0.942720664
PREX1	R	PREX1	V	0.90461033	0.851188306	0.850694095	0.700695184	1.446564784	1.346533375	1.056552193
PTEN	R	PTEN	V	0.969444786	0.999952261	0.990497316	1.004943117	1.019943571	1.016489452	1.006454117
Rab11	R	RAB11A/B	C	0.935614214	0.993029367	1.000376361	1.059559773	0.971349517	1.006817204	1.040722235
Rab25	R	RAB25	V	0.800621891	0.985882386	0.973781515	1.006094431	0.995634802	1.032855342	1.205329962
Rad50	R	RAD50	V	0.95085931	1.000106856	1.004945067	1.065610855	0.999904233	1.002344135	1.021050984
Rad51	R	RAD51	V	0.705964978	1.114754258	0.98296575	0.920216517	0.947230681	0.936079366	0.946440164
Raptor	R	RPTOR	V	0.972693131	0.986365508	1.052422641	1.043293241	0.985137174	0.955860405	1.012162851
Rb	M	RB1	Q	0.93560292	0.980329893	0.989242993	0.995328429	0.963790356	1.017717518	0.954107491
RBM15	R	RBM15	V	0.968732909	0.996907787	1.01611272	1.022970101	1.002969537	0.991410253	0.978195982
Rb_pS807_S811	R	RB1	V	0.975620762	1.044671084	1.079027815	0.969579048	0.987935225	0.982942285	0.852080192
Rheb	M	RHEB	C	0.94343676	0.953007826	1.000758773	1.005115946	1.03565394	1.003457667	1.026237242
Rictor	R	RICTOR	C	0.961037113	0.950130692	1.024262247	0.860841943	1.115392155	1.038059599	0.900881726
Rictor_pT1135	R	RICTOR	V	0.961742818	1.032055832	1.016332895	0.837262629	1.075166545	1.037941676	0.884784324
RIP	R	RIP	C	0.82046922	1.029705992	1.018637953	0.966883422	0.99739169	0.97875573	0.945695152
RPA32_pS4-S8	R	RPA2	C	0.971275014	1.016482734	1.051120794	0.956491026	0.99945894	0.9509222	0.925233599
RSK	R	RPS6KA1/ 2/3	C	0.967998665	1.046840021	1.112160221	1.107006814	0.822703075	0.86045404	0.898525531
S6	M	RPS6	V	0.94369639	1.086127453	1.105517957	1.124201847	0.852193892	0.943127257	0.831743554
S6_pS235_S236	R	RPS6	V	0.958224925	1.16779041	1.122762178	0.964727769	0.726892882	0.912864708	0.539402997
S6_pS240_S244	R	RPS6	V	0.964826402	1.091105892	1.101165742	1.051929456	0.732811452	0.938345924	0.719623673
SCD	M	SCD	V	0.701596657	0.97943992	1.031780686	0.906814184	1.029864646	0.96823394	1.000209792
SDHA	R	SDHA	V	0.959930334	0.881904367	1.002935137	1.108819359	0.975925353	1.004311991	1.084755083
SF2	M	SRSF1	V	0.764103983	0.99906948	1.000135216	1.135788085	1.015052769	1.007053302	1.044680794
Shc_pY317	R	SHC1	V	0.954154466	0.987096928	1.013297957	0.980360365	1.000980662	0.994166095	0.995330463
SHP-2_pY542	R	PTPN11	C	0.963898296	1.038745863	1.009770363	0.957244732	1.03058753	0.927344161	0.983093299
SLC1A5	R	SLC1A5	C	0.935867506	0.96233747	0.976431779	0.886966626	1.053135416	1.013166808	0.916540843
Slfn11	G	SLFN11	C	0.844488819	0.973822894	1.002929993	0.987274518	0.966275231	1.004317027	1.045612278
Smac	M	DIABLO	Q	0.951656525	1.01013343	0.94684092	1.020379768	0.961260264	1.016112525	0.999782425
Smad1	R	SMAD1	V	0.933670982	1.007329224	1.040588264	0.988509407	0.981942744	0.94024933	1.019176942
Smad3	R	SMAD3	V	0.960362328	1.032156567	1.016234081	0.97369584	0.968740482	0.982836902	0.975321352
Smad4	M	SMAD4	V	0.862478927	1.03236328	1.016031308	0.99664518	1.033491643	0.988261891	1.22507595
Snail	M	SNAI1	Q	0.866186843	0.93436156	0.98319276	1.098920298	1.021670977	1.016726952	1.109626613
SOD1-	M	SOD1	V	0.937858133	0.981398721	0.98002292	1.040823493	0.968975844	1.026744588	1.08022201
SOD2	R	SOD2	V	0.857846593	1.045531645	1.003113905	1.022280867	0.934152133	0.914320931	0.997719764
Sox2	R	SOX2	V	0.913244496	0.913899701	0.930268205	1.008567821	0.9962661	1.040835187	1.070250136
Src	M	SRC	V	0.946614684	0.936751386	0.897543687	1.0946107	0.942098169	1.086589228	1.090884242
Src_pY419	R	SRC	V	0.972411885	1.030719072	1.001850019	1.110561145	0.975988996	0.996341909	1.096163763
Src_pY527	R	SRC	V	0.966217575	0.929150205	0.935437671	0.95690239	0.997831342	1.039349834	1.032002752
Stat3	R	STAT3	C	0.965942512	1.061286547	1.040751228	1.090756031	0.954318378	0.910991056	0.886093026
Stat3_pY705	R	STAT3	V	0.741157764	0.978508636	0.986130318	0.952277319	1.001027599	1.020765036	1.078937558
Stat5a	R	STAT5A	V	0.95124478	1.000047739	0.935497816	0.921956123	1.00798199	1.041386797	1.034254809
Stathmin-1	R	STMN1	V	0.962496725	1.03095524	0.960225147	1.037472137	0.949799813	0.996115092	1.041509297

Antibody Name	Antibody Origin	Gene Name	Validation Status	Probabilities (QC Score)	MCF7 NSC BR1	MCF7 NSC BR2	MCF7 NSC BR3	MCF7b BR1	MCF7b BR2	MCF7b BR3
STING	R	TMEM173	V	0.95953455	1.034067159	1.014359901	1.018808439	1.046540887	0.99312638	0.90976298
Syk	M	SYK	V	0.947801906	1.017907521	0.993775281	0.961668057	1.062895455	1.013344545	0.512036794
Tau	M	MAPT	C	0.958500192	0.854581675	1.088148323	0.435097165	1.018858036	1.019396324	1.182090857
TAZ	R	WWTR1	V	0.961498146	0.98611021	0.949016031	0.8081255	1.207179606	1.039184618	0.966492943
TFAM	R	TFAM	V	0.962276172	0.991236198	0.957707301	0.999923882	1.011659276	1.026227665	1.030114205
TFRC	R	TFRC	V	0.961387389	1.013475428	0.953942251	0.789233407	1.089830316	1.012902844	0.934524547
TIGAR	R	TIGAR	V	0.971893629	0.996578091	0.963292618	1.026257806	1.021219322	1.017155555	1.009092932
Transglutaminase	M	TGM2	V	0.919145478	0.937944278	0.994922789	1.018628683	1.043244033	0.996254966	1.027526507
TRIM25	R	TRIM25	C	0.958490113	0.985004957	0.919381688	0.918902244	1.015691696	1.054270793	0.972585933
TSC1	R	TSC1	C	0.968310735	1.008972216	1.000891561	1.050221309	0.977059441	1.006312789	1.094768787
TTF1	R	NKX2-1	V	0.802674726	1.018025531	1.005057239	1.049736062	1.056138679	0.9712471	1.033594181
Tuberin	R	TSC2	V	0.958489143	1.034400829	1.01403259	1.003666742	0.959162778	0.924317979	0.917848528
Tuberin_pT1462	R	TSC2	V	0.935353602	1.060434966	1.017665404	0.931938639	1.006766561	0.968287248	0.906798328
TUFM	R	TUFM	V	0.901895243	1.006782693	1.033133458	1.028485378	1.016396161	0.974745809	1.035207088
TWIST	M	TWIST1	C	0.874287834	0.994898818	1.006741955	0.943523185	0.988634105	1.000584861	1.013228242
Tyro3	R	TYRO3	V	0.930722174	0.963952156	0.962467025	0.948892444	0.96759401	1.043932987	1.016993636
U-Histone-H2B	R	HIST1H2BB	C	0.74899206	1.399394413	0.924709106	0.971479743	0.666861022	0.566182052	1.133969036
UBAC1	R	UBAC1	V	0.96211613	0.979588274	0.939903901	1.018753039	1.010059453	1.027745834	1.06616693
UGT1A	M	UGT1A1/4/5/8/10/7/3	V	0.826107477	0.914573595	1.076144894	1.147981134	0.975577983	0.932634728	1.129576441
ULK1_pS757	R	ULK1	C	0.952360042	0.984831752	0.968609574	1.027650179	1.044365507	0.995190731	1.03115061
VASP	R	VASP	V	0.968212292	1.006955925	0.962462652	1.058470568	0.998274567	1.019164226	1.049899456
VEGFR-2	R	KDR	V	0.962775976	0.949398161	0.930518433	0.864386898	1.169894476	1.040995733	0.938509758
VHL-EPPK1	M	EPPK1	C	0.921548358	0.889310408	1.156357877	0.697849262	1.361981996	1.167791766	0.735892382
Wee1	R	WEE1	C	0.868531581	1.027829583	1.045861035	0.944338077	0.901820568	0.87712885	0.915250743
Wee1_pS642	R	WEE1	C	0.873225285	1.03953906	1.008992283	0.948658769	1.015929452	0.983114277	0.968992114
WIPI1	R	WIPI1	C	0.889638416	1.041230858	1.007332728	0.963783721	1.012221533	0.927734477	0.964609918
WIPI2	R	WIPI2	C	0.923544172	0.993847354	1.004438508	0.956310945	1.048192642	0.99155893	0.972365301
XBP-1	G	XBP1	C	0.867006401	1.020814054	1.027360428	1.167075517	1.018776511	1.040526514	0.812692945
XPA	M	XPA	V	0.914462754	0.979876036	1.039534739	1.038080275	1.020567367	0.935977468	1.087268496
XPF	R	ERCC4	C	0.908946036	0.990967405	1.03073231	0.997134471	1.029649056	0.968904838	0.994293183
XPG	R	ERCC5	C	0.96085233	1.000578667	1.001227552	1.008432638	1.027687778	1.005983831	1.044803739
XRCC1	R	XRCC1	C	0.913699622	1.036803387	1.01167582	1.108731222	0.945690999	0.916300604	1.061865067
YAP	R	YAP1	C	0.946482579	0.985767344	0.93244731	1.020967278	1.027097424	1.011577466	1.01950744
YAP_pS127	R	YAP1	V	0.970022321	0.778867992	0.900803554	0.998213144	0.947663509	1.086957145	1.012444018
YB1_pS102	R	YBX1	V	0.967076669	1.11436288	1.167927963	0.858791201	1.029288654	1.009498074	0.811143404
ZAP-70	R	ZAP70	C	0.951222302	0.976558771	1.010614433	0.969392986	0.923920156	0.996793445	0.995006599

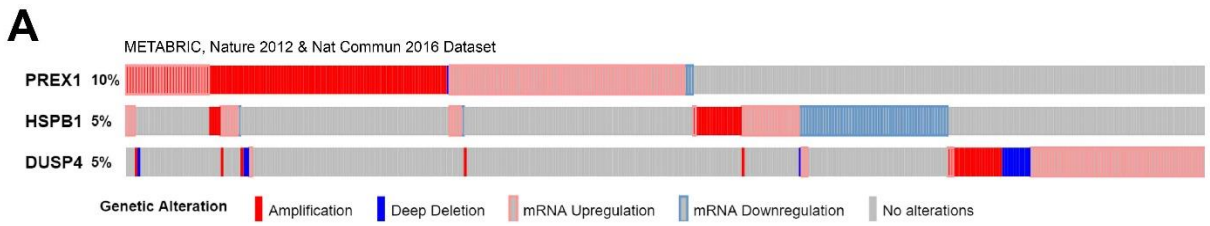

Figure 20. PREX1 is upregulated/overexpressed in breast cancer patients. (A) Genetic alterations of PREX1, HSPB1, and DUSP4 in breast cancer patients from the METABRIC, Nature 2012, & Nat Comm 2016 dataset from The Cancer Genome Atlas.

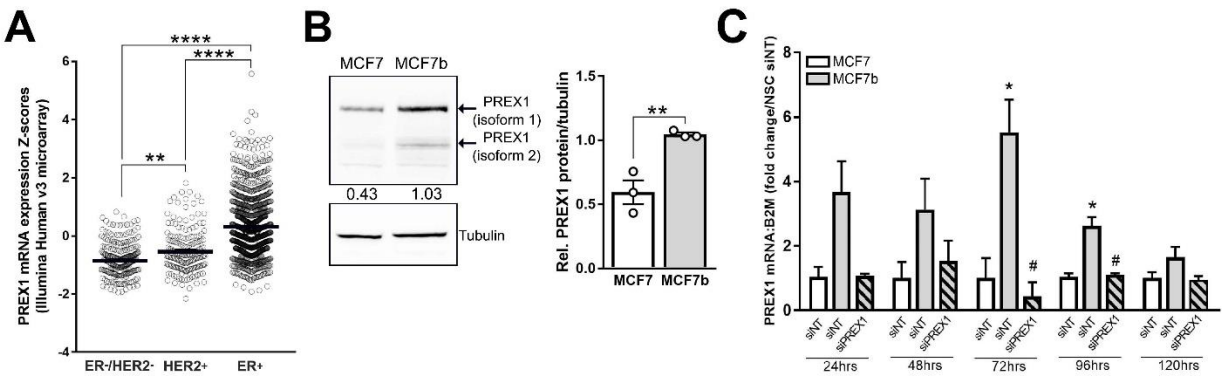

Figure 21. PREX1 is upregulated/overexpressed in ER+ breast cancer patients and MCF7b cells. (A) *PREX1* mRNA expression in each breast cancer subtype of patients in the METABRIC, Nature 2012, & Nat Comm 2016 dataset from The Cancer Genome Atlas. (B) Representative western blot for PREX1 and tubulin in MCF7 and MCF7b cells and quantitation of three western blots. (C) qPCR of *PREX1* normalized to *B2M* in MCF7 and MCF7b cells over 120 hours after transfection with non-targeting or *PREX1*-targeting siRNAs. A: One-way ANOVA with Sidak's multiple comparisons test, **p<0.01 and ****p<0.0001. B: Mann-Whitney t-test, **p<0.01. n=three independent biological replicates. C: One-way ANOVA with Sidak's multiple comparisons test, *p<0.05 compared to MCF7 siNT; $^{\#}$p<0.05 compared to MCF7b siNT. n=three independent biological replicates. Bar graphs indicate mean + standard error of the mean.

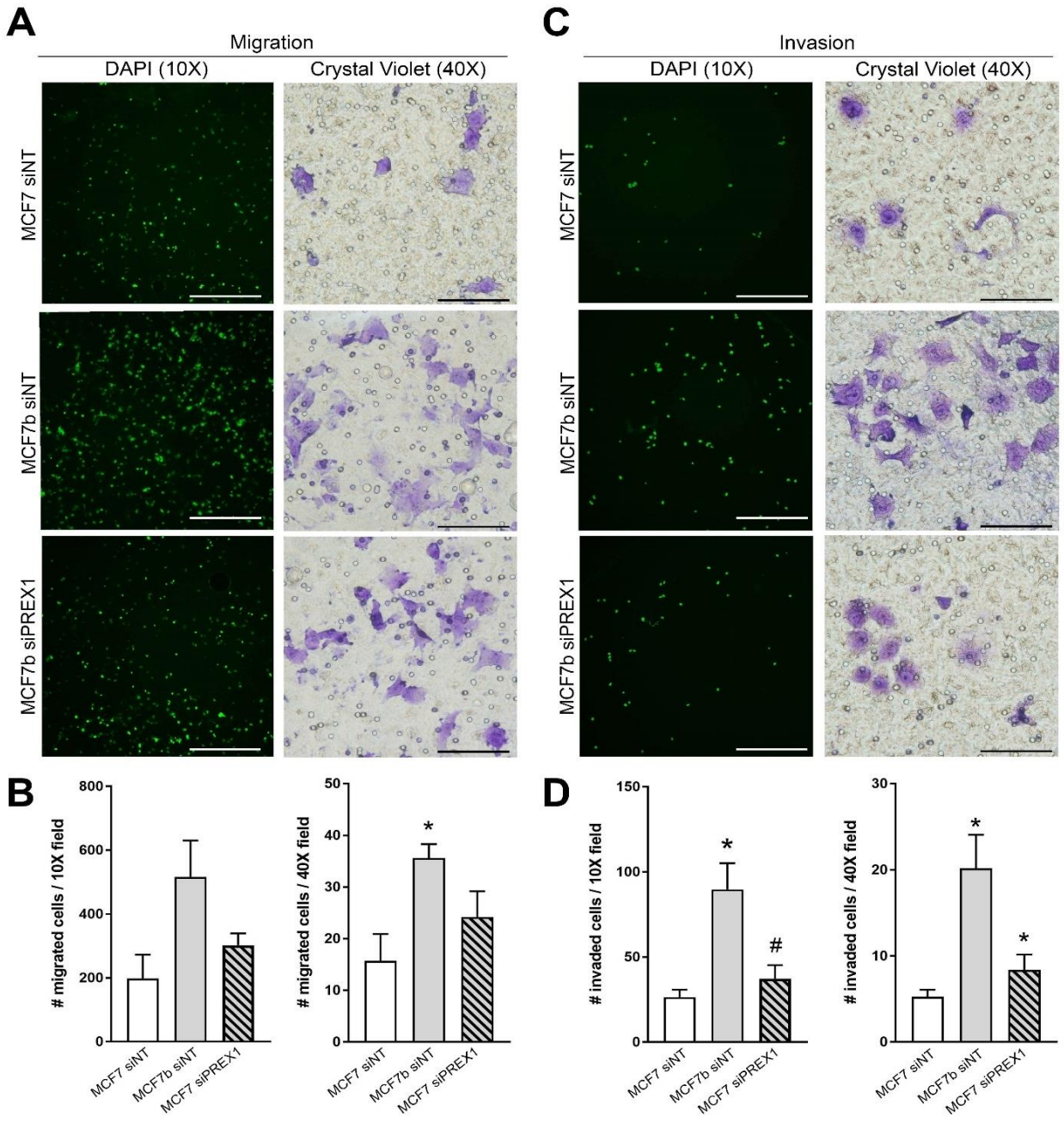

Figure 22. PREX1 knockdown ablates enhanced migration and invasion phenotype of MCF7b cells. (A) Representative images of MCF7 and MCF7b transfected with a non-silencing siRNA (siNT) or PREX1-targeting siRNAs (siPREX1) evaluated for cell migration by DAPI (green pseudocolor) or crystal violet staining. Left panel = 10X, scale bar = 500μm; right panel = 40X, scale bar = 100μm. (B) Quantitation of the number of migrated cells per 10X or 40X field from (A). (C) Representative images of cell invasion of MCF7 and MCF7b transfected with a non-silencing siRNA (siNT) or PREX1-targeting siRNA (siPREX1) assessed in (A). (D) Quantitation of the number of migrated cells per 10X or 40X field from (C). B, D: One-way ANOVA with Sidak's multiple comparisons test. *p<0.05 *vs* MCF7 siNT. #p<0.05 *vs* MCF7b siNT. n=three independent biological replicates. Bar graphs = mean + standard error of the mean.

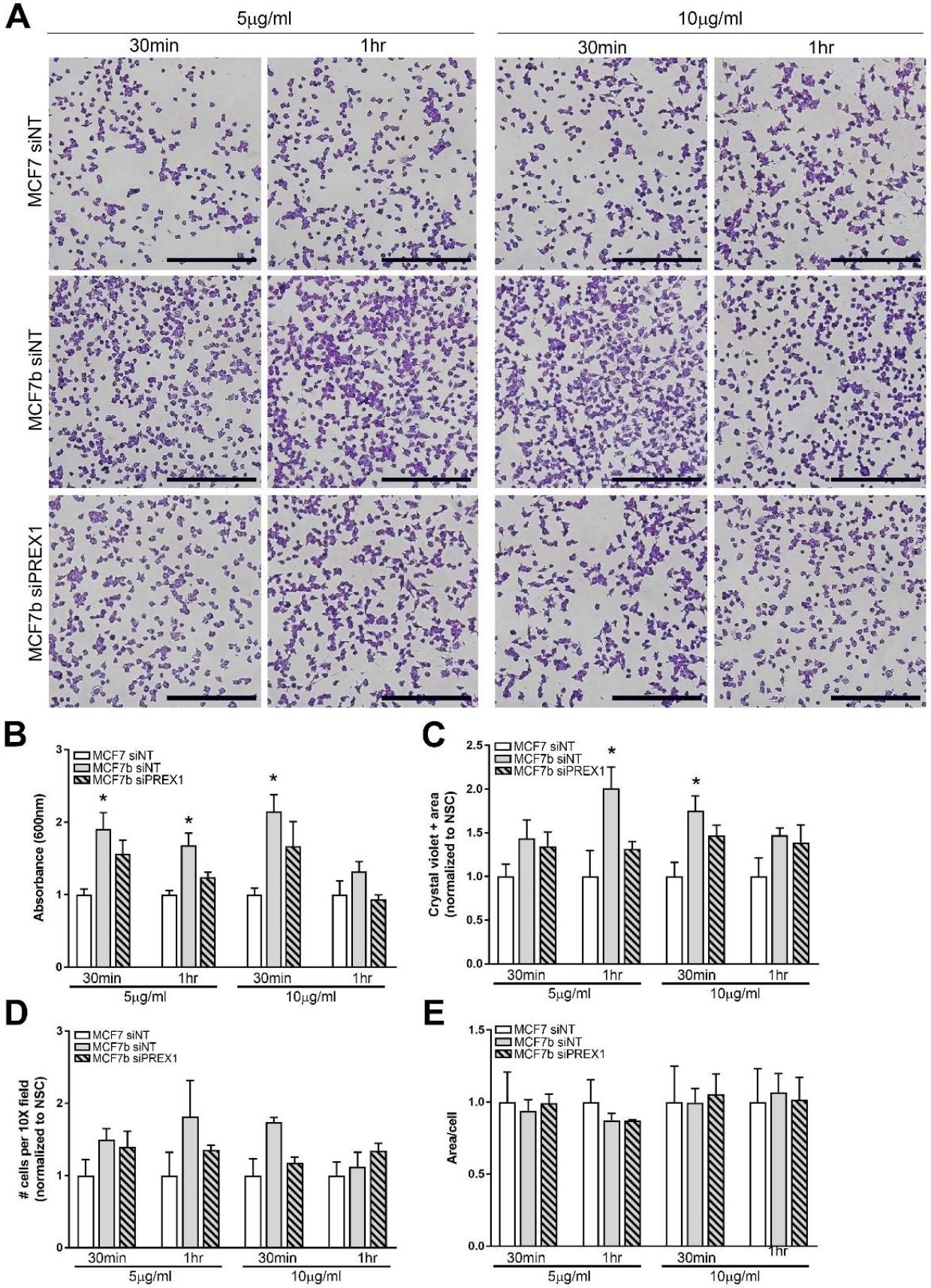
A
5μg/ml
10μg/ml
30min
1hr
30min
1hr
MCF7 siNT
MCF7b siNT
MCF7b siPREX1
B
Absorbance (600nm)
MCF7 siNT
MCF7b siNT
MCF7b siPREX1
30min
1hr
30min
1hr
5μg/ml
10μg/ml
C
Crystal violet + area (normalized to NSC)
MCF7 siNT
MCF7b siNT
MCF7b siPREX1
30min
1hr
30min
1hr
5μg/ml
10μg/ml
D
cells per 10X field (normalized to NSC)
MCF7 siNT
MCF7b siNT
MCF7b siPREX1
30min
1hr
30min
1hr
5μg/ml
10μg/ml
E
Area/cell
MCF7 siNT
MCF7b siNT
MCF7b siPREX1
30min
1hr
30min
1hr
5μg/ml
10μg/ml

Figure 23. Knockdown of PREX1 partially reduces adhesive ability of MCF7b cells. (A) Representative images of adherent MCF7 and MCF7b cells transfected with non-targeting siRNAs (siNT) or PREX1-targeting siRNAs (siPREX) incubated on 5μg/ml or 10μg/ml fibronectin for 30 minutes or 1 hour. All panels = 10X, scale bar = 500μm. (B) Crystal Violet absorbance measurements at 600nm to assess adherent cells from (A). (C-E) Quantitation of (C) total crystal violet area per field, (D) number of cells per field, and (E) area per cell from (A). B-E: One-way ANOVA with Sidak's multiple comparisons test. *$p<0.05$ compared to MCF7 siNT. n= three independent biological replicates. Bar graphs = mean + standard error of the mean.

MCF7b cells efficiently colonize the bone

MCF7 or MCF7b cells were inoculated into nude mice by intracardiac injection without estradiol pellet implantation, and metastatic tumor burden was monitored every 3 weeks by radiography (Figure 24A). A modest increase in lesion number and lesion area was observed in MCF7b-inoculated mice at weeks 18 and 22 post-tumor inoculation (Figure 24B). Radiographic analysis revealed that two mice in the MCF7b group (mouse 11 and 15) harbored significant osteolytic bone destruction in a single tibia (Figure 24C). Mice were sacrificed 22 weeks after tumor cell inoculation, when the aforementioned two mice became paraplegic and moribund, and all mice were analyzed for microCT, flow cytometry, qPCR, and histology (Figure 24D).

MicroCT revealed no substantial differences in bone volume or trabecular microarchitecture in MCF7b-inoculated mice compared to MCF7-inoculated controls (Figure 24E). Using a highly sensitive and human-specific flow cytometry protocol for CD298 expression (135, 156) tumor cells were detected in the bone marrow of 3/9 (33%) MCF7-inoculated and 2/10 (20%) MCF7b-inoculated mice (Figure 24F). qPCR analysis for the human housekeeping genes, beta-2-microglobulin (*B2M*) and hypoxanthine phosphoribosyltransferase 1 (*HPRT1*) (135) detected tumor cells in 2/9 (22%) MCF7-inoculated and 1/10 (10%) MCF7b-inoculated mice (Figure 24G). Histomorphometric analysis of the tibiae did not reveal any significant differences in bone volume between the groups (Figure 24H); however, hematoxylin and eosin staining of tibiae confirmed the presence of substantial tumor burden in the bones of the two mice (mouse 11 and 15) that exhibited extensive osteolytic lesions by radiography (Figure 24I, J and Figure 25). Immunostaining for pan-cytokeratin (135) confirmed the presence of tumor cells in these mice, but did not detect tumor cells in any other MCF7b-inoculated mice or any of the MCF7-inoculated mice (Figure 24J and Figure 25). Mice harboring overt MCF7b lesions (n=2) showed increased TRAP staining on the bone surface and had the highest osteoclast surface/bone surface (Oc.S/BS) and osteoclast number/bone perimeter (N.Oc/B.Pm) compared to other MCF7b-inoculated mice with no overt metastatic lesions or MCF7-inoculated mice (Figure 24J and Figure 26A-C).

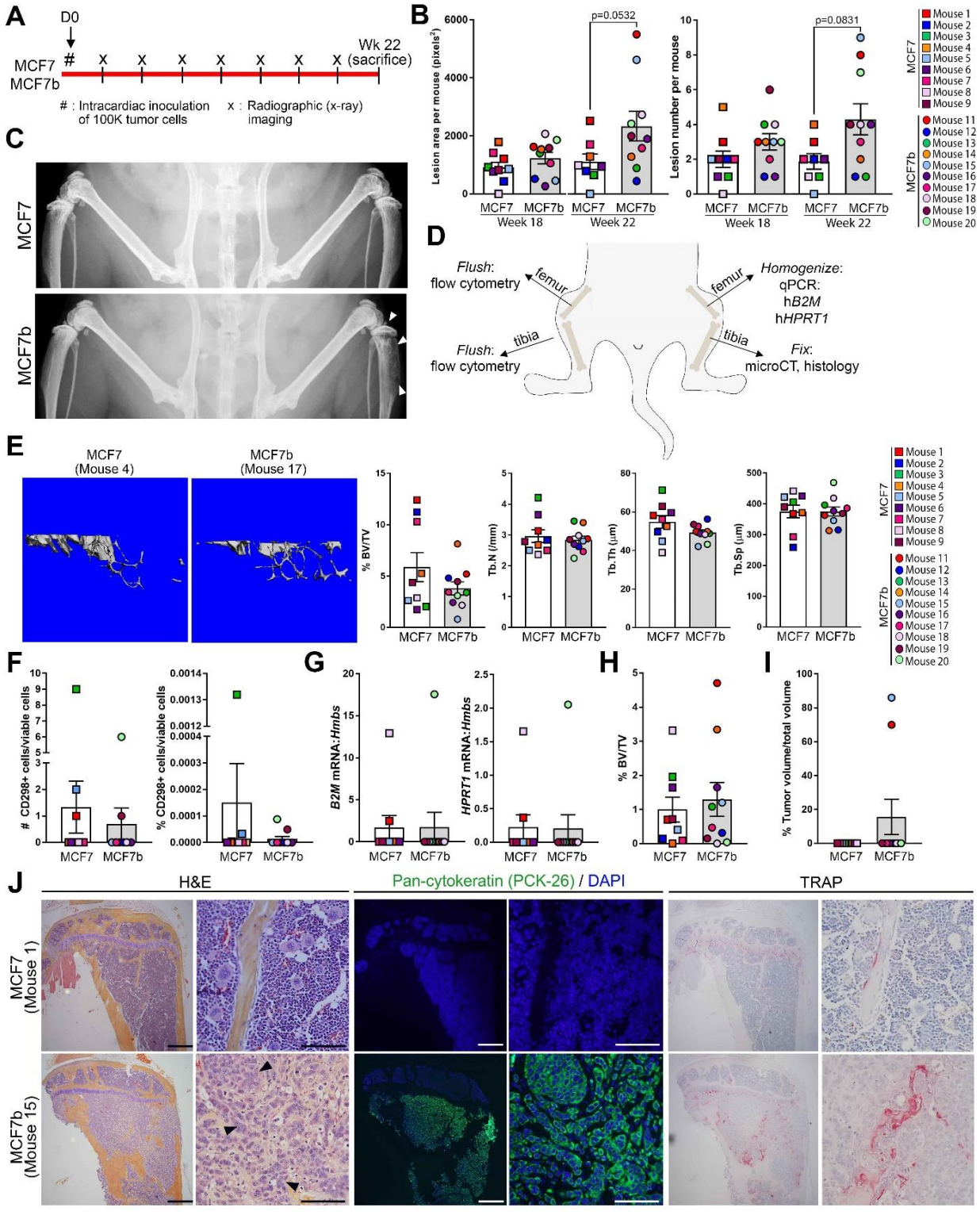
A
D0
Wk 22 (sacrifice)
MCF7
MCF7b
: Intracardiac inoculation of 100K tumor cells
x : Radiographic (x-ray) imaging
B
Lesion area per mouse (pixels²)
p=0.0532
Lesion number per mouse
p=0.0831
MCF7 MCF7b MCF7 MCF7b
Week 18 Week 22
Mouse 1
Mouse 2
Mouse 3
Mouse 4
Mouse 5
Mouse 6
Mouse 7
Mouse 8
Mouse 9
Mouse 11
Mouse 12
Mouse 13
Mouse 14
Mouse 15
Mouse 16
Mouse 17
Mouse 18
Mouse 19
Mouse 20
C
MCF7
MCF7b
D
Flush: flow cytometry
femur
tibia
Homogenize: qPCR: hB2M hHPRT1
Fix: microCT, histology
E
MCF7 (Mouse 4)
MCF7b (Mouse 17)
% BV/TV
Tb.N (/mm)
Tb.Th (µm)
Tb.Sp (µm)
F
CD298+ cells/viable cells
% CD298+ cells/viable cells
G
B2M mRNA:Hmbs
HPRT1 mRNA:Hmbs
H
% BV/TV
I
% Tumor volume/total volume
J
H&E
Pan-cytokeratin (PCK-26) / DAPI
TRAP
MCF7 (Mouse 1)
MCF7b (Mouse 15)

Figure 24. MCF7b cells form overt bone metastases following intracardiac inoculation without estrogen supplementation. (A). Experimental timeline of intracardiac inoculation of MCF7 and MCF7b cells (indicated by #) and radiographic imaging (indicated by x) to sacrifice. n=10 mice inoculated per group. (B) Radiographic assessment of total lesion number per mouse and total lesion area per mouse over time in MCF7- (n= 9) and MCF7b- (n=10) inoculated mice. (C) Representative radiographic images at week 22 for MCF7- and MCF7b- inoculated mice. (D) Schematic indicating methods performed on the hind limbs upon sacrifice. (E) Representative microCT images and analysis of mice in (B). (F) Quantitation of total number and percent of CD298+ tumor cells detected by flow cytometry in the bone marrow of mice described in (B). (G) qPCR of whole bone homogenate for human *B2M* or human *HPRT1* normalized to mouse *Hmbs* (housekeeping gene) from mice described in (B). (H, I) Histomorphometric analysis of (H) bone volume/total volume (%BV/TV) and (I) tumor volume/total volume from mice described in (B). (J) Representative hematoxylin and eosin (H&E), pan-cytokeratin and DAPI, or tartrate-resistant acid phosphatase (TRAP) staining of tibiae from mice described in (B). All panels, left = 4X, right = 40X of the same tibia. Scale bars = 500μm (left panel), 100μm (right panel). B: Mann-Whitney test. Bar graphs = mean ± standard error of the mean.

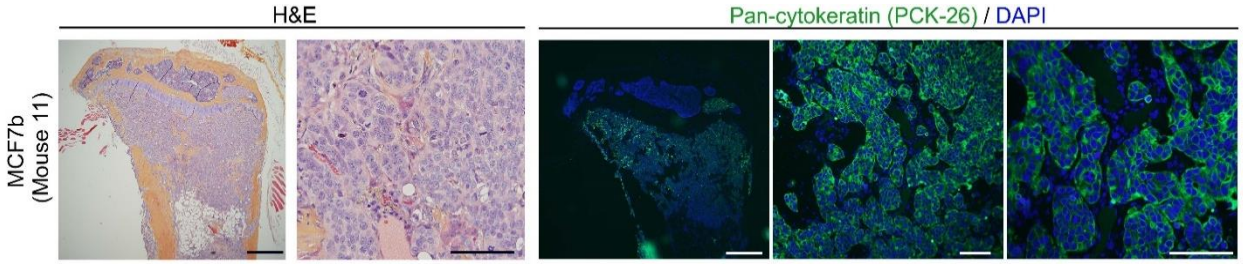

Figure 25. Detection of MCF7b cells in tibiae by pan-cytokeratin immunostaining. Hematoxylin and eosin (H&E) or pan-cytokeratin and DAPI staining of tibiae from mouse 11 inoculated with MCF7b cells via intracardiac injection. H&E panels, left = 4X, right = 40X of the same tibia. Scale bars = 500μm (left panel), 100μm (right panel). Immunofluorescence panels left to right = 4X, 20X, 40X of same tibia. Scale bars = 500μm (left panel) and 100μm (right two panels).

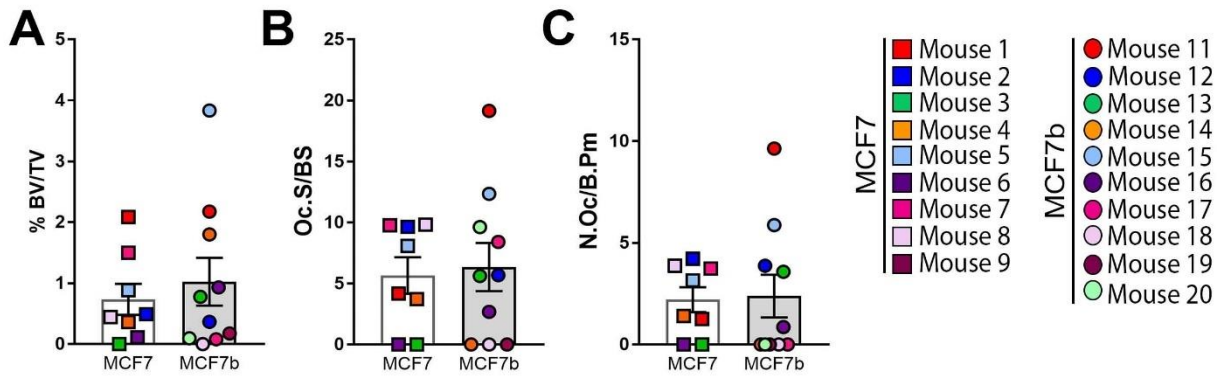

Figure 26. Tibiae bearing MCF7b overt metastases contain more TRAP+ osteoclasts. (A-C) Histomorphometric analysis of (A) bone volume/total volume (%BV/TV), (B) Osteoclast surface/bone surface (Oc.S/BS) and (C) number of osteoclasts/bone perimeter (N.Oc/B.Pm) in MCF7- (n= 9) and MCF7b- (n=10) inoculated mice.

MCF7b cells spontaneously metastasize to skeletal sites

To determine whether MCF7b cells were better adapted to spontaneously metastasize to the bone marrow following re-inoculation, MCF7b and MCF7 cells were implanted into the mammary fat pad of mice supplemented with exogenous estradiol. Surprisingly, MCF7b cells exhibited a significant reduction in primary tumor growth over 8 weeks compared to the MCF7 line Figure 27A). Upon sacrifice, 8/8 (100%) MCF7-inoculated and 3/10 (30%) MCF7b-inoculated mice had discernable primary tumors, and tumor weight per mouse was significantly reduced in MCF7b-inoculated mice (Figure 27B, C). At sacrifice, the hind limbs were processed for flow cytometry and the femur, spine, and lung were processed for qPCR (Figure 27D). Although the total number of CD298+ tumor cells was similar between the two groups, the percent of CD298+ tumor cells detected in the bone marrow of the tibiae and femora was significantly higher in MCF7b-inoculated mice compared to MCF7-inoculated mice (Figure 27E). Since there was a dramatic difference in primary tumor development, we normalized the number and percent of CD298+ tumor cells to the final tumor weight to better assess metastatic potential, which revealed a dramatic increase in MCF7b dissemination to the bone (Figure 27F). Tumor burden as assessed by qPCR was modestly increased in whole femora and significantly increased in spine homogenates in MCF7b-inoculated mice (Figure 27G, H). In contrast, dissemination to the lung was reduced in the MCF7b-inoculated group, although this did not reach statistical significance (Figure 27I).

Analysis of primary tumor homogenates by qPCR revealed that *PREX1* remained upregulated in MCF7b primary tumors at endpoint (Figure 27J), despite the low number of MCF7b primary tumors that persisted at sacrifice (n=3). Using publicly available datasets, we found that in comparison to breast cancer patients with local or lymph node dissemination, *PREX1* mRNA levels were significantly higher in the primary tumors of patients who developed distant metastasis (Figure 27K), as demonstrated by two PREX1 microarray probes. Patients within the distant metastasis group that harbored bone metastases, indicated as red dots in Figure 27K, tended to express above average *PREX1* mRNA.

Discussion

The multi-step progression of the metastatic cascade is well established, but the mechanisms controlling tumor dissemination and colonization of distant organs remain less clear. A major limitation to our understanding of these mechanisms is the lack of *in vivo* models that faithfully recapitulate the spontaneous metastasis, prolonged latency and metastatic outgrowth observed in breast cancer patients. Here, we established a novel bone-selective

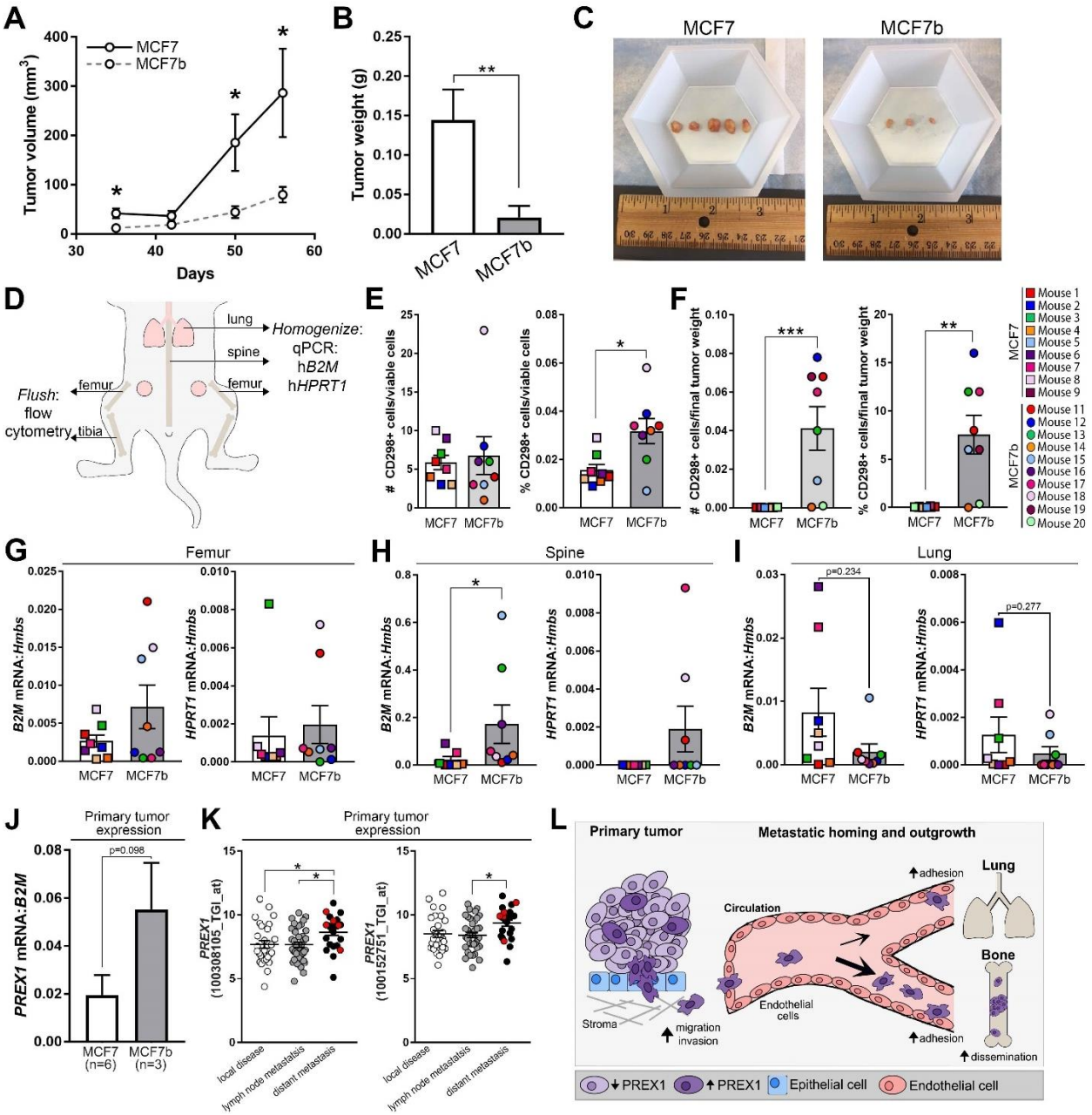
A
Tumor volume (mm3)
MCF7
MCF7b
Days
B
Tumor weight (g)
MCF7
MCF7b
C
MCF7
MCF7b
D
lung
spine
femur
femur
tibia
Flush: flow cytometry
Homogenize: qPCR: hB2M hHPRT1
E
CD298+ cells/viable cells
% CD298+ cells/viable cells
F
CD298+ cells/final tumor weight
% CD298+ cells/final tumor weight
MCF7
MCF7b
G
Femur
B2M mRNA:Hmbs
HPRT1 mRNA:Hmbs
H
Spine
I
Lung
p=0.234
p=0.277
J
Primary tumor expression
PREX1 mRNA:B2M
p=0.098
MCF7 (n=6)
MCF7b (n=3)
K
Primary tumor expression
PREX1 (100308105_TGI_at)
PREX1 (100152751_TGI_at)
local disease
lymph node metastasis
distant metastasis
L
Primary tumor
Metastatic homing and outgrowth
adhesion
Lung
Circulation
Bone
Endothelial cells
Stroma
migration invasion
adhesion
dissemination
PREX1
PREX1
Epithelial cell
Endothelial cell

Figure 27. MCF7b cells grow poorly in the primary site but spontaneously disseminate to skeletal sites. (A) Tumor volume by caliper measurements over 55 days following injection of MCF7 and MCF7b cells into the mammary fat pad. n=8 mice per group at sacrifice. (B) Final tumor weight per mouse after sacrifice from mice described in (A). (C) Representative images of primary tumors collected from mice described in (A). (D) Schematic indicating the methods performed on the hind limbs upon sacrifice. (E) Quantitation of total number and percent of CD298+ tumor cells detected by flow cytometry in the bone marrow of mice described in (A). (F) Normalization of data from (E) to final tumor weight. (G-I) qPCR analysis of whole (G) femur, (H) spine, or (I) lung homogenates for human *B2M* or human *HPRT1* normalized to mouse *Hmbs* (housekeeping gene) from mice described in (A). (J) qPCR of *PREX1* expression in primary tumors isolated from mice described in (A). (K) Analysis of *PREX1* mRNA expression in primary breast tumors from patients with local disease, lymph node metastases, or distant metastases (Kimbung et al. dataset). (L) Working model showing enhanced metastatic potential of MCF7b cells driven by PREX1 upregulation resulting in increased tumor cell dissemination and outgrowth in the bone. Bar graphs = mean ± standard error of the mean.

MCF7 derivative (MCF7b) that is molecularly primed to more efficiently disseminate to and colonize skeletal sites than the parental cell line (Figure 27L). Further, given the ability of MCF7b cells to colonize the bone in the absence of estrogen, these cells provide a clinically relevant model in which to study ER+ tumor cell dissemination and skeletal colonization.

Mechanistically, upregulation of PREX1 drives MCF7b invasion and adhesion and is associated with the development of distant metastasis in breast cancer patients, particularly those with ER+ disease. Similar findings have been demonstrated in metastasis models of melanoma (186) and prostate cancer (187) where PREX1 promotes metastasis to the lungs and lymph nodes, respectively. Moreover*, in vitro* studies suggest that PREX1 activation of downstream Rac signaling is responsible for this enhanced metastatic potential (181, 186, 187); however, this possibility has not been thoroughly investigated *in vivo*. Previous work indicates that PREX1 is activated by CXCR4 (181, 188), a well-known chemokine receptor involved in tumor cell homing to the bone. Thus, investigation into these signaling axes may provide insight into why PREX1 preferentially promotes dissemination to bone over other sites in the MCF7b model.

Intracardiac inoculation of MCF7b cells resulted in overt bone metastases in 20% of mice (2/10 mice), compared with 0% in the MCF7-bearing mice, *in the absence of exogenous estradiol*. Further, these two mice presented with a single tumor-bearing tibia and thus tumor cells were only detected by histology and immunostaining, which were the methods performed on this tibia. Interestingly, the development of overt bone metastases in a small fraction of mice has been observed in similar studies using the ER+ bone metastatic derivatives of MCF7 (MCF7-5624A (164)) and T47D (DBM (71)) cells.

Importantly, the ability of MCF7b cells to colonize the bone in the absence of exogenous estradiol, thus avoiding the detrimental effects on the bone and urinary tract, provides a more physiologically relevant model of tumor dissemination to bone. The two mice harboring bone metastases, mouse 11 and mouse 15, had the second highest (~5% BV/TV) and lowest (~1% BV/TV) bone volume in the MCF7b-inoculated cohort, suggesting that the MCF7b cells can induce osteoblastic or osteolytic bone remodeling, which has been previously reported (133). TRAP staining of tibiae following intracardiac inoculation of MCF7 and MCF7b cells revealed an increase in TRAP+ osteoclasts lining the bone surface in tibiae harboring overt MCF7b metastases compared to MCF7b-inoculated mice with no overt metastases and control MCF7-inoculated mice, suggesting tumor-induced expansion of the osteoclast population. The vicious cycle of bone destruction is a well described process that disrupts physiological bone remodeling, resulting in enhanced osteoclastogenesis, resorption of bone matrix, and localized

release of growth factors and cytokines that promote tumor cell proliferation (57). However, PTHrP and GLI2 expression and basal ERK, AKT, or SMAD signaling, which are known to be activated by bone-derived growth factors such as TGFβ and IGFs (189-191), were unchanged between the MCF7b and parental cell line (Figure 16I and data not shown). These data suggest that these well-known mechanisms of tumor-induced bone disease likely did not trigger the outgrowth of these cells.

The bone marrow is a uniquely fertile microenvironment containing stem cells, osteoblasts, and osteoclasts, which provide a rich source of growth factors and cytokines that support tumor cell homing, survival, and outgrowth. Due to the complexity of the bone microenvironment and limited mouse models, little is known about the timing and molecular signals that drive tumor cell colonization and eventual metastatic progression in the bone. Comparative genomic studies of primary breast tumors with disseminated tumor cells have provided considerable insight into the timing of tumor cell dissemination (11-15), but not the mechanisms driving bone metastasis or metastatic outgrowth. In order to identify these mechanisms, microarray analyses comparing primary tumor samples from patients with and without bone metastases (17) as well as comparison between human ER- parental MDA-MB-231 cells with bone metastatic subclones have been performed (16). These studies have identified several gene signatures(16-18) and key signaling pathways, such as the $CXCR4^{Tumor}$-$CXCL12^{Osteoblast}$ axis (16), that drives tumor cell homing and dissemination to bone. However, these studies have focused on ER- breast cancer cells and similar studies have not been extensively performed in ER+ breast cancer lines. Unfortunately, these published microarrays did not include PREX1 probes and thus we cannot glean any information concerning the association of PREX1 with bone metastasis from these studies. Interestingly, studies performed in the ER- mouse 4T1 cell line found that PREX1 expression was reduced in tumor cells that had metastasized to the bone compared to the primary tumor (18). Taking our data into account, these data suggest that PREX1 may play a different role in ER- disease or that PREX1 is important for tumor cell dissemination to bone but is dispensable for growth in the bone.

Strikingly, MCF7b cells grew poorly following re-inoculation in the primary tumor site despite having enhanced PREX1 mRNA expression at the experimental endpoint and efficiently disseminating to the bone. These data are in support of previously published work showing that PREX1 does not affect *in vitro* proliferation or activation of ERK signaling in breast (192), melanoma (193), or glioblastoma cancer cells (194). Additionally, PREX1 did not alter primary tumor growth in a prostate cancer xenograft model, but did enhance dissemination of tumor cells to the lymph nodes (187) suggesting that PREX1 mediates cell motility rather than cell

proliferation. However, several reports implicate PREX1 in activating IGF-1R/InsR (185), PI3K/AKT (183), and MEK/ERK (183, 195) signaling following growth factor stimulation *in vitro* and that this signaling activation promotes primary tumor growth *in vivo* (181, 183). Many of these studies were performed using exogenous PREX1 expression in ER- tumor cells, namely MDA-MB-231b cells, which do not endogenously express PREX1. Therefore, it is difficult to determine whether these results are physiologically relevant and if other endogenous genetic alterations are confounding factors. In regards to the MCF7b cells, it is also possible that tumor-inhibitory mechanisms are increased in MCF7b cells and may override PREX1 upregulation to prevent primary tumor development. Herein, we demonstrate using flow cytometry and qPCR analyses that MCF7b cells selectively disseminate to skeletal sites from the primary site and are modestly less capable of disseminating to the lung. In addition to these methods, we also attempted pan-cytokeratin immunostaining on the tibiae and lymph nodes of these mice but did not detect any tumor cells in these tissues, likely due to the tumor burden being below the level of detection by this method (data not shown). Overt bone metastases did not develop during the 8-week experimental timeline in the mice harboring MCF7b primary tumors, despite the presence of tumor cells in the bone marrow. However, these results are not surprising given the particularly long latency period (18-22 weeks) prior to the development of overt metastases in the intracardiac study. While this latency period accurately recapitulates human ER+ disease, given the side effects of exogenous estrogen that limit our ability to take the primary tumor models out to a longer timeline, it remains unclear whether spontaneously disseminated MCF7b cells in the bone would eventually progress into overt metastases.

Evaluation of PREX1 expression in breast cancer patient samples has also generated conflicting results. In support of our findings, PREX1 levels were increased in primary breast and prostate tumors of patients who developed distant or lymph node metastases compared to those that did not harbor metastases (181, 187). Using a limited cohort of 36 patients, high PREX1 expression was associated with reduced disease-free survival (185). In contrast, PREX1 expression was associated with improved patient outcome in a study of 2000 breast cancer patients (196). Overall survival in patients harboring PREX1 genetic alterations or those specifically harboring amplification/upregulation of PREX1 was not significantly changed in the two datasets we investigated using cBioPortal for Cancer Genomics (data not shown). Marotti et al. reported reduced PREX1 levels by immunohistochemistry in bone metastases compared to visceral metastasis (182). Importantly, this patient cohort contained ~50 patients and PREX1 expression varied greatly between patients, independent of tumor subtype, making it difficult to interpret PREX1 expression in site-specific metastasis.

In summary, the human ER+ MCF7b cell line represents a clinically relevant model that recapitulates the spontaneous dissemination and prolonged latency period of ER+ breast cancers and preferentially metastasizes to bone. MCF7b cells exhibit enhanced metastatic potential *in vitro*, which our data suggest is driven by upregulation of PREX1. These findings are consistent with elevated PREX1 levels in breast cancer patients, particularly those with ER+ tumors, being associated with distant metastasis. These findings provide a novel animal model in which to investigate tumor cell dissemination to bone and implicate PREX1 in driving bone metastasis.

CHAPTER V

REGULATION OF LIFR AND DORMANCY BY HDAC INHIBITORS IN BREAST CANCER CELLS THAT HOME TO THE BONE

Introduction

Histone modifications play a key role in the epigenetic regulation of gene expression and are predominantly controlled by the balance of histone acetyltransferases (HATs) and histone deacetylases (HDACs). Aberrant expression and activity of HDACs are frequently observed in cancer and result in pro-tumorigenic effects such as proliferation, angiogenesis, and metastasis (197). Thus, HDAC inhibitors (HDACi) have recently emerged as promising cancer therapeutics and have been shown to induce differentiation, cell cycle arrest, and apoptosis (198). Several HDACi are currently FDA approved for hematological malignancies, and more are in clinical trials for the treatment of early, advanced, and metastatic breast cancer (199). Due to the limited preclinical and clinical studies using HDACi, little is known about their effects on disseminated tumor cells and metastatic progression.

Leukemia inhibitory factor (LIF) receptor (LIFR) was previously identified as a breast tumor suppressor and metastasis suppressor (75, 76). Recent evidence indicates that activation of LIFR and downstream STAT3 signaling maintains tumor cells in a dormant state (74). Further, loss of this signaling axis results in enhanced tumor cell proliferation and bone destruction in experimental models of metastasis (74). Currently, the upstream regulators of LIFR expression and activity remain unclear; however, recent studies suggest that histone deacetylase inhibitors (HDACi) stimulate LIFR expression in breast cancer cells (74, 200).

Breast cancer remains the most commonly diagnosed cancer and second leading cause of cancer deaths in women. Over the past decade, genomic studies have provided considerable insights into the molecular landscape of primary breast tumors leading to novel treatment strategies and improved patient survival (10, 11). Despite these advances, a large proportion of breast cancer patients will subsequently develop distant metastases particularly to the bone, lung, or liver for which effective treatment options are limited (57, 58).Recent evidence suggests that tumor cells disseminate to these distant sites early in tumor progression where they may remain in a dormant state for a prolonged period before developing into a clinically detectable metastasis (7, 8). Approximately 70% of breast cancers are positive for estrogen receptor (ER+) and tend to metastasize to bone over visceral organs (176). Based on clinical observations, time to recurrence appears to be associated with estrogen receptor (ER) status, but the mechanism

for this remains unknown. Specifically, patients diagnosed with ER- disease often present with skeletal metastasis within 5 years, whereas those diagnosed with ER+ tumors exhibit a longer latency period of 8-10 years prior to bone relapse. These findings suggest that all breast cancer patients are at significant risk of developing bone metastasis, but that tumor dormancy may be regulated by subtype-specific mechanisms. Importantly, the molecular mechanisms underlying tumor cell colonization of distant sites and effective therapies to target these dormant disseminated tumor cells remain largely unknown and warrant further investigation.

Our studies aimed to determine whether HDACi activate a pro-dormancy program through enhanced LIFR signaling and represent a viable therapeutic strategy to maintain tumor cells in a dormant state. In this chapter, we examined the molecular mechanisms by which HDACi stimulate LIFR and other pro-dormancy genes in cells with low and high metastatic potential. Additionally, we investigated the clinical relevance of these dormancy-associated genes in two independent breast cancer patient cohorts and in an experimental model of bone metastasis. Together, our data indicate that HDACi stimulate expression of numerous dormancy associated genes and may be an effective approach to maintain tumor cells in a persistent state of dormancy and reduce tumor recurrence.

Results

HDAC inhibitors stimulate LIFR expression in breast cancer cells of varying metastatic potential

We first sought to test a panel of diverse HDACi with varying structural for their ability to stimulate LIFR expression. This panel consisted of entinostat, panobinostat, romidepsin, and vorinostat, which are FDA-approved and/or currently in Phase III clinical trials for metastatic breast cancer. HDACi treatment of human breast cancer cell lines with low (MCF7, SUM159) and high (MDA-MB-231b (bone metastatic clone)) metastatic potential significantly increased *LIFR* mRNA expression between 6 and 24 hours in a dose-dependent manner (Figure 28A-D and Figure 29A). Similar results were observed in mouse mammary carcinoma cells of varying metastatic potential (low metastatic potential = D2.0R (141); high metastatic potential = D2A1, 4T1BM2) (Figure 30A-C). Notably, each HDACi stimulated *LIFR* expression in all the breast cancer cell lines tested. Consistent with these findings, LIFR protein levels were also induced during this time period (Figure 28E-J, Figure 29B, and Figure 30D-F).

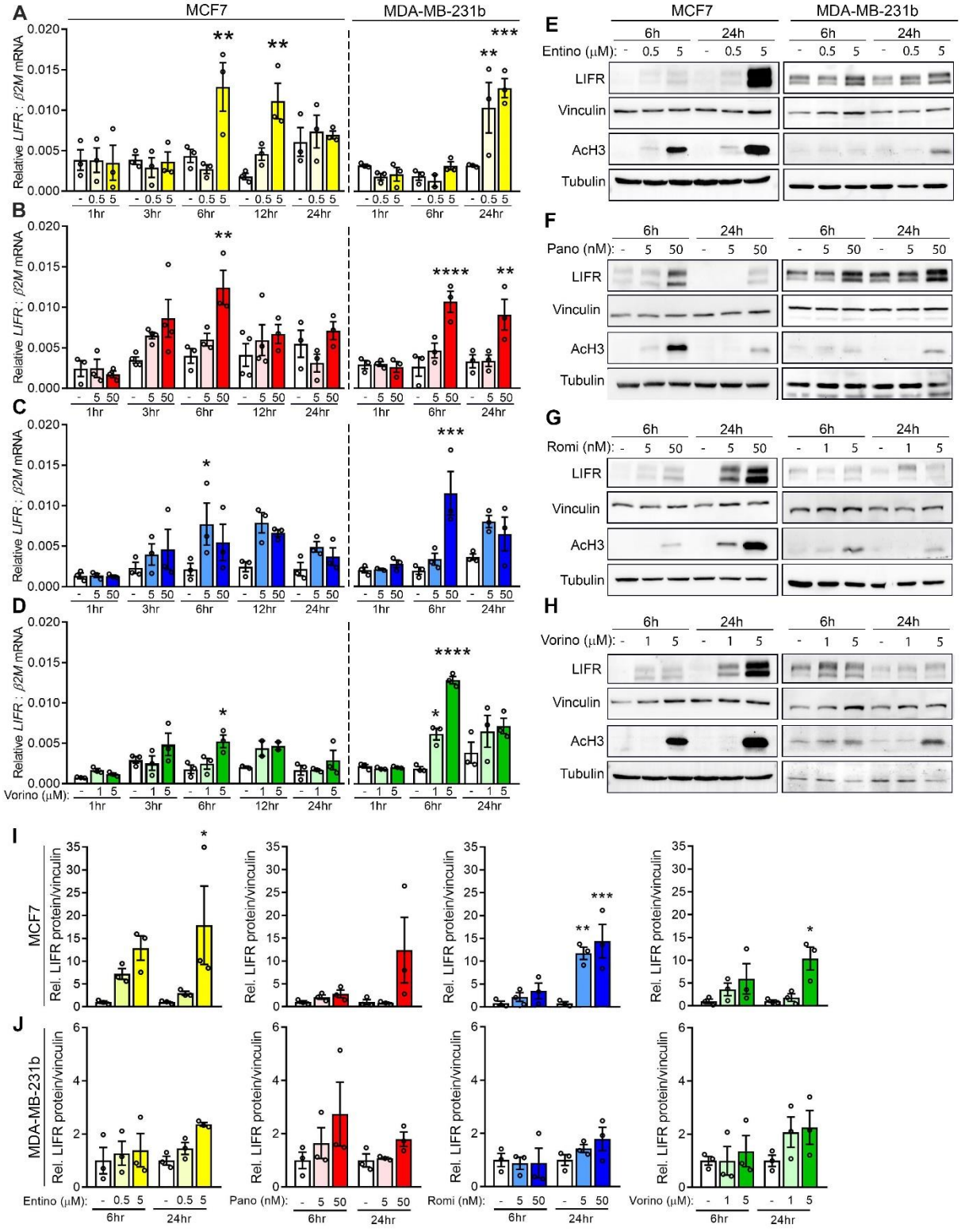
A
MCF7
MDA-MB-231b
Relative LIFR : β2M mRNA
0.020
0.015
0.010
0.005
0.000
- 0.5 5
1hr
3hr
6hr
12hr
24hr
B
- 5 50
C
D
Vorino (μM): - 1 5
E
MCF7
MDA-MB-231b
6h
24h
Entino (μM): - 0.5 5
LIFR
Vinculin
AcH3
Tubulin
F
Pano (nM): - 5 50
G
Romi (nM): - 5 50 - 1 5
H
Vorino (μM): - 1 5
I
MCF7
Rel. LIFR protein/vinculin
J
MDA-MB-231b
Entino (μM): - 0.5 5
Pano (nM): - 5 50
Romi (nM): - 5 50
Vorino (μM): - 1 5

Figure 28. HDAC inhibitors induce LIFR mRNA and protein expression in breast cancer cells. (A-D) LIFR mRNA levels in MCF7 and MDA-MB-231b cells treated with (A) 0.5μM or 5μM entinostat, (B) 5nM or 50nM panobinostat, (C) 5nM or 50nM romidepsin, (D) 1μM or 5μM vorinostat or DMSO (vehicle control) for 1, 3, 6, 12, or 24 hours. (E-H) Representative western blots for LIFR, acetylated histone H3 (AcH3), vinculin (loading control), and tubulin (loading control) protein levels in MCF7 and MDA-MB-231b cells treated with (E) 0.5μM or 5μM entinostat, (F) 5nM or 50nM panobinostat, (G) 5nM or 50nM romidepsin, (H) 1μM or 5μM vorinostat or DMSO (vehicle control) for 6 or 24 hours. (I, J) Quantitation of LIFR protein levels from western blots described in E-H for (I) MCF7 and (J) MDA-MB-231b cells. n=three independent biological replicates for qPCR and western blots. Bar graphs = mean +/- standard error of the mean. A-D, I, J: One-way ANOVA with Sidak's multiple comparisons test, *$p<0.05$, **$p<0.01$, ***$p<0.001$ and ****$p<0.0001$.

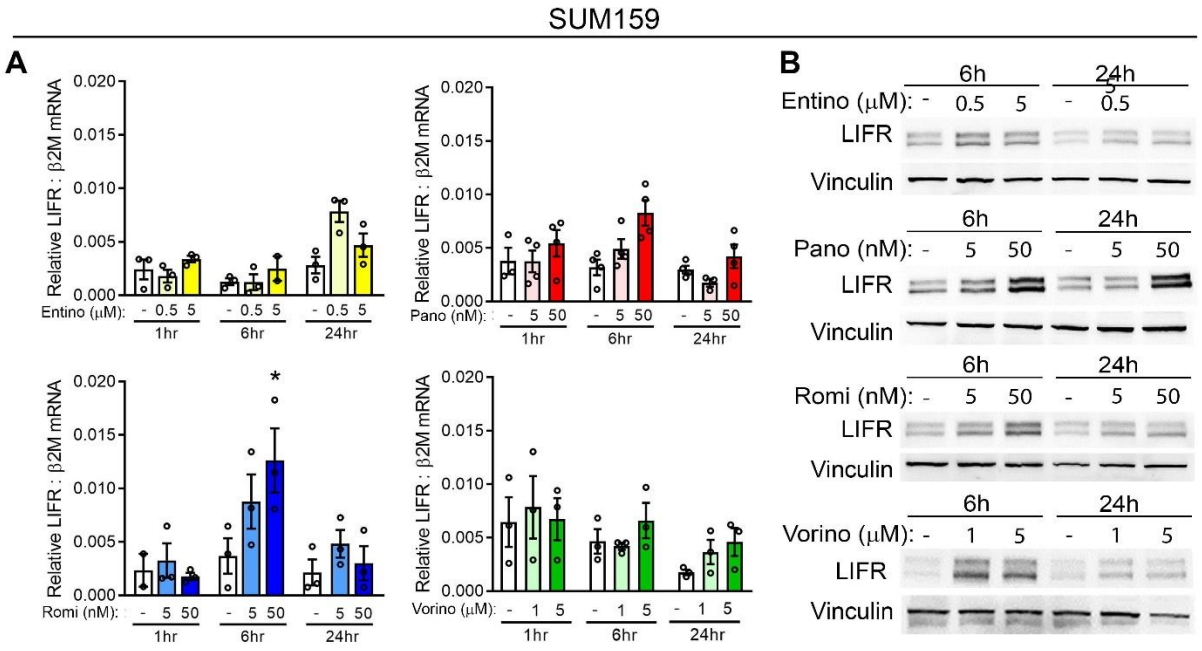

Figure 29. HDAC inhibitors induce LIFR mRNA and protein expression in SUM159 cells. (A) LIFR mRNA levels in SUM159 cells treated with 0.5μM or 5μM entinostat, 5nM or 50nM panobinostat, 5nM or 50nM romidepsin, 1μM or 5μM vorinostat or DMSO (vehicle control) for 1, 6, or 24 hours. (B) Representative western blots for LIFR and vinculin (loading control) protein levels in SUM159 cells treated with 0.5μM or 5μM entinostat, 5nM or 50nM panobinostat, 5nM or 50nM romidepsin, 1μM or 5μM vorinostat, or DMSO (vehicle control) for 6 or 24 hours. n=three independent biological replicates for qPCR and western blots. Bar graphs = mean +/- standard error of the mean. A: One-way ANOVA with Sidak's multiple comparisons test, *p<0.05.

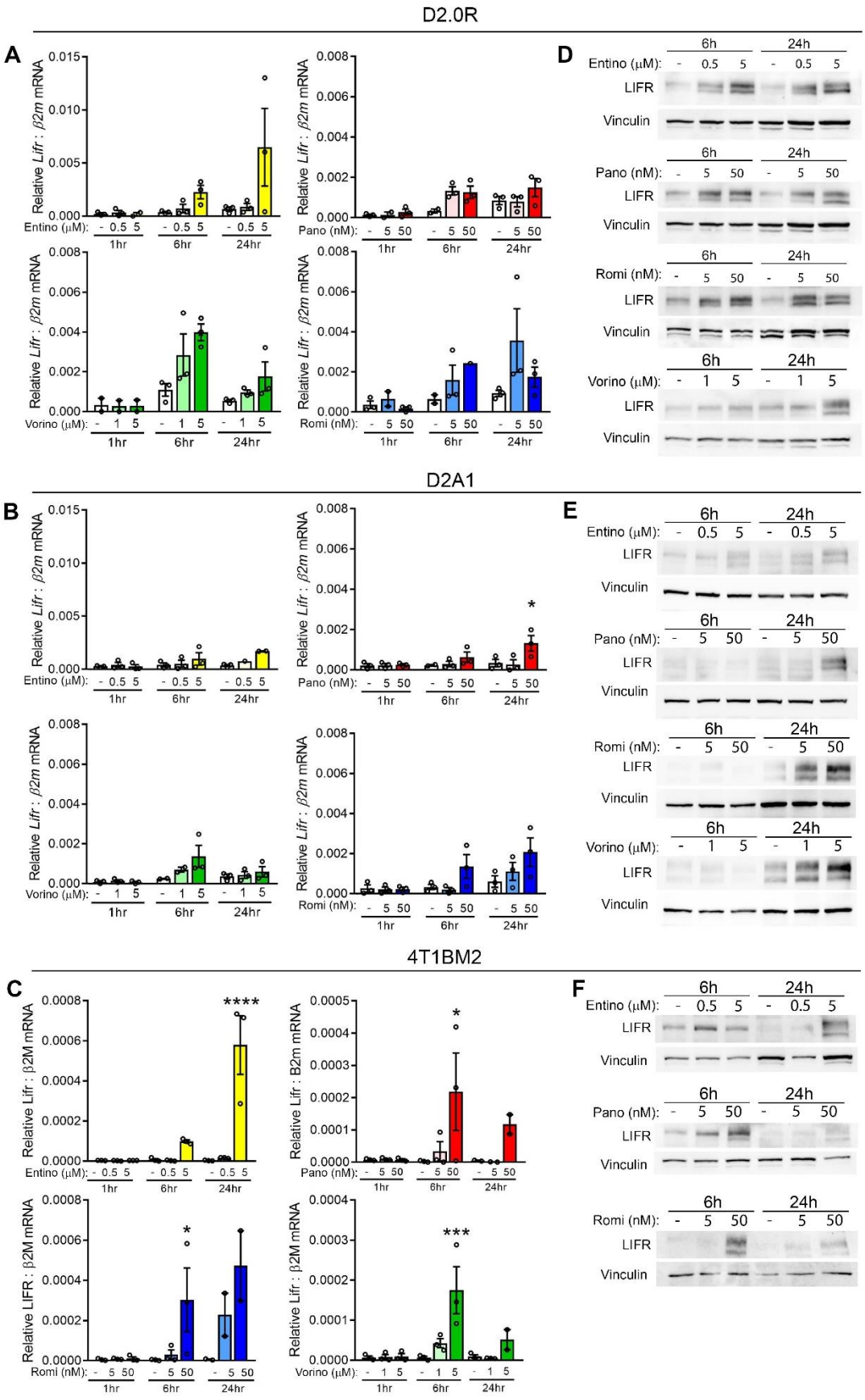
D2.0R
D2A1
4T1BM2
A
B
C
D
E
F
Relative Lifr : β2m mRNA
Relative LIFR : β2M mRNA
Relative Lifr : B2m mRNA
Relative Lifr : β2M mRNA
Entino (μM): - 0.5 5
Pano (nM): - 5 50
Romi (nM): - 5 50
Vorino (μM): - 1 5
1hr
6hr
24hr
6h
24h
LIFR
Vinculin
****
***
*

Figure 30. HDAC inhibitors induce LIFR mRNA and protein expression in mouse mammary carcinoma cells. (A-C) LIFR mRNA levels in (A) D2.0R, (B) D2A1, and (C) 4T1BM2 cells treated with 0.5μM or 5μM entinostat, 5nM or 50nM panobinostat, 5nM or 50nM romidepsin, 1μM or 5μM vorinostat, or DMSO (vehicle control) for 1, 6, or 24 hours. (D-F) Representative western blots for LIFR and vinculin (loading control) protein levels in (D) D2.0R, (E) D2A1, and (C) 4T1BM2 treated with 0.5μM or 5μM entinostat, 5nM or 50nM panobinostat, 5nM or 50nM romidepsin, 1μM or 5μM vorinostat, or DMSO (vehicle control) for 6 or 24 hours. n=three independent biological replicates for qPCR and western blots. Bar graphs = mean +/- standard error of the mean. A-C: One-way ANOVA with Sidak's multiple comparisons test, *p<0.05, **p<0.01, ***p<0.001 and ****p<0.0001.

To explore the molecular mechanism by which HDACi stimulate LIFR expression, breast cancer cells were treated with HDACi for 24 hours followed by removal of the drug for 24-48 hours. Following withdrawal, LIFR protein rapidly returned to basal levels suggesting dynamic and reversible regulation of LIFR expression by HDACi (Figure 31A, B). We postulated that HDACi may directly promote *LIFR* transcriptional activation by altering the acetylation levels along the LIFR promoter. To test this possibility, we performed ChIP-qPCR for acetylated histone H3 lysine 9 (H3K9ac), a marker of active promoters, along *LIFR* transcript variant 1 (*LIFRv1*) or variant 2 (*LIFRv2*) in MCF7 and MDA-MB-231b cells (Figure 31C). MCF7 cells treated with HDACi for 6 hours showed significant enrichment of H3K9ac along the *LIFR*v1 promoter compared to vehicle treated cells (Figure 31D, E). High basal H3K9ac of the *LIFR*v1 promoter was observed in MDA-MB-231b cells, which was not enhanced with HDACi treatment (Figure 31F, G). These findings are consistent with the high LIFR protein expression in these cells; however, MDA-MB-231b cells do not express a functional LIFR since they do not induce downstream signaling in response to ligand stimulation (74, 200). Notably, basal *LIFR*v2 mRNA expression is very low or undetectable and is not induced with HDACi (Figure 32A-C), explaining the lack of promoter acetylation observed for *LIFR*v2 (Figure 31D-G). We next explored whether induction of LIFR by HDACi resulted in enhanced downstream signaling. MCF7 cells stimulated with recombinant LIF and HDACi showed increased STAT3 activation compared to LIF treatment alone (Figure 31H). This enhanced signaling was not due to HDACi-mediated changes in total STAT3 protein levels or STAT3 promoter acetylation (Figure 31J, K and Figure 32D-E). Interestingly, HDACi treatment re-sensitized MDA-MB-231b cells to LIF stimulation, resulting in dramatic STAT3 phosphorylation (Figure 31I). A similar response has been previously reported for MDA-MB-231 cells treated with vorinostat (200) suggesting that numerous HDACi can re-sensitize cells to the ligand.

HDAC inhibitors promote a pro-dormancy program that is mediated by LIFR

To determine whether HDACi promote a pro-dormancy program, we investigated a panel of thirteen dormancy-promoting factors (61, 69, 201-204) following HDACi treatment (Figure 33A). In contrast to the consistent induction of LIFR by all four HDACi in all cell lines tested, we observed cell line-specific and drug-specific stimulation of the other pro-dormancy genes in MCF7 and MDA-MB-231b cells (Figure 33B, C). For example, panobinostat stimulated *AMOT* and *MSK1* expression in MCF7 cells, but *THBS1* and *P4HA1* in MDA-MB-231b cells (Figure 33B, C). Genes that were not changed are not shown, and of important note, HDACi treatment did not significantly reduce the expression of any dormancy-associated genes

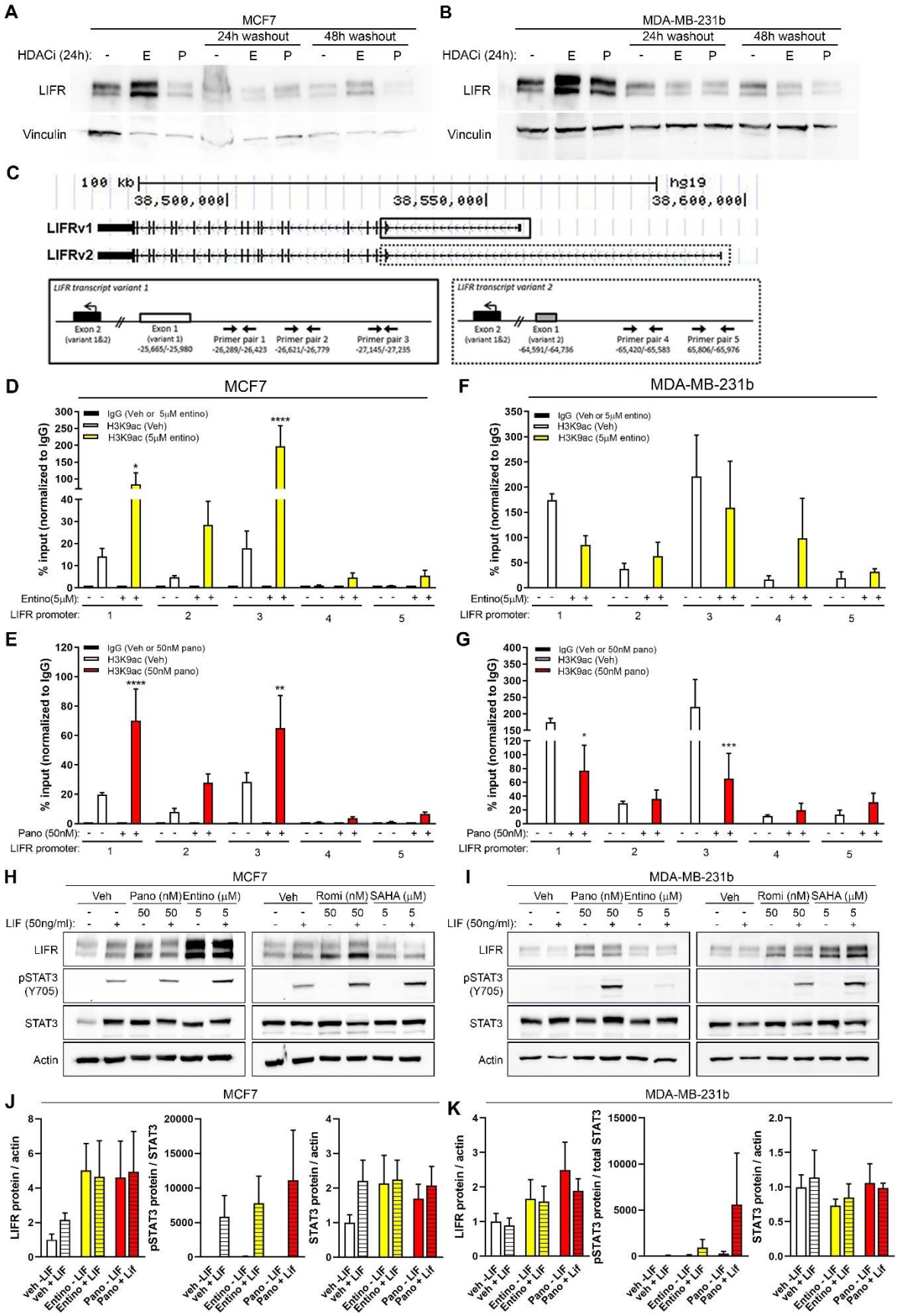
A
MCF7
24h washout
48h washout
HDACi (24h): - E P - E P - E P
LIFR
Vinculin
B
MDA-MB-231b
24h washout
48h washout
HDACi (24h): - E P - E P - E P
LIFR
Vinculin
C
100 kb
hg19
38,500,000
38,550,000
38,600,000
LIFRv1
LIFRv2
LIFR transcript variant 1
Exon 2 (variant 1&2)
Exon 1 (variant 1) -25,665/-25,980
Primer pair 1 -26,289/-26,423
Primer pair 2 -26,621/-26,779
Primer pair 3 -27,145/-27,235
LIFR transcript variant 2
Exon 2 (variant 1&2)
Exon 1 (variant 2) -64,591/-64,736
Primer pair 4 -65,420/-65,583
Primer pair 5 65,806/-65,976
D
MCF7
IgG (Veh or 5μM entino)
H3K9ac (Veh)
H3K9ac (5μM entino)
% input (normalized to IgG)
Entino(5μM):
LIFR promoter: 1 2 3 4 5
F
MDA-MB-231b
IgG (Veh or 5μM entino)
H3K9ac (Veh)
H3K9ac (5μM entino)
% input (normalized to IgG)
Entino(5μM):
LIFR promoter: 1 2 3 4 5
E
IgG (Veh or 50nM pano)
H3K9ac (Veh)
H3K9ac (50nM pano)
% input (normalized to IgG)
Pano (50nM):
LIFR promoter: 1 2 3 4 5
G
IgG (Veh or 50nM pano)
H3K9ac (Veh)
H3K9ac (50nM pano)
% input (normalized to IgG)
Pano (50nM):
LIFR promoter: 1 2 3 4 5
H
MCF7
Veh Pano (nM) Entino (μM) Veh Romi (nM) SAHA (μM)
LIF (50ng/ml):
LIFR
pSTAT3 (Y705)
STAT3
Actin
I
MDA-MB-231b
Veh Pano (nM) Entino (μM) Veh Romi (nM) SAHA (μM)
LIF (50ng/ml):
LIFR
pSTAT3 (Y705)
STAT3
Actin
J
MCF7
LIFR protein / actin
pSTAT3 protein / STAT3
STAT3 protein / actin
veh -LIF
veh + LIF
Entino - LIF
Entino + LIF
Pano - LIF
Pano + Lif
K
MDA-MB-231b
LIFR protein / actin
pSTAT3 protein / total STAT3
STAT3 protein / actin
veh -LIF
veh + LIF
Entino - LIF
Entino + LIF
Pano - LIF
Pano + Lif

Figure 31. Epigenetic regulation of LIFR by HDAC inhibitors and activation of downstream STAT3 signaling. (A, B) Representative western blots for LIFR and vinculin (loading control) in (A) MCF7 and (B) MDA-MB-231b cells treated with 5μM entinostat ("E"), 50nM panobinostat ("P"), or DMSO (vehicle control) for 24 hours followed by drug washout and collection 24 or 48 hours later. (C) UCSC genome browser tracks for *LIFR* variant 1 and 2 and primer pairs used to evaluate promoter acetylation by ChIP-qPCR. Solid lined box indicates primer pairs designed to LIFRv1 and dashed lined box indicates primer pairs designed to LIFRv2. (D, E) ChIP-qPCR showing acetylated histone H3 lysine 9 (H3K9ac) enrichment (% ChIP/input) along the *LIFR* promoter region in MCF7 cells treated with (D) 5μM entinostat, (E) 50nM panobinostat, or DMSO (vehicle control). (F, G) ChIP-qPCR showing acetylated histone H3 lysine 9 (H3K9ac) enrichment (% ChIP/input) along the *LIFR* promoter region in MDA-MB-231b cells treated with (F) 5μM entinostat, (G) 50nM panobinostat, or DMSO (vehicle control). (H-I) Representative western blots for LIFR, pSTAT3 (Y705), total STAT3, and β-actin (loading control) in (H) MCF7 and (I) MDA-MB-231b cells after treatment with 0.5μM or 5μM entinostat, 5nM or 50nM panobinostat, 5nM or 50nM romidepsin, 1μM or 5μM vorinostat, or DMSO (vehicle control) for 24 hours followed by 15 minute treatment with PBS (vehicle control) or recombinant LIF (50ng/ml).(J, K) Quantitation of LIFR, pSTAT3/total STAT3, and STAT3 protein levels in (J) MCF7 and (K) MDA-MB-231b cells from western blots shown in (H, I). n=two independent biological replicates for washout and cytokine treatment western blots and n=three independent biological replicates for ChIP-qPCR. Bar graphs = mean +/- standard error of the mean. D-G: One-way ANOVA with Sidak's multiple comparisons test, *p<0.05, **p<0.01, ***p<0.001 and ****p<0.0001.

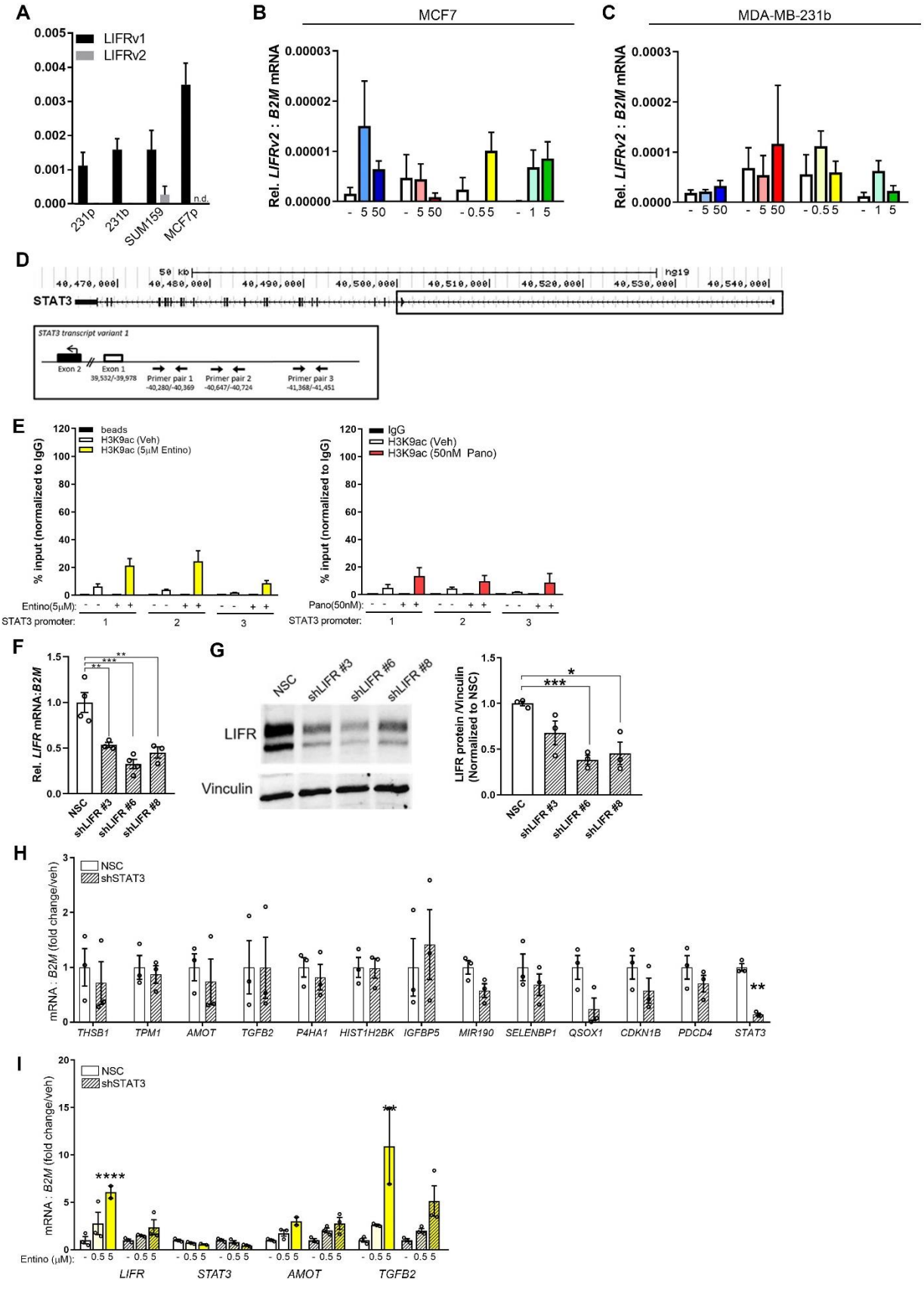
A
LIFRv1
LIFRv2
231p
231b
SUM159
MCF7p
n.d.
B
MCF7
Rel. LIFRv2 : B2M mRNA
C
MDA-MB-231b
D
STAT3
STAT3 transcript variant 1
Exon 2
Exon 1
Primer pair 1
Primer pair 2
Primer pair 3
E
beads
H3K9ac (Veh)
H3K9ac (5μM Entino)
IgG
H3K9ac (50nM Pano)
% input (normalized to IgG)
Entino(5μM):
Pano(50nM):
STAT3 promoter:
F
Rel. LIFR mRNA:B2M
G
NSC
shLIFR #3
shLIFR #6
shLIFR #8
LIFR
Vinculin
LIFR protein /Vinculin (Normalized to NSC)
H
shSTAT3
mRNA : B2M (fold change/veh)
THSB1
TPM1
AMOT
TGFB2
P4HA1
HIST1H2BK
IGFBP5
MIR190
SELENBP1
QSOX1
CDKN1B
PDCD4
STAT3
I
Entino (μM):
LIFR
STAT3
AMOT
TGFB2

Figure 32. LIFR variant 2 is not stimulated by HDAC inhibitors and STAT3 does not mediate induction of pro-dormancy genes. (A) *LIFR* variant 1 (*LIFR*v1) and variant 2 (*LIFR*v2) mRNA levels in MDA-MB-231 parental (231p), bone metastatic MDA-MB-231b (231b), SUM159, and MCF7 cells. (B, C) *LIFR*v2 mRNA levels in (B) MCF7 and (C) MDA-MB-231b cells treated with 0.5μM or 5μM entinostat, 5nM or 50nM panobinostat, 5nM or 50nM romidepsin, 1μM or 5μM vorinostat, or DMSO (vehicle control) for 6 hours. (D) UCSC genome browser tracks for *STAT3* and primer pairs used to evaluate promoter acetylation by ChIP-qPCR. (E) ChIP-qPCR showing acetylated histone H3 lysine 9 (H3K9ac) enrichment (% ChIP/input) along the *STAT3* promoter region in MCF7 cells treated with 5μM entinostat, 50nM panobinostat, or DMSO (vehicle control). (F) mRNA levels of LIFR in MCF7 non-silence control (NSC) and LIFR knockdown lines (#3, #6, #8). (G) Representative western blot of LIFR and vinculin (loading control) and quantitation of LIFR protein levels in MCF7 NSC and LIFR knockdown lines. (H) mRNA levels of dormancy associated genes in MCF7 NSC (control) and MCF7 STAT3 knockdown (shSTAT3) cells. (I) mRNA levels of dormancy associated genes in MCF7 NSC or MCF7 shSTAT3 cells treated with 0.5μM or 5μM entinostat or DMSO (vehicle control). n=two independent biological replicates for qPCR of LIFRv1/LIFRv2 and STAT3 knockdown experiments. n=three independent biological replicates for ChIP-qPCR and LIFR knockdown experiments. Bar graphs = mean +/- standard error of the mean. A, H: Unpaired t-test. F, G, I: One-way ANOVA with Sidak's multiple comparisons test, *p<0.05, **p<0.01, ***p<0.001 and ****p<0.0001.

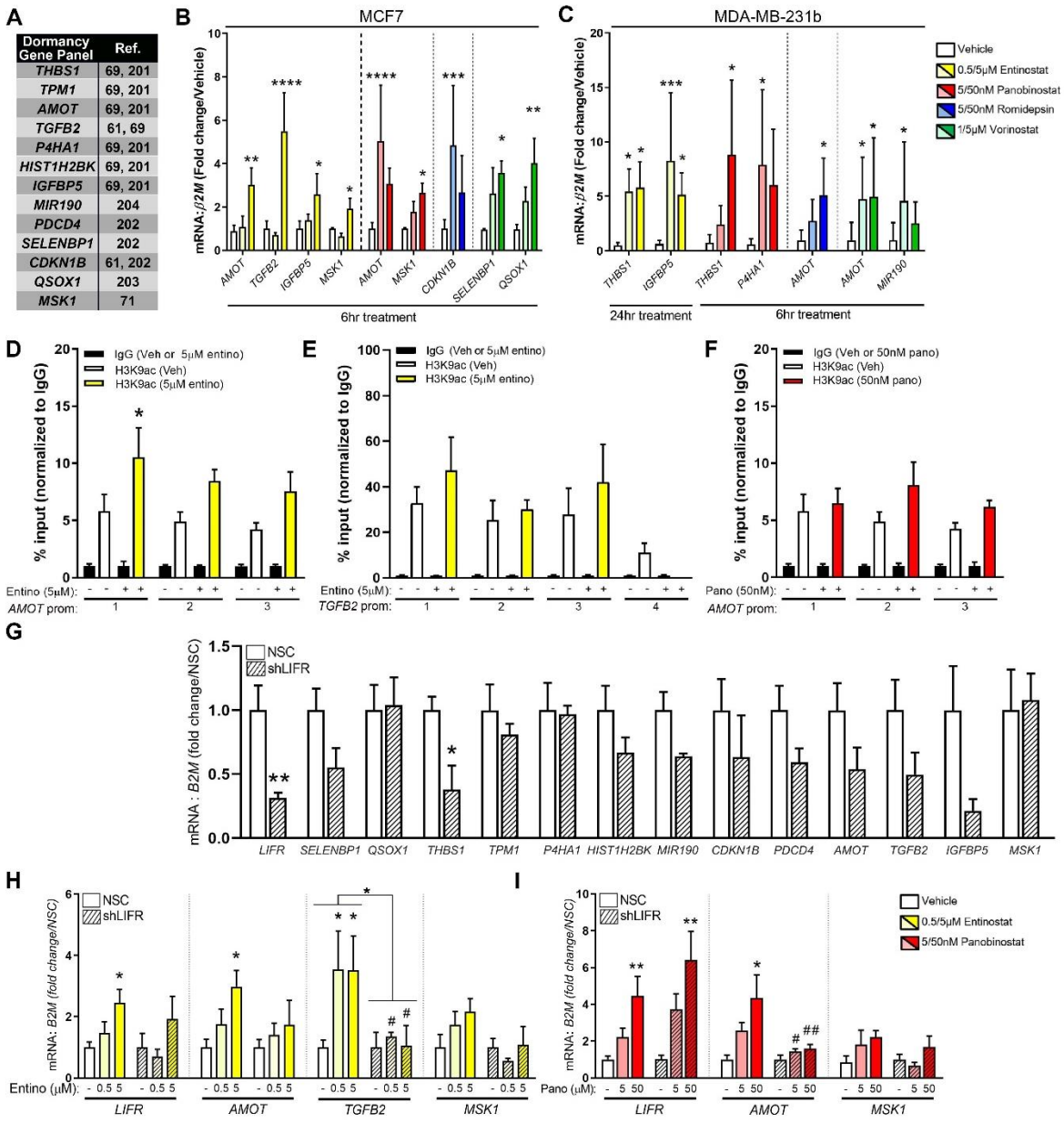

Figure 33. HDACi stimulation of a pro-dormancy gene program is mediated by LIFR. (A) List of thirteen genes and references included in the dormancy associated gene panel. (B) mRNA levels of significantly altered dormancy genes in (B) MCF7 and (C) MDA-MB-231b cells treated with 0.5μM or 5μM entinostat, 5nM or 50nM panobinostat, 5nM or 50nM romidepsin, 1μM or 5μM vorinostat, or DMSO (vehicle control) for 6 or 24 hours. (D-F) ChIP-qPCR showing acetylated histone H3 lysine 9 (H3K9ac) enrichment (% ChIP/input) along the *AMOT* or *TGFB2* promoters in MCF7 cells treated with (D, E) 5μM entinostat or (F) 50nM panobinostat for 6 hours. (G) mRNA levels of dormancy associated genes in MCF7 NSC (control) and MCF7 LIFR knockdown (shLIFR) cells. (H, I) mRNA levels of dormancy associated genes in MCF7 NSC or MCF7 shLIFR cells treated with (H) 0.5μM or 5μM entinostat or (I) 5nM or 50nM panobinostat. n=three independent biological replicates for qPCR and ChIP-qPCR. Bar graphs = mean +/- standard error of the mean. B-F, H, I: One-way ANOVA with Sidak's multiple comparisons test, *p<0.05, **p<0.01, ***p<0.001 and ****p<0.0001. G: Mann-Whitney t-test, *p<0.05, **p<0.01.

included in the panel (data not shown). Interestingly, *AMOT* expression was increased by multiple HDACi in both MCF7 and MDA-MB-231b cells. Further, entinostat-stimulated *TGFB2* expression was particularly intriguing given its role in stem cell reprogramming (205) and promoting dormancy in the bone (61, 72).To further investigate how *AMOT* and *TGFB2* are stimulated, we performed ChIP-qPCR to determine if promoter acetylation was altered following HDACi treatment. Surprisingly, H3K9ac was not dramatically enriched along these promoters following HDACi treatment, suggesting an indirect mechanism (Figure 33D-F). These results led us to explore whether LIFR is required for the induction of these other dormancy-associated factors. To do so, we assessed LIFR expression in a previously published LIFR knockdown MCF7 line (shLIFR #3) (74) as well as in two newly generated knockdown lines (shLIFR #6 and #8). LIFR mRNA and protein expression was most dramatically decreased (~65%) in the MCF7 shLIFR#6 line and therefore this line was used for subsequent studies (Figure 32F, G). LIFR knockdown resulted in a modest reduction in 8 out of the 13 pro-dormancy factors (Figure 33G) including *AMOT* and *TGFB2* by ~50%. Further, HDACi treatment of LIFR knockdown cells blunted the induction of *AMOT*, *TGFB2*, and *MSK1* compared to the control cell line (MCF7 NSC) (Figure 33H, I). Knockdown of STAT3 did not significantly alter any of the dormancy genes or blunt HDACi-mediated induction, suggesting that the effects on these dormancy genes are independent of STAT3 activation by LIFR (Figure 32H, I).

Treatment with HDAC inhibitors slows tumor cell proliferation

Since HDACi augmented LIFR and other dormancy-promoting genes, we determined whether HDACi could promote functional outcomes of dormancy. To do this, we monitored tumor cell proliferation in the presence of low-dose HDACi over 48-hour increments for a total of eight days. Proliferation of MCF7 cells was minimally affected during the first 48 hours but was substantially slowed by >3-fold with HDACi treatment between day 2 and day 8 (Figure 34A). During the final 48 hours, the fold-change in proliferation of HDACi-treated cells fell below one (representing the number of cells seeded on day 6) suggesting a subset of cells underwent cell death (Figure 34A). These results are further supported by a small but significant increase in the sub-G0/G1 population, characteristic of apoptotic cells, with HDACi on day 6 and day 8 (Figure 35A). Entinostat significantly increased the G0/G1 population at day 2, but no dramatic cell cycle changes were observed with long-term HDACi treatment (Figure 35B). Albeit to a lesser extent, long-term HDACi treatment significantly slowed MDA-MB-231b cell proliferation but did not appear to induce cell death (Figure 34B).

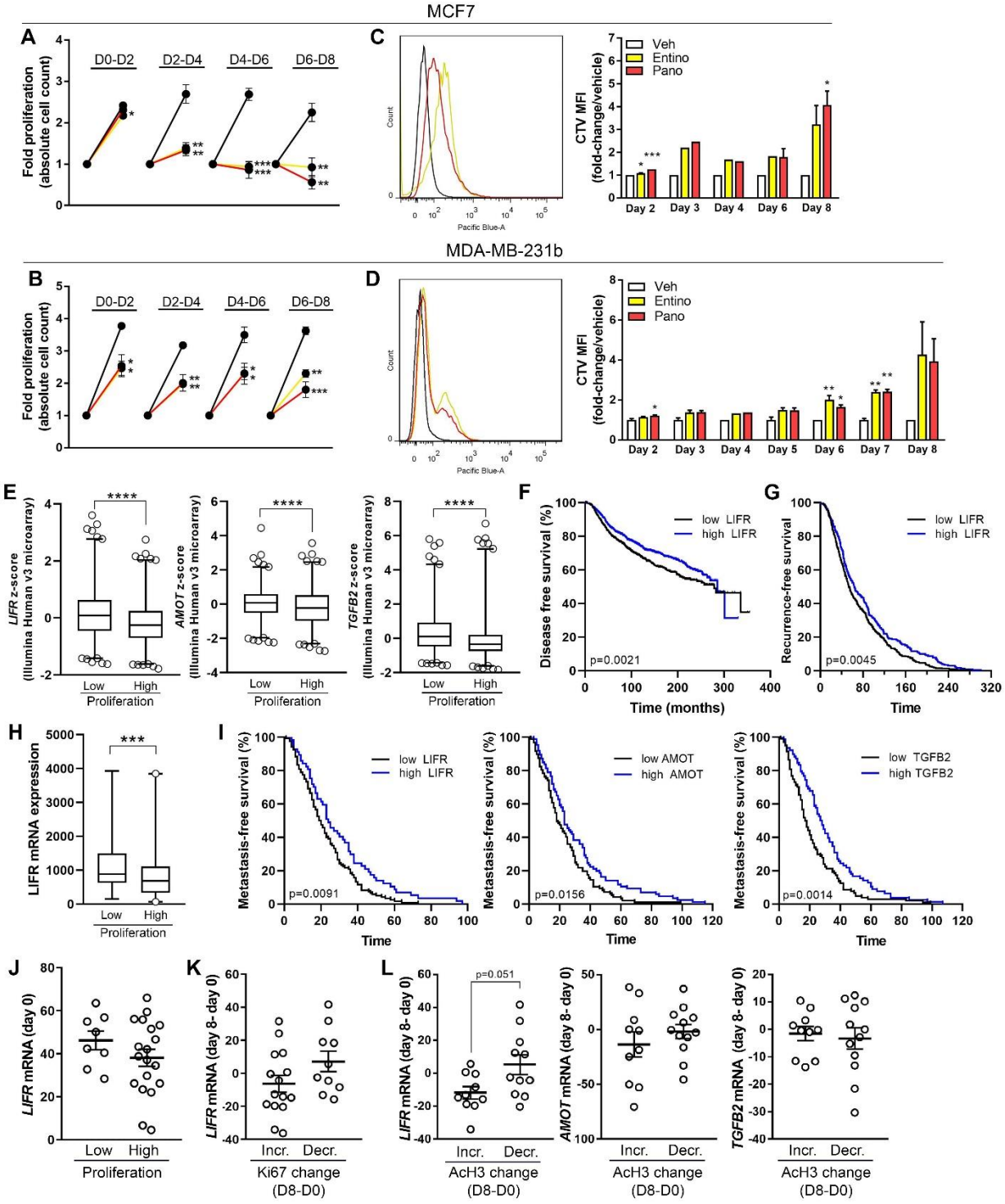
MCF7
A
D0-D2
D2-D4
D4-D6
D6-D8
Fold proliferation (absolute cell count)
C
Count
Pacific Blue-A
CTV MFI (fold-change/vehicle)
Veh
Entino
Pano
Day 2
Day 3
Day 4
Day 6
Day 8
MDA-MB-231b
B
D
Day 5
Day 7
E
LIFR z-score (Illumina Human v3 microarray)
AMOT z-score (Illumina Human v3 microarray)
TGFB2 z-score (Illumina Human v3 microarray)
Low
High
Proliferation
F
Disease free survival (%)
low LIFR
high LIFR
p=0.0021
Time (months)
G
Recurrence-free survival
p=0.0045
Time
H
LIFR mRNA expression
I
Metastasis-free survival (%)
p=0.0091
low AMOT
high AMOT
p=0.0156
low TGFB2
high TGFB2
p=0.0014
J
LIFR mRNA (day 0)
K
LIFR mRNA (day 8- day 0)
Incr.
Decr.
Ki67 change (D8-D0)
L
p=0.051
AcH3 change (D8-D0)
AMOT mRNA (day 8- day 0)
TGFB2 mRNA (day 8- day 0)

Figure 34. Upregulation of a dormancy phenotype inversely correlates with proliferation and metastasis in breast cancer patients. (A, B) Trypan blue exclusion assay to assess fold proliferation in (A) MCF7 and (B) MDA-MB-231b cells treated with 0.5μM entinostat, 5nM panobinostat, or vehicle for a total of eight days. On day 2, 4, 6, and 8, cells were trypsinized and counted followed by reseeding of an equal number of cells per treatment group. Data are presented as fold-proliferation during each 48-hour increment. (C, D) CellTrace Violet proliferation dye was loaded into (C) MCF7 and (D) MDA-MB-231b cells followed by treatment with 0.5μM entinostat, 5nM panobinostat, or vehicle for a total of eight days. Mean fluorescence intensity (MFI) was tracked over eight days using flow cytometry to assess proliferation. n=three independent biological replicates for proliferation and CTV retention experiments. Graphs represent mean +/- standard error of the mean. A-D: Unpaired t-test, *p<0.05, **p<0.01, ***p<0.001 and ****p<0.0001. (E) mRNA levels of *LIFR*, *AMOT*, and *TGFB2* in ER+ breast tumors displaying low or high proliferation (low n=623, high n=603). The data are displayed as z-score values from Illumina Human v3 microarray data (METABRIC, Nature 2012 & Nat Commun 2016). (F) Survival analysis representing the proportion of disease-free patients stratified according to *LIFR* mRNA levels in samples from breast cancer patients (low n=979, high = 999; HR = 1.273; METABRIC, Nature 2012 & Nat Commun 2016 dataset). (G) Analysis of time to recurrence in patients described in (F). (H) *LIFR* mRNA levels in breast tumors displaying low or high proliferation regardless of subtype (low n= 86, high = 106; Bos et. al dataset (GSE12276). (I) Survival analysis representing the proportion of metastasis-free patients stratified according to *LIFR*, *AMOT*, or *TGFB2* mRNA levels in samples from breast cancer patients (*LIFR* low n= 120, high = 57); *AMOT* low = 97, high = 86; *TGFB2* low = 104, high = 78; Bos et. al dataset (GSE12276). (J) *LIFR* mRNA levels pre-treatment (day 0) in tumors displaying low and high proliferation (low n=8, high n=19). (K) *LIFR* mRNA expression change (day 8 – day 0) in tumors that displayed increased or decreased Ki67 levels post-treatment (day 8 – day 0) (low n=15, high = 10). (L) *LIFR*, *AMOT*, or *TGFB2* mRNA expression change (day 8 – day 0) in patients that displayed increased or decreased acetylated histone H3 (AcH3) post-treatment (day 8 – day 0) (low n= 10, high n=12).

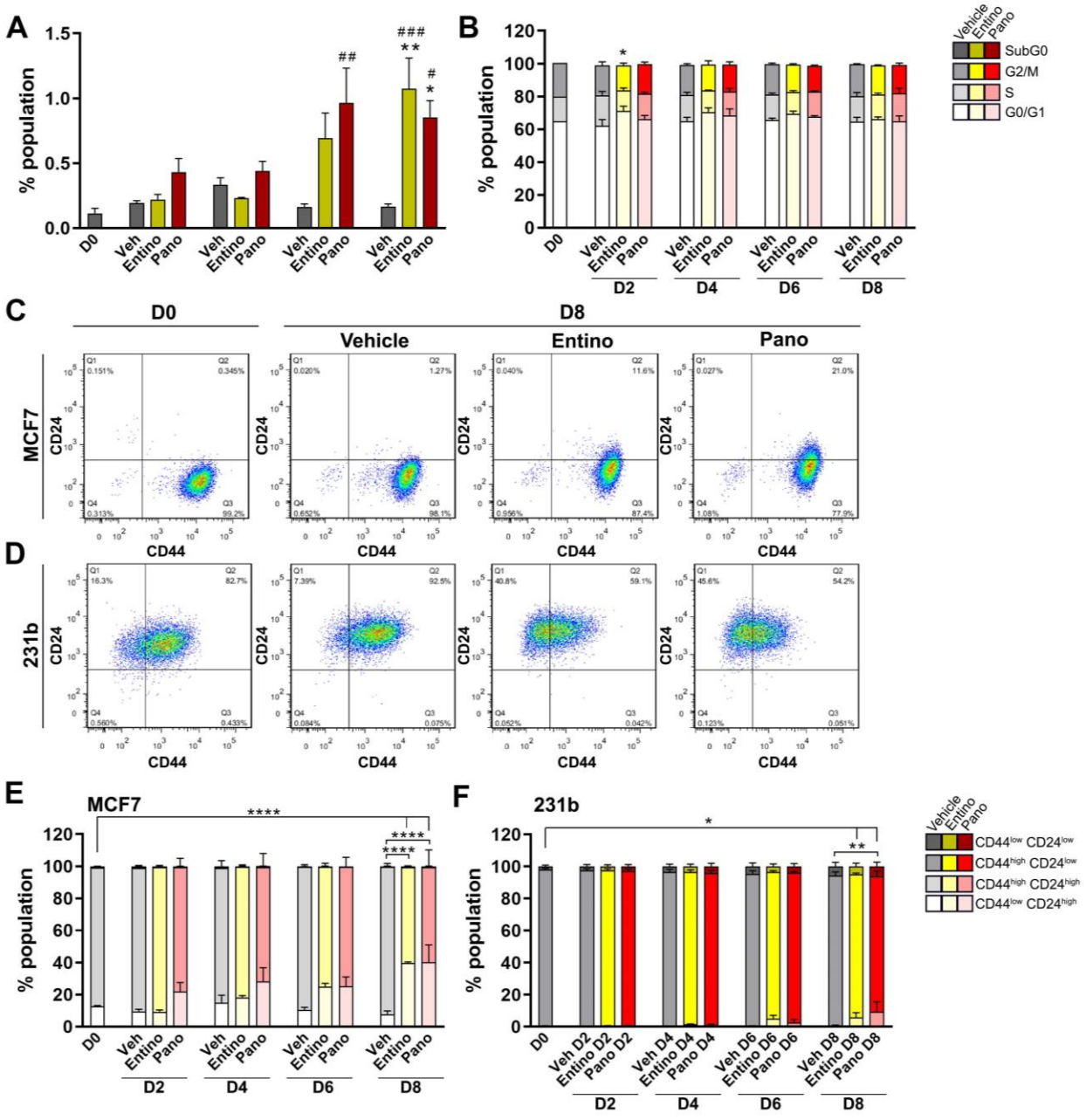

Figure 35. HDAC inhibitors increase cells in the subG0/G1 population but do not alter other cell cycle phases or the cancer stem cell phenotype. (A, B) Fixed cells stained with hoechst 33342 and analyzed by flow cytometry for the (A) subG0/G1 population and (B) G0/G1, S, and G2/M cell cycle phases. (C, D) Representative flow cytometry plots of CD24 and CD44 expression in (C) MCF7 and (D) MDA-MB-231b cells treated with 0.5μM entinostat, 5nM panobinostat, or DMSO (vehicle control) for a total of eight days. Shown are plots from day 0 and day 8. (E, F) Quantitation of flow cytometry data described in (C, D). n=three independent biological replicates for flow cytometry experiments. Bar graphs = mean +/- standard error of the mean. A, B, E, F: One-way ANOVA with Sidak's multiple comparisons test, *p<0.05, **p<0.01, ***p<0.001 and ****p<0.0001.

Given these data, we next sought to determine whether this slowed proliferation was a result of the entire population entering a dormant-like state or equal rates of proliferation and cell death in subsets of the population. To do so, breast cancer cells were loaded with the proliferation dye, CellTrace Violet (CTV) and assessed for dye retention using flow cytometry over eight days of HDACi treatment. Increasing CTV retention was observed over the time course in both MCF7 and MDA-MB-231b cells treated with HDACi (Figure 34C, D). Notably, all MCF7 cells displayed consistent CTV retention indicating that HDACi slowed the proliferation rate of the entire population of cells rather than a subset (Figure 34C). Interestingly, the MDA-MB-231b cells showed two retention peaks on day 8 suggesting that HDACi may differentially affect the proliferation of two subpopulations (Figure 34D). Despite these observations, both populations displayed increased CTV intensity compared to vehicle treated cells. Given the ability of HDACi to reprogram cells and the unfavorable association of cancer stem cells (CSC) with poor prognosis and therapy resistance, we also investigated whether HDACi alter the CSC phenotype, here characterized as $CD24^{Low}/CD44^{High}$ (206, 207). While there was a significant increase in the $CD24^{High}/CD44^{Low}$ population with HDACi treatment, there was no change in the percentage of CSC-like cells (Figure 35C-F).

Upregulation of dormancy-associated genes is inversely associated with proliferation and metastasis in breast cancer patients

Given the stimulation of a pro-dormancy phenotype and decrease in tumor cell proliferation, we next sought to determine the clinical significance of these findings. We specifically investigated *LIFR*, *AMOT*, and *TGFB2* expression in two independent breast cancer patient cohorts for several reasons including their dramatic stimulation by HDACi, possible co-regulation by LIFR, and relevance to tumor dormancy in the bone. In the first patient cohort (METABRIC, Nature 2012 & Nat Commun 2016), tumor proliferation was assessed in ER+ tumors as part of their molecular subtyping classification. Investigation of this dataset revealed significant reductions in mRNA expression of all three pro-dormancy genes in highly proliferative tumors compared to those with low proliferation rates (Figure 34E). Analysis of all primary tumors regardless of proliferation revealed a significant increase in disease-free survival (HR = 1.273, 95% CI: 1.091-1.486) and time to recurrence (HR = 1.262, 95% CI: 1.075-1.483) in patients with high *LIFR* expression (Figure 34F, G). Further, patients with tumor recurrence had significantly lower *LIFR* expression in their primary tumor suggesting an association with metastatic progression (Figure 36A). These data are consistent with previously reported reductions in overall survival in patients with down-regulated LIFR signaling (74). There

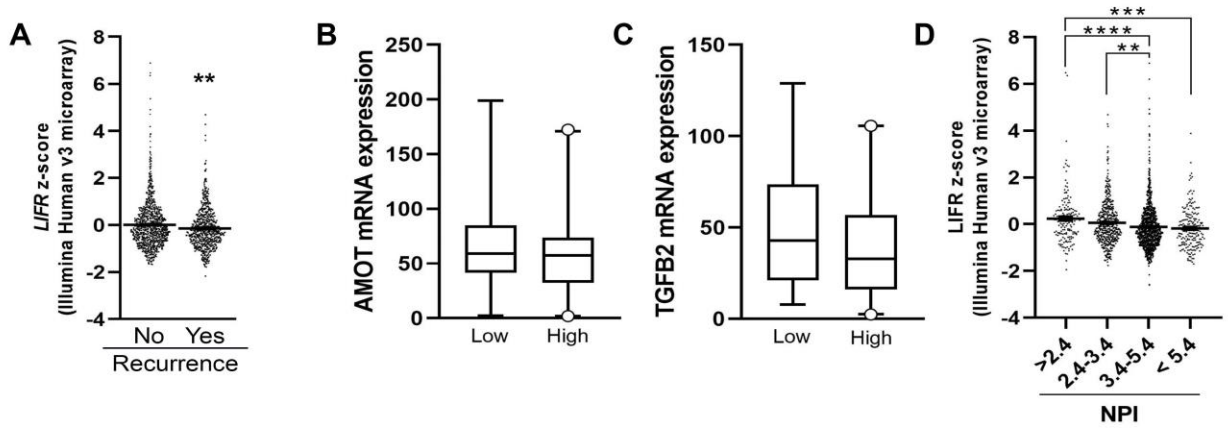

Figure 36. LIFR mRNA levels correlates with prognosis index, recurrence, and proliferation in breast cancer patients. (A, B) mRNA levels of (A) *AMOT* and (B) *TGFB2* tumors displaying low or high proliferation. (C) *LIFR* mRNA levels in breast cancer patients stratified by Nottingham prognostic index (NPI) scores. The data are displayed as z-score values from Illumina Human v3 microarray data (METABRIC, Nature 2012 & Nat Commun 2016). (D) *LIFR* mRNA levels in breast cancer patients stratified by recurrence (no n=1278, yes n=622). The data are displayed as z-score values from Illumina Human v3 microarray data (METABRIC, Nature 2012 & Nat Commun 2016). A: Mann-Whitney t-test, **p<0.01. D: One-way ANOVA with Sidak's multiple comparisons test, **p<0.01, ***p<0.001 and ****p<0.0001

was no significant association of *AMOT* or *TGFB2* expression with these clinical parameters (data not shown). The second patient cohort (Bos et. al dataset (GSE12276)) also revealed a significant reduction in *LIFR* mRNA expression and modest decreases in *AMOT* and *TGFB2* in highly proliferative tumors (Figure 34H and Figure 36B, C). Additionally, decreased *LIFR* expression correlated with increased Nottingham prognostic index scores, which incorporates tumor size, lymph node involvement, and tumor grade to predict patient prognosis following surgery (Figure 36D). Indeed, high expression of *LIFR*, *AMOT*, and *TGFB2* was associated with increased metastasis-free survival in breast cancer patients (*LIFR*: HR=1.486, 95% CI: 1.102-2.004; *AMOT*: HR=1.409, 95% CI: 1.052-1.885; *TGFB2*: HR=1.583, 95% CI: 1.182-2.119; Bos et. al dataset (GSE12276)) (Figure 34I). Given the negative association of these genes with metastasis, we sought to investigate whether HDACi could be used to stimulate pro-dormancy genes in breast cancer patients. While few published studies exist, one publicly available dataset investigated gene expression changes in primary breast tumors before and after HDACi treatment (valproic acid; 8 days; Cohen et. al dataset (GSE83530)). In this cohort, *LIFR* mRNA expression was modestly lower in highly proliferative primary tumors prior to HDACi treatment (Figure 34J). Compared to pre-treatment samples, tumors with reduced proliferation rates had significantly higher *LIFR* expression changes after treatment (Figure 34K). Further, patients with increased peripheral blood acetylation levels, an indicator of effective treatment, had higher *LIFR* expression and a modest increase in *AMOT*, but not *TGFB2*, levels post-treatment (Figure 34L). Together, these patient data suggest that high expression of these pro-dormancy genes, which can be therapeutically increased with HDACi, correlates with reduced tumor proliferation and metastasis.

Combination treatment of HDACi with zoledronic acid reduces the incidence of bone metastasis and mitotic index

Given the clinical association of these dormancy-associated genes with metastasis, we next tested whether HDACi promote dormancy in tumor cells that have metastasized to the bone. Mice were inoculated by intracardiac injection and the following day treatment was initiated (Figure 37A). Previous reports (128, 130) and data from our laboratory indicate that HDACi negatively affect normal bone homeostasis (Figure 38A-C). Although we didn't see any changes in osteoclast number (Figure 38C) and were unable to quantify osteoblast number or bone formation rate due to estradiol effects on the bone, other reports indicate that negative HDACi effects on the bone result from increased osteoclast

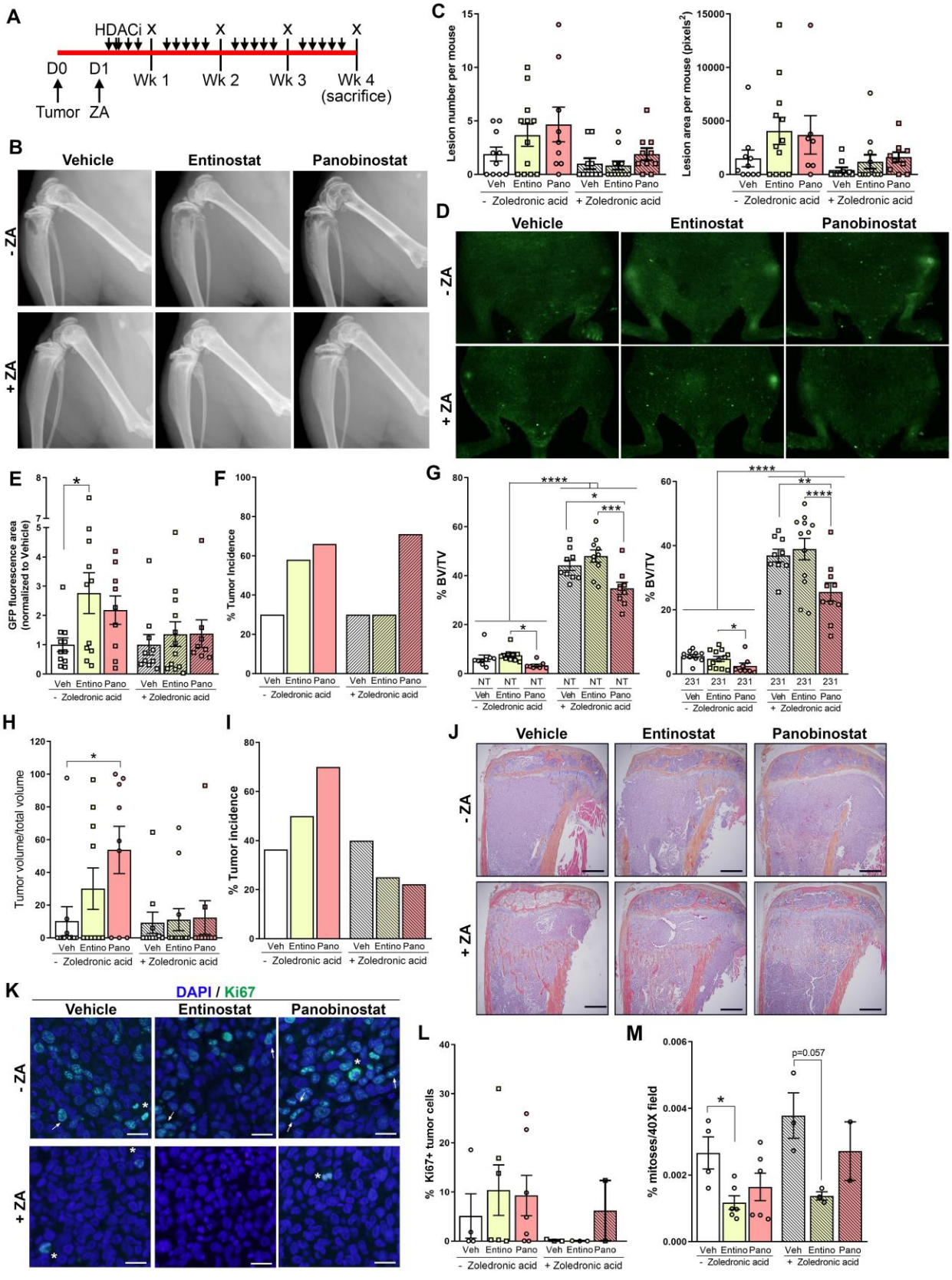
A
HDACi X
X
X
X
D0
D1
Wk 1
Wk 2
Wk 3
Wk 4
(sacrifice)
Tumor
ZA
B
Vehicle
Entinostat
Panobinostat
- ZA
+ ZA
C
Lesion number per mouse
Lesion area per mouse (pixels²)
Veh Entino Pano Veh Entino Pano
- Zoledronic acid + Zoledronic acid
D
Vehicle
Entinostat
Panobinostat
- ZA
+ ZA
E
GFP fluorescence area (normalized to Vehicle)
F
% Tumor Incidence
G
% BV/TV
NT NT NT NT NT NT
231 231 231 231 231 231
H
Tumor volume/total volume
I
% Tumor incidence
J
Vehicle
Entinostat
Panobinostat
- ZA
+ ZA
K
DAPI / Ki67
Vehicle
Entinostat
Panobinostat
- ZA
+ ZA
L
% Ki67+ tumor cells
M
% mitoses/40X field
p=0.057

Figure 37.Combination treatment of HDACi with zoledronic acid reduces tumor incidence and mitotic events in bone-disseminated tumors. (A) Schematic of experimental timeline from intracardiac inoculation of MDA-MB-231b cells (Tumor), injection of zoledronic acid (ZA), treatment with HDAC inhibitors (HDACi) 5X/week, radiographic imaging (x), and sacrifice. n=10-12 mice inoculated per group. (B) Representative radiographs from mice inoculated with MDA-MB-231b cells and treated with HDACi (veh-ZA n=10, entino-ZA n=12, pano-ZA n=9, veh+ZA n=10, entino+ZA n=12, pano+ZA n=10). (C) Radiographic assessment of total lesion number per mouse and total lesion area per mouse over time of mice described in (B). (D) Representative *in vivo* fluorescence images for GFP+ tumor cells in MDA-MB-231b-inoculated mice at endpoint using the CRi Maestro instrument. (E, F) Quantitation of (D) GFP fluorescence area and (E) tumor incidence from images described in (C). (G) microCT analysis of bone volume/total volume (%BV/TV) of non-tumor-inoculated (NT) mice (n=10 mice per group) and MDA-MB-231b-inoculated mice described in (B). (H, I) Analysis of (H) tumor volume/total volume and (I) tumor incidence by histomorphometry of mice described in (B). (J) Representative hematoxylin and eosin (H&E) staining of tibiae from mice described in (B). All panels = 4X and scale bars = 500μm. (K) Representative Ki67 (green) and DAPI (blue) staining of tibiae from mice described in (B). All panels = 40X and scale bars = 20μm. Arrow indicate Ki67+ tumor cells and asterisks indicate mitotic figures. (L) Quantitation of % Ki67+ tumor cells/total tumor cells from images shown in (K). (M) Quantitation of mitoses (# mitotic figures/total cells in 40X field) by DAPI staining from images shown in (K). Bar graphs = mean +/- standard error of the mean. E, G, H, M: One-way ANOVA with Sidak's multiple comparisons test, *p<0.05, **p<0.01, ***p<0.001 and ****p<0.0001.

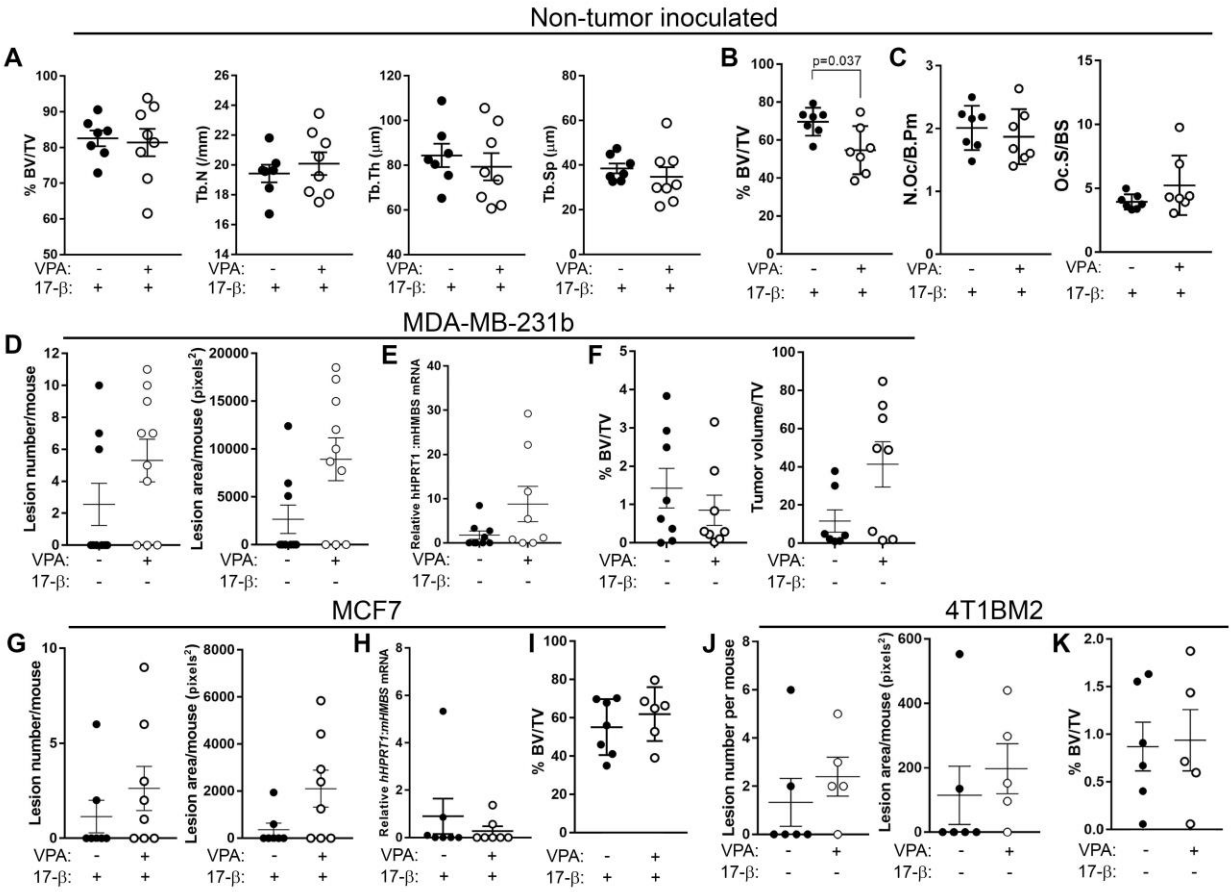

Figure 38. Treatment with HDACi (valproic acid) negatively affects bone and enhances tumor burden. (A) microCT analysis of non-tumor-inoculated mice supplemented with 17β-estradiol and treated with vehicle or valproic acid (VPA) (veh: n=7, VPA: n=9 mice) (B, C) Histomorphometric analysis of (B) bone volume/total volume (%BV/TV) and (C) osteoclast number and surface of mice described in (A). (D) Radiographic assessment of total lesion number per mouse and total lesion area per mouse over time from mice inoculated with MDA-MB-231b cells and treated with vehicle or VPA. (veh: n=8, VPA: 8). (E) qPCR of whole bone homogenate from mice described in (D) for human *B2M* or human *HPRT1* normalized to mouse *Hmbs* (housekeeping gene). (F) Histomorphometric analysis of bone volume/total volume (%BV/TV) and tumor volume/total volume from mice described in (D). (G) Radiographic assessment of total lesion number per mouse and total lesion area per mouse over time from MCF7-inoculated mice supplemented with 17β-estradiol and treated with vehicle or valproic acid (VPA) (veh: n=7, VPA: 8). (H) qPCR of whole bone homogenate from mice described in (G) for human *B2M* or human *HPRT1* normalized to mouse *Hmbs* (housekeeping gene). (I) Histomorphometric analysis of bone volume/total volume (%BV/TV) from mice described in (D). (J) Radiographic assessment of total lesion number per mouse and total lesion area per mouse over time from mice inoculated with 4T1BM2 cells and treated with vehicle or valproic acid (VPA) (veh: n=6, VPA: 5). B: Mann Whitney t-test.

activity and decreased osteoblast number (128, 129). Additionally, HDACi treatment of mice inoculated with MDA-MB-231b, MCF7, or 4T1BM2 cells causes similar negative bone effects and a modest increase in tumor burden (Figure 38D-K). To mitigate these effects, we treated non-tumor inoculated or MDA-MB-231b-inoculated mice with HDACi (entinostat or panobinostat) alone or in combination with the bisphosphonate zoledronic acid (ZA) to block bone resorption (Figure 37A). Radiographic analysis at the endpoint showed a modest increase in lesion number and lesion area in HDACi-treated mice, which was prevented with the addition of ZA (Figure 37B, C). Similarly, *in vivo* fluorescence imaging for GFP+ tumor cells revealed higher GFP fluorescence area and tumor incidence in HDACi treated mice that was also prevented with combination treatment (Figure 37D-F and Figure 39A). Assessment of bone microarchitecture by microcomputed tomography (microCT) and histomorphometry revealed a reduction in bone volume in non-tumor- and MDA-MB-231b-inoculated mice treated with panobinostat regardless of zoledronic acid (Figure 37G and Figure 39B). Additionally, a reduction in trabecular number and increased trabecular spacing were also observed in panobinostat treated mice (Figure 39C-E). In contrast, treatment with entinostat did not induce changes to the bone (Figure 37G and Figure 39C-E). Histological analysis confirmed the increased tumor volume and incidence in HDACi treated mice, which was prevented with ZA (Figure 37H-J and Figure 39F, G). Importantly, the combination treatment resulted in lower tumor incidence with either HDACi compared to the vehicle control group (Figure 37I). Further tumor analysis revealed no significant changes in Ki67 staining between the groups (Figure 37K, L), however the percentage of mitoses was reduced in entinostat treated mice independent of zoledronic acid (Figure 37K, M). Combined, these *in vivo* data suggest that panobinostat, but not entinostat, negatively affects bone microarchitecture in non-tumor-inoculated mice regardless of zoledronic acid combination. The studies presented herein suggest the superiority of entinostat over panobinostat to treat bone metastases as it does not induce negative bone effects and significantly reduces tumor incidence and mitotic rate. However, these anti-tumor effects are most notably observed in combination with zoledronic acid, which is not currently being tested in clinical trials. Our findings demonstrate a critical need to better understand HDACi effects on the bone in the context of breast cancer and suggest combination therapy with a bisphosphonate may result in better anti-tumor effects in breast cancer patients.

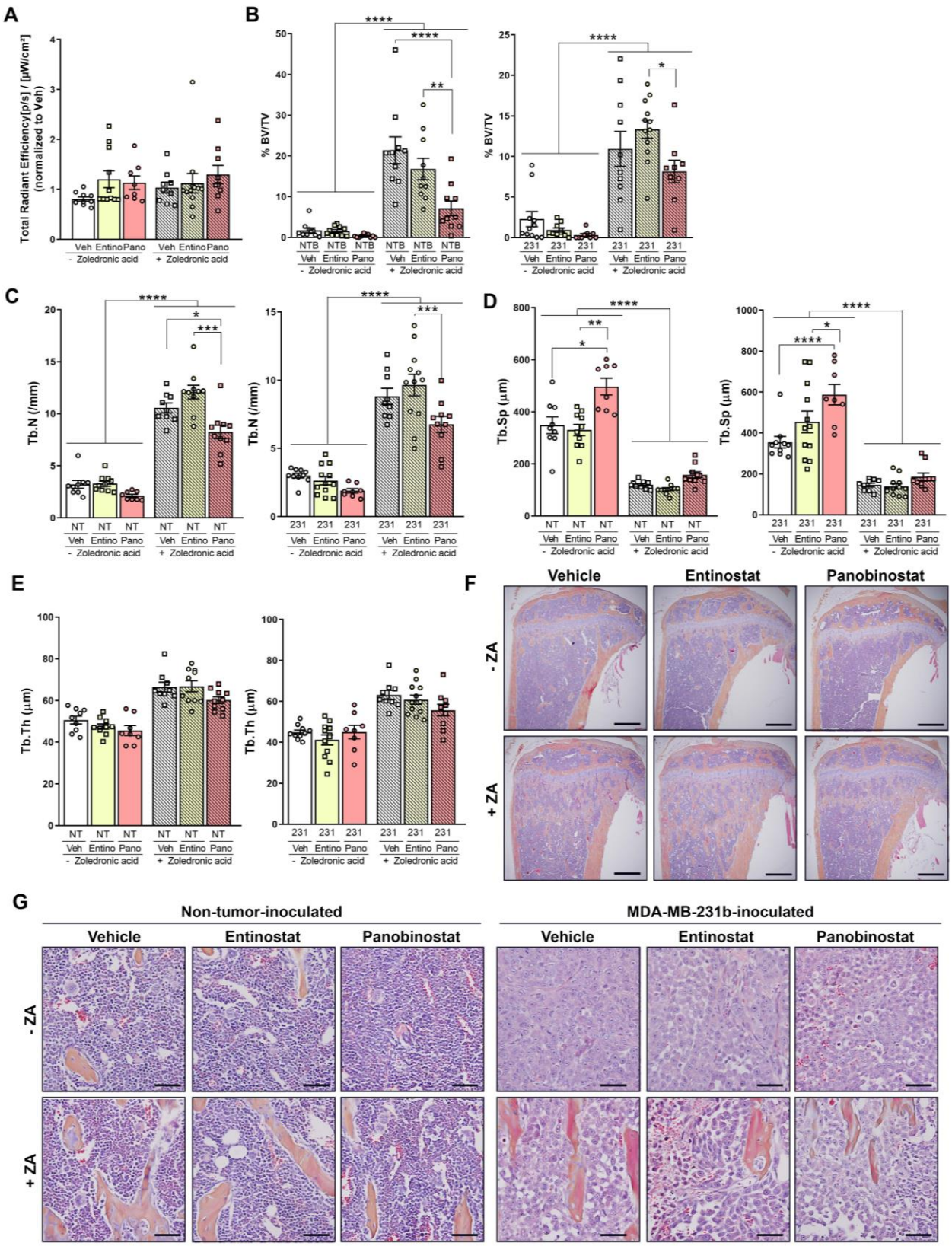
A
Total Radiant Efficiency[p/s] / [µW/cm²] (normalized to Veh)
Veh Entino Pano Veh Entino Pano
- Zoledronic acid
+ Zoledronic acid
B
% BV/TV
NTB NTB NTB NTB NTB NTB
231 231 231 231 231 231
Veh Entino Pano Veh Entino Pano
- Zoledronic acid
+ Zoledronic acid
C
Tb.N (/mm)
NT NT NT NT NT NT
231 231 231 231 231 231
D
Tb.Sp (µm)
E
Tb.Th (µm)
F
Vehicle
Entinostat
Panobinostat
- ZA
+ ZA
G
Non-tumor-inoculated
MDA-MB-231b-inoculated
Vehicle
Entinostat
Panobinostat
- ZA
+ ZA

Figure 39. Panobinostat, but not entinostat, decreases trabecular architecture in non-tumor- and MDA-MB-231b-inoculated mice. (A) Quantitation of total radiant efficiency from MDA-MB-231b-inoculated mice using the IVIS Spectrum Imaging System (veh-ZA n=10, entino-ZA n=12, pano-ZA n=9, veh+ZA n=10, entino+ZA n=12, pano+ZA n=10). (B) Histomorphometric analysis of bone volume from mice described in (A). (C-E) microCT analysis of (C) trabecular number, (D) trabecular spacing, and (E) trabeular thickness in non-tumor-inoculated (NT) (n=10 mice/group) or MDA-MB-231b-inoculated mice described in (A). (F) Representative hematoxylin and eosin (H&E) staining of tibiae from non-tumor-inoculated mice described in (C). All panels = 4X and scale bars = 500μm. (G) Representative zoomed-in images of H&E staining of tibiae from mice described in (A, C). All panels = 40X and scale bars = 20μm. B-D: One-way ANOVA with Sidak's multiple comparisons test, *p<0.05, **p<0.01, ***p<0.001 and ****p<0.0001.

Discussion

Significant progress has been made over the past several years to understand the mechanisms controlling tumor dormancy in various tissues. Notably, many genes known to regulate tumor dormancy appear to do so in a tissue-specific manner. With regards to the bone, LIFR (74), TGFβ2 (61, 201), and MSK1 (71) have recently been identified as dormancy-promoting factors. Despite these advances, few studies have investigated potential therapies to stimulate these genes and maintain bone disseminated tumor cells in a dormant state. Here, we describe the direct epigenetic induction of *LIFR* by HDAC inhibitors (HDACi) and LIFR-mediated stimulation of several other dormancy associated factors including *TGFB2* and *MSK1* in breast cancer cells (Figure 40). High expression of these pro-dormancy genes is associated with low tumor proliferation and increased metastasis-free survival in breast cancer patients. Despite panobinostat negatively effecting normal bone homeostasis, both panobinostat and entinostat decrease tumor incidence when combined with zoledronic acid and decrease mitotic events. Combined, these findings provide insight into the use of HDACi as a means to maintain and promote dormancy in bone-metastatic breast cancer (Figure 40). Importantly. our studies indicate that HDACi treatment in combination with a bisphosphonate such as zoledronic acid is critical for the anti-tumor effects in the bone. These findings are clinically significant given the number of HDACi currently in clinical trials for metastatic breast cancer and suggest that patients should also receive an anti-resorptive agent to prevent tumor progression or increased incidence of bone metastasis.

Bone is a frequent site of metastasis in breast cancer patients and is detectable on autopsy examination in nearly 70% of patients who succumb to disease (57, 58). As previously mentioned, the metastatic latency period is strikingly different between patients with ER+ and ER- disease (149) but the mechanisms underlying this difference remains unclear. A further complicating factor is the discordance between ER positivity in primary tumors and their respective metastases (208-210). For example, a recent study reported ER status was different in ~25% of primary tumor and respective metastasis samples (211). Given these findings, therapies that can effectively induce dormancy regardless of ER expression would be of greatest clinical benefit to breast cancer patients (211). The studies presented herein demonstrate that HDACi dramatically increase LIFR expression, stimulate LIF signaling, and slow tumor cell proliferation in both ER+ and ER- breast cancer cell lines. HDACi differentially stimulated the other dormancy-associated genes in MCF7 and MDA-MB-231b cells, which may represent subtype-specific mechanisms of tumor dormancy and warrants further investigation.

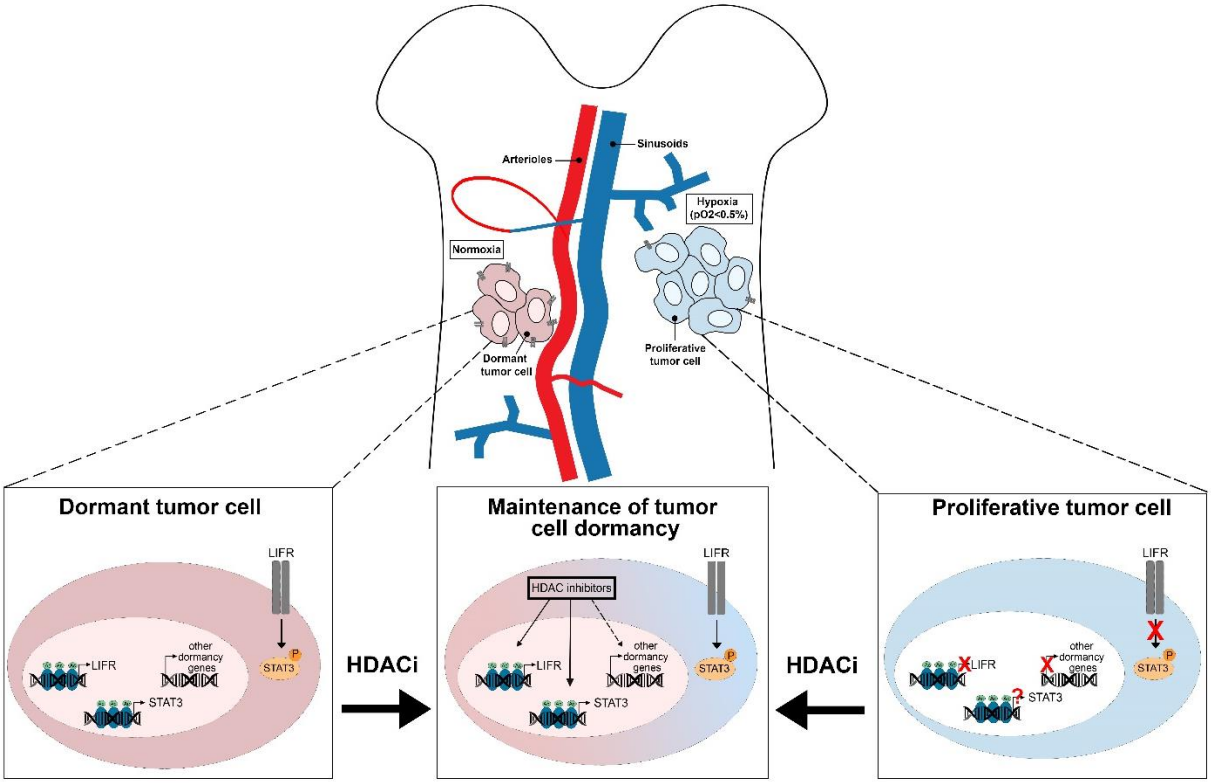

Figure 40. Working model of HDAC inhibitor (HDACi)-mediated maintenance or induction of dormancy through LIFR:STAT3 signaling and other dormancy-associated genes.

Nonetheless, the pro-dormancy effects stimulated by HDACi regardless of ER status suggests that these inhibitors would be useful across multiple breast cancer subtypes.

It remains controversial whether therapies should aim to maintain tumor cells in a chronic state of dormancy or mobilizing dormant tumor cells out of their niche, forcing the cells into a proliferative state and thereby sensitizing them to chemotherapy. Similar to the work presented here, several studies have implicated inhibition of Src (17, 117) or ERK (61, 62, 67, 117) signaling and DNA demethylating agents (65) as a means to maintain tumor cells in a dormant state. By minimizing the proliferative capacity of tumor cells, these approaches aim to prevent metastatic outgrowth and reprogram breast cancer into a chronic treatable disease. The opposite approach involves reactivation of proliferation and targeting tumor cells with effective chemotherapies that are commonly used in the adjuvant setting. Several signaling molecules including MERTK and high ERK/p38 activity ratio have been suggested to promote escape from dormancy (61, 62, 73) and thus could be targeted to promote tumor cell proliferation. Although proliferative tumor cells are more responsive to therapy, the inability to confirm the elimination of all dormant tumor cells and risk of eventual outgrowth remains a major concern with this approach. Additionally, the overlapping mechanisms regulating dormant tumor cells and normal stem cells make it difficult to identify therapies that will selectively target tumor cells for death.

High LIFR expression and signaling is associated with low metastatic potential in breast cancer cells and is often lost in tumor cells that readily metastasize (74). Our results indicate that HDACi stimulate LIFR expression and restore LIF signaling in aggressive breast cancer cells (MDA-MB-231b and 4T1BM2). Previous findings identified STAT3 in a dormancy gene signature (69) and demonstrated that loss of STAT3 results in increased osteolytic bone destruction following intracardiac inoculation of tumor cells (74). While these studies suggest that STAT3 acts a mediator of dormancy, recent work demonstrated that LIFR-induced STAT3 activation results in anti-apoptotic signaling including enhanced BCL-2 and MCL-1 expression, leading to therapy resistance (200). Combined, the ability to re-sensitize tumor cells to LIF, which inhibits tumor growth (212, 213), likely represents another pro-dormancy response initiated by HDACi treatment but requires further investigation.

In addition to histone acetylation, HDACs regulate the acetylation status of many non-histone proteins involved in processes such as transcription, replication, and DNA repair (214). Therefore, HDACi can alter protein acetylation levels, which often regulates protein activity. Recent evidence suggests that LIFR acetylation and phosphorylation of the cytoplasmic domain enhances or suppresses downstream STAT3 activation, respectively. We sought to investigate the role of LIFR protein acetylation/phosphorylation following HDACi treatment, however we

were unable to find antibodies suitable for detecting these changes through LIFR pulldown experiments. Thus, we cannot test if these post-translational modifications are important for LIFR-mediated induction of *AMOT* and *TGFB2* or the restored response of MDA-MB-231b cells to LIF with HDACi treatment. Previous studies have also shown enhanced STAT3 protein acetylation and consequent transcriptional activity in breast cancer cells following treatment with vorinostat (200). Our data indicate that induction of *AMOT* and *TGFB2* is not dependent on STAT3 since knockdown did not alter basal or HDACi-mediated expression. However, given the enhanced signaling potential with HDACi, we cannot rule out the possibility that residual amounts of LIFR or STAT3 in our knockdown lines are sufficient to stimulate these dormancy-associated genes. Additionally, expression of the pro-dormancy genes was not altered with ERK or PI3K inhibitors (74) suggesting that these pathways are likely not mediating the HDACi-induced effects.

Previous evidence indicates that HDACi, specifically valproic acid and vorinostat, cause bone loss in numerous strains of mice (128, 130). Our data indicate that panobinostat, but not entinostat, significantly alters bone volume, trabecular number, and trabecular spacing. Bone volume was reduced by nearly 50% in non-tumor-inoculated mice treated with panobinostat, and combination treatment with zoledronic acid only partially prevented this bone loss. Further, panobinostat treatment of tumor-inoculated mice resulted in higher tumor burden and incidence compared to vehicle or entinostat treated mice, but these effects could be prevented with zoledronic acid. In contrast, entinostat did not negatively affect the bone and combination with zoledronic acid reduced tumor incidence and mitotic index. Given these effects, our findings suggest that HDACi, especially panobinostat, may initiate bone destruction, causing release of tumor-promoting factors from the bone matrix and fueling tumor growth. Although entinostat does not dramatically alter the bone microarchitecture, changes to the bone-resident cells are likely involved in enhancing tumor growth since these effects can be mitigated with zoledronic acid. Importantly, these *in vivo* studies reveal the importance of understanding how anti-cancer therapies affect the normal microenvironment of the bone and how these changes affect tumor cell behavior. Future analyses of apoptosis markers (TUNEL and cleaved PARP) and acetylation levels in the bone will be performed to further assess dormancy status and biological response to HDACi. Whole bone homogenates will also be analyzed by qPCR to further evaluate tumor burden and changes in pro-dormancy gene expression with HDACi treatment. One complicating factor with this method is the difficulty of ensuring detection of gene expression from mouse bone marrow or human tumor cells. Therefore, we will also use the PrimeFlow RNA assay to detect expression levels of various dormancy-associated genes such

as *LIFR*, *AMOT*, and *TGFB2* to analyze RNA levels in individual human tumor cells. These assays will provide further insight into the ability of HDACi to stimulate a pro-dormancy program and induce dormancy *in vivo.* In addition to these effects in the bone, future studies will investigate the ability of HDACi to induce dormancy in breast cancer cells that have metastasized to the lung.

In summary, these data provide mechanistic insight into the epigenetic regulation of LIFR by HDACi and indirect stimulation, potentially through LIFR-mediated signaling, of other known pro-dormancy genes. In breast cancer patients, expression of the dormancy-promoting factors LIFR, AMOT, and TGFβ2 was stimulated with HDACi treatment and inversely correlated with tumor proliferation and metastasis-free survival. Future studies will aim to assess additional markers of cellular dormancy *in vivo* and the effects of HDACi on tumor dormancy in other tissues such as the lung. Combined, these findings offer a potential therapeutic avenue to induce a pro-dormancy program in breast cancer cells of varying metastatic potential that home to bone.

CHAPTER VI

CONCLUSIONS AND FUTURE DIRECTIONS

Conclusions

In recent years, considerable progress has been made towards understanding the mechanisms that regulate dissemination of tumor cells to distant sites and metastatic outgrowth. Accumulating evidence suggests that both the metastatic microenvironment as well as tumor-intrinsic factors play significant roles in controlling the survival, reactivation, and therapeutic resistance of disseminated tumor cells (DTCs) (152, 215). Interestingly, many of the factors known to regulate dormancy appear to do so in a tissue-specific manner (152). Given these findings, the studies presented herein focus on bone metastasis, as this is the most frequent site of recurrence in breast cancer patients. Despite this high prevalence, there are currently no therapeutic options to cure metastatic disease. Thus, there is an urgent need to identify factors regulating tumor dormancy and therapeutic interventions to prevent or control metastatic outgrowth.

One of the largest obstacles in the field of tumor dormancy is the limited number of metastasis models that exhibit prolonged tumor latency periods comparable to those observed in breast cancer patients. The data presented in this dissertation begin to address these challenges with the establishment of novel experimental models of bone metastasis using syngeneic estrogen receptor positive (ER+) D2.0R, human ER- SUM159, and bone-selective human ER+ MCF7 (MCF7b) cell lines. Additionally, we identified highly sensitive methods including flow cytometry and quantitative PCR approaches to detect and quantify ultra-low tumor burden in the bone. While several aggressive ER- cell lines such as the MDA-MB-231 and 4T1 cells are used in bone colonization studies, our characterization of the SUM159 model provides the first ER- experimental bone metastasis model that exhibits extended latency periods. Similarly, the D2.0R model represents the second ER+ syngeneic model used to study bone metastasis following the recently reported SSM2/SSM3 cell lines developed from $STAT1^{-/-}$ mice. Despite estradiol supplementation being necessary for primary tumor formation of ER+ MCF7 cells, it dramatically affects bone homeostasis, resulting in a supra-physiological accumulation of bone (137, 139) and likely confounding our understanding of bone colonization and tumor dormancy. Thus, our reports of MCF7 tumor cell dissemination to bone and the development of overt metastasis by the MCF7b cell line in the absence of 17β-estradiol allows for the more accurate study of these processes in physiologically-relevant environments. For

example, molecular profiling and *in vitro* studies using the MCF7b model identified increased PIP3 Dependent Rac Exchange Factor 1 (PREX1) as a mediator of MCF7b aggressiveness. Of particular importance, the establishment of these models with prolonged latency allows for subtype-specific mechanisms of tumor colonization and dormancy in the bone to be studied in clinically relevant models for the first time.

Approximately 20-30% of breast cancer patients relapse years to decades after primary tumor diagnosis as a result of DTC reactivation (175) Recent evidence suggests that dissemination to distant sites occurs early in tumor progression (7, 8) and even patients with no nodal involvement have a ~15% risk of developing distant metastasis (54). Efforts to therapeutically target dormant tumor cells and either reactivate them to restore sensitivity to chemotherapy or maintain them in a dormant state to prevent recurrence has been a major research focus in recent years (118, 149, 215). Recent studies identified LIFR as a mediator of dormancy in breast cancer cells that metastasize to bone and that HDAC inhibitors (HDACi) stimulate LIFR expression (74, 200). However, the regulation of LIFR expression in breast cancer cells remained unclear and no studies had investigated the potential of HDACi to induce a dormancy phenotype. The studies presented herein demonstrate for the first time that HDACi epigenetically regulate LIFR at the promoter level and indirectly stimulate other pro-dormancy genes in breast cancer cells of varying metastatic potential. Importantly, we provide evidence that LIFR may be an upstream mediator of other dormancy-promoting genes. Moreover, these findings are clinically relevant to breast cancer patients since expression of these dormancy-associated genes inversely correlates with tumor proliferation and metastasis-free survival and could be stimulated using HDACi in a small patient cohort. Using *in vivo* models, we demonstrate that HDACi, namely valproic acid and panobinostat, disrupt normal bone homeostasis, which can be partially prevented with bisphosphonate treatment. Further, tumor incidence and mitotic rate was notably reduced in mice treated with entinostat in combination with zoledronic acid. Our results demonstrate the superiority of entinostat over other HDACi with regards to treating bone metastases. Further, our findings indicate the importance of combination therapy with a bisphosphonate in breast cancer patients to prevent negative effects on the bone and resulting tumor-promoting effects. Overall, this work lays the groundwork for continued exploration of HDAC inhibitors or other LIFR-stimulating therapeutics as means to induce tumor dormancy in breast cancer.

Future Directions

Nearly 80% of breast cancer patients who succumb to disease show evidence of bone metastases upon autopsy. These findings clearly indicate a significant risk of breast cancer patient survivors developing overt bone metastases from DTCs in the bone marrow. These DTCs may coopt physiological niches including the endosteal or perivascular niches in order to remain in a dormant state following dissemination to the bone marrow (Figure 41). Several groups suggest that disrupting these interactions therapeutically, thus reactivating dormant tumor cells, followed by chemotherapy would be an effective treatment option to prevent metastasis. However, with this approach there is significant risk that a subset of dormant tumor cells will remain following treatment due to resistance or that reactivation treatment would induce other molecular changes that make tumor cells more aggressive. Nonetheless, further understanding the mechanisms of tumor dormancy and metastatic outgrowth is of the upmost importance to effectively treat and prevent metastatic recurrence in the future. The data presented herein suggest that PREX1 and LIFR may be key signaling molecules in the dissemination and dormancy status of tumor cells, respectively (Figure 41). In addition to expanding the current understanding of tumor colonization and dormancy, these data offer numerous exciting avenues for future exploration. Several of these research focuses are discussed below and represent opportunities to identify other cell autonomous and microenvironmental regulators of dormancy.

Can these experimental metastasis models be used to identify other regulators of tumor dormancy?

Previous studies have sought to identify metastasis-specific alterations through the generation of bone-tropic lines by repeated *in vivo* passaging (16). Through this process, subclones that preferentially grow in the bone are selected and are molecularly compared to the parental cells. While these studies have provided considerable insights into genes mediating metastasis, they are less likely to identify factors regulated by the microenvironment or those involved in dormancy escape. The MCF7b model presented in this dissertation yielded a small fraction (20%) of mice that developed overt bone metastasis following a prolonged latency period (22 weeks). Given the low frequency of metastatic outgrowth, the MCF7b model represents a valuable tool to identify molecular changes that induce spontaneous exiting of tumor cells from dormancy. Additionally, the prolonged latency period of the MCF7b model allows for the role of microenvironmental factors such as the vasculature and bone-resident cells in metastatic outgrowth to be evaluated, which is not as feasible with the highly aggressive

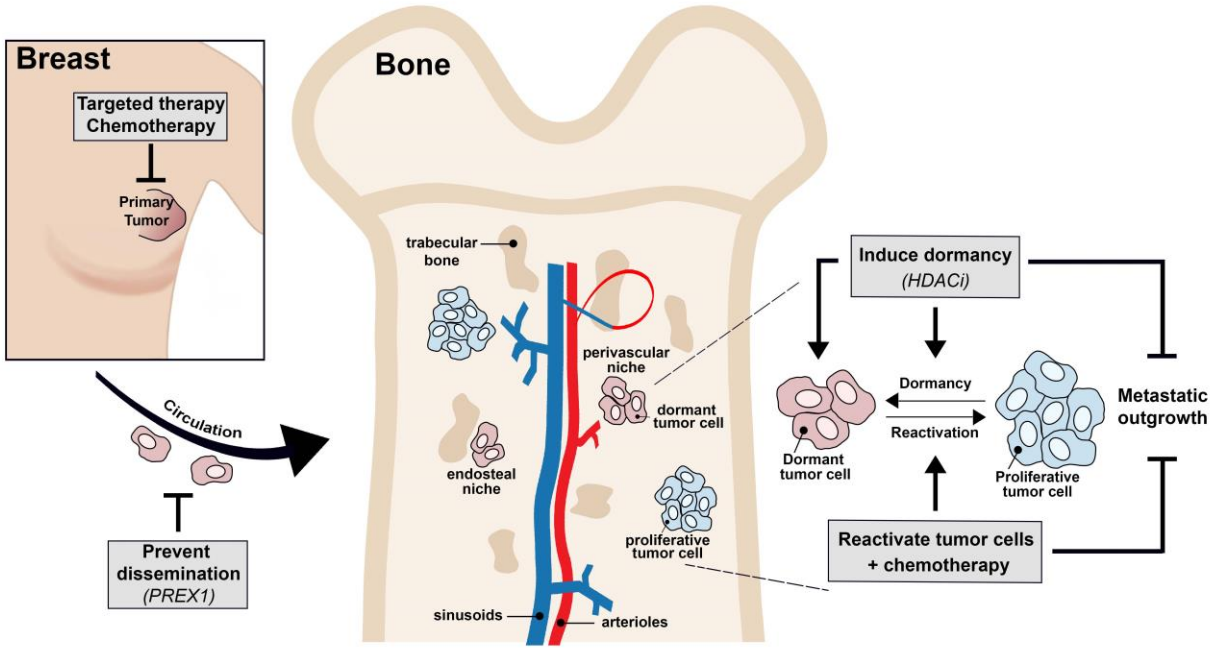

Figure 41. Schematic showing therapeutic approaches to prevent dissemination and metastatic outgrowth of breast cancer cells. Despite advances in effective therapies to treat primary breast tumor, patients remain at significant risk of developing distant metastases. Following dissemination, tumor cells may coopt the endosteal or perivascular niches to remain in a dormant state for a period of time before becoming reactivated. Our data suggest that PREX1 or HDAC inhibitor (HDACi)-mediated induction of LIFR may be viable ways to prevent dissemination or metastatic outgrowth, respectively.

MDA-MB-231 or 4T1 models. Using the CD298 flow cytometry protocol developed in Chapter II, tumor cells could be isolated from these overt metastases and investigated by molecular profiling (RNA sequencing, RPPA, etc). The ability to isolate these cells directly from the bone marrow rather than culturing them *in vitro* would provide a more accurate depiction of their molecular phenotype *in vivo* and potential identify microenvironment-regulated changes.

Importantly, the ability of the MCF7 and D2.0R models to develop overt metastases without estradiol supplementation has not yet been investigated since our studies directly compared these mice to those with estradiol supplementation, which required a common end point. Thus, further investigation or modification (e.g. injection of more tumor cells) of these models may provide additional opportunities to isolate tumor cells and identify regulators of dormancy.

An alternative approach to identify dormancy-associated genes was recently performed using an *in vivo* genome-wide shRNA screen in human ER+ T47D cells (71). Conducting similar unbiased screens using knockdown or overexpression libraries in the metastasis models presented herein ((MCF7 - E2, SUM159, D2.0R, MCF7b) could significantly expand the mechanistic understanding of ER+ and ER- tumor dormancy. The absence of estradiol from the MCF7 - E2 and MCF7b models provides a major advantage over previously published studies since the confounding influences of estradiol on gene expression and tumor growth can be avoided. Moreover, there is a strong need to perform similar studies in immunocompetent models with prolonged tumor latency in order to better understand the contribution of the immune system.

How does PREX1 mediate skeletal-tropism and dissemination?

Our data demonstrate increased dissemination of MCF7b cells to skeletal sites compared to the parental MCF7 cells and implicate PREX1, a PIP3 Rac exchange factor, as a mediator of this dissemination. Currently, the mechanism by which PREX1 promotes preferential metastasis to skeletal sites is unclear. Previous work found that ErbB receptors potentiate PREX1/Rac1 signaling through CXCR4 transactivation to drive tumorigenesis. The CXCL12:CXCR4 complex is one of the most well documented mechanisms promoting tumor cell colonization of the bone (16, 109). These findings suggest that CXCR4 may be involved in the bone-tropism of MCF7b cells. To test this experimentally, deletion of the PREX1 DH-PH domain in tumor cells or treatment with PI3K inhibitors *in vivo* would effectively turn off CXCR4-transduced signaling to PREX1 without affecting CXCR4-mediated homing. Further investigation into PREX1-mediated metastasis to bone may provide additional rationale for

inhibiting upstream dissemination pathways (CXCR4) or identify novel therapeutic targets to prevent recurrence.

How does hypoxia regulate LIFR and pro-dormancy effects induced by HDAC inhibitors?

Despite its extensive network of vasculature, the bone is a particularly hypoxic environment. Whereas most tissues experience oxygen levels between 2% and 9%, levels in the bone range from < 1% - 6% (6, 216-218). Activation of HIF1α and HIF2α in hypoxic environments is known to promote tumor progression and metastasis to various organs including the lungs and liver (219-222). However, the effects of hypoxia on tumor dormancy and colonization in the bone remain less clear. As discussed in Chapter I, urokinase-type plasminogen activator receptor (uPAR) promotes dormancy escape and correlates with increased disseminated tumor cells in the bone marrow. Several studies suggest that hypoxia and HIF signaling mediate uPAR expression and consequently metastatic progression. Consistent with this hypoxia-induced exit from dormancy, hypoxia has been identified as a negative regulator of LIFR in mouse embryonic stem cells and breast cancer cells (74, 80). Further, LIFR mRNA expression was shown to negatively correlate with hypoxia gene activity in breast cancer patients (74). The mechanism for hypoxic repression of LIFR remains unclear; however, data from our laboratory suggest that decreased acetylation and increased methylation of the LIFR promoter in hypoxic conditions may be involved (Figure 42). Additionally, published (74) and preliminary evidence from our laboratory shows that HDAC inhibitors retain their ability to induce LIFR expression in hypoxic conditions (data not shown). Understanding the mechanism responsible for hypoxic repression of LIFR is necessary in order to effectively maintain and induce its expression in the hypoxic bone as well as in hypoxic tumor environments. In addition to LIFR, it remains unclear whether other known pro-dormancy genes are downregulated in hypoxic conditions. Thus, future studies are needed to assess the global effects of hypoxia on tumor dormancy escape.

What is the mechanism by which HDAC inhibitors restore LIFR signaling in aggressive tumor cells?

Evidence presented in Chapter IV and previously published reports from our laboratory (74) and others (200) demonstrates the ability of HDAC inhibitors to re-sensitize MDA-MB-231 cells to ligand stimulation resulting in robust STAT3 activation. According to the Cancer Cell Line Encyclopedia (223, 224) and NCI-60 datasets (225, 226) analyzed using the cBioPortal for

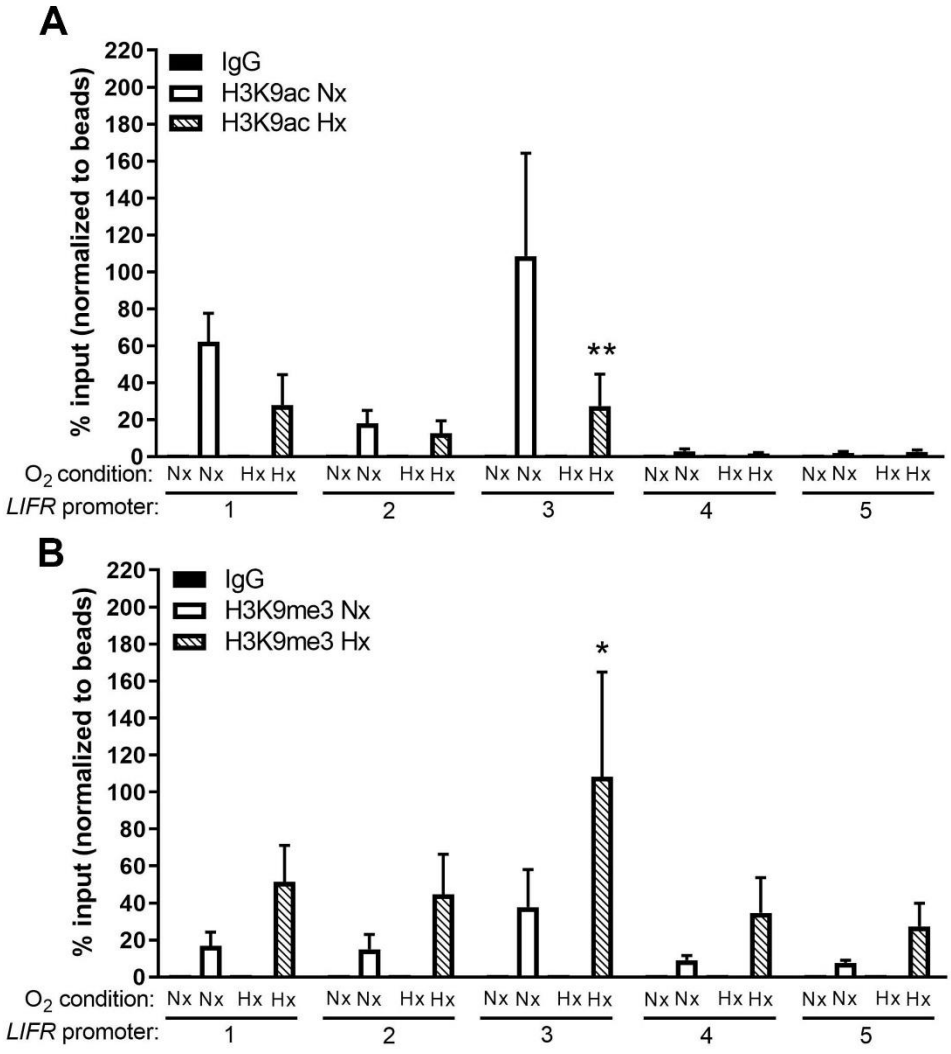

Figure 42. Hypoxia alters acetylation and methylation enrichment along the LIFR promoter. ChIP-qPCR showing (A) acetylated histone H3 lysine 9 (H3K9ac) and (B) methylated histone H3 lysine 9 (H3K9me3) enrichment (% ChIP/input) along the *LIFR* promoter region in MCF7 cells grown in normoxia (Nx) or hypoxia (Hx) for 24 hours.

Cancer Genomics (144, 145) there are no mutations in the LIFR signaling complex (LIF, LIFR, GP130, STAT3) in MDA-MB-231 cells. Additionally, expression of these factors is not significantly altered with HDAC inhibitor treatment (Chapter IV and data not shown). Thus, the mechanisms underlying STAT3 signaling restoration following ligand stimulation and subsequent effects on dormancy remain unclear. Interestingly, several phosphorylation and acetylation sites along the LIFR cytoplasmic domain were recently shown to regulate ligand-mediated STAT3 activation in mouse embryonic stem cells (227). Specifically, acetylation of LIFR promotes heterodimerization with gp130 and consequent STAT3 activation whereas phosphorylation restricts gp130 binding and STAT3 signaling. Importantly, these post-translational modifications have not yet been described or investigated in cancer cells and therefore represent an exciting new area of LIFR biology. These findings are particularly intriguing with regards to the potential of HDAC inhibitors to promote LIFR protein acetylation and STAT3 activation. I hypothesize that loss of functional LIFR signaling, such as that observed in the MDA-MB-231 cells, is due to hyper-phosphorylation of the LIFR protein providing a strong repressive STAT3 signal that outweighs LIFR acetylation in the presence of ligand. However, this balance could be shifted using HDAC inhibitors to stimulate maximal LIFR protein acetylation and gp130 interaction to restore ligand-mediated STAT3 signaling. Unfortunately, a lack of suitable LIFR antibodies has limited our ability to investigate LIFR acetylation and phosphorylation status in basal and HDAC inhibitor conditions. Future investigations using LIFR mutants in these conditions will determine the contribution of these modifications to LIFR signaling.

Previous studies demonstrated that LIFR expression correlates with metastatic potential (74) and is another mechanisms to limit LIFR:STAT3 signaling. For example, the aggressive murine 4T1BM2 cells express very low levels of LIFR and show no apparent STAT3 activation following ligand stimulation. The data presented herein demonstrate enhanced LIFR expression following HDAC inhibitor treatment of 4T1BM2 cells; however, we have not yet investigated whether LIFR:STAT3 signaling can be restored in these conditions. Investigation of other cell lines that express very low levels or a non-functional LIFR will aid in the understanding of how cancer cells turn off the pro-dormancy LIFR:STAT3 signaling axis.

Concluding remarks

The work presented in this dissertation not only provides several models of bone metastasis exhibiting prolonged tumor latency, but also contributes significant insight into the use of HDAC inhibitors to therapeutically induce dormancy. These studies provide a strong

foundation for future endeavors to study novel dormancy regulators and anti-proliferative treatments in clinically relevant models of breast cancer metastasis. Further understanding tumor dormancy and therapeutic approaches to prevent metastatic recurrence has the potential to greatly impact breast cancer survival by transforming breast cancer into a chronic, but manageable, disease.

REFERENCES

1. Paget, S., The Distribution of Secondary Growths in Cancer of the Breast. The Lancet, 1889. 133(3421): p. 571-573.

2. Smith, H.A. and Y. Kang, Determinants of Organotropic Metastasis. Annual Review of Cancer Biology, 2017. 1(1): p. 403-423.

3. Macedo, F., K. Ladeira, F. Pinho, N. Saraiva, N. Bonito, L. Pinto, et al., Bone Metastases: An Overview. Oncol Rev, 2017. 11(1): p. 321.

4. Peinado, H., H. Zhang, I.R. Matei, B. Costa-Silva, A. Hoshino, G. Rodrigues, et al., Pre-metastatic niches: organ-specific homes for metastases. Nat Rev Cancer, 2017. 17(5): p. 302-317.

5. Crane, G.M., E. Jeffery, and S.J. Morrison, Adult haematopoietic stem cell niches. Nat Rev Immunol, 2017. 17(9): p. 573-590.

6. Johnson, R.W., M.E. Sowder, and A.J. Giaccia, Hypoxia and Bone Metastatic Disease. Curr Osteoporos Rep, 2017. 15(4): p. 231-238.

7. Husemann, Y., J.B. Geigl, F. Schubert, P. Musiani, M. Meyer, E. Burghart, et al., Systemic spread is an early step in breast cancer. Cancer Cell, 2008. 13(1): p. 58-68.

8. Sanger, N., K.E. Effenberger, S. Riethdorf, V. Van Haasteren, J. Gauwerky, I. Wiegratz, et al., Disseminated tumor cells in the bone marrow of patients with ductal carcinoma in situ. Int J Cancer, 2011. 129(10): p. 2522-6.

9. Naxerova, K. and R.K. Jain, Using tumour phylogenetics to identify the roots of metastasis in humans. Nat Rev Clin Oncol, 2015. 12(5): p. 258-72.

10. Schmidt-Kittler, O., T. Ragg, A. Daskalakis, M. Granzow, A. Ahr, T.J. Blankenstein, et al., From latent disseminated cells to overt metastasis: genetic analysis of systemic breast cancer progression. Proc Natl Acad Sci U S A, 2003. 100(13): p. 7737-42.

11. Klein, C.A., T.J.F. Blankenstein, O. Schmidt-Kittler, M. Petronio, B. Polzer, N.H. Stoecklein, et al., Genetic heterogeneity of single disseminated tumour cells in minimal residual cancer. The Lancet, 2002. 360(9334): p. 683-689.

12. Weckermann, D., B. Polzer, T. Ragg, A. Blana, G. Schlimok, H. Arnholdt, et al., Perioperative activation of disseminated tumor cells in bone marrow of patients with prostate cancer. J Clin Oncol, 2009. 27(10): p. 1549-56.

13. Gundem, G., P. Van Loo, B. Kremeyer, L.B. Alexandrov, J.M.C. Tubio, E. Papaemmanuil, et al., The evolutionary history of lethal metastatic prostate cancer. Nature, 2015. 520(7547): p. 353-357.

14. Hosseini, H., M.M. Obradovic, M. Hoffmann, K.L. Harper, M.S. Sosa, M. Werner-Klein, et al., Early dissemination seeds metastasis in breast cancer. Nature, 2016.

15. Harper, K.L., M.S. Sosa, D. Entenberg, H. Hosseini, J.F. Cheung, R. Nobre, et al., Mechanism of early dissemination and metastasis in Her2(+) mammary cancer. Nature, 2016.

16. Kang, Y., P.M. Siegel, W. Shu, M. Drobnjak, S.M. Kakonen, C. Cordón-Cardo, et al., A multigenic program mediating breast cancer metastasis to bone. Cancer Cell, 2003. 3(6): p. 537-549.

17. Zhang, X.H., Q. Wang, W. Gerald, C.A. Hudis, L. Norton, M. Smid, et al., Latent bone metastasis in breast cancer tied to Src-dependent survival signals. Cancer Cell, 2009. 16(1): p. 67-78.

18. Bidwell, B.N., C.Y. Slaney, N.P. Withana, S. Forster, Y. Cao, S. Loi, et al., Silencing of Irf7 pathways in breast cancer cells promotes bone metastasis through immune escape. Nat Med, 2012. 18(8): p. 1224-31.

19. Vogelstein, B., N. Papadopoulos, V.E. Velculescu, S. Zhou, L.A. Diaz, Jr., and K.W. Kinzler, Cancer genome landscapes. Science, 2013. 339(6127): p. 1546-58.

20. Baxter, E., K. Windloch, F. Gannon, and J.S. Lee, Epigenetic regulation in cancer progression. Cell Biosci, 2014. 4: p. 45.

21. You, J.S. and P.A. Jones, Cancer genetics and epigenetics: two sides of the same coin? Cancer Cell, 2012. 22(1): p. 9-20.

22. Mehrotra, J., M. Vali, M. McVeigh, S.L. Kominsky, M.J. Fackler, J. Lahti-Domenici, et al., Very High Frequency of Hypermethylated Genes in Breast Cancer Metastasis to the Bone, Brain, and Lung. Clinical Cancer Research, 2004. 10(9): p. 3104-3109.

23. Shi, X., A. Tasdogan, F. Huang, Z. Hu, S.J. Morrison, and R.J. DeBerardinis, The abundance of metabolites related to protein methylation correlates with the metastatic capacity of human melanoma xenografts. Science Advances, 2017. 3(11).

24. Vanharanta, S., W. Shu, F. Brenet, A.A. Hakimi, A. Heguy, A. Viale, et al., Epigenetic expansion of VHL-HIF signal output drives multiorgan metastasis in renal cancer. Nat Med, 2013. 19(1): p. 50-6.

25. Lu, X. and Y. Kang, Chemokine (C-C motif) ligand 2 engages CCR2+ stromal cells of monocytic origin to promote breast cancer metastasis to lung and bone. J Biol Chem, 2009. 284(42): p. 29087-96.

26. Li, X., R. Loberg, J. Liao, C. Ying, L.A. Snyder, K.J. Pienta, et al., A destructive cascade mediated by CCL2 facilitates prostate cancer growth in bone. Cancer Res, 2009. 69(4): p. 1685-92.

27. Luo, X., Y. Fu, A.J. Loza, B. Murali, K.M. Leahy, M.K. Ruhland, et al., Stromal-initiated changes in the bone promote metastatic niche development. Cell reports, 2016. 14(1): p. 82-92.

28. Zheng, Y., D. Basel, S.-O. Chow, C. Fong-Yee, S. Kim, F. Buttgereit, et al., Targeting IL-6 and RANKL signaling inhibits prostate cancer growth in bone. Clinical & Experimental Metastasis, 2014. 31(8): p. 921-933.

29. Zheng, Y., S.-O. Chow, K. Boernert, D. Basel, A. Mikuscheva, S. Kim, et al., Direct Crosstalk Between Cancer and Osteoblast Lineage Cells Fuels Metastatic Growth in Bone via Auto-Amplification of IL-6 and RANKL Signaling Pathways. Journal of Bone and Mineral Research, 2014. 29(9): p. 1938-1949.

30. Sethi, N., X. Dai, C.G. Winter, and Y. Kang, Tumor-derived JAGGED1 promotes osteolytic bone metastasis of breast cancer by engaging notch signaling in bone cells. Cancer Cell, 2011. 19(2): p. 192-205.

31. Zhuang, X., H. Zhang, X. Li, X. Li, M. Cong, F. Peng, et al., Differential effects on lung and bone metastasis of breast cancer by Wnt signalling inhibitor DKK1. Nat Cell Biol, 2017. 19(10): p. 1274-1285.

32. Jung, Y., J. Wang, A. Schneider, Y.X. Sun, A.J. Koh-Paige, N.I. Osman, et al., Regulation of SDF-1 (CXCL12) production by osteoblasts; a possible mechanism for stem cell homing. Bone, 2006. 38(4): p. 497-508.

33. Chatterjee, S., B. Behnam Azad, and S. Nimmagadda, The intricate role of CXCR4 in cancer. Adv Cancer Res, 2014. 124: p. 31-82.

34. Zhang, X.H., X. Jin, S. Malladi, Y. Zou, Y.H. Wen, E. Brogi, et al., Selection of bone metastasis seeds by mesenchymal signals in the primary tumor stroma. Cell, 2013. 154(5): p. 1060-1073.

35. Wang, J., R. Loberg, and R.S. Taichman, The pivotal role of CXCL12 (SDF-1)/CXCR4 axis in bone metastasis. Cancer Metastasis Rev, 2006. 25(4): p. 573-87.

36. Kukreja, P., A.B. Abdel-Mageed, D. Mondal, K. Liu, and K.C. Agrawal, Up-regulation of CXCR4 expression in PC-3 cells by stromal-derived factor-1alpha (CXCL12) increases endothelial adhesion and transendothelial migration: role of MEK/ERK signaling pathway-dependent NF-kappaB activation. Cancer Res, 2005. 65(21): p. 9891-8.

37. Engl, T., B. Relja, D. Marian, C. Blumenberg, I. Muller, W.D. Beecken, et al., CXCR4 chemokine receptor mediates prostate tumor cell adhesion through alpha5 and beta3 integrins. Neoplasia, 2006. 8(4): p. 290-301.

38. Graham, N. and B.-Z. Qian, Mesenchymal Stromal Cells: Emerging Roles in Bone Metastasis. International Journal of Molecular Sciences, 2018. 19(4): p. 1121.

39. Hamidi, H. and J. Ivaska, Every step of the way: integrins in cancer progression and metastasis. Nature Reviews Cancer, 2018. 18(9): p. 533-548.

40. Barthel, S.R., D.L. Hays, E.M. Yazawa, M. Opperman, K.C. Walley, L. Nimrichter, et al., Definition of molecular determinants of prostate cancer cell bone extravasation. Cancer Res, 2013. 73(2): p. 942-52.

41. Shen, F., Y. Zhang, D.L. Jernigan, X. Feng, J. Yan, F.U. Garcia, et al., Novel Small-Molecule CX3CR1 Antagonist Impairs Metastatic Seeding and Colonization of Breast Cancer Cells. Mol Cancer Res, 2016. 14(6): p. 518-27.

42. Jamieson, W.L., S. Shimizu, J.A. D'Ambrosio, O. Meucci, and A. Fatatis, CX3CR1 is expressed by prostate epithelial cells and androgens regulate the levels of CX3CL1/fractalkine in the bone marrow: potential role in prostate cancer bone tropism. Cancer Res, 2008. 68(6): p. 1715-22.

43. Shiozawa, Y., A.M. Havens, Y. Jung, A.M. Ziegler, E.A. Pedersen, J. Wang, et al., Annexin II/annexin II receptor axis regulates adhesion, migration, homing, and growth of prostate cancer. Journal of cellular biochemistry, 2008. 105(2): p. 370-380.

44. Shiozawa, Y., E.A. Pedersen, A.M. Havens, Y. Jung, A. Mishra, J. Joseph, et al., Human prostate cancer metastases target the hematopoietic stem cell niche to establish footholds in mouse bone marrow. J Clin Invest, 2011. 121(4): p. 1298-312.

45. Wang, H., C. Yu, X. Gao, T. Welte, A.M. Muscarella, L. Tian, et al., The osteogenic niche promotes early-stage bone colonization of disseminated breast cancer cells. Cancer Cell, 2015. 27(2): p. 193-210.

46. Schneider, J.G., S.R. Amend, and K.N. Weilbaecher, Integrins and bone metastasis: integrating tumor cell and stromal cell interactions. Bone, 2011. 48(1): p. 54-65.

47. Kwakwa, K.A. and J.A. Sterling, Integrin alphavbeta3 Signaling in Tumor-Induced Bone Disease. Cancers (Basel), 2017. 9(7).

48. PÉCHEUR, I., O. PEYRUCHAUD, C.-M. SERRE, J. GUGLIELMI, C. VOLAND, F. BOURRE, et al., Integrin αvβ3 expression confers on tumor cells a greater propensity to metastasize to bone. The FASEB Journal, 2002. 16(10): p. 1266-1268.

49. Sloan, E.K., N. Pouliot, K.L. Stanley, J. Chia, J.M. Moseley, D.K. Hards, et al., Tumor-specific expression of αvβ3 integrin promotes spontaneous metastasis of breast cancer to bone. Breast Cancer Research, 2006. 8(2): p. R20-R20.

50. Li, X.Q., J.T. Lu, C.C. Tan, Q.S. Wang, and Y.M. Feng, RUNX2 promotes breast cancer bone metastasis by increasing integrin alpha5-mediated colonization. Cancer Lett, 2016. 380(1): p. 78-86.

51. Ghajar, C.M., H. Peinado, H. Mori, I.R. Matei, K.J. Evason, H. Brazier, et al., The perivascular niche regulates breast tumour dormancy. Nat Cell Biol, 2013. 15(7): p. 807-17.

52. Price, T.T., M.L. Burness, A. Sivan, M.J. Warner, R. Cheng, C.H. Lee, et al., Dormant breast cancer micrometastases reside in specific bone marrow niches that regulate their transit to and from bone. Science Translational Medicine, 2016. 8(340): p. 340ra73-340ra73.

53. Correa, D., R.A. Somoza, P. Lin, W.P. Schiemann, and A.I. Caplan, Mesenchymal stem cells regulate melanoma cancer cells extravasation to bone and liver at their perivascular niche. Int J Cancer, 2016. 138(2): p. 417-27.

54. Pan, H., R. Gray, J. Braybrooke, C. Davies, C. Taylor, P. McGale, et al., 20-Year Risks of Breast-Cancer Recurrence after Stopping Endocrine Therapy at 5 Years. N Engl J Med, 2017. 377(19): p. 1836-1846.

55. Pantel, K. and R.H. Brakenhoff, Dissecting the metastatic cascade. Nat Rev Cancer, 2004. 4(6): p. 448-56.

56. Morgan, T.M., P.H. Lange, M.P. Porter, D.W. Lin, W.J. Ellis, I.S. Gallaher, et al., Disseminated Tumor Cells in Prostate Cancer Patients after Radical Prostatectomy and without Evidence of Disease Predicts Biochemical Recurrence. Clinical Cancer Research, 2009. 15(2): p. 677-683.

57. Johnson, R.W., E. Schipani, and A.J. Giaccia, HIF targets in bone remodeling and metastatic disease. Pharmacol Ther, 2015. 150: p. 169-77.

58. Coleman, R.E., Metastatic bone disease: clinical features, pathophysiology and treatment strategies. Cancer Treat Rev, 2001. 27(3): p. 165-76.

59. Braun, S., F.D. Vogl, B. Naume, W. Janni, M.P. Osborne, R.C. Coombes, et al., A Pooled Analysis of Bone Marrow Micrometastasis in Breast Cancer. New England Journal of Medicine, 2005. 353(8): p. 793-802.

60. Kobayashi, A., H. Okuda, F. Xing, P.R. Pandey, M. Watabe, S. Hirota, et al., Bone morphogenetic protein 7 in dormancy and metastasis of prostate cancer stem-like cells in bone. The Journal of Experimental Medicine, 2011. 208(13): p. 2641-2655.

61. Bragado, P., Y. Estrada, F. Parikh, S. Krause, C. Capobianco, H.G. Farina, et al., TGF-beta2 dictates disseminated tumour cell fate in target organs through TGF-beta-RIII and p38alpha/beta signalling. Nat Cell Biol, 2013. 15(11): p. 1351-61.

62. Yu-Lee, L.Y., G. Yu, Y.C. Lee, S.C. Lin, J. Pan, T. Pan, et al., Osteoblast-Secreted Factors Mediate Dormancy of Metastatic Prostate Cancer in the Bone via Activation of the TGFbetaRIII-p38MAPK-pS249/T252RB Pathway. Cancer Res, 2018. 78(11): p. 2911-2924.

63. Taichman, R.S., L.R. Patel, R. Bedenis, J. Wang, S. Weidner, T. Schumann, et al., GAS6 receptor status is associated with dormancy and bone metastatic tumor formation. PLoS One, 2013. 8(4): p. e61873.

64. Shiozawa, Y., E.A. Pedersen, L.R. Patel, A.M. Ziegler, A.M. Havens, Y. Jung, et al., GAS6/AXL Axis Regulates Prostate Cancer Invasion, Proliferation, and Survival in the Bone Marrow Niche. Neoplasia, 2010. 12(2): p. 116-IN4.

65. Sosa, M.S., F. Parikh, A.G. Maia, Y. Estrada, A. Bosch, P. Bragado, et al., NR2F1 controls tumour cell dormancy via SOX9- and RARbeta-driven quiescence programmes. Nat Commun, 2015. 6: p. 6170.

66. Xue, A., M. Xue, C. Jackson, and R.C. Smith, Suppression of urokinase plasminogen activator receptor inhibits proliferation and migration of pancreatic adenocarcinoma cells via regulation of ERK/p38 signaling. Int J Biochem Cell Biol, 2009. 41(8-9): p. 1731-8.

67. Aguirre-Ghiso, J.A., D. Liu, A. Mignatti, K. Kovalski, L. Ossowski, and T. Hunter, Urokinase Receptor and Fibronectin Regulate the ERKMAPK to p38MAPK Activity Ratios That Determine Carcinoma Cell Proliferation or Dormancy In Vivo. Molecular Biology of the Cell, 2001. 12(4): p. 863-879.

68. Adam, A.P., A. George, D. Schewe, P. Bragado, B.V. Iglesias, A.C. Ranganathan, et al., Computational identification of a p38SAPK-regulated transcription factor network required for tumor cell quiescence. Cancer Res, 2009. 69(14): p. 5664-72.

69. Kim, R.S., A. Avivar-Valderas, Y. Estrada, P. Bragado, M.S. Sosa, J.A. Aguirre-Ghiso, et al., Dormancy Signatures and Metastasis in Estrogen Receptor Positive and Negative Breast Cancer. PLOS ONE, 2012. 7(4): p. e35569.

70. Sosa, M.S., P. Bragado, and J.A. Aguirre-Ghiso, Mechanisms of disseminated cancer cell dormancy: an awakening field. Nature reviews. Cancer, 2014. 14(9): p. 611-622.

71. Gawrzak, S., L. Rinaldi, S. Gregorio, E.J. Arenas, F. Salvador, J. Urosevic, et al., MSK1 regulates luminal cell differentiation and metastatic dormancy in ER+ breast cancer. Nature Cell Biology, 2018. 20(2): p. 211-221.

72. Yumoto, K., M.R. Eber, J. Wang, F.C. Cackowski, A.M. Decker, E. Lee, et al., Axl is required for TGF-beta2-induced dormancy of prostate cancer cells in the bone marrow. Sci Rep, 2016. 6: p. 36520.

73. Cackowski, F.C., M.R. Eber, J. Rhee, A.M. Decker, K. Yumoto, J.E. Berry, et al., Mer Tyrosine Kinase Regulates Disseminated Prostate Cancer Cellular Dormancy. J Cell Biochem, 2017. 118(4): p. 891-902.

74. Johnson, R.W., E.C. Finger, M.M. Olcina, M. Vilalta, T. Aguilera, Y. Miao, et al., Induction of LIFR confers a dormancy phenotype in breast cancer cells disseminated to the bone marrow. Nat Cell Biol, 2016. 18(10): p. 1078-1089.

75. Chen, D., Y. Sun, Y. Wei, P. Zhang, A.H. Rezaeian, J. Teruya-Feldstein, et al., LIFR is a breast cancer metastasis suppressor upstream of the Hippo-YAP pathway and a prognostic marker. Nat Med, 2012. 18(10): p. 1511-7.

76. Iorns, E., T.M. Ward, S. Dean, A. Jegg, D. Thomas, N. Murugaesu, et al., Whole genome in vivo RNAi screening identifies the leukemia inhibitory factor receptor as a novel breast tumor suppressor. Breast Cancer Research and Treatment, 2012. 135(1): p. 79-91.

77. Bolin, C., K. Tawara, C. Sutherland, J. Redshaw, P. Aranda, J. Moselhy, et al., Oncostatin m promotes mammary tumor metastasis to bone and osteolytic bone degradation. Genes Cancer, 2012. 3(2): p. 117-30.

78. Wysoczynski, M., K. Miekus, K. Jankowski, J. Wanzeck, S. Bertolone, A. Janowska-Wieczorek, et al., Leukemia Inhibitory Factor: A Newly Identified Metastatic Factor in Rhabdomyosarcomas. Cancer Research, 2007. 67(5): p. 2131-2140.

79. Maruta, S., S. Takiguchi, M. Ueyama, Y. Kataoka, Y. Oda, M. Tsuneyoshi, et al., A role for leukemia inhibitory factor in melanoma-induced bone metastasis. Clinical & Experimental Metastasis, 2008. 26(2): p. 133.

80. Jeong, C.H., H.J. Lee, J.H. Cha, J.H. Kim, K.R. Kim, J.H. Kim, et al., Hypoxia-inducible factor-1 alpha inhibits self-renewal of mouse embryonic stem cells in Vitro via negative regulation of the leukemia inhibitory factor-STAT3 pathway. J Biol Chem, 2007. 282(18): p. 13672-9.

81. Wang, N., F. Docherty, H.K. Brown, K. Reeves, A. Fowles, M. Lawson, et al., Mitotic quiescence, but not unique “stemness,” marks the phenotype of bone metastasis-initiating cells in prostate cancer. The FASEB Journal, 2015. 29(8): p. 3141-3150.

82. Mundy, G.R., Metastasis to bone: causes, consequences and therapeutic opportunities. Nature Reviews Cancer, 2002. 2: p. 584.

83. Kakonen, S.M., K.S. Selander, J.M. Chirgwin, J.J. Yin, S. Burns, W.A. Rankin, et al., Transforming growth factor-beta stimulates parathyroid hormone-related protein and osteolytic metastases via Smad and mitogen-activated protein kinase signaling pathways. J Biol Chem, 2002. 277(27): p. 24571-8.

84. Sterling, J.A., B.O. Oyajobi, B. Grubbs, S.S. Padalecki, S.A. Munoz, A. Gupta, et al., The Hedgehog Signaling Molecule Gli2 Induces Parathyroid Hormone-Related Peptide Expression and Osteolysis in Metastatic Human Breast Cancer Cells. Cancer Research, 2006. 66(15): p. 7548-7553.

85. Johnson, R.W., M.P. Nguyen, S.S. Padalecki, B.G. Grubbs, A.R. Merkel, B.O. Oyajobi, et al., TGF-beta promotion of Gli2-induced expression of parathyroid hormone-related protein, an important osteolytic factor in bone metastasis, is independent of canonical Hedgehog signaling. Cancer Res, 2011. 71(3): p. 822-31.

86. Javelaud, D., K.S. Mohammad, C.R. McKenna, P. Fournier, F. Luciani, M. Niewolna, et al., Stable Overexpression of Smad7 in Human Melanoma Cells Impairs Bone Metastasis. Cancer Research, 2007. 67(5): p. 2317-2324.

87. Mohammad, K.S., D. Javelaud, P.G.J. Fournier, M. Niewolna, C.R. McKenna, X.H. Peng, et al., TGF-β-RI Kinase Inhibitor SD-208 Reduces the Development and Progression of Melanoma Bone Metastases. Cancer research, 2011. 71(1): p. 175-184.

88. Biswas, S., J.S. Nyman, J. Alvarez, A. Chakrabarti, A. Ayres, J. Sterling, et al., Anti-Transforming Growth Factor ß Antibody Treatment Rescues Bone Loss and Prevents Breast Cancer Metastasis to Bone. PLoS ONE, 2011. 6(11): p. e27090.

89. Ottewell, P.D., The role of osteoblasts in bone metastasis. Journal of Bone Oncology, 2016. 5(3): p. 124-127.

90. Ernst, D.S., I.F. Tannock, E.W. Winquist, P.M. Venner, L. Reyno, M.J. Moore, et al., Randomized, Double-Blind, Controlled Trial of Mitoxantrone/Prednisone and Clodronate Versus Mitoxantrone/Prednisone and Placebo in Patients With Hormone-Refractory Prostate Cancer and Pain. Journal of Clinical Oncology, 2003. 21(17): p. 3335-3342.

91. Saad, F., G. For the Zoledronic Acid Prostate Cancer Study, D.M. Gleason, G. For the Zoledronic Acid Prostate Cancer Study, R. Murray, G. For the Zoledronic Acid Prostate Cancer Study, et al., Long-Term Efficacy of Zoledronic Acid for the Prevention of Skeletal

Complications in Patients With Metastatic Hormone-Refractory Prostate Cancer. JNCI: Journal of the National Cancer Institute, 2004. 96(11): p. 879-882.

92. Ruppender, N.S., A.R. Merkel, T.J. Martin, G.R. Mundy, J.A. Sterling, and S.A. Guelcher, Matrix Rigidity Induces Osteolytic Gene Expression of Metastatic Breast Cancer Cells. PLoS ONE, 2010. 5(11): p. e15451.

93. Page, J.M., A.R. Merkel, N.S. Ruppender, R. Guo, U.C. Dadwal, S. Cannonier, et al., Matrix Rigidity Regulates the Transition of Tumor Cells to a Bone-Destructive Phenotype through Integrin β3 and TGF-β Receptor Type II. Biomaterials, 2015. 64: p. 33-44.

94. Thomas, R.J., T.A. Guise, J.J. Yin, J. Elliott, N.J. Horwood, T.J. Martin, et al., Breast cancer cells interact with osteoblasts to support osteoclast formation. Endocrinology, 1999. 140(10): p. 4451-8.

95. Guise, T.A., J.J. Yin, S.D. Taylor, Y. Kumagai, M. Dallas, B.F. Boyce, et al., Evidence for a causal role of parathyroid hormone-related protein in the pathogenesis of human breast cancer-mediated osteolysis. Journal of Clinical Investigation, 1996. 98(7): p. 1544-1549.

96. Thomas, R.J., T.A. Guise, J.J. Yin, J. Elliott, N.J. Horwood, T.J. Martin, et al., Breast Cancer Cells Interact with Osteoblasts to Support Osteoclast Formation. Endocrinology, 1999. 140(10): p. 4451-4458.

97. Johnson, R.W., Y. Sun, P.W.M. Ho, A.S.M. Chan, J.A. Johnson, N.J. Pavlos, et al., Parathyroid Hormone-Related Protein Negatively Regulates Tumor Cell Dormancy Genes in a PTHR1/Cyclic AMP-Independent Manner. Frontiers in Endocrinology, 2018. 9: p. 241.

98. Lu, X., E. Mu, Y. Wei, S. Riethdorf, Q. Yang, M. Yuan, et al., VCAM-1 promotes osteolytic expansion of indolent bone micrometastasis of breast cancer by engaging alpha4beta1-positive osteoclast progenitors. Cancer Cell, 2011. 20(6): p. 701-14.

99. Lawson, M.A., M.M. McDonald, N. Kovacic, W. Hua Khoo, R.L. Terry, J. Down, et al., Osteoclasts control reactivation of dormant myeloma cells by remodelling the endosteal niche. Nat Commun, 2015. 6: p. 8983.

100. Campisi, J., Aging, Cellular Senescence, and Cancer. Annual review of physiology, 2013. 75: p. 685-705.

101. Clarke, B.L. and S. Khosla, Androgens and Bone. Steroids, 2009. 74(3): p. 296-305.

102. Smith, E.P., B. Specker, and K.S. Korach, Recent experimental and clinical findings in the skeleton associated with loss of estrogen hormone or estrogen receptor activity(). The Journal of steroid biochemistry and molecular biology, 2010. 118(4-5): p. 264-272.

103. Nakamura, T., Y. Imai, T. Matsumoto, S. Sato, K. Takeuchi, K. Igarashi, et al., Estrogen Prevents Bone Loss via Estrogen Receptor α and Induction of Fas Ligand in Osteoclasts. Cell, 2007. 130(5): p. 811-823.

104. Ottewell, P.D., N. Wang, H.K. Brown, C.A. Fowles, P.I. Croucher, C.L. Eaton, et al., OPG-Fc inhibits ovariectomy-induced growth of disseminated breast cancer cells in bone. Int J Cancer, 2015. 137(4): p. 968-77.

105. Morrissey, C., M.P. Roudier, A. Dowell, L.D. True, M. Ketchanji, C. Welty, et al., Effects of androgen deprivation therapy and bisphosphonate treatment on bone in patients with metastatic castration-resistant prostate cancer: Results from the University of Washington Rapid Autopsy Series. Journal of Bone and Mineral Research, 2013. 28(2): p. 333-340.

106. Smith, M.R., R.E. Coleman, L. Klotz, K. Pittman, P. Milecki, S. Ng, et al., Denosumab for the prevention of skeletal complications in metastatic castration-resistant prostate cancer: comparison of skeletal-related events and symptomatic skeletal events. Annals of Oncology, 2015. 26(2): p. 368-374.

107. Fizazi, K., M. Carducci, M. Smith, R. Damião, J. Brown, L. Karsh, et al., Denosumab versus zoledronic acid for treatment of bone metastases in men with castration-resistant prostate cancer: a randomised, double-blind study. The Lancet, 2011. 377(9768): p. 813-822.

108. Sun, Y.X., A. Schneider, Y. Jung, J. Wang, J. Dai, J. Wang, et al., Skeletal localization and neutralization of the SDF-1(CXCL12)/CXCR4 axis blocks prostate cancer metastasis and growth in osseous sites in vivo. J Bone Miner Res, 2005. 20(2): p. 318-29.

109. Conley-LaComb, M.K., L. Semaan, R. Singareddy, Y. Li, E.I. Heath, S. Kim, et al., Pharmacological targeting of CXCL12/CXCR4 signaling in prostate cancer bone metastasis. Mol Cancer, 2016. 15(1): p. 68.

110. Zhao, Y., R. Bachelier, I. Treilleux, P. Pujuguet, O. Peyruchaud, R. Baron, et al., Tumor alphavbeta3 integrin is a therapeutic target for breast cancer bone metastases. Cancer Res, 2007. 67(12): p. 5821-30.

111. Khalili, P., A. Arakelian, G. Chen, M.L. Plunkett, I. Beck, G.C. Parry, et al., A non-RGD-based integrin binding peptide (ATN-161) blocks breast cancer growth and metastasis in vivo. Mol Cancer Ther, 2006. 5(9): p. 2271-80.

112. Brooks, P., R. Clark, and D. Cheresh, Requirement of vascular integrin alpha v beta 3 for angiogenesis. Science, 1994. 264(5158): p. 569-571.

113. Cirkel, G.A., B.M. Kerklaan, F. Vanhoutte, A.V. der Aa, G. Lorenzon, F. Namour, et al., A dose escalating phase I study of GLPG0187, a broad spectrum integrin receptor antagonist, in adult patients with progressive high-grade glioma and other advanced solid malignancies. Investigational New Drugs, 2016. 34: p. 184-192.

114. Hersey, P., J. Sosman, S. O'Day, J. Richards, A. Bedikian, R. Gonzalez, et al., A randomized phase 2 study of etaracizumab, a monoclonal antibody against integrin αvβ3, ± dacarbazine in patients with stage IV metastatic melanoma. Cancer, 2010. 116(6): p. 1526-1534.

115. Bierie, B. and H.L. Moses, TGFβ: the molecular Jekyll and Hyde of cancer. Nature Reviews Cancer, 2006. 6: p. 506.

116. Raymaekers, K., S. Stegen, N. van Gastel, and G. Carmeliet, The vasculature: a vessel for bone metastasis. BoneKEy Rep, 2015.

117. El Touny, L.H., A. Vieira, A. Mendoza, C. Khanna, M.J. Hoenerhoff, and J.E. Green, Combined SFK/MEK inhibition prevents metastatic outgrowth of dormant tumor cells. The Journal of Clinical Investigation, 2014. 124(1): p. 156-168.

118. Ghajar, C.M., Metastasis prevention by targeting the dormant niche. Nature reviews. Cancer, 2015. 15(4): p. 238-247.

119. Morera, L., M. Lübbert, and M. Jung, Targeting histone methyltransferases and demethylases in clinical trials for cancer therapy. Clinical epigenetics, 2016. 8: p. 57-57.

120. Lawrence, M., S. Daujat, and R. Schneider, Lateral Thinking: How Histone Modifications Regulate Gene Expression. Trends in Genetics, 2016. 32(1): p. 42-56.

121. Li, Y. and E. Seto, HDACs and HDAC Inhibitors in Cancer Development and Therapy. Cold Spring Harbor perspectives in medicine, 2016. 6(10): p. a026831.

122. Kratzsch, T., S.A. Kuhn, A. Joedicke, U.K. Hanisch, P. Vajkoczy, J. Hoffmann, et al., Treatment with 5-azacitidine delay growth of glioblastoma xenografts: a potential new treatment approach for glioblastomas. Journal of Cancer Research and Clinical Oncology, 2018. 144(5): p. 809-819.

123. Thakur, S., X. Feng, Z. Qiao Shi, A. Ganapathy, M. Kumar Mishra, P. Atadja, et al., ING1 and 5-Azacytidine Act Synergistically to Block Breast Cancer Cell Growth. PLOS ONE, 2012. 7(8): p. e43671.

124. Xu, J., J.-Y. Zhou, M.A. Tainsky, and G.S. Wu, Evidence that Tumor Necrosis Factor–Related Apoptosis-Inducing Ligand Induction by 5-Aza-2′-Deoxycytidine Sensitizes Human Breast Cancer Cells to Adriamycin. Cancer Research, 2007. 67(3): p. 1203-1211.

125. Rodríguez-Paredes, M. and M. Esteller, Cancer epigenetics reaches mainstream oncology. Nature Medicine, 2011. 17: p. 330.

126. Connolly, R.M., H. Li, R.C. Jankowitz, Z. Zhang, M.A. Rudek, S.C. Jeter, et al., Combination Epigenetic Therapy in Advanced Breast Cancer with 5-Azacitidine and Entinostat: A Phase II National Cancer Institute/Stand Up to Cancer Study. Clinical cancer research : an official journal of the American Association for Cancer Research, 2017. 23(11): p. 2691-2701.

127. Seto, E. and M. Yoshida, Erasers of histone acetylation: the histone deacetylase enzymes. Cold Spring Harb Perspect Biol, 2014. 6(4): p. a018713.

128. McGee-Lawrence, M.E., A.L. McCleary-Wheeler, F.J. Secreto, D.F. Razidlo, M. Zhang, B.A. Stensgard, et al., Suberoylanilide hydroxamic acid (SAHA; vorinostat) causes bone loss by inhibiting immature osteoblasts. Bone, 2011. 48(5): p. 1117-26.

129. Senn, S.M., S. Kantor, I.J. Poulton, M.J. Morris, N.A. Sims, T.J. O'Brien, et al., Adverse effects of valproate on bone: Defining a model to investigate the pathophysiology. Epilepsia, 2010. 51(6): p. 984-993.

130. Pratap, J., J. Akech, J.J. Wixted, G. Szabo, S. Hussain, M.E. McGee-Lawrence, et al., The Histone Deacetylase Inhibitor, Vorinostat, Reduces Tumor Growth at the Metastatic

Bone Site and Associated Osteolysis, but Promotes Normal Bone Loss. Molecular Cancer Therapeutics, 2010. 9(12): p. 3210-3220.

131. Ren, G., M. Esposito, and Y. Kang, Bone metastasis and the metastatic niche. J Mol Med (Berl), 2015. 93(11): p. 1203-12.

132. Campbell, J.P., A.R. Merkel, S.K. Masood-Campbell, F. Elefteriou, and J.A. Sterling, Models of bone metastasis. J Vis Exp, 2012(67): p. e4260.

133. Wright, L.E., P.D. Ottewell, N. Rucci, O. Peyruchaud, G.M. Pagnotti, A. Chiechi, et al., Murine models of breast cancer bone metastasis. BoneKEy Reports, 2016. 5: p. 804.

134. Peyruchaud, O., B. Winding, I. Pécheur, C.-M. Serre, P. Delmas, and P. Clézardin, Early Detection of Bone Metastases in a Murine Model Using Fluorescent Human Breast Cancer Cells: Application to the Use of the Bisphosphonate Zoledronic Acid in the Treatment of Osteolytic Lesions. Journal of Bone and Mineral Research, 2001. 16(11): p. 2027-2034.

135. Sowder, M.E. and R.W. Johnson, Enrichment and detection of bone disseminated tumor cells in models of low tumor burden. Scientific Reports, 2018. 8: p. 14299.

136. Barkan, D., H. Kleinman, J.L. Simmons, H. Asmussen, A.K. Kamaraju, M.J. Hoenorhoff, et al., Inhibition of metastatic outgrowth from single dormant tumor cells by targeting the cytoskeleton. Cancer Res, 2008. 68(15): p. 6241-50.

137. Dall, G., J. Vieusseux, A. Unsworth, R. Anderson, and K. Britt, Low Dose, Low Cost Estradiol Pellets Can Support MCF-7 Tumour Growth in Nude Mice without Bladder Symptoms. J Cancer, 2015. 6(12): p. 1331-6.

138. Gustafsson, K.L., H. Farman, P. Henning, V. Lionikaite, S. Moverare-Skrtic, J. Wu, et al., The role of membrane ERalpha signaling in bone and other major estrogen responsive tissues. Sci Rep, 2016. 6: p. 29473.

139. Gakhar, G., M. Wight-Carter, G. Andrews, S. Olson, and T.A. Nguyen, Hydronephrosis and urine retention in estrogen-implanted athymic nude mice. Vet Pathol, 2009. 46(3): p. 505-8.

140. Capietto, A.H., S.R. Chan, B. Ricci, J.A. Allen, X. Su, D.V. Novack, et al., Novel ERalpha positive breast cancer model with estrogen independent growth in the bone microenvironment. Oncotarget, 2016. 7(31): p. 49751-49764.

141. Morris, V.L., A.B. Tuck, S.M. Wilson, D. Percy, and A.F. Chambers, Tumor progression and metastasis in murine D2 hyperplastic alveolar nodule mammary tumor cell lines. Clinical & Experimental Metastasis, 1993. 11(1): p. 103-112.

142. Yoneda, T., A. Sasaki, and G.R. Mundy, Osteolytic bone metastasis in breast cancer. Breast Cancer Research and Treatment, 1994. 32(1): p. 73-84.

143. Kusuma, N., A. Burrows, X. Ling, L. Jupp, R.L. Anderson, and N. Pouliot, Bone-derived soluble factors and laminin-511 cooperate to promote migration, invasion and survival of

bone-metastatic breast tumor cells AU - Denoyer, Delphine. Growth Factors, 2014. 32(2): p. 63-73.

144. Cerami, E., J. Gao, U. Dogrusoz, B.E. Gross, S.O. Sumer, B.A. Aksoy, et al., The cBio Cancer Genomics Portal: An Open Platform for Exploring Multidimensional Cancer Genomics Data. Cancer Discovery, 2012. 2(5): p. 401-404.

145. Gao, J., B.A. Aksoy, U. Dogrusoz, G. Dresdner, B. Gross, S.O. Sumer, et al., Integrative Analysis of Complex Cancer Genomics and Clinical Profiles Using the cBioPortal. Science signaling, 2013. 6(269): p. pl1-pl1.

146. Coleman, R.E., Clinical features of metastatic bone disease and risk of skeletal morbidity. Clin Cancer Res, 2006. 12(20 Pt 2): p. 6243s-6249s.

147. Weilbaecher, K.N., T.A. Guise, and L.K. McCauley, Cancer to bone: a fatal attraction. Nat Rev Cancer, 2011. 11(6): p. 411-25.

148. Senft, D. and Z.e.A. Ronai, Adaptive Stress Responses During Tumor Metastasis and Dormancy. Trends in cancer, 2016. 2(8): p. 429-442.

149. Gomis, R.R. and S. Gawrzak, Tumor cell dormancy. Mol Oncol, 2016.

150. Croucher, P.I., M.M. McDonald, and T.J. Martin, Bone metastasis: the importance of the neighbourhood. Nat Rev Cancer, 2016. 16(6): p. 373-86.

151. Kan, C., G. Vargas, F. Le Pape, and P. Clézardin, Cancer Cell Colonisation in the Bone Microenvironment. International Journal of Molecular Sciences, 2016. 17(10): p. 1674.

152. Dasgupta, A., A.R. Lim, and C.M. Ghajar, Circulating and disseminated tumor cells: harbingers or initiators of metastasis? Mol Oncol, 2017. 11(1): p. 40-61.

153. Han, H.H., S.H. Lee, B.G. Kim, J.H. Lee, S. Kang, and N.H. Cho, Estrogen Receptor Status Predicts Late-Onset Skeletal Recurrence in Breast Cancer Patients. Medicine (Baltimore), 2016. 95(8): p. e2909.

154. Savci-Heijink, C.D., H. Halfwerk, G.K.J. Hooijer, H.M. Horlings, J. Wesseling, and M.J. van de Vijver, Retrospective analysis of metastatic behaviour of breast cancer subtypes. Breast Cancer Res Treat, 2015. 150(3): p. 547-57.

155. Ogba, N., N.G. Manning, B.S. Bliesner, S.K. Ambler, J.M. Haughian, M.P. Pinto, et al., Luminal breast cancer metastases and tumor arousal from dormancy are promoted by direct actions of estradiol and progesterone on the malignant cells. Breast Cancer Res, 2014. 16(6): p. 489.

156. Lawson, D.A., N.R. Bhakta, K. Kessenbrock, K.D. Prummel, Y. Yu, K. Takai, et al., Single-cell analysis reveals a stem-cell program in human metastatic breast cancer cells. Nature, 2015. 526(7571): p. 131-5.

157. Kowalik, A., M. Kowalewska, and S. Gozdz, Current approaches for avoiding the limitations of circulating tumor cells detection methods-implications for diagnosis and treatment of patients with solid tumors. Transl Res, 2017. 185: p. 58-84 e15.

158. Yu, M., A. Bardia, B.S. Wittner, S.L. Stott, M.E. Smas, D.T. Ting, et al., Circulating Breast Tumor Cells Exhibit Dynamic Changes in Epithelial and Mesenchymal Composition. Science, 2013. 339(6119): p. 580-584.

159. Holen, I., M. Walker, F. Nutter, A. Fowles, C.A. Evans, C.L. Eaton, et al., Oestrogen receptor positive breast cancer metastasis to bone: inhibition by targeting the bone microenvironment in vivo. Clin Exp Metastasis, 2016. 33(3): p. 211-24.

160. Braun, S., K. Pantel, P. Müller, W. Janni, F. Hepp, C.R.M. Kentenich, et al., Cytokeratin-Positive Cells in the Bone Marrow and Survival of Patients with Stage I, II, or III Breast Cancer. New England Journal of Medicine, 2000. 342(8): p. 525-533.

161. Walker, E.C., R.W. Johnson, Y. Hu, H.J. Brennan, I.J. Poulton, J.-G. Zhang, et al., Murine Oncostatin M Acts via Leukemia Inhibitory Factor Receptor to Phosphorylate Signal Transducer and Activator of Transcription 3 (STAT3) but Not STAT1, an Effect That Protects Bone Mass. The Journal of Biological Chemistry, 2016. 291(41): p. 21703-21716.

162. Van Keymeulen, A., A.S. Rocha, M. Ousset, B. Beck, G. Bouvencourt, J. Rock, et al., Distinct stem cells contribute to mammary gland development and maintenance. Nature, 2011. 479: p. 189.

163. Inman, J.L., C. Robertson, J.D. Mott, and M.J. Bissell, Mammary gland development: cell fate specification, stem cells and the microenvironment. Development, 2015. 142(6): p. 1028-1042.

164. Ganapathy, V., W. Banach-Petrosky, W. Xie, A. Kareddula, H. Nienhuis, G. Miles, et al., Luminal breast cancer metastasis is dependent on estrogen signaling. Clinical & experimental metastasis, 2012. 29(5): p. 10.1007/s10585-012-9466-4.

165. Eyles, J., A.-L. Puaux, X. Wang, B. Toh, C. Prakash, M. Hong, et al., Tumor cells disseminate early, but immunosurveillance limits metastatic outgrowth, in a mouse model of melanoma. The Journal of Clinical Investigation, 2010. 120(6): p. 2030-2039.

166. Romero, I., C. Garrido, I. Algarra, A. Collado, F. Garrido, and A.M. Garcia-Lora, T Lymphocytes Restrain Spontaneous Metastases in Permanent Dormancy. Cancer Research, 2014. 74(7): p. 1958-1968.

167. Gonzalez, H., I. Robles, and Z. Werb, Innate and acquired immune surveillance in the postdissemination phase of metastasis. The FEBS Journal: p. n/a-n/a.

168. Fillmore, C.M. and C. Kuperwasser, Human breast cancer cell lines contain stem-like cells that self-renew, give rise to phenotypically diverse progeny and survive chemotherapy. Breast Cancer Research : BCR, 2008. 10(2): p. R25-R25.

169. Perou, C.M., Molecular stratification of triple-negative breast cancers. Oncologist, 2010. 15 Suppl 5: p. 39-48.

170. Comprehensive molecular portraits of human breast tumours. Nature, 2012. 490(7418): p. 61-70.

171. Savci-Heijink, C.D., H. Halfwerk, G.K. Hooijer, H.M. Horlings, J. Wesseling, and M.J. van de Vijver, Retrospective analysis of metastatic behaviour of breast cancer subtypes. Breast Cancer Res Treat, 2015. 150(3): p. 547-57.

172. Eddaoudi, A., S.L. Canning, and I. Kato, Flow Cytometric Detection of G0 in Live Cells by Hoechst 33342 and Pyronin Y Staining, in Cellular Quiescence: Methods and Protocols, H.D. Lacorazza, Editor. 2018, Springer New York: New York, NY. p. 49-57.

173. Kim, K.H. and J.M. Sederstrom, Assaying Cell Cycle Status Using Flow Cytometry. Curr Protoc Mol Biol, 2015. 111: p. 28 6 1-11.

174. Aguirre-Ghiso, J.A., Models, mechanisms and clinical evidence for cancer dormancy. Nature Reviews Cancer, 2007. 7: p. 834.

175. Early Breast Cancer Trialists' Collaborative, G., Comparisons between different polychemotherapy regimens for early breast cancer: meta-analyses of long-term outcome among 100 000 women in 123 randomised trials. Lancet, 2012. 379(9814): p. 432-444.

176. Schröder, J., T. Fietz, A. Köhler, V. Petersen, H. Tesch, L. Spring, et al., Treatment and pattern of bone metastases in 1094 patients with advanced breast cancer – Results from the prospective German Tumour Registry Breast Cancer cohort study. European Journal of Cancer, 2017. 79: p. 139-148.

177. Hsieh, C.-Y., R.C. Santell, S.Z. Haslam, and W.G. Helferich, Estrogenic Effects of Genistein on the Growth of Estrogen Receptor-positive Human Breast Cancer (MCF-7) Cells in Vitro and in Vivo. Cancer Research, 1998. 58(17): p. 3833-3838.

178. Liu, Y., D. El-Ashry, D. Chen, I.Y.F. Ding, and F.G. Kern, MCF-7 breast cancer cells overexpressing transfectedc-erbB-2 have anin vitro growth advantage in estrogen-depleted conditions and reduced estrogen-dependence and tamoxifen-sensitivityin vivo. Breast Cancer Research and Treatment, 1995. 34(2): p. 97-117.

179. Gottardis, M.M., S.P. Robinson, and V.C. Jordan, Estradiol-stimulated growth of MCF-7 tumors implanted in athymic mice: A model to study the tumoristatic action of tamoxifen. Journal of Steroid Biochemistry, 1988. 30(1): p. 311-314.

180. Lee, A.V., S. Oesterreich, and N.E. Davidson, MCF-7 Cells—Changing the Course of Breast Cancer Research and Care for 45 Years. JNCI: Journal of the National Cancer Institute, 2015. 107(7): p. djv073-djv073.

181. Sosa, M.S., C. Lopez-Haber, C. Yang, H. Wang, M.A. Lemmon, J.M. Busillo, et al., Identification of the Rac-GEF P-REX1 as an essential mediator of ErbB signaling in breast cancer. Molecular cell, 2010. 40(6): p. 877-892.

182. Marotti, J.D., K.E. Muller, L.J. Tafe, E. Demidenko, and T.W. Miller, P-Rex1 Expression in Invasive Breast Cancer in relation to Receptor Status and Distant Metastatic Site. International Journal of Breast Cancer, 2017. 2017: p. 4537532.

183. Dillon, L.M., J.R. Bean, W. Yang, K. Shee, L.K. Symonds, J.M. Balko, et al., P-REX1 creates a positive feedback loop to activate growth factor receptor, PI3K/AKT, and MEK/ERK signaling in breast cancer. Oncogene, 2015. 34(30): p. 3968-3976.

184. Ebi, H., C. Costa, A.C. Faber, M. Nishtala, H. Kotani, D. Juric, et al., PI3K regulates MEK/ERK signaling in breast cancer via the Rac-GEF, P-Rex1. Proceedings of the National Academy of Sciences, 2013. 110(52): p. 21124-21129.

185. Montero, J.C., S. Seoane, A. Ocaña, and A. Pandiella, P-Rex1 participates in Neuregulin-ErbB signal transduction and its expression correlates with patient outcome in breast cancer. Oncogene, 2010. 30: p. 1059.

186. Lindsay, C.R., S. Lawn, A.D. Campbell, W.J. Faller, F. Rambow, R.L. Mort, et al., P-Rex1 is required for efficient melanoblast migration and melanoma metastasis. Nature Communications, 2011. 2: p. 555.

187. Qin, J., Y. Xie, B. Wang, M. Hoshino, D.W. Wolff, J. Zhao, et al., Upregulation of PIP3-Dependent Rac Exchanger 1 (P-Rex1) Promotes Prostate Cancer Metastasis. Oncogene, 2009. 28(16): p. 1853-1863.

188. Kremer, K.N., B.A. Dinkel, R.M. Sterner, D.G. Osborne, D. Jevremovic, and K.E. Hedin, TCR-CXCR4 signaling stabilizes cytokine mRNA transcripts via a PREX1-Rac1 pathway: implications for CTCL. Blood, 2017. 130(8): p. 982-994.

189. Guo, X. and X.-F. Wang, Signaling cross-talk between TGF-β/BMP and other pathways. Cell research, 2009. 19(1): p. 71-88.

190. Neuzillet, C., A. Tijeras-Raballand, R. Cohen, J. Cros, S. Faivre, E. Raymond, et al., Targeting the TGFβ pathway for cancer therapy. Pharmacology & Therapeutics, 2015. 147: p. 22-31.

191. Rahman, M.S., N. Akhtar, H.M. Jamil, R.S. Banik, and S.M. Asaduzzaman, TGF-β/BMP signaling and other molecular events: regulation of osteoblastogenesis and bone formation. Bone Research, 2015. 3: p. 15005.

192. Barrio-Real, L., C. Lopez-Haber, V. Casado-Medrano, A.G. Goglia, J.E. Toettcher, M.J. Caloca, et al., P-Rex1 is dispensable for Erk activation and mitogenesis in breast cancer. Oncotarget, 2018. 9(47): p. 28612-28624.

193. Ryan, M.B., A.J. Finn, K.H. Pedone, N.E. Thomas, C.J. Der, and A.D. Cox, ERK/MAPK Signaling Drives Overexpression of the Rac-GEF, PREX1, in BRAF- and NRAS-mutant Melanoma. Molecular cancer research : MCR, 2016. 14(10): p. 1009-1018.

194. Gont, A., M. Daneshmand, J. Woulfe, S.J. Lavictoire, and I.A.J. Lorimer, PREX1 integrates G protein-coupled receptor and phosphoinositide 3-kinase signaling to promote glioblastoma invasion. Oncotarget, 2017. 8(5): p. 8559-8573.

195. Liu, H.-J., L.M. Ooms, N. Srijakotre, J. Man, J. Vieusseux, J.E. Waters, et al., PtdIns(3,4,5)P(3)-dependent Rac Exchanger 1 (PREX1) Rac-Guanine Nucleotide Exchange Factor (GEF) Activity Promotes Breast Cancer Cell Proliferation and Tumor

Growth via Activation of Extracellular Signal-regulated Kinase 1/2 (ERK1/2) Signaling. The Journal of Biological Chemistry, 2016. 291(33): p. 17258-17270.

196. Cheng, W.-Y., T.-H.O. Yang, and D. Anastassiou, Development of a Prognostic Model for Breast Cancer Survival in an Open Challenge Environment. Science Translational Medicine, 2013. 5(181): p. 181ra50-181ra50.

197. Falkenberg, K.J. and R.W. Johnstone, Histone deacetylases and their inhibitors in cancer, neurological diseases and immune disorders. Nat Rev Drug Discov, 2014. 13(9): p. 673-91.

198. West, A.C. and R.W. Johnstone, New and emerging HDAC inhibitors for cancer treatment. J Clin Invest, 2014. 124(1): p. 30-9.

199. Eckschlager, T., J. Plch, M. Stiborova, and J. Hrabeta, Histone Deacetylase Inhibitors as Anticancer Drugs. Int J Mol Sci, 2017. 18(7).

200. Zeng, H., J. Qu, N. Jin, J. Xu, C. Lin, Y. Chen, et al., Feedback Activation of Leukemia Inhibitory Factor Receptor Limits Response to Histone Deacetylase Inhibitors in Breast Cancer. Cancer Cell, 2016. 30(3): p. 459-473.

201. Almog, N., L. Ma, R. Raychowdhury, C. Schwager, R. Erber, S. Short, et al., Transcriptional Switch of Dormant Tumors to Fast-Growing Angiogenic Phenotype. Cancer Research, 2009. 69(3): p. 836-844.

202. Oki, T., K. Nishimura, J. Kitaura, K. Togami, A. Maehara, K. Izawa, et al., A novel cell-cycle-indicator, mVenus-p27K-, identifies quiescent cells and visualizes G0-G1 transition. Scientific reports, 2014. 4: p. 4012-4012.

203. Pernodet, N., F. Hermetet, P. Adami, A. Vejux, F. Descotes, C. Borg, et al., High expression of QSOX1 reduces tumorogenesis, and is associated with a better outcome for breast cancer patients. Breast cancer research : BCR, 2012. 14(5): p. R136-R136.

204. Almog, N., C. Briggs, A. Beheshti, L. Ma, K.P. Wilkie, E. Rietman, et al., Transcriptional changes induced by the tumor dormancy-associated microRNA-190. Transcription, 2013. 4(4): p. 177-191.

205. Onder, T.T., N. Kara, A. Cherry, A.U. Sinha, N. Zhu, K.M. Bernt, et al., Chromatin-modifying enzymes as modulators of reprogramming. Nature, 2012. 483(7391): p. 598-602.

206. Al-Hajj, M., M.S. Wicha, A. Benito-Hernandez, S.J. Morrison, and M.F. Clarke, Prospective identification of tumorigenic breast cancer cells. Proceedings of the National Academy of Sciences, 2003. 100(7): p. 3983-3988.

207. Chaffer, C.L., I. Brueckmann, C. Scheel, A.J. Kaestli, P.A. Wiggins, L.O. Rodrigues, et al., Normal and neoplastic nonstem cells can spontaneously convert to a stem-like state. Proceedings of the National Academy of Sciences, 2011. 108(19): p. 7950-7955.

208. Lower, E.E., E.L. Glass, D.A. Bradley, R. Blau, and S. Heffelfinger, Impact of metastatic estrogen receptor and progesterone receptor status on survival. Breast Cancer Research and Treatment, 2005. 90(1): p. 65-70.

209. Broom, R.J., P.A. Tang, C. Simmons, L. Bordeleau, A.M. Mulligan, F.P. O'Malley, et al., Changes in Estrogen Receptor, Progesterone Receptor and Her-2/neu Status with Time: Discordance Rates Between Primary and Metastatic Breast Cancer. Anticancer Research, 2009. 29(5): p. 1557-1562.

210. Sighoko, D., J. Liu, N. Hou, P. Gustafson, and D. Huo, Discordance in hormone receptor status among primary, metastatic, and second primary breast cancers: biological difference or misclassification? The oncologist, 2014. 19(6): p. 592-601.

211. Lower, E.E., S. Khan, D. Kennedy, and R.P. Baughman, Discordance of the estrogen receptor and HER-2/neu in breast cancer from primary lesion to first and second metastatic site. Breast cancer (Dove Medical Press), 2017. 9: p. 515-520.

212. Douglas, A.M., G.A. Goss, R.L. Sutherland, D.J. Hilton, M.C. Berndt, N.A. Nicola, et al., Expression and function of members of the cytokine receptor superfamily on breast cancer cells. Oncogene, 1997. 14: p. 661.

213. Douglas, A.M., S.L. Grant, G.A. Gross, D.R. Clouston, R.L. Sutherland, and C.G. Begley, Oncostatin M induces the differentiation of breast cancer cells. International Journal of Cancer, 1998. 75(1): p. 64-73.

214. Glozak, M.A., N. Sengupta, X. Zhang, and E. Seto, Acetylation and deacetylation of non-histone proteins. Gene, 2005. 363: p. 15-23.

215. Linde, N., G. Fluegen, and J.A. Aguirre-Ghiso, The Relationship Between Dormant Cancer Cells and Their Microenvironment. Advances in cancer research, 2016. 132: p. 45-71.

216. Spencer, J.A., F. Ferraro, E. Roussakis, A. Klein, J. Wu, J.M. Runnels, et al., Direct measurement of local oxygen concentration in the bone marrow of live animals. Nature, 2014. 508(7495): p. 269-73.

217. Chow, D.C., L.A. Wenning, W.M. Miller, and E.T. Papoutsakis, Modeling pO2 Distributions in the Bone Marrow Hematopoietic Compartment. I. Krogh's Model. Biophys J., 2001. 81(2): p. 675-684.

218. Harrison, J.S., P. Rameshwar, V. Chang, and P. Bandari, Oxygen saturation in the bone marrow of healthy volunteers. Blood, 2002. 99(1): p. 394.

219. Yang, M.-H., M.-Z. Wu, S.-H. Chiou, P.-M. Chen, S.-Y. Chang, C.-J. Liu, et al., Direct regulation of TWIST by HIF-1α promotes metastasis. Nature Cell Biology, 2008. 10: p. 295.

220. Finger, E.C., L. Castellini, E.B. Rankin, M. Vilalta, A.J. Krieg, D. Jiang, et al., Hypoxic induction of AKAP12 variant 2 shifts PKA-mediated protein phosphorylation to enhance migration and metastasis of melanoma cells. Proceedings of the National Academy of Sciences of the United States of America, 2015. 112(14): p. 4441-4446.

221. Erler, J.T., K.L. Bennewith, M. Nicolau, N. Dornhöfer, C. Kong, Q.-T. Le, et al., Lysyl oxidase is essential for hypoxia-induced metastasis. Nature, 2006. 440: p. 1222.

222. Chaturvedi, P., D.M. Gilkes, C.C.L. Wong, Kshitiz, W. Luo, H. Zhang, et al., Hypoxia-inducible factor-dependent breast cancer-mesenchymal stem cell bidirectional signaling promotes metastasis. The Journal of clinical investigation, 2013. 123(1): p. 189-205.

223. Barretina, J., G. Caponigro, N. Stransky, K. Venkatesan, A.A. Margolin, S. Kim, et al., The Cancer Cell Line Encyclopedia enables predictive modelling of anticancer drug sensitivity. Nature, 2012. 483: p. 603.

224. The Cancer Cell Line Encyclopedia, C., N. Stransky, M. Ghandi, G.V. Kryukov, L.A. Garraway, J. Lehár, et al., Pharmacogenomic agreement between two cancer cell line data sets. Nature, 2015. 528: p. 84.

225. Pfister, T.D., W.C. Reinhold, K. Agama, S. Gupta, S.A. Khin, R.J. Kinders, et al., Topoisomerase I levels in the NCI-60 cancer cell line panel determined by validated ELISA and microarray analysis and correlation with indenoisoquinoline sensitivity. Molecular cancer therapeutics, 2009. 8(7): p. 1878-1884.

226. Kohn, K.W., B.M. Zeeberg, W.C. Reinhold, and Y. Pommier, Gene expression correlations in human cancer cell lines define molecular interaction networks for epithelial phenotype. PloS one, 2014. 9(6): p. e99269-e99269.

227. Wang, X.-j., Y. Qiao, M.M. Xiao, L. Wang, J. Chen, W. Lv, et al., Opposing Roles of Acetylation and Phosphorylation in LIFR-Dependent Self-Renewal Growth Signaling in Mouse Embryonic Stem Cells. Cell Reports, 2017. 18(4): p. 933-946.